Diffuse and discrete sources of Galactic X-ray emission

Alex Hands

A thesis submitted to the University of Leicester
for the degree of Doctor of Philosophy

October 2003

X-ray and Observational Astronomy Group
Department of Physics and Astronomy
University of Leicester

Declaration

I hereby declare that no part of this thesis has been previously submitted to this or any other university as part of the requirements for a higher degree. The work described herein was conducted by the under-signed except for contributions from colleagues and other workers who are acknowledged in the text.

Alexander Hands

October 2003

Preface

The work presented in this thesis includes important contributions from colleagues. As my supervisor, Professor Robert Warwick has made significant editorial contributions to all parts of this thesis, however, Chapter 4 in particular is the product of our combined efforts and the results therein are soon to be published in a paper following a very similar format.

Some of the work presented in Chapter 3, specifically the data from the North Polar Spur, has previously been published in a paper written by Dr Richard Willingale and, although some of the conclusions in the chapter differ from the published work, Dr Willingale has also contributed to the discussion of all results in this section.

The remaining sections of this thesis have involved less collaboration and therefore are more predominantly my own work.

Acknowledgements

There are so many people to whom I owe thanks for their help and support over the last three years that inevitably I will forget to mention a name or two. However, I am extremely grateful to the following people for their invaluable advice, assistance, tolerance and friendship during my time at Leicester.

Firstly, I must thank my supervisor, Bob Warwick, for the enormous amount of help he has consistently provided throughout my PhD. I could not have asked for a more patient and diligent supervisor to guide me from my initial bewildered ignorance right through to the torturous process of writing a thesis. I am also especially grateful to Dick Willingale for a countless number of discussions on the soft X-ray background and his ever-present willingness to solve problems arising from the idiosyncrasies of Q.

The time I have spent working has been made considerably easier by the various stress-relieving activities I have shared with others. Therefore I would like to thank everyone I played football with for allowing me to take out any work-related frustrations on their ankles, no hard feelings! Similarly I thank Simon, Nick, Lee, Gary, Andrew and Ann-Marie for not taking it personally on the numerous occasions that squash/tennis balls have narrowly avoided injuring them. On a less physical but equally important note, I thank the entire XBlast crew of Simon, Nick, Darren, James and Darach for providing me with probably far too much practice at a very distracting game! Also I would like to thank Kim and Simon for being excellent office mates and ensuring I almost never needed to unlock or lock-up the office; Tim A for alleviating the tedium of lab demonstrating; Tim R for being a fellow devotee of the coffee room; Kevin for providing unusually sane conversation; Masa for several useful chats about the Galactic Centre; and, of course, all the Taj regulars who have ensured that Friday remains the least productive day of the week. Special thanks go to Simon Good and Nick Schurch who, being common to nearly all the above activities, have been friends from the start and made my time in Leicester much more enjoyable.

Finally my greatest thanks go to those people closest to me. First of all to my Mum, Dad and brother, Ben, for their unshakable belief in me and for reminding me of the more important things in life. But most of all to Sarah, for her amazing support throughout my time as a postgraduate, not just for my work. Her love and encouragement, and her reassuring confidence in me, have been the essential cornerstones of my life for the past three years.

Dedication

This thesis is dedicated to my grandmother, Barbara Winifred Dawkins, who was, and continues to be, my inspiration.

"Nature and Nature's laws lay hid by night.
God said, *'Let Newton be!'* and all was light."

- Alexander Pope

"It did not last, the Devil shouting *'Ho!
Let Einstein be!'* restored the status quo."

- J.C. Squire

Diffuse and discrete sources of Galactic X-ray emission

Alexander D P Hands

Abstract

Our Galaxy is a luminous X-ray source by virtue of its discrete X-ray source populations and various large-scale diffuse processes which produce the ultra-hot interstellar medium. This thesis presents an analysis of the properties of a variety of Galactic X-ray emitting components, based on data from the EPIC CCD cameras onboard ESA's *XMM-NEWTON* satellite observatory. In total 51 individual observations are analysed for which the combined exposure time is nearly 900 ks.

X-ray spectra measured over a wide range in Galactic longitude and latitude are used to disentangle the different components of the diffuse soft X-ray background (SXRB). The SXRB is comprised primarily of a two-temperature Galactic halo, an unabsorbed local hot bubble (LHB) and, in certain directions, an extended plasma "superbubble", all with temperatures in the range 1–3 million K. Observations towards the Galactic Plane provide evidence that the LHB may be larger in extent than has previously been assumed, with some of the emission lying behind an absorption wall with a column density of $N_H \sim 3 \times 10^{20}$ cm^{-2}.

The diffuse hard X-ray phenomenon known as the Galactic ridge is investigated at various locations both on and near to the Galactic Plane. The spectrum of the ridge at high energies is well described by a thermal plasma model with a temperature of $10^{8.0}$ K. The exact nature of this emission is uncertain but several possibilities are discussed in this thesis. The surface brightness of the ridge is measured as $\sim 10^{-10}$ erg s^{-1} cm^{-2} deg^{-2}(2–10 keV), of which ~15% is due to point sources and a further ~2% has been resolved and identified as extended supernova remnants and HII regions

In the region of *XMM-NEWTON* 's X-ray Galactic Plane Survey (XGPS), a total of 424 discrete X-ray sources have been detected. Cumulative log N - log S distributions, including data from other satellites, illustrate how the dominating source population changes from Galactic X-ray binaries at high fluxes to extragalactic objects at fainter fluxes. However, an additional lower luminosity population, possibly associated with cataclysmic variables and RS CVns, appears to contribute significantly at intermediate X-ray fluxes.

Contents

List of Figures

List of Tables

Chapter 1

Introduction

1.1 On the origin of X-rays

X-rays occupy a high energy section of the electromagnetic spectrum with energies in the range 0.1 to 100 keV, corresponding to a wavelength range of 124 to 0.124Å. X-rays can be readily produced in the laboratory by replicating the original experiment of Röntgen in which electrons were accelerated towards a crystalline target which subsequently started emitting X-rays due to fluorescence. In astrophysical terms, however, several different mechanisms exist for the production of X-rays. These can be divided into two types:thermal and non-thermal.

1.1.1 Thermal processes

Thermal processes may be defined as those generated by a particle population, usually electron dominated, which follows a Maxwellian distribution, *i.e.* is in thermal equilibrium. The simplest form of is blackbody radiation. Any object with a non-zero temperature emits radiation and for a perfect emitter the intensity distribution of such radiation follows Planck's law with a peak level determined entirely by temperature. Blackbody radiation is generally a good approximation for stellar emission as stars are near perfect emitters, although the emission is modified by absorption in the stellar atmosphere. Also derived from a thermal electron population is thermal bremsstrahlung emission. This occurs when electrons (or other charged particles) undergo acceleration in the electrostatic field of surrounding ions (see Figure 1.1(a)). Bremsstrahlung radiation also has a characteristic distribution which enables determination of the temperature of the emitting material from analysis of the spectrum. Bremsstrahlung dominates the continuum emission from optically thin plasmas emitting in the X-ray band although other features arising from processes involving bound electron states, such as emission edges produced by radiative recombination, are also present.

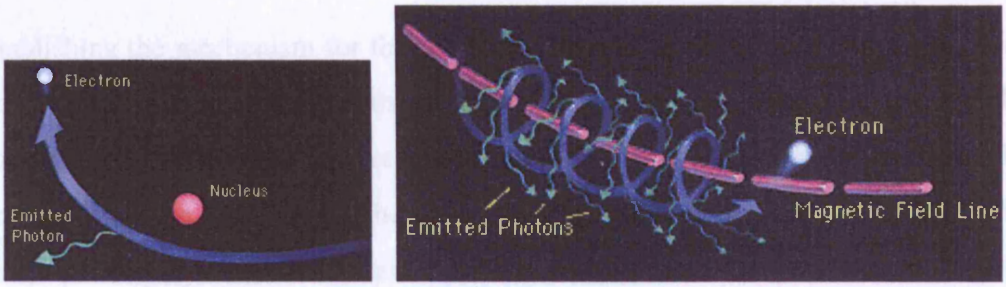

(a) Bremsstrahlung (b) Synchrotron

FIGURE 1.1. Graphical representations of bremsstrahlung and synchrotron emission processes. Bremsstrahlung is described as thermal if the population of electrons follows a Maxwellian distribution, whereas synchrotron emission is always non-thermal and requires the presence of a magnetic field and electrons moving at relativistic speeds.

1.1.2 Non-thermal processes

Non-thermal emission mechanisms are also very important in understanding the spectral characteristics of astrophysical X-ray sources. Firstly there is non-thermal bremsstrahlung radiation which is produced in the same way as thermal bremsstrahlung but from an electron population with a non-Maxwellian distribution, for example cosmic ray electrons. Other important non-thermal production mechanisms include synchrotron radiation and inverse Compton scattering. Synchrotron radiation is the relativistic form of cyclotron radiation whereby highly relativistic electrons are accelerated in a magnetic field producing tightly beamed radiation with a maximum energy cut off proportional to the ratio of magnetic field strength to electron momentum. Inverse Compton scattering is the interaction between a photon and a relativistic electron which, unlike standard Compton scattering, results in an increased photon energy. Both synchrotron and inverse Compton radiation typically exhibit a spectrum in the form of a power law, over a limited spectral band, and are major components in describing emission from high energy phenomena such as supernova remnants (SNRs) and active Galactic nuclei (AGN).

1.1.3 Discrete line emission

Establishing the mechanism for the production of the observed continuum emission is necessary in order to understand the physics of the source in question. However by definition the continuum emission is relatively featureless and therefore it is often difficult to ascertain its origin. By contrast line emission provides a wealth of information regarding the temperature, ionisation condition, elemental abundances and so on of the emitting material. Line emission is excited when a bound electron is either knocked out of its orbit by a collision or an incident photon, or raised to a higher energy state within the bound system. In the latter case the electron returns to its ground state, emitting a photon in the process. In the former case an electron in a higher energy state fills the hole left by the ejected electron, again emitting a photon. The hole this electron leaves behind may be filled by another in a higher state and so on, creating a cascade of transitions and subsequent photon emission.

The centroid energy of the emitted photon in a transition between two bound electron states is equal to the difference in the energy levels of the states (see Figure 1.2(a)). However several different mechanisms contribute to the broadening of the emission line, giving it an overall shape called a Voigt profile. The line is naturally broadened due to uncertainty in the lifetime of the excited energy state which is related to a spread in energy via the Heisenberg uncertainty principle, $\Delta \mathrm{E} \Delta \mathrm{t} \geq \hbar$. Other broadening effects are Doppler broadening, whereby the kinetic motion of the ions causes a Doppler shift in the line energy, and collisional broadening which occurs when the energy levels themselves are affected by collisions/interactions with other particles.

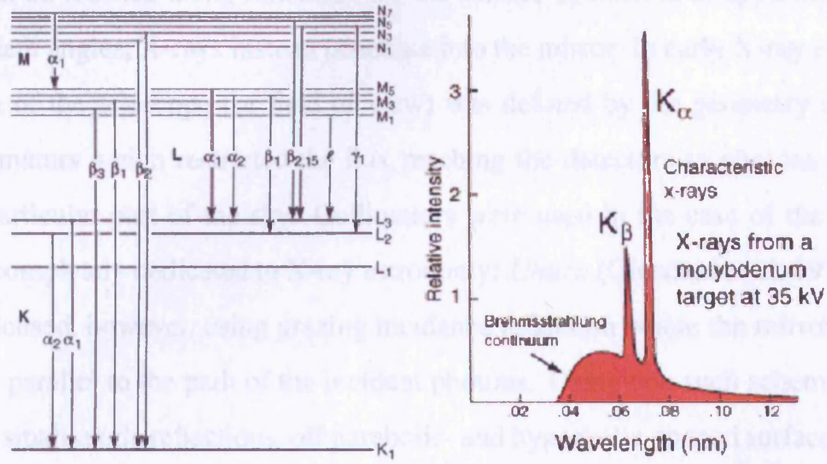

(a) Atomic transitions (b) Continuum + lines spectrum

FIGURE 1.2. *Left panel:*Transitions in atoms or ions which give rise to emission lines. Allowed transitions follow the selection rules $\Delta l = \pm 1$ and $\Delta j = 0, \pm 1$. *Right panel:* Example of a spectrum (plotted against wavelength) with both bremsstrahlung continuum and K shell (n=2 (K_α) or n=3 (K_β) $\rightarrow$ n=1) line emission.

As some ionic species only exist in significant numbers in plasmas beyond a certain temperature, emission lines that are identified as coming from a specific transition within such a species are invaluable in determining both the nature of the emission (*i.e.* thermal/non-thermal) and the temperature of the emitting plasma. In reality plasma emission is a complex composition of continuum and line emission (see Figure 1.2), analysis of which requires accurate physical models, as well as good spectroscopic data, to determine parameters such as temperature and elemental abundance.

1.2 A brief history of X-ray astronomy

The study of cosmic X-rays differs from more conventional (*i.e.* optical) astronomy for two fundamental reasons associated with the physical interactions of high energy photons. The Earth's atmosphere absorbs almost all X-rays long before they reach the ground which means that any system designed to detect X-rays must operate in space and therefore also be able to withstand a rocket launch. Secondly, unlike low energy photons which can be focused using reflection off the surface of mirrors at approximately normal incident angles, X-rays instead penetrate into the mirror. In early X-ray experiments the beam of the telescope (or field of view) was defined by the geometry of mechanical collimators which restricted the flux reaching the detectors to photons originating from a particular part of the sky. Collimators were used in the case of the first X-ray satellite completely dedicated to X-ray astronomy: *Uhuru* (Giacconi et al. 1971). X-rays can be focused, however, using grazing incidence reflection where the mirror alignment is almost parallel to the path of the incident photons. Using one such scheme involving two such small-angle reflections, off parabolic- and hyperbolic-shaped surfaces (a Wolter type-I arrangement), X-rays from a specific part of the sky may be focused onto a single point as shown schematically in Figure 1.3.

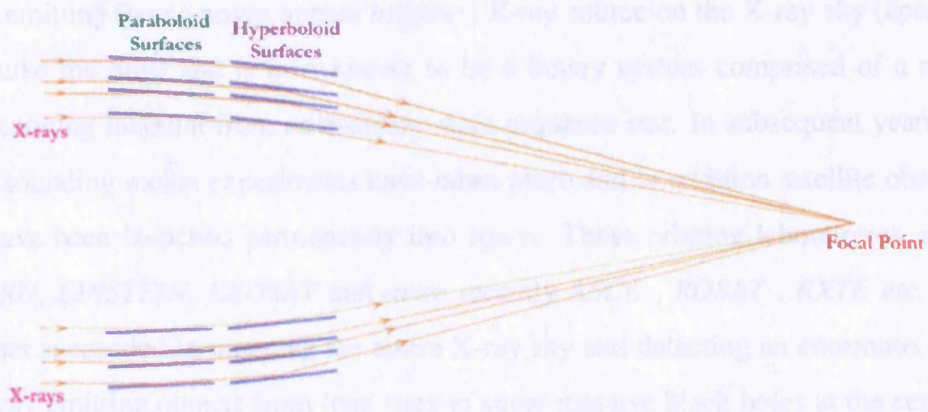

FIGURE 1.3. The focusing of X-ray photons by a Wolter type-I arrangement of grazing incidence reflection. X-rays from a specific direction are doubly reflected off surfaces with parabolic and hyperbolic curvature respectively and focused onto a single point.

Methods for detecting X-rays have also evolved over recent decades. The first rocket and satellite experiments were equipped with non-imaging proportional counters. These are gas filled detectors similar to Geiger counters except that the charge pulse produced by a photon interaction is proportional to the energy if the photon, thus allowing some degree of energy resolution. Later satellites such as *EINSTEIN* , *EXOSAT* & *ROSAT* carried imaging proportional counters which used the localisation of the charge pulses to determine the arrival direction of the incident photons. More recently the development of charge coupled devices (CCDs), such as those used onboard *XMM-NEWTON* , has enhanced the energy resolution capabilities of X-ray detectors. In CCDs incident photons create electron-hole pairs which deposit charge on nearby electrodes within a specific element or pixel. The charge information is stored and passed sequentially along a column of pixels to a read-out line which transfers information row-by-row for further processing. In this way a large number of photons can be recorded in a short time interval, reducing the risk of photon pile-up.

The first experiment to successfully detect X-rays from a cosmic source other than the Sun was launched on board a sounding rocket in 1962. This rocket flight detected an extremely bright X-ray source in the constellation of Scorpius and was thus named Scorpius X-1 (usually abbreviated to Sco X-1). Sco X-1 remains the brightest continuously emitting (some novae appear brighter) X-ray source on the X-ray sky (apart from of course the Sun) and is now known to be a binary system comprised of a neutron star accreting material from an ordinary main sequence star. In subsequent years many more sounding rocket experiments have taken place and in addition satellite observatories have been launched permanently into space. These orbiting laboratories, such as *UHURU*, *EINSTEIN*, *EXOSAT* and more recently *ASCA* , *ROSAT* , *RXTE etc.* , have together succeeded in mapping the entire X-ray sky and detecting an enormous variety of X-ray emitting objects from lone stars to super-massive black holes at the centres of distant galaxies. The study of X-rays provides important information in our attempt to answer questions about the origin, evolution and fate of our universe.

1.3 *XMM-NEWTON*

The work described in this thesis is based on observational data from instruments onboard ESA's X-ray Multi-Mirror (XMM) satellite. This section provides a summary of technical information regarding the capabilities of these instruments and a comparison with other satellites is given in §1.3.2. Much of this information is taken from the *XMM-NEWTON* users handbook which is available online[1].

[1] www.xmm.ac.uk/onlines/uhb/xmm_uhb.html

Launched in 1999, *XMM-NEWTON* is equipped with three Wolter type-1 X-ray telescopes and a 30 cm optical/UV telescope, thus is capable of simultaneous observations in two distinct parts of the electromagnetic spectrum. The optical monitor (OM) has a micro-channel plate CCD detector in its focal plane. Two of the X-ray telescopes include reflection gratings which divert roughly half the flux to an array off detectors offset from the telescope axis. The effect of these reflection gratings on the incoming light is disperse it, in a similar way to a prism dispersing visible light, so that high resolution spectroscopy may be performed on the incident flux. The remaining light continues, undeflected, to two European Photon Imaging Cameras (EPIC) located in the respective focal planes. These are the MOS cameras. The third X-ray telescope also has an EPIC camera at the primary focus although in this case there is no reflection grating present so all the flux reaches the camera. Figure 1.4 shows a sketched layout of all the components of *XMM-NEWTON* , including the relative positions of the different types of detecting instruments. *XMM-NEWTON* occupies a highly elliptical orbit giving an advantageous target visibility window of up to 40 hours.

1.3.1 The EPIC instruments

This thesis relies on data from *XMM-NEWTON* 's three EPIC instruments, which provide spatial, spectral and temporal information relating to the target field. As mentioned above there are two different types of EPIC detectors:two MOS (Metal Oxide Semi-conductor, see Turner et al. 2001) cameras and one pn camera (Strüder et al. 2001). Each type has a distinct CCD layout (see Figure 1.5) and also differ in fundamentally in terms of properties such as quantum efficiency and readout times. A quantitative comparison between the two types, covering a variety of properties, is given in Table 1.1. Each MOS camera consists of 7 front-illuminated CCD chips of 600×600 pixels each. Six chips surround a separate chip in a roughly circular layout. The central chip is slightly vertically offset from the other chips, following the curvature of the telescopes' focal surface. On board *XMM-NEWTON* the two MOS cameras are rotated 90°with respect to each other in order to minimise data loss caused by gaps between the CCD chips. In contrast the pn camera has 12 back-illuminated chips of 64×200 pixels, all of which are

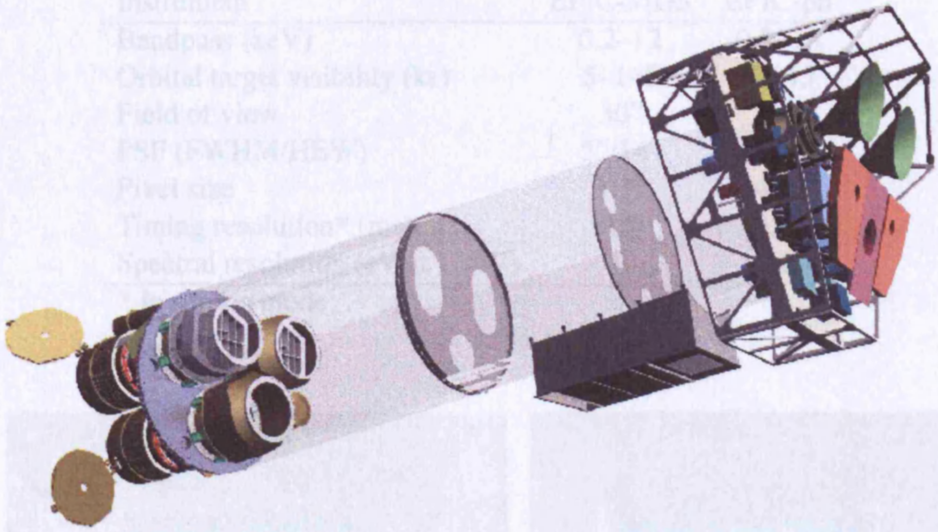

FIGURE 1.4. Sketch of the *XMM-NEWTON* observatory. The mirror module assemblies are visible to the lower left. Two of these are equipped with reflection grating arrays. On the right hand side the instruments are shown:two EPIC-MOS cameras with their radiators (green funnels), the EPIC-pn camera with radiator (purple) and two (light blue) RGS detectors also with radiators (red). The OM camera is obscured by the lower mirror module.

co-planar. The field of view of the pn is very similar to the MOS, *i.e.* $\sim$ 30', although as the total area is smaller, a lower fraction of CCD area falls outside the region open to the sky during an observation. This has implications later on for the measurement of the instrumental background (see §2.4). Each camera can be operated in a variety of modes of data acquisition whereby the CCD area used for readout is altered to improve timing resolution and/or to reduce pile up and allow observation of very bright sources. More information can be found online about the various modes, however only the full-frame modes, in which the whole CCD area is used for imaging, are relevant to this thesis.

Table 1.1. Comparative table for the EPIC-MOS and EPIC-pn cameras.

Instrument	EPIC-MOS	EPIC-pn
Bandpass (keV)	0.2–12	0.2–15
Orbital target visibility (ks)	5–145	5-145
Field of view	30"	30"
PSF (FWHM/HEW)	5"/14"	6"/15"
Pixel size	1.1"	4.1"
Timing resolution* (ms)	1.5	0.03
Spectral resolution (eV at 1 keV)	70	80

* In timing mode

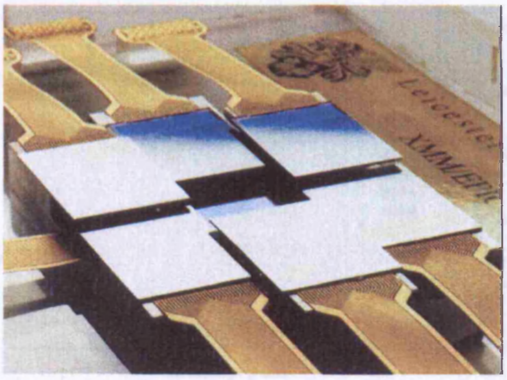

(a) MOS

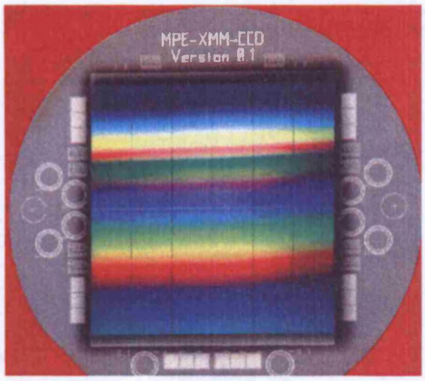

(b) pn

FIGURE 1.5. The EPIC-MOS and EPIC-pn CCD arrays. The central MOS chip is vertically offset from the other 6 in accordance with the curvature of the focal surface. The two MOS cameras are rotated 90° with respect to each other on *XMM-NEWTON* to reduce the effect of gaps between chips.

The point spread function

The key factor which determines the angular resolution of a telescope is its ability to focus photons onto as narrow a region as possible. The critical parameter which measures this ability, determined by the mirror module assembly, is the point spread function (PSF) which represents the distribution of flux across the CCDs from a single point source. Although there is some variance among *XMM-NEWTON* 's three X-ray telescopes, each achieves an on-axis PSF of $\sim$ 6" (FWHM) and a half-energy width (the width which contains 50% of the total energy) of $\sim$ 15" at 1.5 keV. Crucially with *XMM-NEWTON* , although the shape of the PSF is variable, the energy enclosed within a given radius does not change substantially with off-axis angle on the CCDs (see Figure 1.6(a)). This enables an invariant treatment of point sources irrespective of where they appear in the detector. Although Figure 1.6(a) appears to show a strong dependence on energy for the PSF, this is largely because the W90 radius is plotted, *i.e.* that which encircles 90% of the total energy. As can be seen in Figure 1.6(b) there is almost no variation with energy, at least in the range 0.1–5 keV, of energy encircling radii up to about 80%. Both of these invariants are important considerations to allow the equal treatment of point source detections later in the thesis.

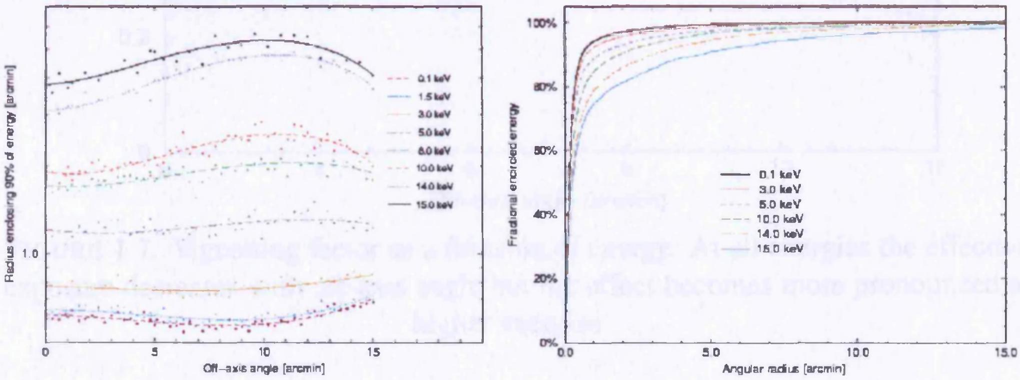

(a) Dependence on off-axis angle (b) Energy as a function of radius

FIGURE 1.6. Characteristics of the telescopes' point spread function (PSF) at different energies. *Left panel:*For energies less than 10 keV the 90% energy radius varies by less than 20% over a range of off-axis angles. *Right panel:*The fraction of encircled energy for an on-axis source is not greatly affected by energy up to a value of $\sim$ 80% for energies less than 5 keV.

Vignetting

Off-axis angle is also an important consideration when considering the effective area off the mirrors. The on-axis dependence of effective area on energy can be seen in Figure 1.8 which compares *XMM-NEWTON* with other satellites. However the effective area also decrease with off-axis angle. This effect, called 'vignetting' and caused by fewer photons reaching the focal plane, reduces the effective exposure of the outer regions of the CCDs by a factor of $\sim$ 3. The quantitative effect of vignetting is dependent on the

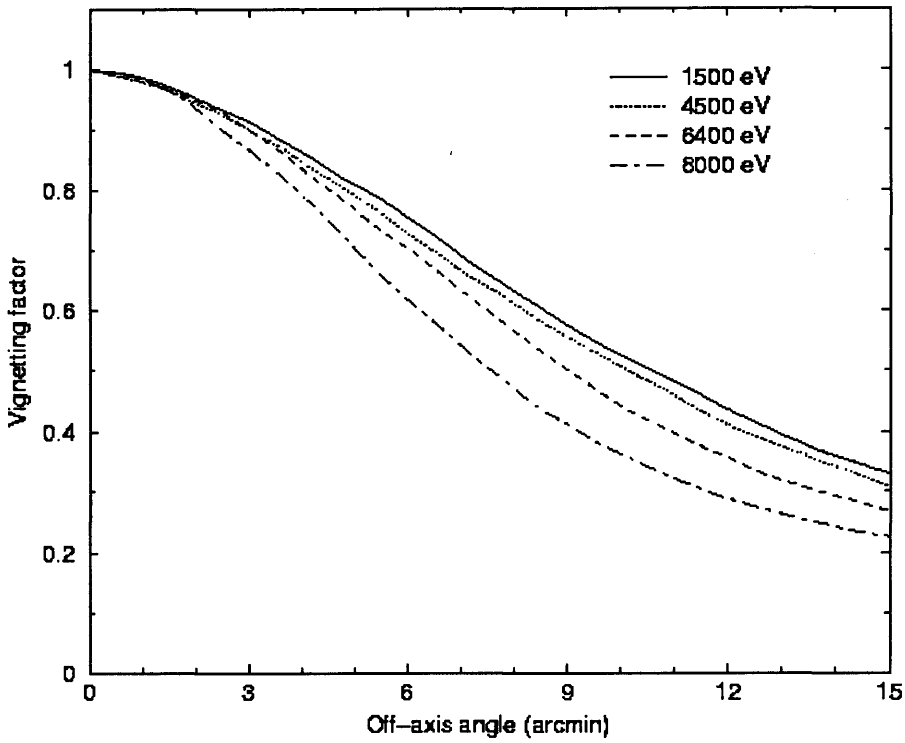

FIGURE 1.7. Vignetting factor as a function of energy. At all energies the effective exposure decreases with off-axis angle but the effect becomes more pronounced at higher energies.

energy range being considered, as can be seen in Figure 1.7. Therefore when corrections are applied for the vignetting, the correct energy range must be applied.

1.3.2 Comparison with other X-ray satellites

XMM-NEWTON is the latest in a long line of successful X-ray telescope missions. In this section a brief summary is given for three other missions, only one of which (*CHANDRA*) remains in operation today. Several parameters which describe the capabilities of each satellite are compared in Table 1.2. Perhaps the most important aspect to any satellite mission is the number of photons which may be a collected in a specific time interval from a given source. The best measure of this is the effective area of the telescope's mirrors and this property is shown graphically for each satellite, as a function of energy, in Figure 1.8. Clearly the launch of *XMM-NEWTON* represented a dramatic leap in the X-ray collecting power of space telescopes.

ROSAT

The Röntgensatellite, or ROSAT, operated throughout the 1990s equipped with a single X-ray telescope which could be operated with one of two instruments:a position sensitive proportional counter (PSPC), with a 2°field of view, and a high resolution imager (HRI) with a smaller field of view of around 0.6°but a much improved spatial resolution. The PSPC was used to complete an all-sky survey in the several soft (<2 keV) X-ray bands during its first six months of operation. Also on board was a wide field camera (WFC) operating in the extreme ultra-violet (EUV) band with a field of view of 5°. This was also used to complete an all-sky survey, this time in the 60–200 eV band.

ASCA

The advanced satellite for cosmology and astrophysics (ASCA) was launched in early 1993 and continued to operate until 2000. *ASCA* was Japan's fourth X-ray satellite mission (following the successes of Hakucho, Tenma and Ginga) and was the first mission, world-wide, to use CCD detectors for X-ray astronomy. *ASCA* 's payload consisted of four X-ray telescopes working in conjunction with either gas imaging spectrometers (GIS) or solid-state imaging spectrometers (SIS). The GIS detectors were comprised of proportional counters with a spatial resolution of $\sim$ 0.5' and an energy resolution of $\sim$ 2% (at 6 keV). The SIS CCD arrays had improved spatial and energy resolution compared to the GIS but suffered from severe degradation over the lifetime of the mission which affected their capabilities. One key feature of *ASCA* was its broad bandpass (0.4–12 keV) which made it an effective tool for investigating the X-ray spectral properties from both Galactic and extragalactic sources.

CHANDRA

More contemporary to *XMM-NEWTON* , *CHANDRA* (formerly the advanced X-ray astrophysics facility or AXAF) was launched in mid-1999 into a highly eccentric orbit similar to that of *XMM-NEWTON* . *CHANDRA* provides unparalleled angular resolution

Table 1.2. Comparison of *XMM-NEWTON* 's capabilities with three other X-ray satellites.

Satellite	*ROSAT*	*ASCA*	*CHANDRA*	*XMM-NEWTON*
Mirror effective area (cm^2 at 1 keV)	400	350	800	4650
Imaging effective area (cm^2 at 1 keV)	200	-	400	2400
Spectroscopic resolving power†	1	9	400–1000	500*
Mirror resolution (arcsec)	3.5	73	0.2	6
CCD energy range (keV)	0.1–2.4	0.5–10	0.1–10	0.2–15
Orbit target visibility (hrs)	1.3	0.9	50	40
Number of science instruments	1	4	1	6

* For the RGS instruments.
† E/dE at 0.5 keV

of less than an arcsecond in conjunction with a wide band pass of 0.1–10 keV and a large collecting area. *CHANDRA* consists of one Wolter type-1 telescope which may have any one of four detectors positioned in the focal plane, two of which also involve transmission gratings for spectroscopic purposes. The AXAF charged coupled imaging spectrometers are comprised of one 4-chip (ACIS-I) and one 6-chip (ACIS-S) CCD array designed for imaging and spectroscopy respectively (ACIS-S is typically used in conjunction with a high energy transmission grating - HETG). Also available is a high resolution camera (HRC) consisting of 2 micro-channel plate detectors, HRC-I and HRC-S, again individually optimised for imaging and spectroscopy (HRC-S is used in conjunction with a low energy transmission grating - LETG). In combination these instruments are capable of an angular resolution better than 0.5 arcseconds (on-axis), with a field of view of $\sim$ 30'$\times$30', similar to *XMM-NEWTON* . Combined with a low internal background these capabilities enable *CHANDRA* to detect extremely faint point sources even in crowded fields with substantial diffuse background emission.

1.4 Point source populations

Since the detection of the first (non-solar) cosmic X-ray source in 1962, the number of known discrete X-ray sources has grown exponentially. By 1970 about 60 X-ray sources

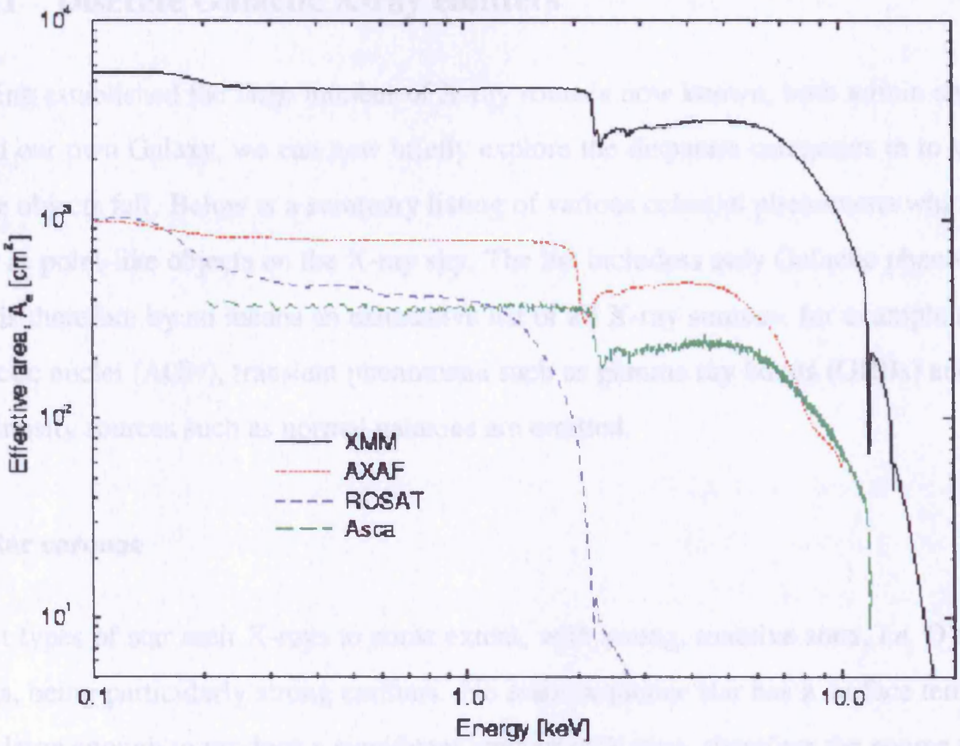

FIGURE 1.8. The effective area of *XMM-NEWTON* 's mirrors compared to other X-ray satellites (AXAF = *CHANDRA*). The logarithmic scale helps to show the huge advantage *XMM-NEWTON* has in terms of photon collecting capability.

had been detected, all with rocket or balloon flights, rising to $\sim$ 700 by 1980 with the addition of satellite observations from *Uhuru*, *Ariel V* and *HEAO-1*, and even further to $\sim$ 8000 by 1990 with the source catalogues of *Einstein* and *EXOSAT* . The biggest leap in known X-ray source number in recent history was provided by *ROSAT* which established a catalogue of over 200,000 sources from both the all-sky survey and pointed observations. The vast majority of these sources are point-like although a small fraction of extended objects also contribute. With serendipitous detections by *XMM-NEWTON* and *CHANDRA* coming in at an extremely high rate the current number is likely to be around half a million and will continue to rise, probably reaching several million during the lifetime of these satellites.

1.4.1 Discrete Galactic X-ray emitters

Having established the large number of X-ray sources now known, both within and beyond our own Galaxy, we can now briefly explore the disparate categories in to which these objects fall. Below is a summary listing of various celestial phenomena which appear as point-like objects on the X-ray sky. The list includess only Galactic phenomena and is therefore by no means an exhaustive list of all X-ray sources, for example active galactic nuclei (AGN), transient phenomena such as gamma ray bursts (GRBs) and low luminosity sources such as normal galaxies are omitted.

Stellar coronae

Most types of star emit X-rays to some extent, with young, massive stars, *i.e.* O and B types, being particularly strong emitters. No main sequence star has a surface temperature large enough to produce a significant amount of X-rays, therefore the source of the X-rays is thought to be extremely hot plasma (T $\sim 10^7$ K) located in the coronal part of the stellar atmosphere. The spectra are often rich in emission lines although the relatively low luminosity means that long observations are required to obtain an adequate number of counts. X-ray luminosity is often greater in relatively young stars (Kunte et al. 1988) which may be a result of a dependence on stellar rotation. Coronal emission is also visible in binary systems such as RS CVn variables which do not have mass transfer but emit X-rays via flare outbursts from the component stars.

X-ray binaries

The brightest class of X-ray emitters, these systems can be divided into two classes:high mass X-ray binaries (HMXB) and low mass X-ray binaries (LMXB). Both consist of a normal (main sequence) star in close orbit around a black hole or neutron star (White 1989). The compact object (BH/NS) accretes matter from the companion star, forming an accretion disk which is luminous in the X-ray band. In LMXBs accretion occurs through 'Roche lobe overflow', when part of the companion star overlaps the Lagrangian point between the two objects, causing matter to become gravitationally bound to the compact object. Conversely, in HMXBs accretion occurs through the capture of stellar winds from the companion star by the compact object. For example, Sco X-1, the brightest object on the X-ray sky (apart from the Sun), is a LMXB with a neutron star as the compact accreter. The distinction between high and low mass refers to the mass of the companion star with high mass meaning approximately double (or more) the mass of the Sun.

Cataclysmic variables

CVs are active binary systems which consist of a white dwarf star and a normal companion star. The white dwarf accretes matter from its companion, releasing gravitational potential energy in the form of X-rays (Schwope et al. 2002). Two forms of variability, where the X-ray flux undergoes spontaneous and rapid change, give CVs their name. The first of type of outburst, called classical novae, occur when the hydrogen-rich material accreted onto the white dwarf's surface undergoes sudden nuclear fusion. The second type, dwarf nova outbursts, are the result of temporary increases in the accretion rate and are generally of lower amplitude than classical novae. CVs generally fall into two categories: non-magnetic CVs have an accretion disk similar to X-ray binaries, and magnetic CVs (those in which the white dwarf is highly magnetised) where the accretion is funnelled by the magnetic field onto the poles of the white dwarf companion. There is also an intermediate class where a moderate magnetic field does not prevent an accretion disk being formed but does disrupt the inner portion (Haberl 2002).

Supernova remnants

Supernova remnants (SNRs) are the remains of exploded stars, *i.e.* hot gases ejected into space by supernova explosions. The X-rays are generated from the remaining stellar material which has been heated by the explosion (*e.g.* Cassiopeia A, Willingale, Bleeker, van der Heyden & Kaastra 2003). As some are many hundreds of light years wide they only appear as point-like objects if they are a sufficient distance away from us. SNRs can fall into several categories which describe their morphology:shell-like remnants have a ring-like structure, crab-like remnants are centre-filled and composite remnants which can appear as either crab-like or shell-like depending on which wave band they are observed in. The morphological variation is largely unimportant in the point source context although it can have a wider implication, for instance on whether or not a SNR contains a pulsar within its structure.

Isolated neutron stars

Neutron stars are the end product of stellar evolution for a star several times the mass of the sun. Those which are not associated with a SNR or close binary system are called isolated neutron stars. They were either blown away from a companion during the supernova explosion or never had a companion in the first place. INSs radiate either due to the glow from the initial explosion or by accreting matter from the interstellar medium (Ikhsanov 2003), therefore they can be detected in the X-ray band although they are more commonly observed with pulsed radio emission (*i.e.* pulsars).

1.5 The Soft X-ray Background

1.5.1 Initial Discovery

The Soft X-ray Background (SXRB) was first discovered by sounding rocket experiments in the late 1960s. Henry et al. (1968), scanning the northern Galactic hemisphere between the Galactic centre and anti-centre, observed significant emission at around $\frac{1}{4}$ keV which appeared to be negatively correlated with the absorption column density due to Galactic neutral Hydrogen. Previous studies had already postulated the existence of an extragalactic X-ray background above 2 keV (*e.g.* Gursky et al. 1963) and this anti-correlation with absorption pointed towards a similar origin for the soft X-rays. Further sounding rocket observations were carried out by Henry et al. (1968) and Bumner et al. (1969), which verified the presence of $\frac{1}{4}$ keV emission and the finding by Henry et al. (1968) that the fitted absorption cross sections were significantly less than predictions from atomic physics. Several alternative theories were considered to account for the spatial variation and intensity of the $\frac{1}{4}$ keV emission. Galactic point source emission (such as stellar coronae or X-ray binaries) was largely ruled out as a plausible explanation due primarily to the extremely high source density that would be required. A preferred explanation was that the emission originated from a hot intergalactic medium (Snowden 2000) with the apparent reduction in absorption cross sections caused by the clumping of the interstellar medium. Once a region of absorbing material becomes optically thick, adding more material to it does not significantly increase the absorption level. Therefore if the ISM is arranged in clumps of matter the average absorption cross section, over a solid angle larger than the clumping scale, will appear to be less than would be expected for an even distribution of the known amount of absorbing material. Even with the clumping argument the requirement for an additional component above the extrapolation of an extragalactic power law seen at higher energies still existed. An extragalactic origin for this component was generally assumed in spite of the significant emission from the Galactic Plane through which, due to the steep functional dependence of optical depth with lower X-ray energies, no extragalactic $\frac{1}{4}$ keV emission could possibly be observed. This emission was instead assumed to be either from unresolved point sources or spurious due to unknown contamination.

1.5.2 Origin of the SXRB

The hypothesis that the SXRB was of extragalactic (or at least distant) origin was undermined in the 1970s by an extended series of sounding rocket observations conducted at the University of Wisconsin. Both the Small Magellanic Cloud (SMC) and Large Magellanic Cloud (LMC) were used to perform shadowing experiments in order to identify how much, if any, of the SXRB was of local origin. The results showed surprisingly that 75% of the observed $\frac{1}{4}$ keV signal originated in front of the SMC whilst the equivalent fraction for the LMC was more than 90% (McCammon et al. 1971 and Long et al. 1976 respectively). These investigations, along with others, also showed that the general anti-correlation of $\frac{1}{4}$ keV intensity with Galactic absorption column was not reflected over smaller scales of a few degrees. The Wisconsin data also showed that the X-ray hardness ratio (or colour) of the SXRB did not change significantly over large variations in

$\frac{1}{4}$ keV surface brightness. Therefore either the absorbing material was clumped to such an extent that the energy dependence of the cross section was lost, or alternatively the SXRB was unabsorbed and therefore of local origin. By successfully fitting the observed X-ray spectrum from the sounding rocket data without a significant absorption column, Hayakawa et al. (1978) came to the latter conclusion.

Also around this time came a clarification of the probable nature of the mechanism behind the SXRB. Non-thermal Synchrotron production was unlikely because the electron energy required to produce $\frac{1}{4}$ keV emission in a Galactic magnetic field of ~ 3 μG is $> 10^{13}$ eV and such electrons would only have a lifetime of less than 10^4 years. Inverse Compton scattering of the Cosmic Microwave background required an electron energy of only ~ 250 MeV, however the number of electrons which would be necessary to create the SXRB was unreasonably large. Therefore a thermal mechanism, such as the hot interstellar medium model, was deemed much more likely. Thermal bremsstrahlung emission from a hot plasma proved a reasonable model for the observed spectrum, but required too high a space density, and thus excessive pressures, if Galactic in origin. The inclusion of collisionally-excited line emission, however, successfully provided the most suitable explanation for the origin of the SXRB. Spectral fitting of the data from different detectors on board the sounding rocket flights showed that at least two plasma temperatures were required at ~ 0.09 keV and ~ 0.12–0.18 keV respectively (de Korte et al. 1976).

1.5.3 The Satellite Era

The main problems with the observational data retrieved from sounding rocket experiments were the short durations of the exposures (each flight lasted only about 5 minutes) and the large field of view of the instruments. With the satellite observations which became prevalent in the 1980s and beyond, both the spatial and spectral resolution of SXRB observations were substantially improved. Both SAS-3 and HEAO 1 performed all-sky surveys of the SXRB (Marshall & Clark 1984 and Garmire et al. 1992 respectively) and were able to resolve distinct spatial features such as the Eridanus X-ray Enhancement and the Monogem Ring. More recently *ROSAT* has provided us with detailed maps of the SXRB in the three distinct energy bands of $\frac{1}{4}$ keV, $\frac{3}{4}$ keV and 1.5 keV (Snowden et al. 1995; Snowden et al. 1997). The additional energy bands highlight some interesting features that are particularly relevant to this thesis such as the North Polar Spur (NPS) and a bright 'bulge' around the Galactic Centre. *ROSAT* was able to separate the SXRB into several hot plasma components, located both in front of and beyond the Galactic absorption column. The temperatures of these components are in reasonably good agreement with the sounding rocket data (Snowden et al. 1998; Kuntz & Snowden 2000) although further comparisons and analysis is deferred until §3.

1.6 Galactic Ridge X-ray Emission

The X-ray sky viewed in hard X-rays (canonically defined as those with energies > 2 keV) is markedly different to that observed in lower energy bands. This is due to the fact that the interstellar medium is largely transparent to such high energy photons, reducing the dominance of local sources of emission that is apparent in the soft X-ray maps of *ROSAT* . Probably the best known Galactic feature in the hard X-ray band is a narrow band of emission along the Galactic Plane known as the Galactic ridge. This was first observed by the *HEAO-1* satellite (Worrall et al. 1982) and the full extent of the was later revealed by *EXOSAT* (Warwick et al. 1985).

Figure 1.9 shows the map of the Galactic Plane obtained by *EXOSAT* in the 2–6 keV band. The Galactic ridge X-ray emission (GRXE) is clearly visible as a green stripe

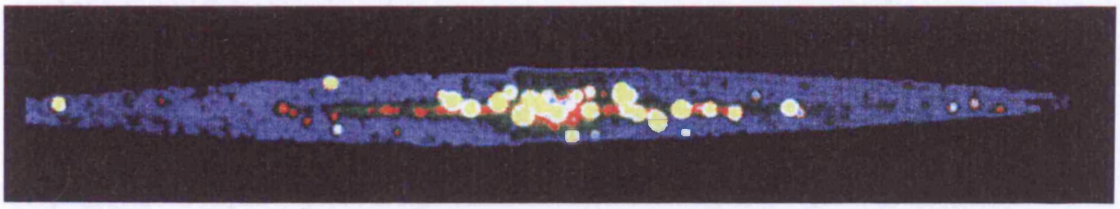

FIGURE 1.9. *EXOSAT* image of the Galactic ridge. The yellow circles represent bright X-ray binaries and the ridge can be seen as a narrow green stripe above the blue background.

extending out to $\sim 40°$longitude either side of the Galactic Centre. The origin of this emission remains uncertain with regards to whether the mechanism which produces the hard flux is thermal or non-thermal and problems in explaining the source in more detail exist in either case. More recent observations by *ASCA* (Kaneda et al. 1997) and *RXTE* (Valinia & Marshall 1998) have led to very different conclusions as to the nature of the production mechanism, highlighting the requirement for higher resolution spectroscopy. In §5 data from the EPIC-MOS cameras are used to more accurately determine the characteristics of the GRXE, in conjunction with results from other satellites, and the implications of the likely production mechanism are discussed further.

1.7 Thesis objectives

This thesis is mainly concerned with Galactic emission and the list of objectives given below reflects this fact. However in order to establish both the level and nature of Galactic emission, care must be taken to correctly model both extragalactic and non-sky backgrounds. Treatment of this latter form of contamination is described in §2.

The main themes of this thesis are as follows:

1. To investigate the properties of the discrete X-ray source population in the Galactic Plane detected at faint fluxes. For this purpose an extensive catalogue of sources is created which includes information such as position, multi-band X-ray flux, hardness ratio and correlations with other catalogues.

2. To investigate the open question of the nature of the Galactic ridge and attempt to ascertain the most likely physical model which can explain its existence.

3. To measure the flux from the soft X-ray background over a range of Galactic coordinates and thereby establish the balance between foreground and background emission and extended Galactic features.

Chapter 2

Data Reduction

2.1 Overview

This chapter describes in detail the techniques and processes used to reduce the data from the EPIC instruments on board *XMM-NEWTON* to more accessible forms such as 2-D images or X-ray spectra. This should allow the analysis contained in following chapters to be understood in the context of what conclusions the reduced data are capable of supporting.

2.2 Data reduction methods

As with most other X-ray satellites, *XMM-NEWTON* has its own specific data-analysing software intended to facilitate and standardise the processing of raw data. The *XMM-NEWTON* Science Analysis System (SAS) is a cooperative effort of the Science Operations Centre (SOC) and the Survey Science Centre (SSC). For each observation the SSC produces pipeline products for each *XMM-NEWTON* instrument, including event lists, exposure maps, images, source spectra, source lists, optical viewing charts *etc.* All the data featured in this thesis come from the EPIC instruments on board *XMM-NEWTON* . The majority of the analysis discussed in this thesis utilises only the EPIC-MOS and EPIC-pn event lists and exposure maps produced by the SAS. All subsequent analysis performed using these files is done outside the SAS environment. The reason for this is that throughout this thesis the focus of interest is on either faint X-ray point sources or low surface brightness diffuse emission, *i.e.* objects with low X-ray count rates. Therefore, due to significant problems with early versions of the SAS software, especially for source detection, an alternative approach was used. This involved writing independent data processing programs using the programming language Q, a Fortran-based code specifically designed to process astronomical data[1]. An advantage of the approach we have adopted is that it injects a high degree of quality control which is of particular importance when detecting large numbers of point sources, some of which will inevitably be confused by other point sources or gaps in the detectors' CCDs.

2.3 Observations

In order to study both point source populations and low surface brightness diffuse emission, a relatively large combined exposure time is required to acquire sufficient data for meaningful analysis. The investigation into point sources uses data from *XMM-NEWTON* 's X-ray Galactic Plane Survey (XGPS), referred to in §1. The 22 XGPS observations are also the source of investigations into Galactic diffuse emission, along with 3 observations near the galactic centre, 3 in the North Polar Spur, 5 in the southern Galactic 'bulge' and 7 high latitude fields. Details of all these observations are given in Table 2.1.

		Galactic Coordinates			
Obs	Observation Date	Longitude (°)	Latitude (°)	Exposure [a]	Name
1	2000-10-08	19.15374	-0.02457	8393	Ridge 1
2	2002-09-21	19.57109	-0.02576	13667	Ridge 2
3	2000-10-11	19.98889	-0.02746	12044	Ridge 3
4	2000-10-12	20.40215	0.00260	9256	Ridge 4
5	2002-09-17	20.83234	0.00167	13667	Ridge 5

[1]See www.star.le.ac.uk/~rw/q/q_manual.html

6	2001-03-08	19.41494	0.37047	7794	XGPS 1
7	2001-03-10	19.41384	-0.31829	9144	XGPS 2
8	2001-03-10	19.81352	0.37576	9144	XGPS 3
9	2001-03-10	19.81350	-0.31768	9144	XGPS 4
10	2001-03-22	20.21470	0.37158	9994	XGPS 5
11	2001-03-22	20.21342	-0.32198	8794	XGPS 6
12	2001-03-24	20.61462	0.37174	7637	XGPS 7
13	2002-02-29	20.61276	-0.32042	13167	XGPS 8
14	2001-03-26	21.01233	0.37190	11894	XGPS 9
15	2001-10-03	21.01174	-0.32102	9767	XGPS 10
16	2002-09-19	21.21276	0.02574	8409	XGPS 11
17	2002-09-27	21.38317	0.32224	7367	XGPS 12
18	2002-03-13	21.40010	-0.34625	6666	XGPS 13
19	2002-03-11	21.61474	0.02584	7269	XGPS 14
20	2002-03-27	21.81140	0.37264	7274	XGPS 15
21	2002-03-15	21.81288	-0.32069	7762	XGPS 16
22	2002-03-29	22.01171	0.02638	7274	XGPS 17
23	2003-03-20	7.00000	-0.28890	6619	XGPS 27
24	2003-03-20	7.16672	0.00000	6619	XGPS 28
25	2003-03-28	7.33337	0.28892	6619	XGPS 29
26	2003-04-03	7.50000	0.00000	6619	XGPS 31
27	2003-03-28	15.00000	0.28879	12267	NXGPS 44
28	2003-03-28	15.00000	-0.28866	10047	NXGPS 45
29	2003-04-08	15.16654	0.00000	8667	NXGPS 46
30	2003-04-06	15.33325	-0.28866	8667	NXGPS 48
31	2003-04-04	15.50000	0.00000	8667	NXGPS 49
32	2003-03-08	14.83342	0.00000	8667	NXGPS 50
33	2000-09-23	1.08240	-0.14380	15809	GC1
34	2001-04-01	0.57667	-0.04623	25144	GC3
35	2000-09-11	359.55472	-0.04543	23894	GC7

36	2002-03-11	1.04526	-3.87234	24024	Baades Window
37	2002-03-12	0.46300	-2.71100	24024	Baades Foreground
38	2001-09-13	0.55749	-8.00000	13467	Bulge-8
39	2002-03-14	0.00000	-12.00000	12329	Bulge-12
40	2001-03-09	0.38996	-5.48719	16444	Field III
41	2001-02-28	25.00000	20.00000	14494	Field IV
42	2001-02-28	20.00000	30.00000	14494	Field V
43	2001-03-04	20.00000	40.00000	14644	Field VI
44	2000-07-31	169.75909	-59.75184	57673	SDS-1
45	2000-08-02	169.75909	-59.75184	59691	SDS-1
46	2000-08-04	170.35470	-59.49096	63128	SDS-2
47	2000-08-06	169.61303	-59.35913	37510	SDS-3_cal
48	2000-08-08	169.01391	-59.61686	24241	SDS-4_cal
49	2002-08-12	169.15448	-60.01018	47567	SDS-5
50	2002-08-08	169.90903	-60.14430	49267	SDS-6
51	2002-08-09	170.50999	-59.88277	47781	SDS-7

[a]Total MOS 1 exposure in seconds.

2.4 Internal EPIC Background

Possibly the most significant problem associated with analysing low flux sources (especially diffuse emission) with EPIC instruments data comes from the internal background of the detectors themselves. These events originate from charged particle interactions which deposit charge across multiple pixels (Read & Ponman 2003). Although the fraction of these cosmic ray events which are rejected is $\sim 99\%$ (see Lumb et al. 2002), the remainder is sufficient to produce a rate of ~ 0.9 count s^{-1}(0.2–12 keV) in a single MOS camera which is very similar to the signal from the diffuse X-ray background in the Galactic Plane, excluding point sources. In the case of the MOS cameras, a substantial fraction of the outer CCDs lie outside the exposed sky area and thus the spectrum of this internal background can be well estimated using exclusively events recorded in these regions. The same can be done with the pn camera although due to a much lower number of CCD pixels in the unexposed area, the signal to noise is significantly reduced. This inadvertent consequence of the CCD geometry is shown more clearly in Figure 2.1.

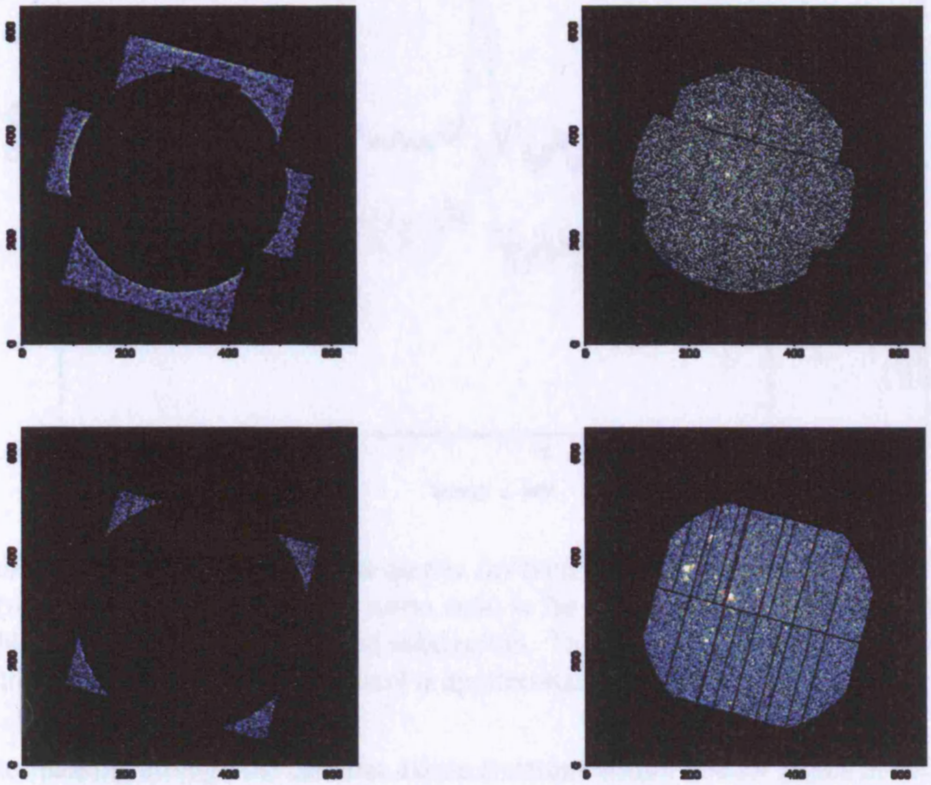

FIGURE 2.1. Example MOS 2 (upper) and pn (lower) images with data from both exposed (RHS) and unexposed (LHS) regions of the CCDs. Each MOS camera has a significantly greater number of pixels in the unexposed region, allowing for better estimation of the internal background.

The events recorded in these unexposed regions contain exactly the same information as those recorded in the central field of view, so spectra can easily be created for background subtraction. Figure 2.2 shows a combined 'edges' spectrum for the MOS cameras and a similar spectrum for the pn. Both spectra are the sum of data from several observations totalling $\sim$ 350 ks of combined observing time. The difference in scale is due to the difference in unexposed collecting area for each camera and is deceptive as the pn actually has almost double the internal background per pixel of each MOS.

Also visible in Figure 2.2 are the detector fluorescent lines generated when charged

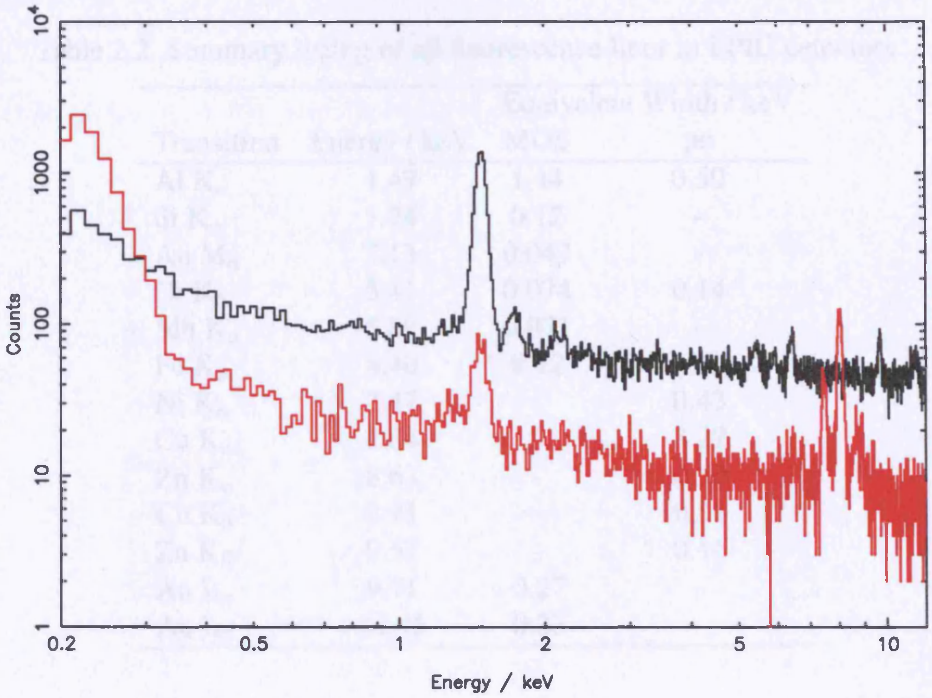

FIGURE 2.2. Internal background spectra for both the combined MOS (black) and pn (red) cameras. The signal to noise ratio is far better for the MOS data which enables better spectral background subtraction. The difference in scale is artificial, the pn background level per pixel is approximately double that of the MOS.

particles passing through the cameras excite electrons within neutral atoms in the materials from which the instruments are constructed. Unlike the cosmic ray particles, this fluorescence emission is not distributed uniformly across the CCDs. For example the extremely prominent line in the MOS cameras at $\sim$ 1.5 keV, corresponding to Aluminium K-shell emission, is significantly weaker in each central MOS CCD as they lie slightly below the outer CCDs and thus are shadowed from emission originating above the focal plane. Table 2.2 gives a summary listing of all the significant fluorescence lines in the energy range 0.2–12 keV for both the MOS and pn cameras. The presence of such a strong internal background and the spatial variation of the fluorescence lines demands care when subtracting the background prior to spectral analysis. The method employed in order to subtract the instrument background is outlined in §2.7.2.

Table 2.2. Summary listing of all fluorescence lines in EPIC detectors.

Transition	Energy / keV	Equivalent Width / keV MOS	pn
Al K_α	1.49	1.44	0.50
Si K_α	1.74	0.12	-
Au M_α	2.13	0.047	-
Cr K_α	5.41	0.074	0.14
Mn K_α	5.89	0.071	-
Fe K_α	6.40	0.12	0.083
Ni K_α	7.47	-	0.43
Cu K_α	8.04	-	3.22
Zn K_α	8.63	-	0.50
Cu K_β	8.91	-	0.51
Zn K_β	9.57	-	0.16
Au L_α	9.71	0.27	-
Au L_β	11.45	0.23	-

2.5 Filtering Event Lists

The raw EPIC event list files contain a variety of information about each 'event' recorded by the CCDs of, for example, the MOS 1 camera. Such information includes the time of the event, the CCD chip on which it registered, the energy and pattern of the event and the pixel position of where it was detected. Each event is recorded with a characteristic 'pattern' on the CCD pixel array. This is a measure of how many pixels recorded a deposit of charge associated with that particular event and the pattern which these pixels form. Figure 2.3 shows the most common examples of these patterns, broken down into groups such as singles, doubles, triples *etc.* . For very bright sources it may be necessary to only use single pixel events in order to reduce the effect of pile up, however none of the observations listed in Table 2.1 contain objects bright enough for pile up to be a problem. Therefore throughout this analysis the pattern ranges used for filtering event lists are the maximum for which the EPIC spectral response files are well calibrated. This pattern range is between 0 and 12 (inclusive) for both MOS cameras and between 0 and 4 for the pn.

In addition events may be flagged if they display a signature which indicates they may not be real, for example being recorded outside the instrument field of view or on a bad CCD row/column. Only events which satisfy flag=0, *i.e.* no warning flags, are used to produce a light curve for each particular observation.

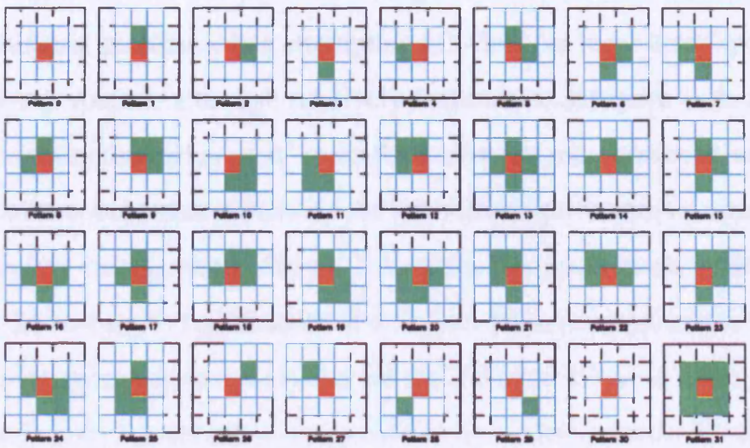

FIGURE 2.3. Recognised photon event patterns centred on the (red) pixel with the highest charge deposit. Other pixels recording a deposit of charge are coloured green. The ranges which have good calibration for spectral response files are 0–12 and 0–4 for the MOS and pn cameras respectively.

2.5.1 Light curves & proton flares

For each observation the timing information for every recorded event is used to create a "full-field" light curve showing how the count rate varies during the course of the exposure. In addition to the flag and pattern information, two other filters used to create the light curve; firstly events are rejected if their energy is above 12 keV or below 200 eV and secondly a spatial flag is applied so that only regions with an exposure $> 25\%$ of the maximum, on-axis, value are included. Ideally each light curve, extracted in this way, would remain constant during the observation, consistent with the absence of astronomical objects that are variable on the time scale of a few kiloseconds and bright enough to contribute more X-ray counts than the diffuse background emission. Unfortunately there is a source of contamination which results in this not being the case for the majority of observations. Within its orbit through the Earth's magnetosphere *XMM-NEWTON* occasionally encounters clouds of low energy protons which can be focused by the XMM mirrors onto the detectors. Such proton-induced events are not flagged as suspect by the pipeline processing system, and as a result they can produce significant contamination of the full-field light curve, with the measured intensity sometimes reaching levels many hundred times greater than the quiescent background signal. These proton 'flare' intervals are a significant problem when attempting full-field (or large area) spectral analysis, as the flare X-ray spectra, although relatively featureless, are quite variable. For detection of point sources the inclusion of some flare intervals may however be advantageous if the extra source counts gained increase the statistical significance of a particular source (despite the higher background). Figure 2.4 makes this point more quantitatively. The graph shows the statistical significance of a source detection against the fraction of the observation with proton flare contamination for different levels of flare intensity. The black curve in Figure 2.4 should be compared to the others individually to see the effect of flaring at different intensities. It can be seen that including flare intervals at double the quiescent intensity will increase the significance of a source irrespective of how long the flare interval is, whereas at 10 times the quiescent intensity the significance is only increased if the flare takes up 90% or more of the light curve. The absolute significance numbers on the Y axis are unimportant but are typical for a low flux point source in a 5 ks observation with a background flux appropriate to the MOS cameras.

As the amount of flare contamination varies considerably amongst the XGPS observations, an intensity cut of 3 times the quiescent level was selected as the best compromise between keeping as much exposure time as possible without drowning out the real sky signal with proton flux.

In practice the application of this method significantly affects the exposure time included for source detection for approximately 50% of the XGPS observations. Figure 2.5 shows light curves for all 22 XGPS observations with cut-offs shown representing both the quiescent signal and three times this value for source detection. Two of the observations (XGPS 14 & XGPS 15) have excessive flaring throughout the entire exposure and the intensity is such that if a cut was imposed at three times the expected quiescent level all data would be rejected. Instead the quiescent level is deemed to be that of the flare itself and an equivalent factor of three increase in intensity is permitted to detect

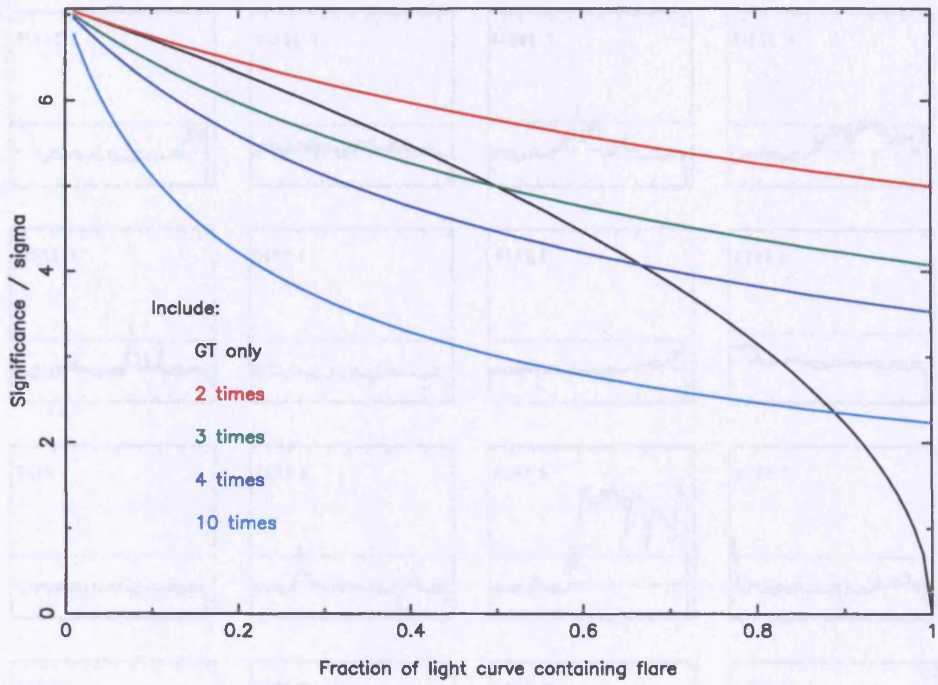

FIGURE 2.4. The effect of proton flaring on the statistical significance of a source detection. The black line shows how the significance is reduced as more of the exposure is excluded due to contamination and the coloured lines show how this reduction can be tempered by the additional counts from flaring intervals which are included according to the magnitude of the flare. For example if the light curve contamination is 100% then some flare intervals must be included to retain any data. Curves are plotted for n=2, 3, 4 & 10, where n is the magnitude of flare relative to the quiescent level.

sources. Although detailed source analysis is only performed on the XGPS observations, the same procedure is used on all observations so that point source regions may be excluded when examining diffuse emission. As mentioned previously it is imperative to exclude all regions of proton flaring before extracting spectral information from a wide field of view and therefore a cut off is imposed on each light curve at the quiescent level. Figure 2.6 shows the difference the two cut thresholds have on the light curve of Ridge 3 for source detection and spectral extraction respectively.

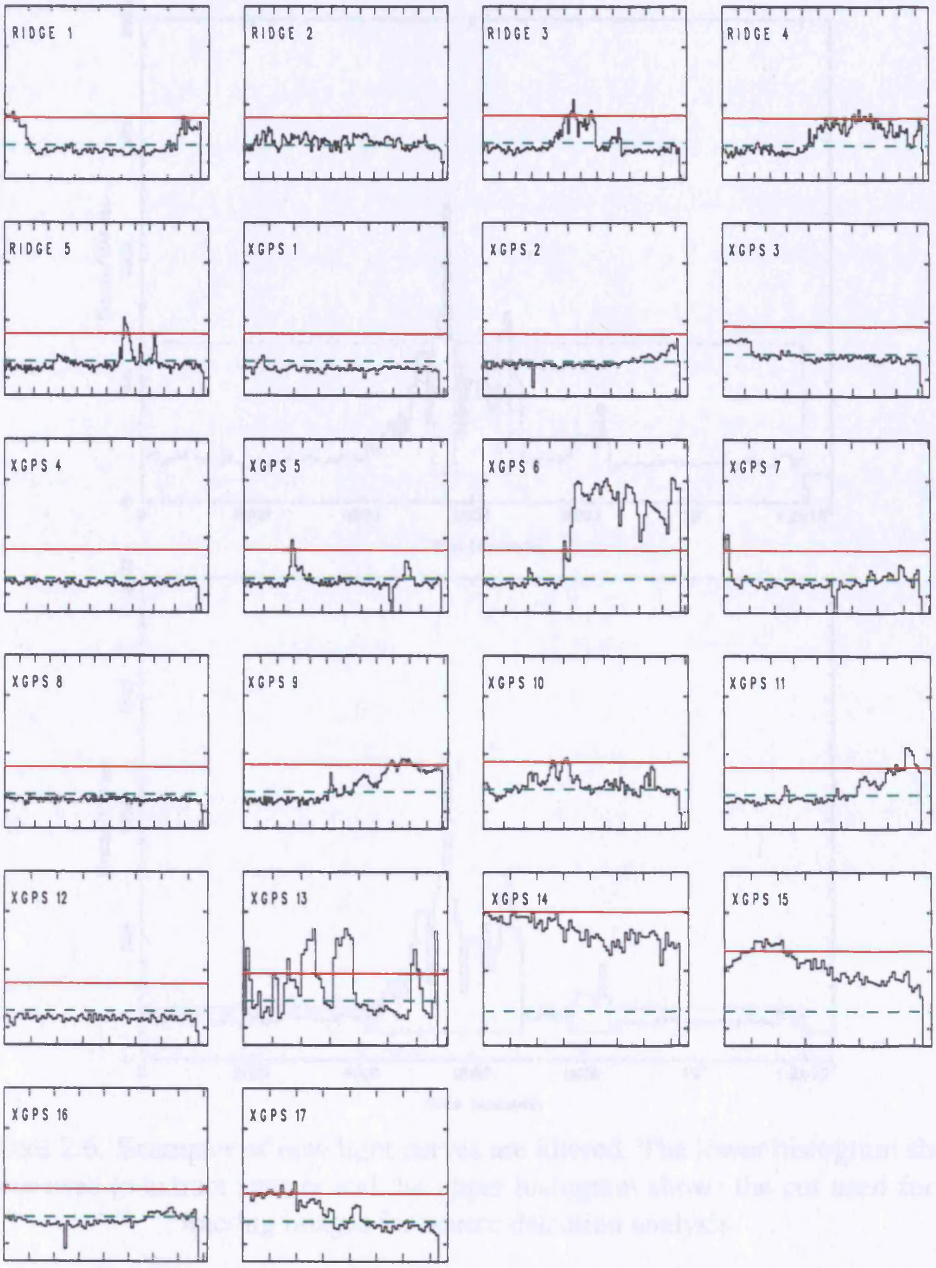

FIGURE 2.5. MOS 1 full-field light curves for all 22 XGPS observations. In each case the units of the vertical axis are counts per 100 s in the full 0.2–12 keV band. The scaling is logarithmic with the three tick marks corresponding to 100, 1000 and 10000 counts per 100 s, respectively. The unit of the horizontal axis is time with tick marks every 1000 s. The thresholds used to exclude the most intense background flares are shown in each case (solid red line). The more stringent thresholds use to extract datasets with "near-quiescent" background conditions are also indicated (dashed green line).

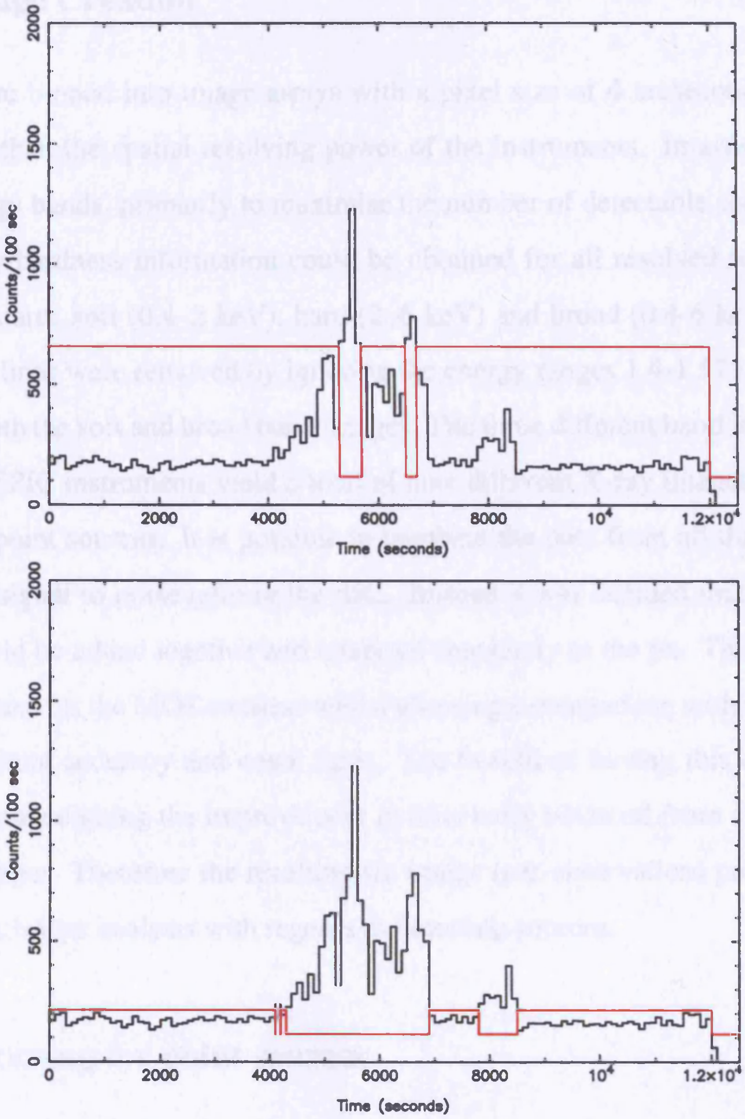

FIGURE 2.6. Examples of how light curves are filtered. The lower histogram shows the cut used to extract spectra and the upper histogram shows the cut used for extracting images for source detection analysis.

2.6 Source Detection

Having established the time periods from which data will be accepted, the next step is to bin the events spatially to produce images which can be systematically searched for point sources.

2.6.1 Image Creation

The data were binned into image arrays with a pixel size of 4 arcseconds, a factor of $\sim$ 4 smaller than the spatial resolving power of the instruments. Images were created in three energy bands, primarily to maximise the number of detectable sources, but also so that X-ray hardness information could be obtained for all resolved sources. These energy bands are: soft (0.4–2 keV), hard (2–6 keV) and broad (0.4-6 keV). Prominent fluorescence lines were removed by ignoring the energy ranges 1.4-1.575 keV & 1.675-1.8 keV in both the soft and broad band images. The three different band images for each of the three EPIC instruments yield a total of nine different X-ray images which can be scanned for point sources. It is possible to combine the data from all three cameras to improve the signal to noise ratio in the data. Instead it was decided that the two MOS cameras would be added together and analysed separately to the pn. This enhances the photon statistics for the MOS cameras whilst allowing a comparison with the pn for both source positional accuracy and count rates. The benefit of having this quality control was seen as outweighing the improvement in sensitivity obtained from adding all three cameras together. Therefore the resulting six image (per observation) provide the basis for all further image analysis with regards to detecting sources.

2.6.2 Scanning for point sources

The source detection algorithm relies on several stages of analysis but with each image treated in exactly the same way and subject to the same criteria for source identification, whichever energy band and camera (pn / combined MOS) it is derived from. Due to the effect of vignetting the effective exposure at a given point on a CCD varies according to how far it is from the central observation axis of the instrument. In order to define a spatial quality flag, only those regions of the CCDs which have an effective exposure of at least 25% of the on-axis value (in practice this threshold usually includes all sky-illuminated regions) are scanned for point sources. The exposure map used to determine this boundary is the band 3 (2–4.5 keV) exposure image produced by the SAS pipeline software. The fact that this energy band does not exactly match any of the source detection bands is unimportant because it represents nothing more than a convenient reproducible method for defining the solid angle over which the source detection algorithms have been used. Initially the raw image is lightly smoothed in order to both make point sources and any luminous unresolved features (such as galaxy clusters) stand out above the background. These bright regions (typically the brightest 5% of all pixels) are then excluded before the remaining data are heavily smoothed to produce a sky background map. Light smoothing is performed using a circular mask of radius 2 pixels (8 arcseconds), with a Gaussian weighting function. Conversely the mask used for heavy smoothing is a square, of side forty pixels (2.7 arcminutes), with no weighting function. Figure 2.7 shows an example of this process in operation using combined MOS data from Ridge 1. The first image shows the lightly smoothed raw image with contour plots for both the $>25\%$ on-axis exposure quality flag and for the brightest 5% of pixels which are removed before creating the background map. The second image shows this background map uncorrected for vignetting so that the centre appears slightly brighter than the edge regions.

The lightly smoothed image is then systematically scanned for peaks in the data above an arbitrary brightness threshold that varies significantly between observations.

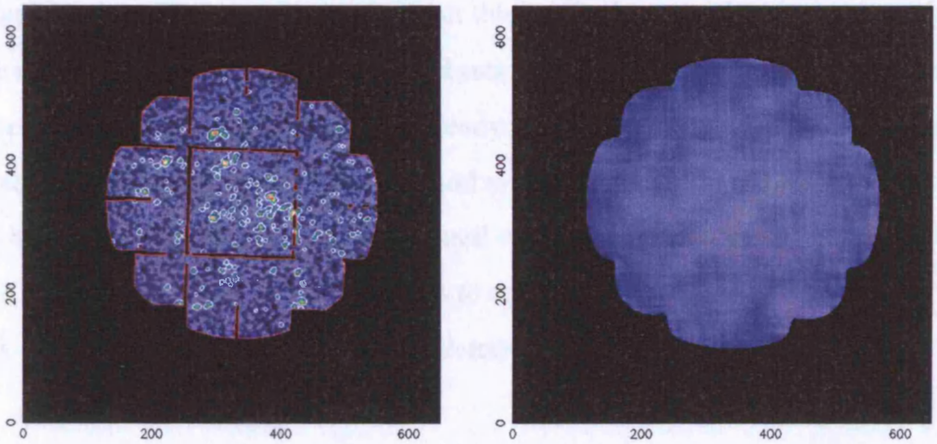

FIGURE 2.7. The process of creating background images. The left-hand image shows the lightly smoothed data with bright regions contoured in white and the boundaries imposed by the minimum exposure threshold shown in red. The right-hand image depicts the heavily smoothed background image, having removed the bright regions.

The only requirement on this search threshold is that it must be sufficiently low to allow for the reduced brightness level at the edges of each observation due to vignetting. At each point where a peak in the data is found, the total count within a beam radius of 4 pixels (16 arcseconds) is taken for both the raw unsmoothed image and the background map. For the point spread function (PSF) of the EPIC instruments this beam radius captures on average $\sim$ 70% of the flux from a point source. In order for a peak to qualify as a source, two selection criteria are applied:

1. $\geq$ 10 counts above background level
2. $\geq 5\sigma$ significance above background level

The minimum number of counts corresponds to a minimum on-axis flux sensitivity (for a 5 ks observation) of $\sim 10^{-14}$ erg s^{-1} cm^{-2}(0.4–6 keV) for a Galactic absorbing column of 10^{22} cm^{-2}. As the photon counts follow Poisson statistics the 2nd criterion means that the number of counts in the raw image must be above that of the background by an amount at least five times $\sqrt{B}$, where B is the number of counts in the background beam area. Figure 2.8 shows an example of this peak scanning process, again using Ridge 1 data, with circles overlayed at each point where a peak was found and checked in the image. Green circles represent peaks which do not contain enough counts to satisfy the criteria above and red circles represent peaks which do and are therefore classified as point sources. The sources detected via this method are used to create a quality flag which is then used to mask out all detected sources as well as all bright regions (though in some cases the bright regions flag will already contain all detected source positions) in a reiteration of the creation of the background map. Subsequently the same peak scanning and source detection algorithm is performed using the new background map to test for source significance. This iterative process to optimise source detection (shown in Figure 2.9) is repeated until no new sources are detected.

2.6.3 Merging source lists

The source detection algorithm, applied to all data sets, produces six separate source lists per observation. These are merged to produce a single list per observation by correlating sources between the lists using a separation threshold of 5 pixels (20 arcseconds) to

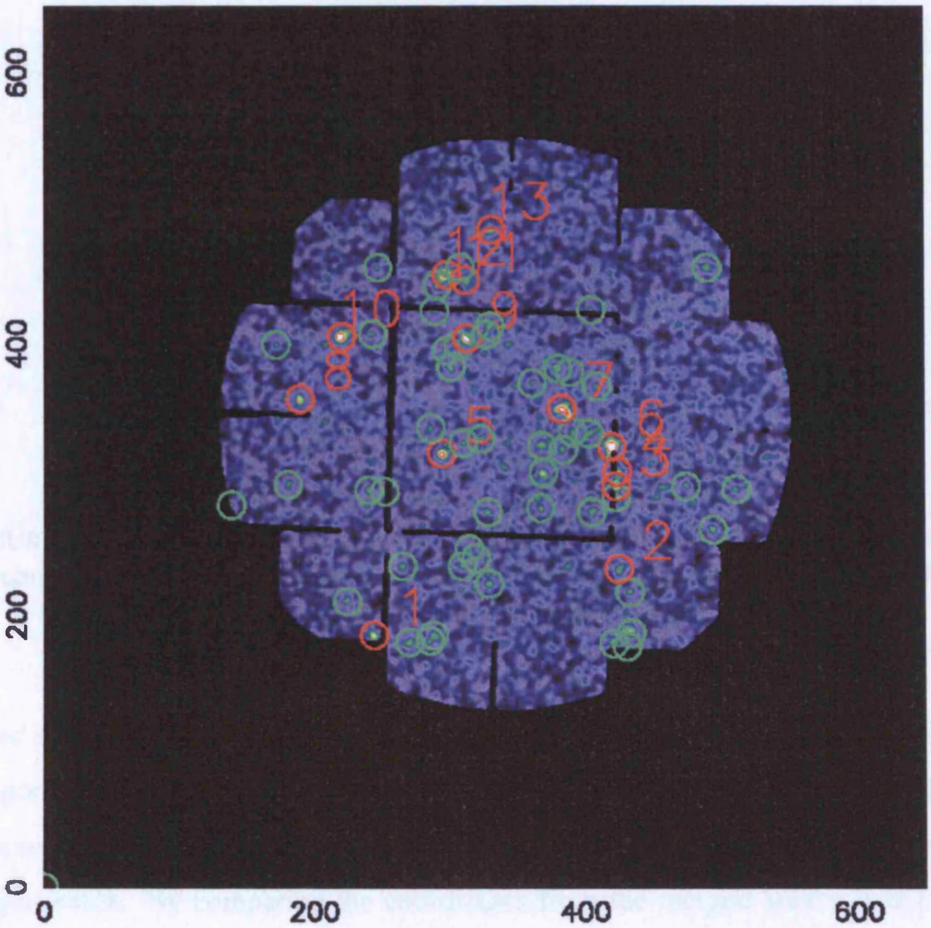

FIGURE 2.8. The source detection algorithm. Each smoothed image is scanned for peaks at an arbitrary low threshold and at each peak the counts of both the raw data and the background are measured within a 4 pixel radius. A peak qualifies as a source (red circles) if the two selection criteria (see text) are passed.

distinguish between sources. Although positional agreement between common source detections is usually significantly better than this threshold, it was chosen so that sources would not be identified as distinct if the separation between them was less than the angular resolution of the EPIC instruments. Figure 2.10 shows an example of the differing results of source detection between the MOS and pn cameras, this time using data from a central region of Ridge 3. In the broad energy band (0.4–6 keV) four sources are detected in the region displayed but only one of them is detected in both the pn and combined MOS cameras. The position offsets for detections of the same source in two detector channels or in different bandpasses of the same detector were found to be dis-

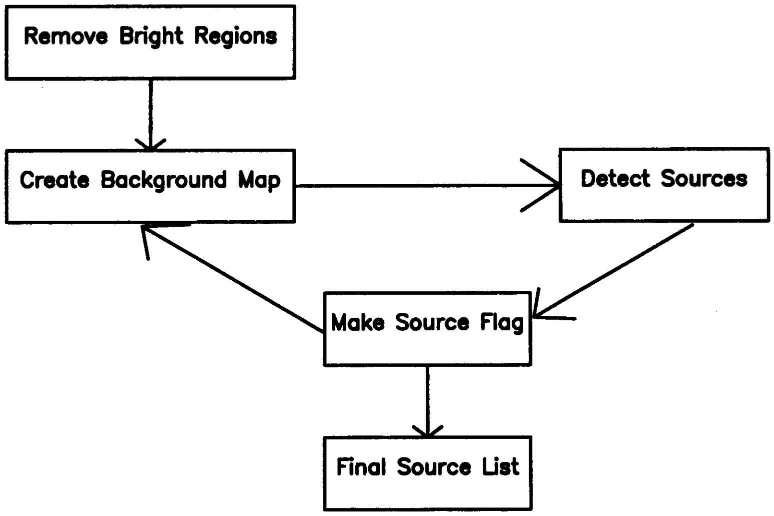

FIGURE 2.9. Flow chart depicting the iterative process used to detect sources. The sequence is repeated until no new sources are detected, thereby maximising the efficiency of both source detection and the creation of background maps.

tributed such that 68% (90%) were contained within a radius of $\approx 2.8''$ ($\approx 4''$). Also of importance when creating a full source list across all observations is consideration that many of the XGPS observations overlap and therefore some areas of the sky are surveyed twice. By comparing the coordinates from the merged source lists for each observation, any sources detected in more than one pointing are removed using the same 5 pixel spatial discriminator as used for merging individual observation lists.

2.6.4 Measuring Source Flux

Having created a single merged source list for each observation, the count rates of each source in each camera (pn & combined MOS) and energy band are then calculated. This is done using a similar technique to that used for detecting sources, *i.e.* measuring the flux within a certain beam radius in both the raw data and background images. However, whereas a beam radius of 4 pixels is appropriate to maximise source detection, for a more accurate determination of source flux a beam radius of 6 pixels (24 arcseconds) is preferable. For a typical point spread function this radius captures 80% rather than 70% of point source flux. The flux of each point source must also be corrected for the

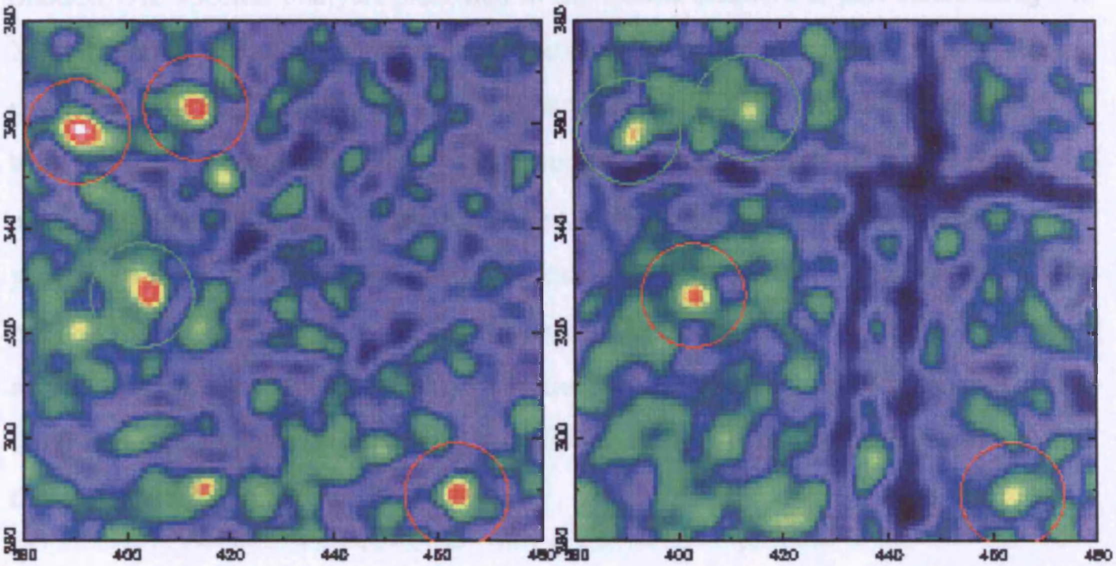

FIGURE 2.10. Zoomed in example of the results of source detection in different cameras. The left-hand image shows a region of combined MOS data where four peaks have been tested and three sources have been found. The right-hand image shows the same region in the pn camera where one extra source has been detected whereas two other peaks that were identified as sources in the MOS data do not qualify in the pn data. This highlights the importance of searching for sources in different detectors and energy bands.

off-axis angle at which it was detected, due to the effect of vignetting on X-ray photons passing through the detector mirrors. This correction factor is calculated using exposure maps produced by the SAS pipeline in appropriate energy bands. Therefore 6 fluxes are recorded for each individual source, representing three energy bands and two different instruments.

2.7 Spectral Extraction

Whether investigating point sources or diffuse emission, much information can be obtained from analysis of the associated X-ray spectrum. As stated previously in §2.5.1, this requires strict filtering of each observation light curve in order to prohibit contamination from proton flares of unknown spectral form. As only quiescent periods of each light curve may be used for spectral analysis, all data from XGPS 14 & XGPS 15 are omitted. All spectral analysis presented in the results chapters is performed using the XSPEC software package, with spectral files created by filtering EPIC event lists in a similar way to that described for source detection. Due to different allowances for overhead time the pn camera generally has shorter exposures than each MOS camera which, after ignoring all proton flare intervals, leaves comparatively little data for spectral analysis. Also there is far greater difficulty in estimating the internal background with the pn, due primarily to the lack of CCD pixels which remain unexposed to the sky during an observation. As a result of these difficulties the spectral analysis of both sources and diffuse emission focuses on data from the MOS cameras which are combined to improve the signal to noise ratio.

2.7.1 Point Sources

The combined spectrum of all the point sources is extracted using two separate spatial flags, one foreground and one background. The foreground flag consists of an array of circles, centred on the identified source positions, of radius 6 pixels (24 arcseconds) which for a typical point spread function represents 80% of the total source flux. A second array of annular rings is used to extract a background spectrum. These annuli extend from a radius of 6 pixels to a radius of 20 pixels around each source position giving a total area ten times greater than that used to extract the foreground spectrum. Where two sources occur close to each other the region occupied by one source is removed from the overlapping annulus area of the other source (Figure 2.11). This method leads to a factor ~ 4 more counts in the background spectra than in the foreground spectra. To create a net source spectrum the background is subtracted from the foreground using the ratio of pixel area, corrected for the effect of vignetting. One minor problem exists when it comes to subtracting the background spectrum. The total signal in the foreground spectrum is comprised of three components: source flux, 'real' sky background and instrumental background. The problem comes from the fact that whilst the sky signal is vignetted across the field of view, the internal background is not. Therefore when the background spectrum is subtracted using the effective (vignetting-corrected) area ratio the scaling is not correct for the internal background contribution. However as the ratio of real area pixels is typically within one percent of the effective area ratio, this approximation is an extremely good one and does not noticeably affect the resulting net source spectrum. A detailed knowledge of the spectral shape of the internal instrument background is therefore not needed to create a net source spectrum, however this is required for any analysis of emission covering the whole observational field of view.

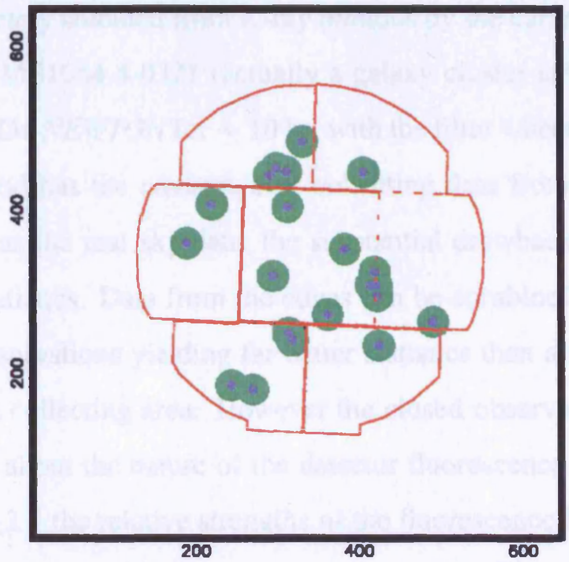

FIGURE 2.11. Example of regions used for source and background spectrum extraction. Blue circles show the regions from which source spectral data are extracted and green annuli show the regions from which appropriate background data are collected.

2.7.2 Diffuse Emission

Having detected and removed X-ray point sources from each field the subsequent and more problematic step is to extract and analyse what remains, *i.e.* the diffuse X-ray background. By the nature of diffuse emission the number of photons recorded from the X-ray background is many times lower per pixel than for point sources. In order to achieve good enough statistics for spectral analysis it is often, though not always, necessary to combine data from several observations in a similar area of the sky. This is especially pertinent to the shallow observations in the Galactic Plane which, as single observations, are too short to achieve sufficient signal to noise from the diffuse background.

Internal background modelling

Key to this analysis is an understanding of the spectrum of the internal background for the EPIC instruments. There are two effective methods for estimating this background. The first is to use data from the edges of the CCDs which are unexposed to the sky as outlined in §2.4. Alternatively one can use data from 'closed' observations in which the detectors are completely shielded from X-ray photons by the camera's filter wheel. One such observation is MS1054.4-0321 (actually a galaxy cluster at redshift 0.83!) which was observed by *XMM-NEWTON* for $\sim$ 10 ks, with the filter wheel closed, in June 2001. Although this method has the advantage of collecting data from exactly the same regions of the CCDs as the real sky data, the substantial drawback is the exposure time and therefore the statistics. Data from the edges can be combined from a large number *XMM-NEWTON* observations yielding far better statistics than a closed observation, in spite of the reduced collecting area. However the closed observation does provide important information about the nature of the detector fluorescence lines. As has already been mentioned in §2.4 the relative strengths of the fluorescence lines are know to vary across the field of view in both MOS and pn cameras (Lumb et al. 2002). By selecting only events occurring in the energy bands of strong fluorescence lines (some of which will of course be continuum cosmic ray events rather than fluorescence) from MS1054.4-0321 this effect can be demonstrated graphically. Figure 2.12 shows smoothed images of events selected in two narrow energy bands; 1.400–1.575 keV and 1.675–1.800 keV representing Aluminium and Silicon fluorescence respectively. Aluminium fluorescence is weaker in the central CCD chip of the MOS 1 camera (and similarly for MOS 2), however Silicon fluorescence is enhanced in the central chip due to the presence of Silicon in the rear of the outer chips which are positioned slightly above it.

A direct comparison of these two methods for estimating the combined internal background spectrum of the EPIC-MOS cameras is shown in Figure 2.13. The MS1054.4-0321 ('closed') spectrum is scaled so it is equivalent to the pixel area of the edges spectrum. As with Figure 2.2 the data which comprise the edges spectrum are comprised from a variety of observations in order to improve the signal to noise ratio. As expected the Aluminium fluorescence line is stronger in the 'edges' spectrum due to the deficiency

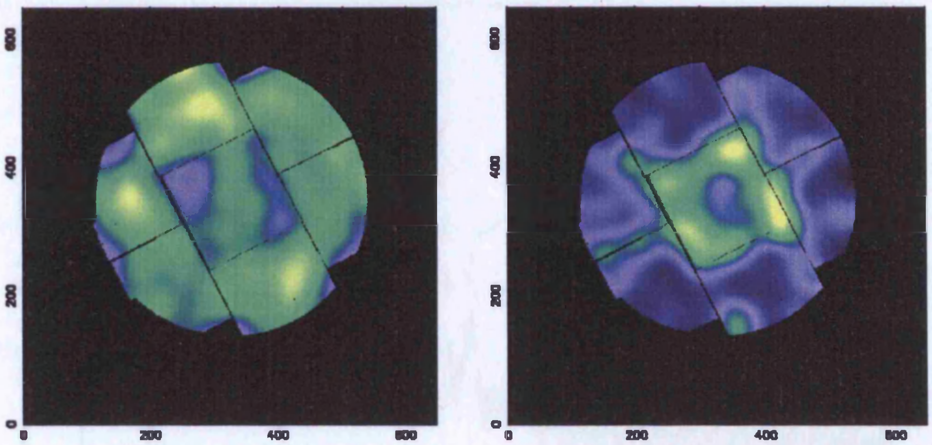

FIGURE 2.12. The distribution of fluorescence emission due to Aluminium (LHS) and Silicon (RHS) from 'closed cal' observation MS1054.4-0321. The smoothed images show a depletion of Al and an enhancement of Si in the central MOS 1 CCD.

of Aluminium in the central CCD of each MOS camera. Similarly Silicon fluorescence emission is clearly stronger in the 'closed' spectrum due to the central chip enhancement shown in Figure 2.12. However, in spite of the substantial variation in fluorescence line strengths the level of continuum flux is in good agreement between the two spectra. This implies that the edges can indeed be used as an estimator of the internal instrument background, provided that care is taken in the energy regimes of the fluorescence line emission.

The data from the MOS CCD edges are modelled using a simple polynomial (in counts space) fit, taking care to exclude the line emission energy bands before fitting. This model only applies to data above 0.4 keV as the response function calibration does not justify using data at lower energies. A generic background spectrum was then created directly from this model, removing the strongest fluorescence lines of Al K, Si K & Au M as all are clearly non-uniform over the field of view. This necessitates that in all future spectral analysis these lines, where appropriate, must be included in any spectral model applied to data where this ideal background spectrum has been subtracted. The other weaker fluorescence lines (all above 5 keV) are left in the generic background spectrum to avoid unnecessarily over-complicating future spectral models with extra

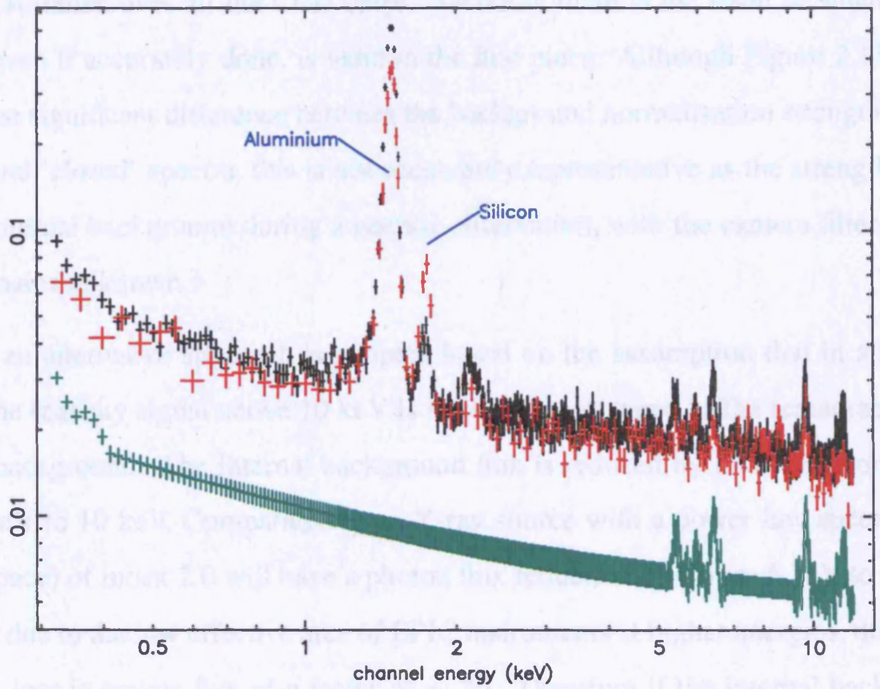

FIGURE 2.13. A comparison of the EPIC-MOS internal background from the CCD edges (black) and across the whole CCD area of the closed observation MS1054.4-0321 (red). The strengths of several fluorescence line are different however the level of continuum flux is identical within the errors. The fitted background spectrum used for subtraction, with appropriate errors, is shown in green, scaled by a factor of three for clarity.

Gaussian components. This clearly introduces some uncertainty into the background subtraction, especially around Fe K (6.4 keV) which is likely to be over-subtracted as it appears stronger in the edges spectrum.

Background Scaling

Having obtained a viable spectral model for the internal background the crucial parameter becomes the scaling for background subtraction. The obvious method of scaling simply by the pixel area ratio of edges to in-field produces reasonable results though not without introducing uncertainties. These lie firstly with the difficulty in estimating how many pixels can potentially be flagged as being outside the field of view, this is estimated by subtracting the number of pixels in the exposed regions from the total number of pixels summed over all the CCD chips. Secondly there is the issue of whether this scaling, even if accurately done, is valid in the first place. Although Figure 2.13 seems to show no significant difference between the background normalisation strengths of the 'edges' and 'closed' spectra, this is not necessarily representative as the strength of the in-field internal background during a normal observation, with the camera filter wheels open, remains unknown.

Here an alternative approach is adopted based on the assumption that in all observations the real sky signal above 10 keV is negligible compared to the remarkably hard internal background. The internal background flux is reduced by a factor of only 1.25 from 5 keV to 10 keV. Comparatively an X-ray source with a power law spectrum (in photon space) of index 2.0 will have a photon flux reduction of 4 from 5 keV to 10 keV. However due to the low effective area of EPIC instruments at higher energies, this translates to a loss in counts flux of a factor of $\sim$ 50. Therefore if the internal background comprises 50% of the total signal at 5 keV (as is approximately the case for the Galactic Plane observations) then the expected contribution at 10 keV is 98%, again assuming a spectral slope of 2.0. For the off-plane observations the equivalent figure is over 99% but in either case the accuracy of the assumption that all the $>$ 10 keV flux will be internal background is far better than an area scaling method. By assuming that the measured continuum flux in the range 10–11 keV (excludes Au L shell fluorescence) is due entirely to the internal background, the background subtraction scaling parameter follows trivially for each individual diffuse spectrum. Some examples of these scaling parameters are shown in Table 2.3 along with the equivalent value estimated from pixel are scaling. The variation in the area scaling parameter is caused entirely by the number of sources removed from the field of view. For example SDS 1 is a much longer exposure than the other observations and as a result more sources are detected, thus reducing the number of pixels available for diffuse emission analysis. This factor similarly affects the 10–11 keV flux scaling parameter, as fewer pixels results in less in-field flux in any energy band. The additional scatter in the flux scaling parameter is likely to be due to real variation in the amount of internal background flux at around the 10 percent level.

Table 2.3. Background spectrum subtraction scaling parameters. Variation is caused primarily by the number of pixels available for diffuse analysis after point source removal.

	Background scaling method	
Region	10–11 keV Flux	Pixel Area
XGPS[a]	3.05	2.74
SDS	2.33	2.29
Bulge-8	3.10	2.64
GC 1	2.58	2.70
Field IV	2.72	2.64

[a]Combined data from 19 XGPS fields

2.8 Detecting Extended Objects

XMM-NEWTON provides not only superior spatial and spectral resolution to previous X-ray satellites which have surveyed the Galactic Plane, the key advantage when searching for extended objects, such as supernova remnants (SNRs) is the extremely large photon collecting area which the EPIC instruments possess. The technique for detecting extended objects outlined in this section applies only to the 17 XGPS & 5 Ridge observations, in spite of their relatively short exposures, as they provide a large survey area of $\sim$ 3 square degrees in a region known to contain several radio-emitting extended objects (Altenhoff et al. 1979) including HII regions and SNRs. Also of benefit is the fact that these observations overlap and therefore gaps in the survey region are kept to a minimum. This, however, does not apply so well with the pn camera so for this reason, combined with the need for accurate background estimation, only data from the MOS cameras are used to analyse the diffuse background. As with source detection and spectral analysis, data from these two cameras are combined to improve the signal to noise and thereby enhance the potential for extended object detection.

In order for faint extended objects to be visible, both point sources and the non-sky background must be removed so that the remaining images represent only the true diffuse X-ray background. The main problem in achieving this comes from uncertainties in estimating the amount of non-sky background in each observation. In order to produce a flat diffuse X-ray background image, the genuine 'sky' events for each exposure must be corrected for the effect of vignetting. Therefore obtaining a reasonable estimate of the background contributions is essential to avoid over-enhancing (or indeed under-enhancing if the background contributions are over-estimated) the outer regions of the field of view. To simplify this analysis diffuse X-ray images are made in just two energy bands; the same soft and hard bands (0.4–2 keV & 2–6 keV respectively) used for source detection analysis. Again strong fluorescence lines are removed from the soft band. At each stage of diffuse background image creation it is crucial to know how many counts are in each image and each energy band following the light curve filtering process. To achieve this sensitivity and to maximise the amount of exposure time available for each diffuse background image, light curves are created for each observation in the same two energy bands used to display the images, rather than the broader range of 0.2–12 keV used to filter data for source detection and spectral analysis. The maximum permitted count rates are set strictly at 0.7 count s^{-1}(soft band) and 0.8 count s^{-1}(hard band). These values were derived from observations with no proton flaring and, when applied to other, more contaminated observations, results in the exclusion of all noticeable proton flare intervals. Some proton flaring events will of course occur during the accepted time intervals. These are important and how they are processed is outlined in §2.8.2.

2.8.1 Internal Background

The strength of the EPIC-MOS internal background is likely to be variable as shown by considering flux in the 10–11 keV energy band over a variety of observations (see §2.7.2). However this variation is small and for the purposes of image analysis it is a reasonable approximation to deem the background to be constant. This is further justified by the consideration that, at least in the case of short exposures, each observation contains insufficient data in the unexposed CCD regions to accurately determine the internal background level for that observation. However, a canonical constant value to use as the background level still needs to be established. It can easily be seen by examining data occurring within the proton flare intervals that the CCD edges also are affected by this form of contamination. Therefore, as there is no way of distinguishing between

Table 2.4. Mean internal background count rates, calculated using data from the CCD edges of 6 observations with minimal flaring.

	Count rates[a]	
Energy Band	MOS 1	MOS 2
Soft (0.4–2 keV)	0.84	0.98
Hard (2–6 keV)	1.70	1.79

[a]In units of 10^{-6} count s^{-1} pix^{-1}

flare events and internal background events in the edges, only those observations with minimal or no flaring are suitable for use in determining the background constant. The observations selected for this purpose are Ridge 1, XGPS 1, 4, 5, 8 & 12. The relatively quiescent nature of the light curves of these observations can be seen in Figure 2.5. The mean edge fluxes for each MOS camera in both energy bands were calculated separately by averaging the values from all 6 observations, weighted by the quiescent exposure time. The final values, given in units of count s^{-1} pix^{-1}, are listed in Table 2.4.

2.8.2 Flare contamination

The stringent light curve cuts, at 0.7 count $s^{-1}$and 0.8 count s^{-1}, for soft and hard energy bands respectively, ensure that the majority of proton flare events are excluded from data selection. However a comparison of the quiescent period count rates of all relevant observations implies a residual low level flare contamination. Figure 2.14 shows the in-field count rates of 20 Galactic Plane observations (as XGPS 14 & XGPS 15 have no periods of genuine quiescence), calculated after the light curve filter has taken effect. Clearly there is substantial variance between observations which cannot be removed by simply lowering the light curve cut thresholds - this would reduce the quiescent exposure times of several observations to almost zero. The count rates shown in Figure 2.14 include the internal background counts caused by cosmic ray events, however the observed variance is too great to be explained by fluctuations in this signal. The contribution of the internal background is approximately 0.13 count s^{-1}& 0.24 count s^{-1}in the soft and hard bands respectively, therefore a signal variability of up to 200% would be required

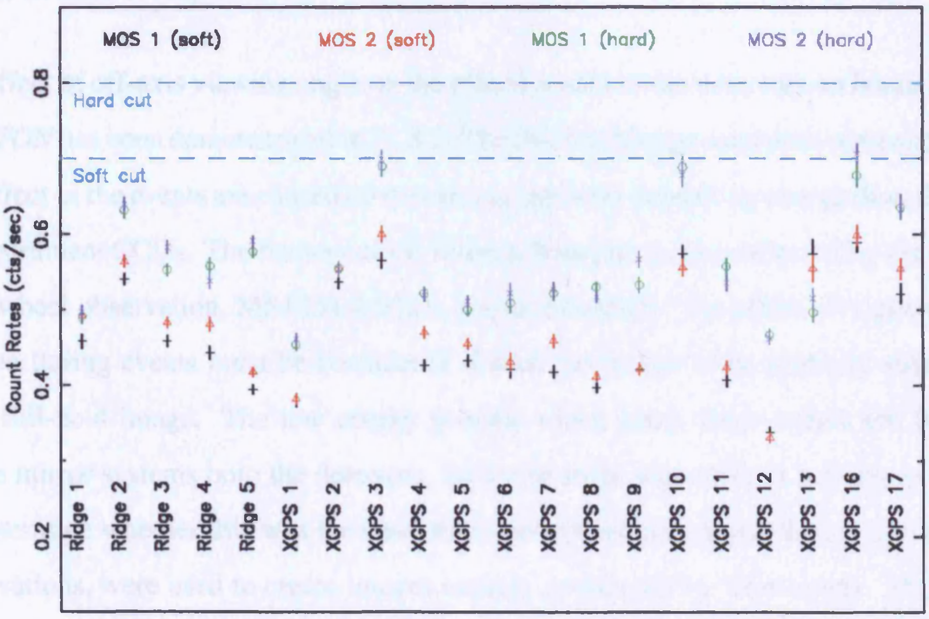

FIGURE 2.14. Average count rates of Galactic Plane observations after removal of proton flaring time intervals. The high level of count rates in some observations (*e.g.* XGPS 16) is caused by the presence of proton events in the 'quiescent' periods of the light curves. These are subtracted from the data using a spatial model for the distribution of these events estimated using extremely large flares.

to account for the changes in total count rate.

The alternative and far more likely explanation is a residual flux contribution from proton flaring events. The number of these events can be estimated by subtracting an average count rate from the total for all observations. This average value is calculated using the same observations as were used to estimate the mean internal background level (*i.e.* Ridge 1, XGPS 1, 4, 5, 8 & 12), again using the quiescent exposure times as a weighting function. However as there is no apparent systematic difference between the two MOS cameras, the data are combined to create a MOS average. The mean values determined in this way are 0.436 count s^{-1}(soft band) and 0.496 count s^{-1}(hard band). Before any attempt can be made to subtract remaining flare events from the main image, the distribution of these events across the field of view must be investigated.

Profile of flare events

The effect of off-axis viewing angle on the effective area of the detectors on board *XMM-NEWTON* has been demonstrated in §1.3.1. The internal background does not experience this effect as the events are caused by cosmic ray particles depositing charge directly onto the instrument CCDs. The flatness of the internal background is confirmed by the closed filter wheel observation, MS1054.4-0321, discussed earlier. The effect of vignetting, if any, on flaring events must be considered if such events are to be spatially subtracted off a full-field image. The low energy protons which cause these events are focused by the mirror systems onto the detectors, therefore some vignetting is entirely possible. To determine whether this was the case, three periods of substantial flaring, in separate observations, were used to create images entirely dominated by flare events. The count rates in these flare intervals were at least a factor of ten greater than the quiescent levels.

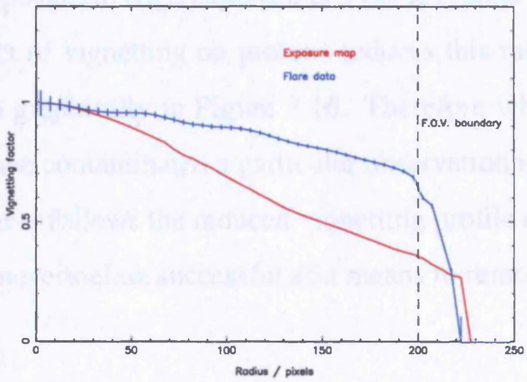

FIGURE 2.15. Radial profiles of data from an observation containing a massive flare and a typical exposure map. The effect of vignetting, although much stronger for photons passing through the mirrors, is also clearly visible in images made with data from soft proton interactions.

The flaring event images showed evidence of some vignetting but less than that of the real sky events. This effect is shown more clearly with real flare data in Figure 2.15. These images were then compared to the vignetting of real sky events by manipulating a 2–4.5 keV exposure map and dividing one by the other to obtain a flat net result. In order to achieve this flat result each exposure map required a constant to be added across the whole field, approximately equal to 1.5 times the total exposure. For example if

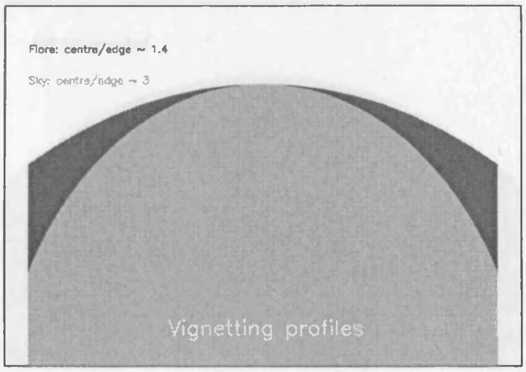

FIGURE 2.16. Example cross-sections showing the reduced effect of vignetting on flaring events caused by protons. The spatial distribution of such events is modelled by manipulating an exposure map to fit the profile of flare-dominated images. In effect this involves adding a constant value, equal to 1.5 times the maximum exposure, to the exposure image. Flare events are subsequently subtracted from the raw data using this approximate distribution.

the ratio of on-axis exposure to edge exposure is 3 (as is typical for the MOS cameras), then the reduced effect of vignetting on protons reduces this ratio for flaring events to ~ 1.4. This is shown graphically in Figure 2.16. Therefore when the number of flare counts estimated to have contaminated a particular observation is subtracted, the spatial distribution of the counts follows the reduced vignetting profile described. This process is rather arbitrary but nevertheless successful as a means to remove residual flare data.

2.8.3 Image construction

Using data from both exposed and unexposed CCD regions, the number and distribution of non-sky events may be estimated for each observation. A schematic representation of the relative contributions of sky events, proton flaring events & internal background events is shown in Figure 2.17. Having subtracted the estimated background contributions from each observation, the images are then corrected for the effect of vignetting using SAS pipeline produced exposure maps, identical to those used to correct point source fluxes. As exposure times vary substantially between observations, especially after flaring intervals are removed, each observation is normalised by the total on-axis exposure which remains after light curve filtering. Point sources are removed using a cir-

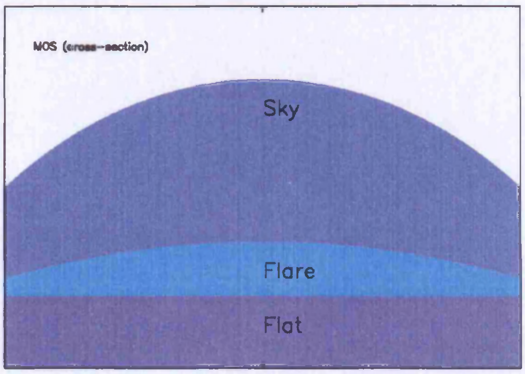

FIGURE 2.17. Schematic cross-section showing the three components of a MOS image (after point sources have been removed). The three components are: a flat internal background (bottom), a moderately vignetted proton flare background (middle) and the fully vignetted real sky data.

cular mask of radius 8 pixels (32 arcseconds), although for exceptionally bright sources the mask size is increased to minimise source flux leakage. Finally the observations are mosaiced together on a Galactic coordinate grid (see Figure 2.18) and heavily smoothed to enhance the visibility of extended features. The net effect of this image creation process is to normalise the observations such that the number of counts in each is approximately constant. Although this creates a slightly artificial uniformity in the diffuse X-ray background images, the benefit of being able to detect some extended objects in the images justifies the background subtraction process.

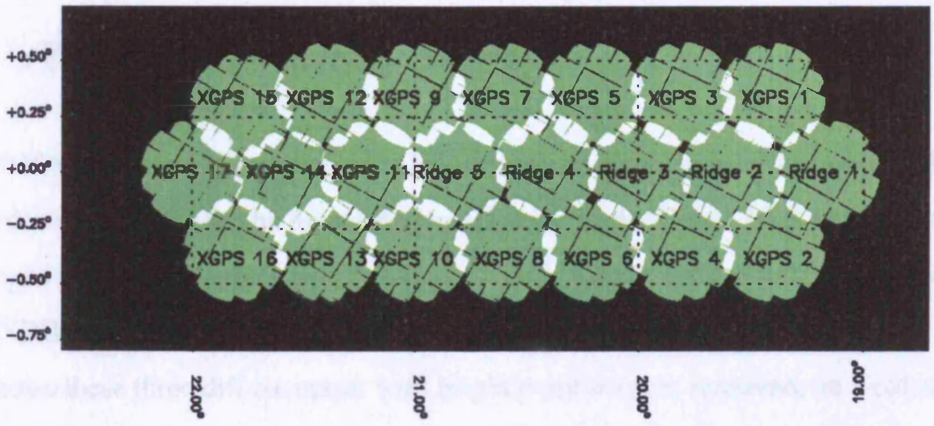

FIGURE 2.18. Mosaic showing the overlap of XGPS observations. Combined MOS fields of view are plotted on a Galactic coordinate grid.

Chapter 3

The Soft X-ray Background

3.1 Overview

This chapter looks at the Galactic soft X-ray background (SXRB) and attempts to gauge the balance between local and distant emission using data from both *XMM-NEWTON* and rosat X-ray satellites. This is accomplished by comparing X-ray spectra from observations over a wide sky region, covering a large range of Galactic interstellar absorption. The physical parameters of the hot plasmas responsible for the observed X-ray emission are calculated and compared to previous results.

3.2 The *ROSAT* All-Sky Survey

The *ROSAT* All-Sky Survey (hereafter RASS) diffuse X-ray maps (Snowden et al. 1995, Snowden et al. 1997) are the most detailed all-sky images of the SXRB available to date. Arranged into three distinct energy bands ($\frac{1}{4}$ keV, $\frac{3}{4}$ keV and 1.5 keV) they show how the SXRB varies across $\sim$ 98% of the sky with an angular resolution of $\sim$ 12'. Figure 3.1 shows these three diffuse maps, with bright point sources removed, on a colour scale with white representing maximum intensity. The positions of individual or clusters of *XMM-NEWTON* observations are marked on each map, exact coordinates can be found in Table 2.1 in §2. The two maps of most interest are the $\frac{1}{4}$ keV and $\frac{3}{4}$ keV maps as the comparable data to the 1.5 keV band from *XMM-NEWTON* is contaminated by a strong Aluminium fluorescence line.

The focus of investigation for this chapter is split into two parts conveniently delineated by the energy ranges of the $\frac{1}{4}$ keV and $\frac{3}{4}$ keV RASS maps. Although the area covered by the *XMM-NEWTON* observations marked in Figure 3.1 is small compared to the all-sky coverage of *ROSAT* , the spectral resolution of *XMM-NEWTON* provides a powerful tool for the separation and parameterisation of the emission components.

The SXRB at $\frac{1}{4}$ keV is highly variable across the sky and has at least two competing sources, the Galactic Halo and the Local Hot Bubble (LHB), both of which are thought to be hot plasmas at a temperature of $\sim$ 0.1 keV (or $10^{6.1}$K). The RASS map shows a general anti-correlation of the $\frac{1}{4}$ keV signal with interstellar absorption, as has been known for some time and implying that at least part of the emission originates beyond the LHB. Conversely, shadowing experiments have shown that a significant fraction of the emission must originate locally (Snowden 2000). Clearly a detailed disassociation of the two components, such as that performed by Kuntz & Snowden (2000), is not possible with a handful of *XMM-NEWTON* observations. However, by examining data from observations over a range of Galactic latitudes it is possible to ascertain the balance of the two components in specific directions. For this to be possible the actual *ROSAT* PSPC data which give rise to the $\frac{1}{4}$ keV counts shown in Figure 3.1 are used in joint fits with the X-ray spectra extracted from each *XMM-NEWTON* observation.

The second focus of this chapter rests on the high surface brightness features clearly visible in the $\frac{3}{4}$ keV map (and to a lesser extent in the 1.5 keV map) shown in Figure 3.1. Probably the most distinct of these is the broad stripe of emission roughly centred at l=25°, b=30°, known as the North Polar Spur (NPS). The NPS is commonly associated with radio Loop 1 and a variety of different theories have been proposed to explain its origin. These range from a nearby supernova remnant (Berkhuijsen et al. 1971) or combination of stellar winds and SNRs caused by the Sco-Cen OB association (Egger & Aschenbach 1995) to part of a bipolar hypershell originating from starburst activity at the Galactic Centre (Sofue 1994; Sofue 2000). Recent observations have favoured the model of a diffuse superbubble filled with plasma at a temperature of $\sim$ 0.26 keV

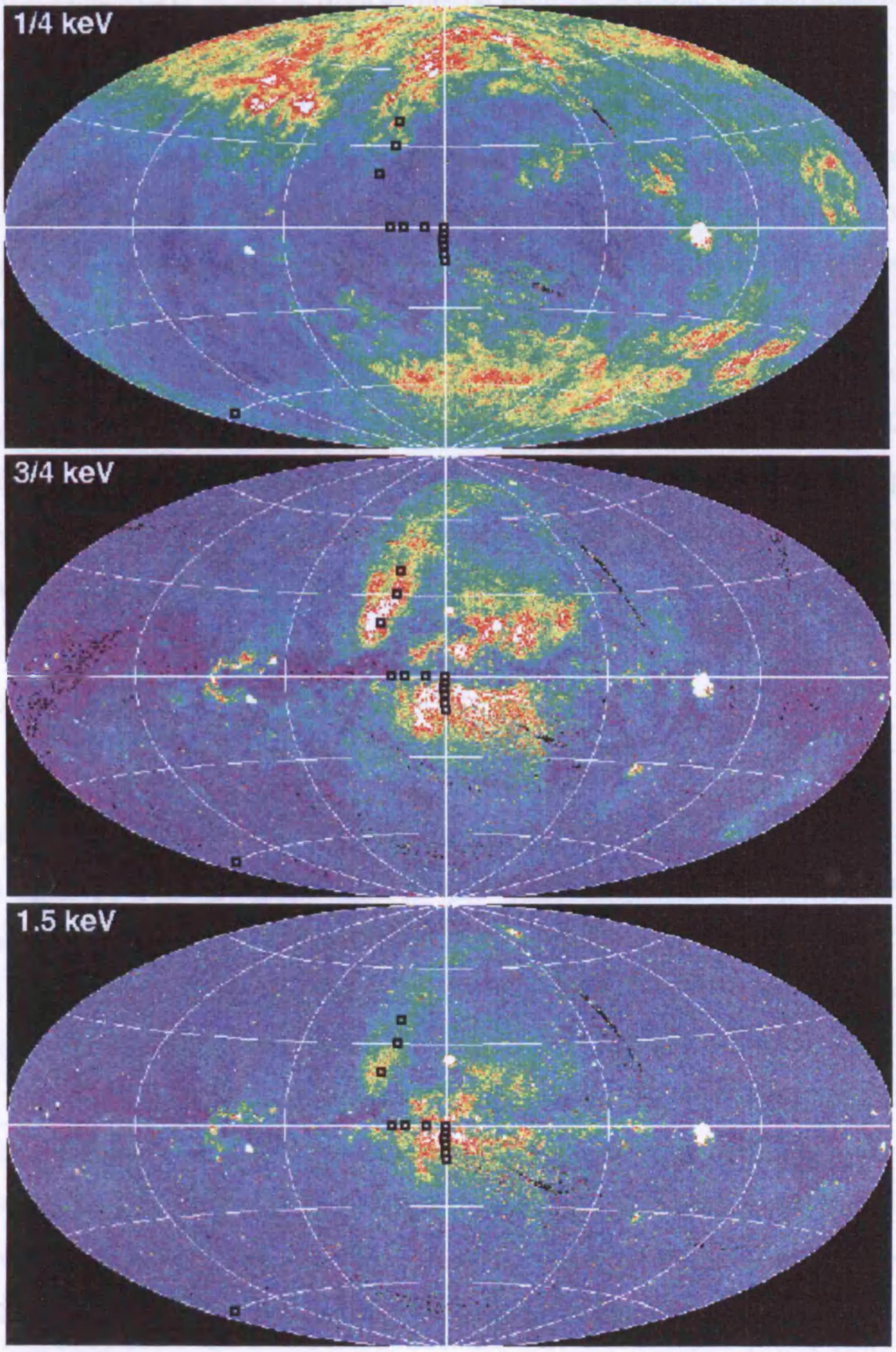

FIGURE 3.1. *ROSAT* All-Sky Survey (RASS) maps in three energy bands; $\frac{1}{4}$ keV, $\frac{3}{4}$ keV and 1.5 keV. The angular resolution is 12' and the colour scale ranges from blue (faint) to white (bright). Observations (or observation clusters) from which spectra are extracted are marked with empty black squares.

located at a distance of $\sim$ 200 pc from us, not far from the Sco-Cen OB association which may provide a pointer as to its origin. The other high surface brightness regions which appear above and below the Galactic Centre may have a common origin with the NPS or alternatively they may be part of an X-ray bulge component, as suggested by Snowden et al. (1997). For convenience this latter emission is referred to as "bulge" emission throughout this chapter, although this is not meant to prejudice the determination of the location of its source (*i.e.* it could also be referred to as Loop 1 bubble or superbubble emission). Similarly the 5 observations which are located in the bright region south of the Galactic Centre are referred to as the southern bulge fields. The *XMM-NEWTON* data from the most recent NPS analysis (Willingale et al. 2003) is used along with comparable data from below the Galactic Centre to investigate whether or not the bright $\frac{3}{4}$ keV RASS features have properties consistent with a common origin.

3.3 Spectral Fitting

In this section the results of spectral fitting are presented for each individual observation with the exception of the SDS (Subaru Deep Survey) fields and XGPS fields which are respectively added together to improve the signal to noise of the data. All spectra shown are full-field spectra derived by adding together the two EPIC-MOS cameras for reasons outlined in §2. The energy range considered for the purposes of this spectral modelling is 0.4–1.6 keV which includes the strong Al K fluorescence line from the MOS detectors. The latter feature is modelled with a Gaussian line, the strength of which is allowed to float freely. In the case of all three NPS spectra and the combined spectrum from the SDS observations, the counts above 1.6 keV are entirely due to extragalactic flux consistent with Lumb et al. (2002). Four of the five southern bulge observations contain a hard excess, dependent on Galactic latitude, that is modelled in this section with a simple power law as it does not significantly affect the modelling of the SXRB. Similarly the spectrum of the Galactic Ridge above 1.6 keV is clearly dominated by hard Galactic emission which does contribute to the observed signal in the $\frac{3}{4}$ keV band. Therefore although the models shown for these regions include components that are not part of the

Table 3.1. Key to individual model component colours in plotted spectra.

Model Component	Colour
Extragalactic power law	Dark blue
Local Hot Bubble	Purple
Southern Bulge/NPS	Green
Halo (low temp)	Light Blue
Halo (high temp)	Orange
Others*	Black

* Components that are unimportant to the SXRB such as the Al K fluorescence line or higher temperature plasmas towards the Galactic Plane.

SXRB or the extragalactic signal, discussion of these hard components is confined to §5. The MOS instruments operate to a lower energy than 0.4 keV, however this threshold is imposed due to a combination of problems arising from poor calibration and uncertainty with background subtraction at low energy. A proper investigation of the $\frac{1}{4}$ keV signal requires measurement at lower energies and for this purpose the data from the R1 and R2 *ROSAT* PSPC bands (*i.e.* those which when combined form the $\frac{1}{4}$ keV band) are included in the spectral fitting, scaled to a field of view that is equivalent to the MOS cameras.

The XSPEC model used to describe each thermal component is APEC (Astrophysical Plasma Emission Code) which is the successor to the Raymond & Smith Plasma code. Imperfections to this code, specifically discrepancies between calculated and measured Fe XVII line ratios (see Brown et al. 1998), can be found on the WWW[1]. Each spectrum contains an extragalactic power law or EPL (although in fields with high absorption this is too weak to be visible on the scale used). The normalisation and slope of the EPL were fixed at the value measured by Lumb et al. (2002), *i.e.* 9.0 photons s^{-1} cm^{-2} sr^{-1} keV^{-1} at 1 keV and slope Γ=1.4.

The results of the spectral fitting, including physical parameters derived from each model, are shown below for 4 groups of observations classified as follows:

- NPS fields:Field IV, Field V & Field VI, all located in the north polar spur.

- Southern bulge fields:Baades Window, Baades Foreground, Bulge 8, Bulge 12 &

[1] see http://cxc.harvard.edu/atomdb/issues_caveats.html

Field III, located in the bright $\frac{3}{4}$ keV region below the Galactic Centre.

- SDS fields:Single spectrum compiled from seven SDS observations, each located around (l,b) $\sim$ 170°, -60°
- Galactic Plane/Galactic Centre:A single Galactic Centre observation, GC 1, plus three observation clusters along the Galactic Plane - GPS (20°), GPS (15°) & GPS (7°), comprised of 18, 6 & 4 pointings respectively.

To illustrate the large variation in count rates, four spectra, one from each group, are shown on the same axis in Figure 3.2. In individual spectral plots, different components such as the LHB, the Galactic Halo emission, the extragalactic power law *etc.* are plotted separately so the contribution of each is visible at any specific energy. Table 3.1 gives a key to the colours used for each component.

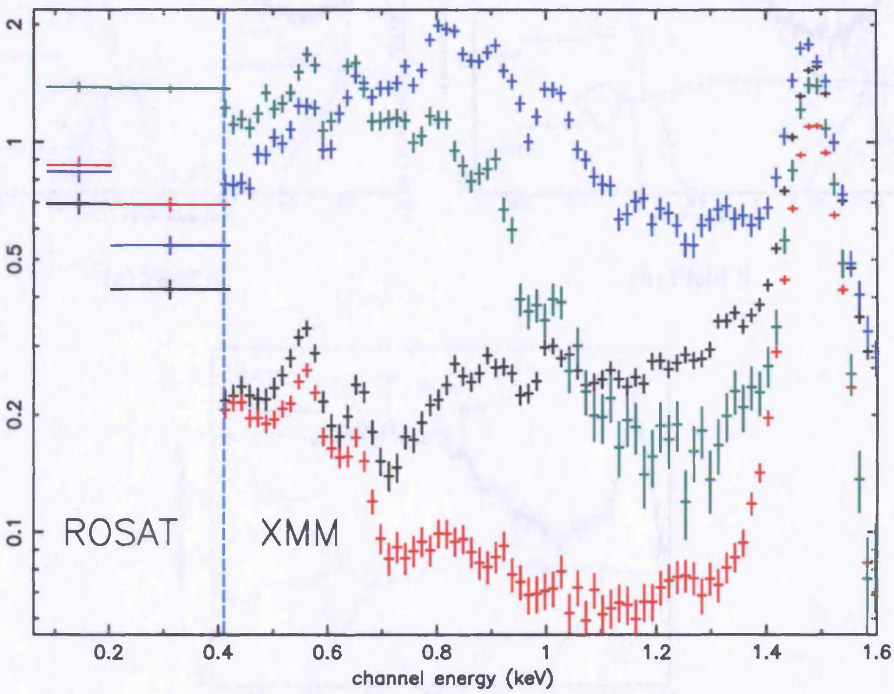

FIGURE 3.2. Comparative plot showing the variation in count rate in four distinct directions. The spectra plotted are as follows:*black:*GPS (20°) in the Galactic Plane, *red:*SDS at high latitude, *green:*Field V in the north polar spur, and *blue:*Baades Window in the southern bulge. The energy regimes of both *ROSAT* and *XMM-NEWTON* data are labelled. The strong *XMM-NEWTON* Al fluorescence line is clearly visible in all spectra at $\sim$ 1.5 keV.

3.3.1 NPS fields

The three NPS spectra were each modeled with an extragalactic power law (EPL) component and three thermal components. The hottest of the thermal components (at a temperature of ~ 0.25 keV or $10^{6.5}$ K) models the bright $\frac{3}{4}$ keV emission visible in the RASS map. The absorption on this component was allowed to float. The other two thermal components both have temperatures of ~ 0.1 keV ($10^{6.07}$ K) representing emission from the LHB and Galactic Halo respectively. Although each field may also contain a second, higher temperature Halo component (see §3.3.3), this is too weak to be seen in the NPS spectra. The full Galactic HI absorption column is applied to the Galactic Halo

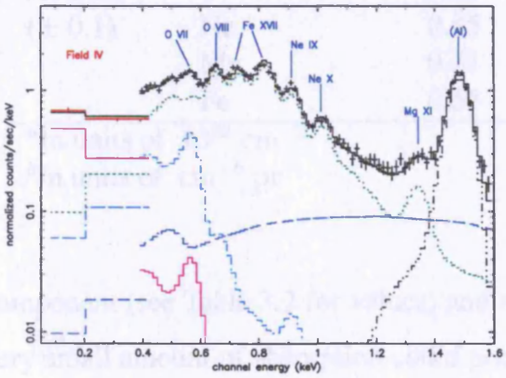

(a) Field 4

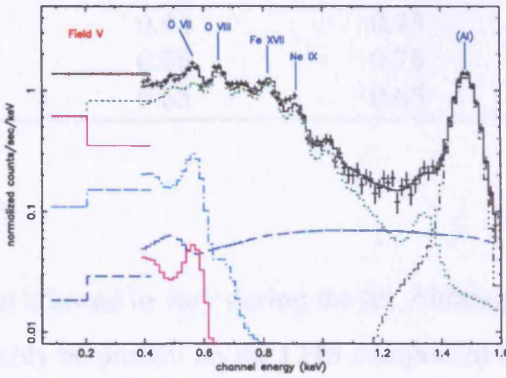

(b) Field 5

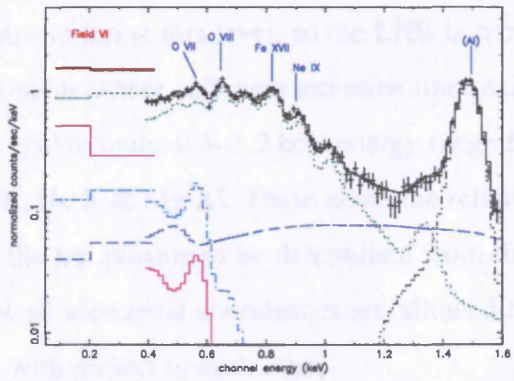

(c) Field 6

FIGURE 3.3. Spectral fits for Fields 4, 5 & 6. The separate components are shown individually to illustrate the contribution of each to a particular energy band, see Table 3.1 for key to colours/components.

Table 3.2. Spectral fit parameters for NPS fields. Temperatures are in keV with errors quoted at the 90% confidence level.

Component	Parameter	Observation Field IV	Field V	Field VI
Reduced χ^2		1.6	2.0	1.0
Full N_H[a]		0.080	0.055	0.040
LHB	Temp.	0.090 ±0.009	0.090 ±0.010	0.131 ±0.030
	EM[b]	0.0040 ±0.0004	0.0042 ±0.0005	0.0048 ±0.0008
Halo	Temp.	0.089 ±0.006	0.088 ±0.010	0.085 ±0.025
	EM[b]	0.11 ±0.05	0.083 ±0.060	0.026 ±0.019
$\frac{3}{4}$ keV	Temp.	0.273 ±0.005	0.248 ±0.006	0.261 ±0.005
(NPS)	EM[b]	0.134 ±0.005	0.101 ±0.002	0.072 ±0.004
	N_H[a](%)	0.078 (98%)	0.032 (58%)	0.02 (50%)
Abunds.	O	0.29	0.32	0.31
(± 0.1)	Ne	0.45	0.44	0.43
	Mg	0.81	0.76	0.76
	Fe	0.65	0.65	0.65

[a]In units of 10^{22} cm^{-2}

[b]In units of cm^{-6} pc

component (see Table 3.2 for values) and not allowed to vary during the fit. Although a very small amount of absorption could possibly be present on the LHB component (the so called 'local fluff', Kuntz & Snowden 2000), the parameters derived from the spectral fit are dependent almost entirely on the $\frac{1}{4}$ keV *ROSAT* data which alone is insufficient to accurately determine absorption at this level, so the LHB is left unabsorbed. Elemental abundances are determinable where sufficient emission lines exist in the spectrum. Several emission lines are visible in the 0.5–1.2 keV energy range from ions such as O VII, O VIII, Fe XVII, Ne IX, Ne X & Mg XI. These allow the relative (to solar) abundances of several elements in the hot plasma to be determined from the spectral fit. However, due to the fact that not all elemental abundances are allowed to vary, these values are better viewed as being with respect to each other.

The X-ray spectra of all three NPS fields are shown in Figure 3.3 and the values, plus errors, of all parameters derived from the NPS field fits are given in Table 3.2. Contour plots showing how χ^2 is affected by variation in NPS temperature and absorption column are also shown in Figure 3.4.

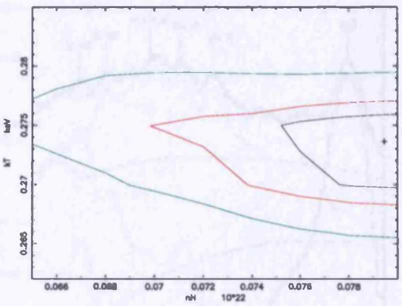

(a) Field 4

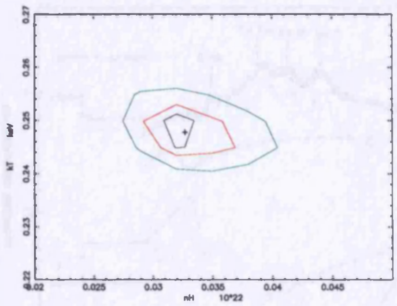

(b) Field 5

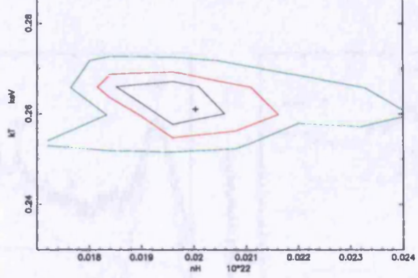

(c) Field 6

FIGURE 3.4. Temperature vs. N_H contour plots for bulge component in Fields 4, 5 & 6. Contours are plotted at the 68%. 90% and 99% confidence intervals.

3.3.2 Southern Bulge Fields

Spectral analysis of the southern bulge fields followed an almost identical method as the NPS fields. The only discernible difference is that in 4 out of 5 of the bulge fields (all except Bulge 12, the field farthest from the Galactic Centre) there is an excess of hard flux above the cosmic X-ray background at energies greater than ~ 2 keV. As mentioned previously this flux is modelled with a simple absorbed power law, the details of which are unimportant in this chapter but are reviewed in §5. The X-ray spectra are shown in Figure 3.5 and all spectral fit parameters for the LHB, Halo & Bulge components, including elemental abundances, are given in Table 3.3. Contour plots showing how χ^2 is affected by variation in bulge temperature and absorption column are also shown in Figure 3.6.

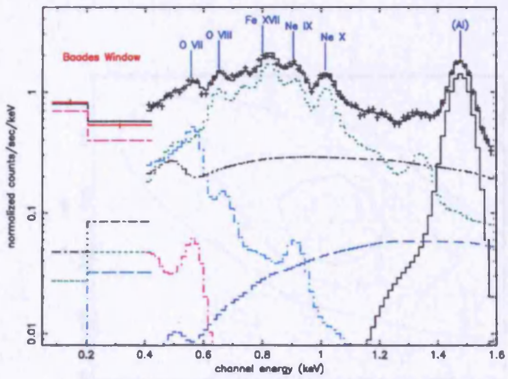

(a) Baades-Window

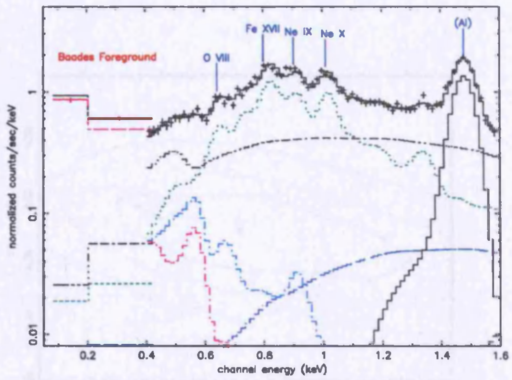

(b) Baades-Foreground

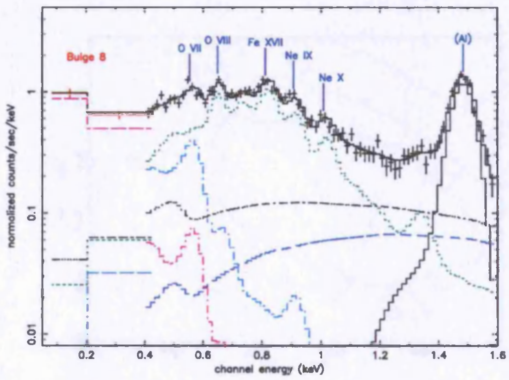

(c) Bulge 8

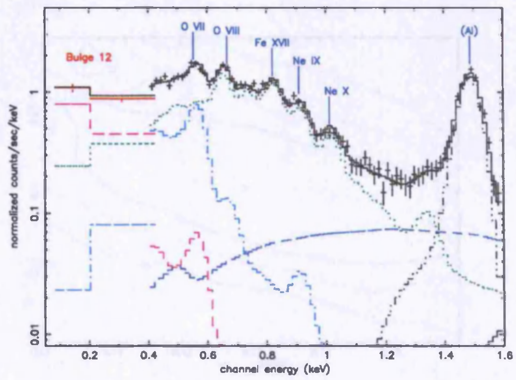

(d) Bulge 12

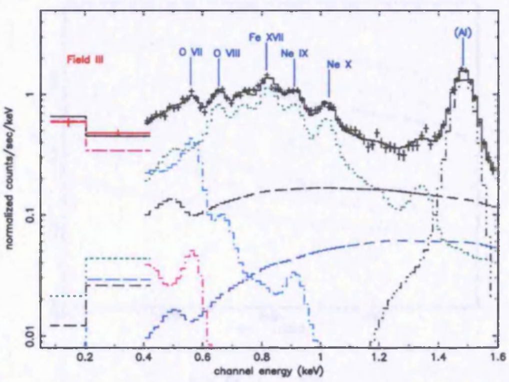

(e) Field III

FIGURE 3.5. Spectral fits for Baades-Window, Baades Foreground, Bulge 8, Bulge 12 & Field III. The separate components are shown individually to illustrate the contribution of each to a particular energy band, see Table 3.1 for key to colours/components.

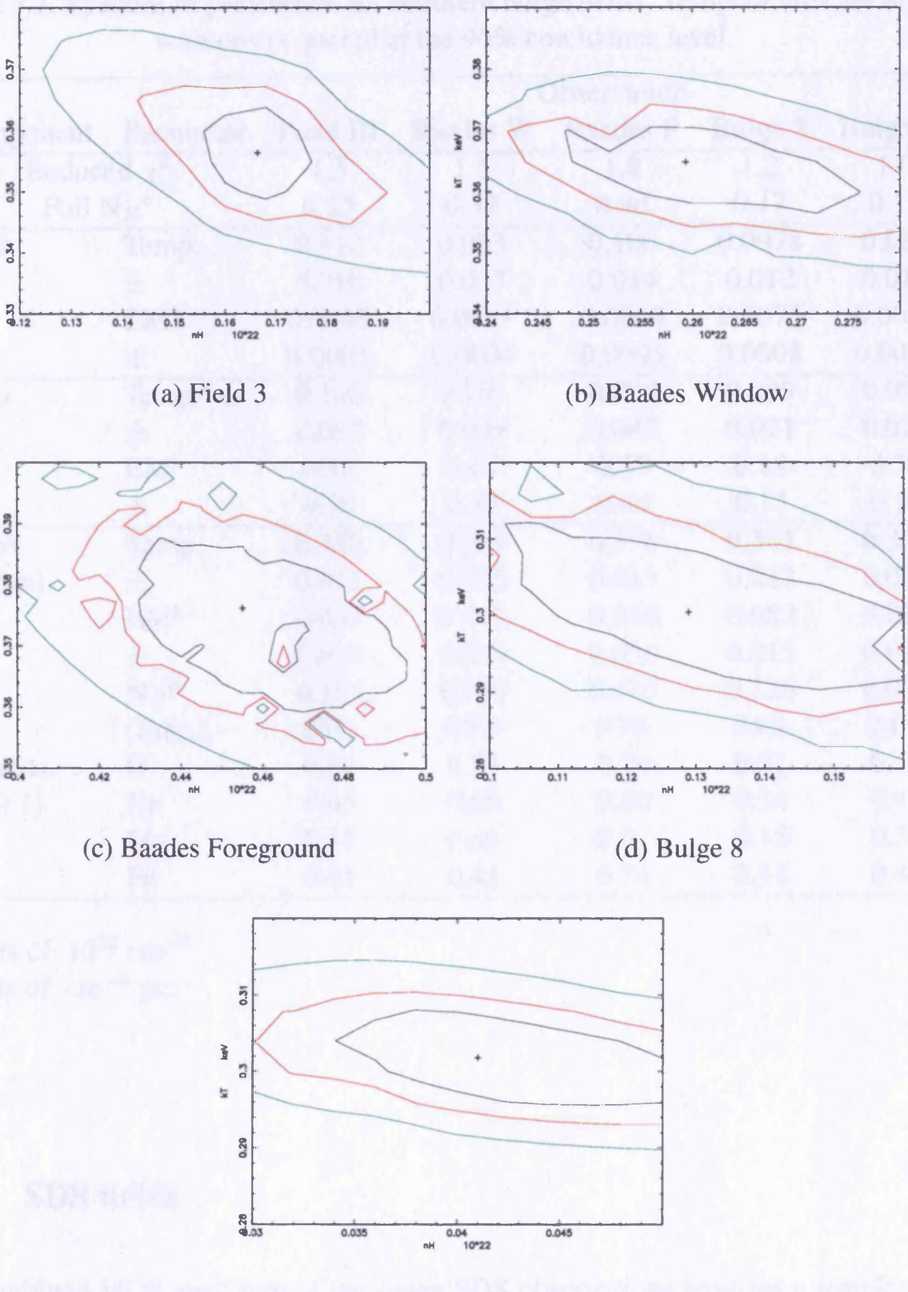

(a) Field 3 (b) Baades Window

(c) Baades Foreground (d) Bulge 8

(e) Bulge 12

FIGURE 3.6. Temperature vs. N_H contour plots for bulge component in 5 southern bulge fields. Contours are plotted at the 68%. 90% and 99% confidence intervals.

Table 3.3. Spectral fit parameters for southern bulge fields. Temperatures are in keV with errors quoted at the 90% confidence level.

		Observation				
Component	Parameter	Field III	Baades W	Baades F	Bulge 8	Bulge 12
Reduced χ^2		1.3	1.5	1.8	1.2	1.0
Full N_H[a]		0.25	0.32	0.46	0.17	0.13
LHB	Temp.	0.110	0.093	0.106	0.0978	0.082
	$\pm$	0.010	0.007	0.014	0.012	0.018
	EM[b]	0.0048	0.0061	0.0069	0.0075	0.0053
	$\pm$	0.0005	0.0004	0.0005	0.0008	0.0024
Halo	Temp.	0.100	0.103	0.098	0.099	0.094
	$\pm$	0.012	0.009	0.043	0.021	0.013
	EM[b]	0.32	0.67	0.57	0.18	0.31
	$\pm$	0.20	0.32	0.44	0.13	0.14
$\frac{3}{4}$ keV	Temp.	0.358	0.367	0.376	0.301	0.303
(Bulge)	$\pm$	0.011	0.010	0.013	0.012	0.006
	EM[b]	0.083	0.160	0.250	0.082	0.083
	$\pm$	0.010	0.010	0.030	0.015	0.006
	N_H[a]	0.165	0.254	0.445	0.125	0.031
	(Frac.)	67%	79%	97%	74%	24%
Abunds.	O	0.64	0.73	0.70	0.51	0.45
($\pm$ 0.1)	Ne	0.65	0.69	0.60	0.54	0.41
	Mg	0.45	0.44	0.31	0.45	0.38
	Fe	0.41	0.41	0.34	0.55	0.41

[a]In units of 10^{22} cm^{-2}
[b]In units of cm^{-6} pc

3.3.3 SDS fields

The combined MOS spectrum of the seven SDS observations requires a simpler model than the NPS & Bulge fields which all contain a huge amount of $\frac{3}{4}$ keV signal. The lack of this emission enables the detection of a 2nd, hotter halo component, at a temperature of $\sim 10^{6.4}$ K (see Kuntz & Snowden 2000). The RASS $\frac{1}{4}$ keV data is again needed to establish the balance between the contributions of LHB and halo emission, although this is complicated by the presence of the extra halo temperature. Both halo components are

Table 3.4. Spectral fit parameters for SDS data. Temperatures are in keV with errors quoted at the 90% confidence level.

Component	Parameter	SDS (combined)
	Reduced χ^2	1.2
	Full $N_H{}^a$	0.025
LHB	Temp.	0.104 ±0.007
	EM^b	0.0054 ±0.0006
Halo$_{lo}$	Temp.	0.081 ±0.006
	EM^b	0.023 ±0.003
Halo$_{hi}$	Temp.	0.225 ±0.008
	EM^b	0.0024 ±0.0002

^{a}In units of 10^{22} cm^{-2}

^{b}In units of cm^{-6} pc

assumed to experience the full Galactic Hydrogen absorption column (2.5×10^{20} cm^{-2}) which, with no absorption on the LHB component, somewhat simplifies the fit. All abundances are fixed at solar values. The resultant parameters are shown in Table 3.4 together with their respective errors. The spectrum itself is shown in Figure 3.7.

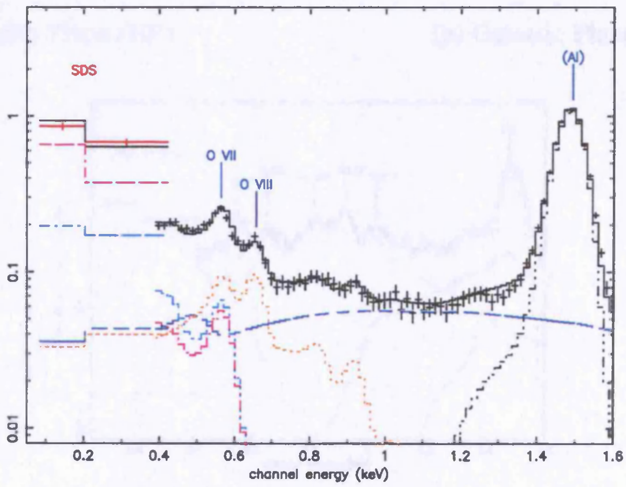

FIGURE 3.7. Spectral fit for combined SDS fields. The separate components are shown individually to illustrate the contribution of each to a particular energy band, see Table 3.1 for key to colours/components.

3.3.4 Galactic Plane & Galactic Centre

Analysing the soft regions of the MOS spectra from the four separate positions along the Galactic Plane, including one very close to the Galactic Centre, is hindered by the not insignificant contribution of the hot plasma which produces the GRXE to the $\frac{3}{4}$ keV band. To avoid having to leave too many parameters free and cripple the spectral fitting algorithm the parameters derived from the hard part of the spectrum (plasma temperatures, normalisations, abundances, *etc.*) are fixed before detailed modelling of the soft spectrum takes place (see §5 for details).

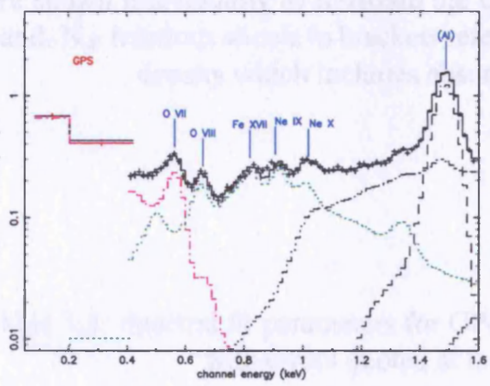

(a) Galactic Plane (20°)

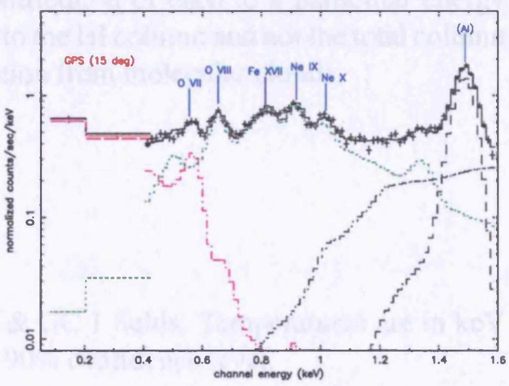

(b) Galactic Plane (15°)

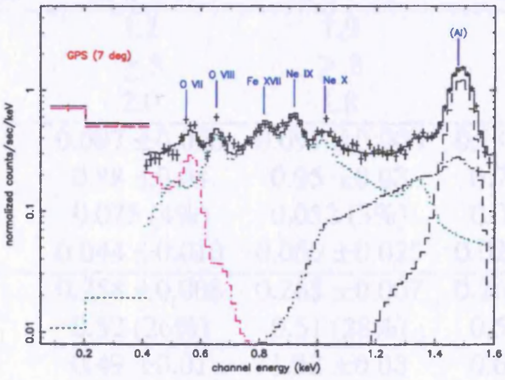

(c) Galactic Plane (7°)

FIGURE 3.8. Spectral fits for Galactic Plane at 20°, 15°& 7deg. The separate components are shown individually to illustrate the contribution of each to a particular energy band, see Table 3.1 for key to colours/components.

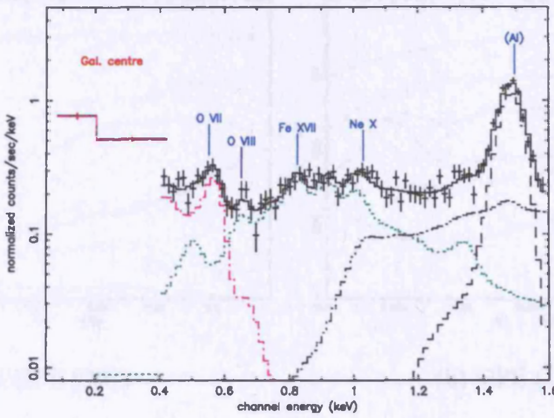

FIGURE 3.9. Spectral fit for Galactic Centre observation. The separate components are shown individually to illustrate the contribution of each to a particular energy band. N_H fractions shown in brackets refer to the HI column and not the total column density which includes absorption from molecular clouds.

Table 3.5. Spectral fit parameters for GPS & GC 1 fields. Temperatures are in keV with errors quoted at the 90% confidence level.

		Observation (longitude /°)			
Component	Parameter	GPS (20)	GPS (15)	GPS (7)	GC 1 (1)
	Reduced χ^2	1.2	1.9	1.9	1.3
	Full $N_H{}^a$	≥ 8	≥ 8	≥ 8	≥ 10
	$N_H{}^a$(HI)	2.0	1.8	1.5	1.4
	Temp.	0.097 ±0.003	0.091 ±0.006	0.119 ±0.012	0.097 ±0.009
LHB	CF	0.88 ±0.04	0.95 ±0.03	0.76 ±0.15	0.88 ±0.06
	$N_H{}^a$	0.075 (4%)	0.052 (3%)	0.077 (5%)	0.043 (3%)
	EM^b	0.044 ±0.010	0.060 ±0.025	0.024 ±0.012	0.039 ±0.013
	Temp.	0.258 ±0.008	0.263 ±0.007	0.265 ±0.009	0.266 ±0.015
$\frac{3}{4}$ keV	$N_H{}^a$	0.52 (26%)	0.51 (28%)	0.54 (36%)	0.52 (37%)
	EM^b	0.49 ±0.01	1.32 ±0.03	0.63 ±0.02	0.44 ±0.02
Abunds	O	0.14	0.21	0.28	0.10
(± 0.1)	Ne	0.12	0.15	0.27	0.12
	Mg	0.15	0.20	0.27	0.13
	Fe	0.08	0.10	0.17	0.11

[a] In units of 10^{22} cm^{-2} (Full N_H includes molecular clouds)
[b] In units of cm^{-6} pc

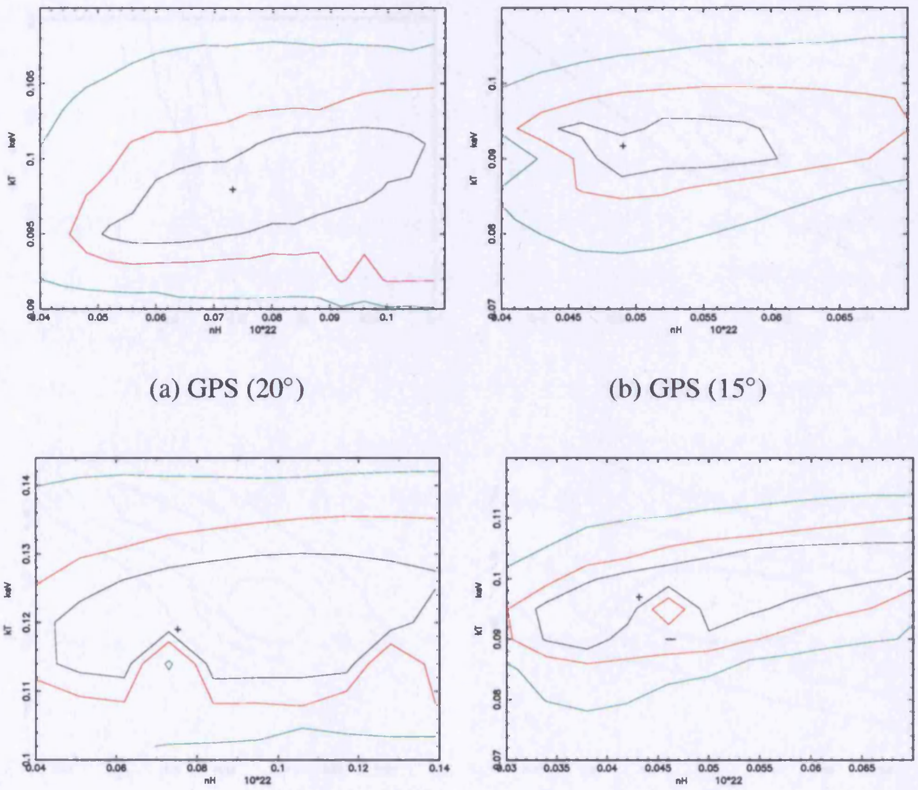

(a) GPS (20°) (b) GPS (15°)

(c) GPS (7°) (d) GC 1

FIGURE 3.10. Temperature vs. N_H contour plots for LHB for Galactic Plane & Galactic Centre fields. Contours are plotted at the 68%, 90% and 99% confidence levels.

These four spectra are important because due to the huge Galactic column in each of their respective directions ($> 10^{22}\text{cm}^{-2}$) the optical depth for soft X-ray photons is extremely large. Therefore all the measured $\frac{1}{4}$ keV emission and $\frac{3}{4}$ keV emission must originate from a relatively local origin, hence no Galactic halo components are considered. However no single unabsorbed ~ 0.1 keV component is sufficient to fit both the $\frac{1}{4}$ keV RASS data and the ever-present O VII emission line (clearly visible in all these spectra). In fact an absorbed 0.1 keV component is still required to account for the O VII line emission but this does not remove the need for an unabsorbed component as well. As both of these ~ 0.1 keV components must be within a few hundred parsecs of the Sun, they are modelled as a single source with partial covering absorption. In

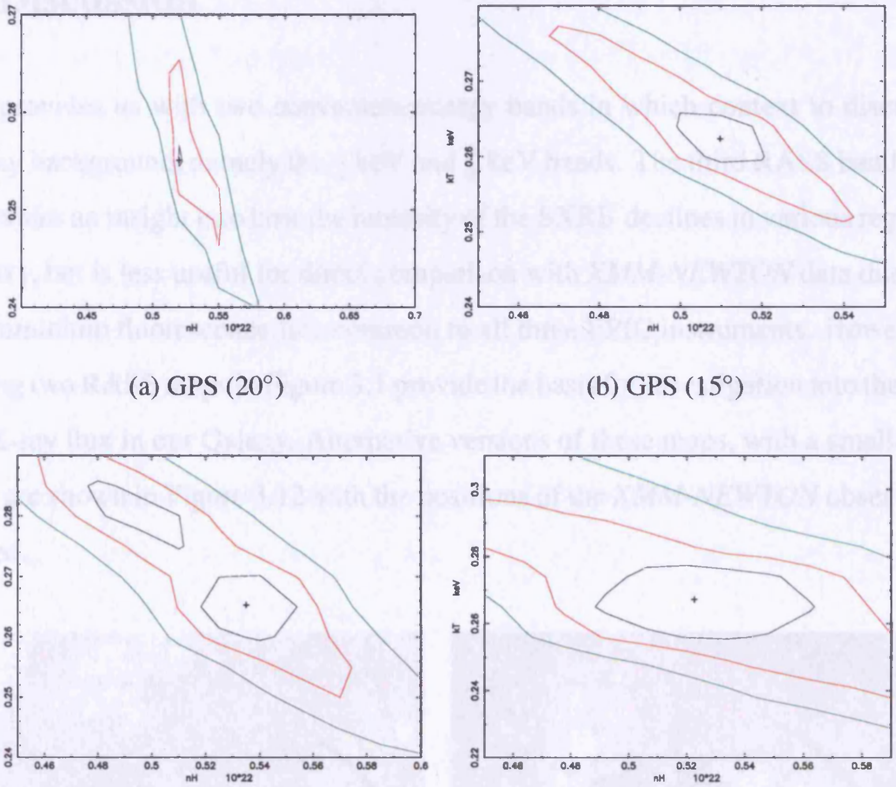

(a) GPS (20°) (b) GPS (15°)

(c) GPS (7°) (d) GC 1

FIGURE 3.11. Bulge component temperature vs. N_H contour plots for Galactic Plane & Galactic Centre fields. Contours are plotted at the 68%, 90% and 99% confidence levels.

this way acceptably good fits were obtained to the <0.6 keV regions of all four Galactic Plane spectra. These are shown in Figure 3.8 and the derived parameters, with errors, are given in Table 3.5. The interpretation of these results is discussed in §3.4. The full Galactic absorption figure (*i.e.* including molecular Hydrogen) given in Table 3.5 is an approximate figure based on a large scale CO survey, see §5.5.1 for more details.

3.4 Discussion

ROSAT provides us with two convenient energy bands in which context to discuss the soft X-ray background, namely the $\frac{1}{4}$ keV and $\frac{3}{4}$ keV bands. The third RASS band, at 1.5 keV, provides an insight into how the intensity of the SXRB declines in various regions of the Galaxy, but is less useful for direct comparison with *XMM-NEWTON* data due to the large Aluminium fluorescence line common to all three EPIC instruments. However the remaining two RASS maps in Figure 3.1 provide the basis for investigation into the origin of soft X-ray flux in our Galaxy. Alternative versions of these maps, with a smaller field of view, are shown in Figure 3.12 with the positions of the *XMM-NEWTON* observations overlayed.

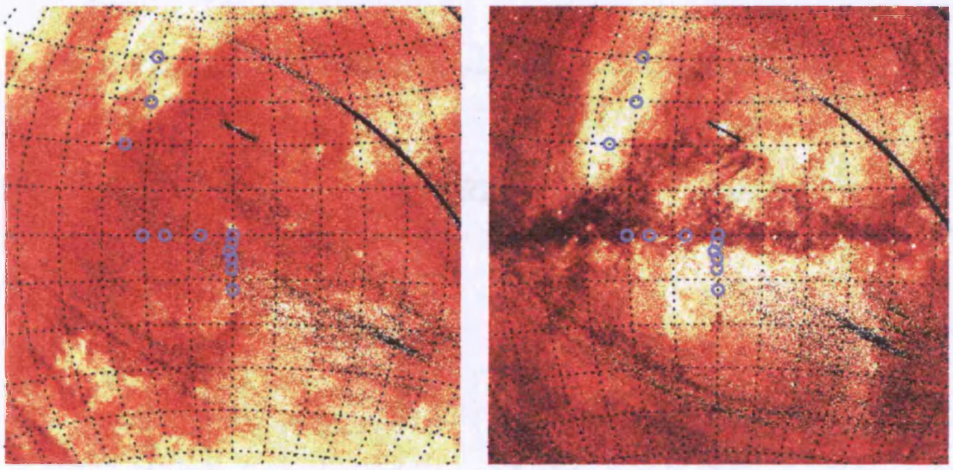

(a) $\frac{1}{4}$ keV (b) $\frac{3}{4}$ keV

FIGURE 3.12. Zoomed in RASS maps in the $\frac{1}{4}$ and $\frac{3}{4}$ keV bands. Blue circles represent the positions of *XMM-NEWTON* observations in the field of view. The angular projection is azimuthal equal-area (Lambert) and the grids show 10 degree squares in Galactic coordinates.

3.4.1 $\frac{1}{4}$ keV emission

Analysis of the components which contribute to the $\frac{1}{4}$ keV band utilises two specific regions in the spectra of each observation. The $\frac{1}{4}$ keV band itself is entirely covered, by definition, by the *ROSAT* PSPC R1 & R2 bands and these two data points per spectrum are vital in establishing the crucial separation of local and distant origins of the flux. However there is one further important diagnostic tool needed to establish the nature of the $\frac{1}{4}$ keV signal and this is the O VII emission line which is a signature of X-ray emitting plasma at temperatures around $10^{6.1}$ K. It is important to note that the effective area the PSPC instrument at the O VII line is only $\sim$ 20% of the peak value, in other words *ROSAT* was relatively insensitive to both O VII line emission and the surrounding continuum flux. This fact plays a vital role in the separation of individual $\frac{1}{4}$ keV components, especially within the Galactic Plane. Figure 3.13 shows a comparison of count rates between the high latitude SDS observations and 3 separate regions in the Galactic Plane in the R1 & R2 band of the PSPC and the 0.5–0.6 keV energy range in the MOS spectrum (representing O VII line emission).

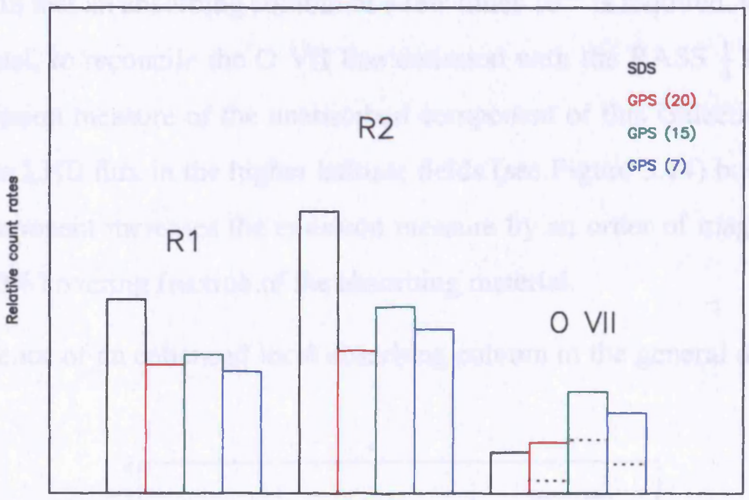

FIGURE 3.13. Relative count rate histogram. Dotted lines indicate estimated contamination of O VII line (or 0.5–0.6 keV energy range) from bulge emission. Following this correction the variation in O VII emission is significantly less than in the R1 & R2 bands.

There is some scatter between the different Galactic Plane fields, primarily because of the varying strengths of the hotter $\frac{3}{4}$ plasma which contaminates to some extent, however the most noticeable feature is the fact that the SDS fields exhibit a much stronger signal in the PSPC bands but have the lowest flux in the O VII band. In fact the emission measures of the 0.1 keV plasmas which produce the O VII line in all four cases are remarkably similar, therefore the primary SXRB flux variation between the Galactic Plane and the higher latitude fields lies at energies below ~ 0.4 keV.

Intrinsically this does not seem to be a problem as LHB flux is by no means isotropic, however the dilemma becomes apparent when considering the level of absorption on the soft flux. None of the Galactic Plane O VII emission can originate from a Galactic halo that lies beyond the very large absorption column in that direction, therefore the default assumption is that it must be LHB emission. An unabsorbed LHB model fitted to the PSPC data can be made to correctly predict the O VII line flux by increasing the Oxygen abundance (by a factor of ~ 5) but as well as this being an unrealistically high abundance, altering the model in this way does not account for the continuum flux in the energy range 0.4–0.5 keV. However, an unabsorbed 0.1 keV plasma fitted to the O VII line (which does correctly model the continuum emission) drastically over-predicts the flux in the RASS $\frac{1}{4}$ keV band. In fact an absorbing column of a few times 10^{20} is required, within a partial covering model, to reconcile the O VII line emission with the RASS $\frac{1}{4}$ keV flux. The effective emission measure of the unabsorbed component of this Galactic Plane flux is comparable to LHB flux in the higher latitude fields (see Figure 3.14) but including the absorbed component increases the emission measure by an order of magnitude, in line with the $\sim 90\%$ covering fraction of the absorbing material.

The existence of an enhanced local absorbing column in the general direction of the

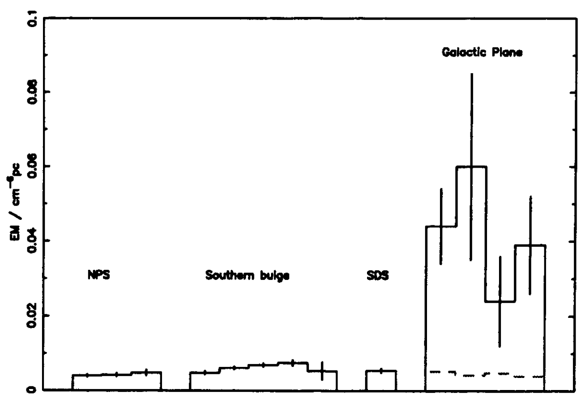

FIGURE 3.14. The variance in LHB emission measure between observations. The dotted histogram shows contribution of the unabsorbed emission from the Galactic Plane.

Galactic Centre has previously been inferred by Warwick et al. (1993) and Hutchinson et al. (1998) using a combination of X-ray and EUV data to establish line-of-sight absorption columns for a number of point sources. Hutchinson et al. (2003) have produced a map showing how the distance to a column density of $10^{20}\mathrm{cm}^{-2}$ varies across the sky. There is a clear shortening of this distance (and therefore an increase in the HI density) in the direction of the Loop I superbubble. This absorption 'wall' is also apparent in the spectra of the NPS and southern bulge (see Willingale, Hands, Warwick, Snowden & Burrows (2003) and following section). The values quoted in Table 3.5 show that the scale of the absorption column in front of the bulk of the $\frac{1}{4}$ keV emission towards the Galactic Plane is of the order a few times $10^{20}\mathrm{cm}^{-2}$ which is approximately two orders of magnitude greater than the local fluff but also a similar factor lower than the full Galactic HI column. The $\frac{1}{4}$ keV emission which originates beyond the wall, detected by *XMM-NEWTON* only because of the presence of O VII, must be from plasma within a distance scale of the order of a few hundred parsecs because the absorption on the hotter bulge component, expected to be located within $\sim$ 1–2 kpc towards the Galactic Plane (see later), is an order of magnitude higher. Therefore the density of $\sim$ 0.1 keV plasma is predicted to be higher towards the Galactic Plane than in other directions. Table 3.6 gives distances to the $\mathrm{N_H} = 10^{20}\mathrm{cm}^{-2}$ wall, d_w, based on Hutchinson et al. (2003), along with electron densities and pressures derived from the emission measure of the LHB flux. The entries for the four data sets in the Galactic Plane include (in brackets) the equivalent parameters for the plasma beyond the absorption wall. Whether or not the flux from this region of hot plasma is described as LHB emission is a matter of preference. The densities given in Table 3.6 indicate that if LHB plasma is present beyond an enhanced absorption feature then in order for the extended bubble to remain within a range of $\sim$ 200 pc, the density of the plasma beyond the column would need to be at least double that of the more local plasma. This could be a result of clumping or possibly an interspersal of hot plasma and cold neutral absorber. As the existence of this absorbed component is reliant on a single Oxygen line, the data quality is insufficient to resolve this matter. The temperature of the LHB plasma is, in all cases, consistent with previous studies with an average temperature of 0.1 keV or $10^{6.06}$ K.

Table 3.6. Electron densities and pressures in the LHB. d_w represents the line-of-sight distance in parsecs to a total absorption column of 10^{20} cm^{-2}. The values in brackets are estimates of equivalent parameters for a region of the LHB lying beyond an inferred absorption feature in the Galactic Plane. The emission measures used for these estimates are the larger values plotted in Figure 3.14 with a canonical distance of 100 pc.

	d_w	EM	n_e	Pressure
	pc	cm^{-6} pc	cm^{-3}	cm^{-3} K
Field IV	40	0.0040	0.0100	18800
Field V	60	0.0042	0.0084	15700
Field VI	90	0.0048	0.0073	20000
Field III	90	0.0048	0.0073	16800
Baades Window	80	0.0061	0.0087	17000
Baades Foreground	85	0.0069	0.0090	19900
Bulge 8	100	0.0075	0.0087	17700
Bulge 12	110	0.0053	0.0069	11900
SDS	150	0.0054	0.0060	13000
GPS (20)	45 (100)	0.0050 (0.044)	0.0105 (0.0210)	21300 (42500)
GPS (15)	50 (100)	0.0046 (0.060)	0.0096 (0.0245)	18200 (46500)
GPS (7)	60 (100)	0.0048 (0.024)	0.0089 (0.0155)	22200 (38500)
GC1	70 (100)	0.004 (0.039)	0.0076 (0.0197)	15300 (40000)

The other known source of $\frac{1}{4}$ keV emission is the Galactic Halo. Here we need only consider the higher latitude observations as no significant soft X-ray flux could conceivably penetrate through the absorption in the Galactic Plane. *ROSAT* studies of the SXRB have discovered Galactic Halo emission at a similar temperature to the LHB, *i.e.* ~ 0.1 keV (Snowden et al. 1998). A more detailed analysis of the same data found evidence for a second Halo temperature at around 0.2 keV or $\sim 10^{6.5}$ K (Kuntz & Snowden 2000). In all cases disentangling the lower temperature Halo component from the LHB is problematic however, in the case of the NPS and southern bulge fields, the extensive emission around 0.25–0.35 keV will completely dominate over any hotter Halo component, rendering such a component undetectable. The SDS spectrum therefore becomes by far the most suitable for determining Halo parameters. Table 3.4 gives the two temperatures as 0.081 ± 0.006 and 0.225 ± 0.008 keV respectively, however these parameters are heavily correlated in the fitting process, as shown in Figure 3.15. Clearly both temperatures can be decreased quite substantially without seriously affecting the quality of the fit. This is largely due to the O VII line which contains flux from both components. The best fit values (which in fact serve more as upper limits in each case) are entirely consistent, within the errors, with the values derived by Kuntz & Snowden (2000) from all-sky data. The emission measure of the 2nd hotter Halo component is approximately a factor of ten lower than the cooler component, so it is unsurprising that it was not detected in the initial analysis of the RASS data.

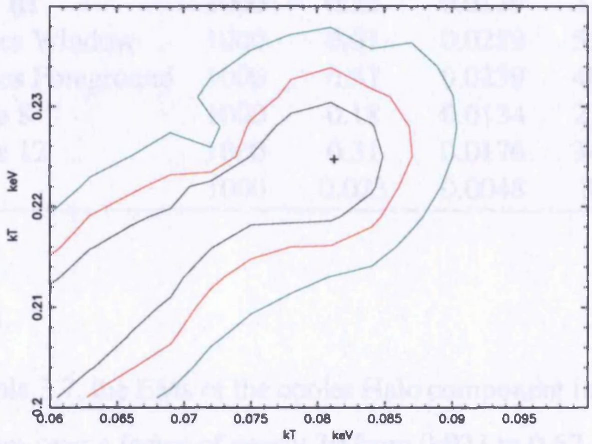

FIGURE 3.15. Contour plot for two halo temperatures in SDS spectrum. The curved shape indicates a strong correlation between the two components which implies that the data are insufficient to accurately determine the two halo temperatures. Contours are plotted at the 68%, 90% and 99% confidence intervals.

The temperatures and emission measures quoted in Tables 3.2 and 3.3 are the best-fit values obtained from each spectrum. However as establishing the temperature of the cooler Halo component in these observations depends primarily on the data around the O VII emission line (the energy regions just above and below this point are dominated by LHB and bulge emission respectively), the constraints on the temperature are poor. Figure 3.16 shows an example of this problem for the southern bulge observation, Field III. Clearly there is a very large correlation between the temperature of the plasma and its normalisation, therefore the errors quoted for these values are underestimated. No such correlation exists for the temperature and normalisation of the LHB components in each of the NPS and southern bulge observations because the LHB dominates below ~ 0.4 keV. Snowden et al. (1998) found that the emission measure of the Galactic Halo varies from near zero to $> 0.02\mathrm{cm}^{-6}\mathrm{pc}$, the latter value being very similar to that obtained

Table 3.7. Electron pressures and densities in the Galactic Halo. The assumed extent of the halo is 1000 pc in all directions with both the density and pressure scaling as $d^{-0.5}$ if this canonical figure is altered.

	d_{GH} pc	EM cm^{-6} pc	n_e cm^{-3}	Pressure cm^{-3} K
Field IV	1000	0.11	0.0105	19500
Field V	1000	0.083	0.0091	16700
Field VI	1000	0.026	0.0051	9100
Field III	1000	0.32	0.0179	37400
Baades Window	1000	0.67	0.0259	55700
Baades Foreground	1000	0.57	0.0239	48900
Bulge 8	1000	0.18	0.0134	27700
Bulge 12	1000	0.31	0.0176	34600
SDS	1000	0.023	0.0048	8100

from the SDS fields.

As shown in Table 3.7, the EMs of the cooler Halo component in the NPS and southern bulge fields varies over a factor of nearly 30 from 0.023 to 0.67 cm^{-6}pc. Following the results in the Galactic Plane it is plausible that not of all of this flux is genuinely from the Halo, originating instead from beyond a a local absorber, with a column of density of

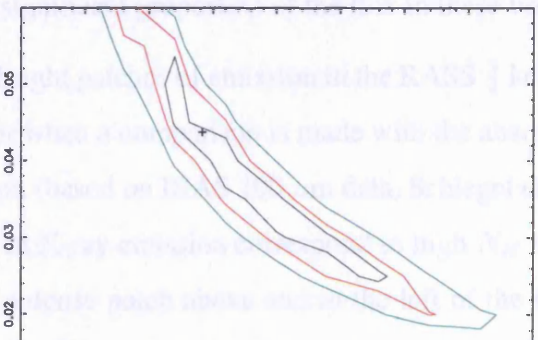

FIGURE 3.16. Contour plot showing the variation of χ^2 with Galactic Halo temperature and normalisation. The example shown (Field III) is typical of all the NPS and southern bulge fields, showing a large correlation between the temperature and emission measure (normalisation). Contours are plotted at the 68%, 90% and 99% confidence intervals.

$\sim 10^{20}\text{cm}^{-2}$, but in front of the source of the $\frac{3}{4}$ keV emission, *e.g.* the Loop I superbubble. This model may be a way of reducing the huge variation in Halo flux and thus the densities and pressures shown in Table 3.7 (calculated using a canonical distance of 1000 pc across the Halo), however the spectral data is insufficient to satisfactorily establish a quantifiable distinction between Halo flux and absorbed local emission. The identification of such absorbed local emission is only possible from observations in the Galactic Plane because of the absence of Halo flux, hence in these higher latitude observations a similar or related component remains speculative. However the speculative geometry shown in Figure 3.17 includes a provision for plasma to exist beyond the absorption wall for the higher latitude fields as well as the Galactic Plane fields. The local absorber itself replicates the enhanced absorption mapped by Hutchinson et al. (1998) which does cover most of the higher latitude fields.

3.4.2 $\frac{3}{4}$ keV emission

Discussion of the $\frac{3}{4}$ keV emission in this section relates to the highly prominent features visible in the central RASS map in Figure 3.1. Other contributors to flux in this energy band, such as the hotter Galactic Halo component and the CXB, are not discussed here as they represent an insignificant proportion of the flux in these bright areas.

At first glance the bright patches of emission in the RASS $\frac{3}{4}$ keV map do not seem to be connected. However when a comparison is made with the absorption column density maps of the same region (based on IRAS 100 μm data, Schlegel et al. (1998)) , it seems apparent that the gaps in X-ray emission correspond to high N_H regions both along the Galactic Plane and in a dense patch above and to the left of the Galactic Centre. This latter absorption region can also be seen in the absorption wall maps of Hutchinson et al. (1998). The data in Tables 3.2, 3.3 and 3.5 show that the temperatures of the bulge components in most of the fields, both on-plane and off-plane, are in the range 0.25-0.3 keV. The three fields which do not lie in this range all exhibit temperatures of ~ 0.36 keV and attempts to fit the data from these fields with thermal models at temperatures below 0.3 keV do not produce satisfactory results. The emission measures of the bulge component in the NPS are very similar to those in the southern bulge fields, however the emission measures of the bulge component in the Galactic Plane spectra are several times higher. At this point care must be taken because, unlike with the ~ 0.1 keV components, the relative elemental abundances in the ~ 0.3 keV components were allowed to vary. This variation is necessary in regions where several emission lines are visible as the APEC plasma code uses solar abundances to predict line strengths and there is every possibility that the abundances in a Galactic diffuse plasma will not exactly match those of the Sun. However allowing only a few elemental abundance to vary highlights a particular problem with the fitting process. Some ions have several emission lines in the 0.5–1 keV region (particularly Fe XVII) and as the spectral resolution of the EPIC instruments is insufficient to resolve them from each other the abundance values can decrease substantially with the flux replaced by an increase in the continuum level. This has the effect of driving up the normalisation of the thermal component as the abundances are reduced to whatever level necessary required to achieve the best fit to the emission lines. This means that the abundances quoted in Tables 3.2, 3.3 and 3.5 should be treated with caution, especially where the fractions are significantly less than 0.5. Fixing the abundances at unity (with respect to solar) is unlikely to be a representative model of the true situation but, in the absence of other data, it is the best compromise to allow a comparison of the continuum flux.

Therefore in order to compare the strength of the bulge component in each data set, all emission measures are recalculated by re-normalising the bulge plasma model with relative abundances set to solar values. This method inevitably has the effect of drastically reducing the quality of the spectral fits around the emission lines, *i.e.* in the energy range 0.5–1.0 keV, but for the purposes of comparing emission measures this is unimportant. These renormalised emission values are given in Table 3.8. The scatter in emission measure is drastically reduced with this technique, implying that a single plasma bubble, with an approximately constant internal density, could indeed account for the observed $\frac{3}{4}$ keV emission. In this model the variation in surface brightness in Figure 3.12(a) is predominantly due to absorption effects. Table 3.8 also gives electron densities and pressures for the hot plasma based on a possible geometry of the Loop 1 superbubble given

Table 3.8. Emission measures renormalised to solar abundances for all fields which contain $\frac{3}{4}$ keV bulge emission (*i.e.* all except SDS). The distances (d_{SB}) used to calculate the electron densities and pressures are based on the geometry shown in Figure 3.17.

	d_{SB} pc	EM_{renorm} cm^{-6} pc	n_e cm^{-3}	Pressure cm^{-3} K
Field IV	730	0.064	0.0094	53400
Field V	790	0.050	0.0080	41200
Field VI	510	0.036	0.0084	45800
Field III	1100	0.045	0.0064	47800
Baades Window	1110	0.090	0.0090	69000
Baades Foreground	1130	0.118	0.0102	80200
Bulge 8	1030	0.048	0.0068	42900
Bulge 12	920	0.040	0.0066	41700
GPS (20°)	790	0.081	0.0101	54500
GPS (15°)	940	0.275	0.0171	93900
GPS (7°)	1100	0.181	0.0128	71000
GC1	1180	0.073	0.0079	43700

in Figure 3.17.

Having inferred the $\frac{3}{4}$ keV emission measures and absorption columns from many different observations it is subsequently important to attempt to ascertain the location(s) of the plasma(s) responsible for the emission. The model adopted by Willingale, Hands, Warwick, Snowden & Burrows (2003) assumes that the Loop 1 superbubble is responsible for the $\frac{3}{4}$ keV emission from the NPS and also the bright emission seen above and below the Galactic Centre, referred to in this analysis as the northern and southern bulge. There is clear evidence from maps of Galactic N_H, particularly from IRAS data, that the gaps in X-ray emission seen in both the $\frac{3}{4}$ keV and 1.5 keV RASS maps are caused by absorption. The amount of absorption in the off-plane directions of both the NPS and the southern bulge ranges from 24% to 98% of the full Galactic column with an average value of $\sim$ 70%. As the lines of sight of these observations are directed out of the Galactic Disk, this implies that the origin of the emission is relatively local. The spectra of Field V and Field VI imply that due to the lower column densities in these fields the superbubble emission (*i.e.* the NPS) should be visible in the $\frac{1}{4}$ keV band as well as the

$\frac{3}{4}$ keV band. This is indeed the case as can be seen in Figure 3.12(a) and there is also a hint of a similar effect in Bulge-12. The band of absorption between the NPS and the northern bulge must therefore be in front of the Loop 1 bubble. Egger & Aschenbach (1995) have proposed that this absorption is a result of an interaction between the Loop 1 bubble and the LHB. As none of the observations discussed in this chapter are located within this region this cannot be confirmed or denied. However the possibility that the LHB extends further than previously thought, supported by the large variation in "halo" emission measures in the NPS and southern bulge, does support this theory.

The Galactic Plane data implies an absorption column of $5 \times 10^{21}\text{cm}^{-2}$ in front of the $\frac{3}{4}$ keV emission which corresponds to a much larger fraction of total Galactic HI than would be expected for a distance of only 100–200 pc in the disk. Snowden et al. (1997) derived a column of $4.4 \times 10^{21}\text{cm}^{-2}$ in front of the $\frac{3}{4}$ keV emission and inferred from this that the source of the emission was probably distant. A mean Hydrogen density of $1\ \text{cm}^{-3}$ would require a distance of 1.7 kpc to achieve a column density of $5 \times 10^{21}\text{cm}^{-2}$. An ISM density such as this is not unreasonable in this direction. For example, Diplas & Savage (1994) observed a star at Galactic coordinates 21.1°, -0.5°at a distance of 280 pc with a column density of 10^{21}cm^{-2}, far greater than the equivalent value for stars at similar distances in other parts of the plane. If the HI responsible for this absorption is indeed located in front of the Loop 1 bubble it could be further evidence for an interaction with the LHB as part of Egger & Aschenbach (1995)'s model is an absorption wall formed between the two plasma bubbles. However, one substantial problem with this model, noted by Snowden et al. (1997), is that the absorption stripe between the northern and southern bulge clearly lies along the Galactic Plane and it is unlikely that a compression zone between two interacting plasma bubbles would form an absorption band with, coincidentally, exactly this alignment. The bubble interaction model would need to be combined with a massively increased density of HI at low Galactic latitudes to produce a believable model for such an absorption band. Conversely, evidence of a distant origin for at least some of the $\frac{3}{4}$ keV emission was found by Park et al. (1997) using a molecular cloud in the Galactic Plane to perform a shadowing experiment. They found that $\sim 43\%$ of the emission in the $\frac{3}{4}$ keV band was located beyond the molecular cloud which itself is located $\sim$ 3 kpc away at Galactic coordinates 10°, 0°. Although this does require that there is a source of $\frac{3}{4}$ keV X-ray emitting material at large distances, the fraction of 43% is entirely consistent with the contribution to the $\frac{3}{4}$ keV band from another, slightly hotter, plasma component, present in all the Galactic Plane fields, which forms part of the Galactic Ridge X-ray Emission (GRXE) and is discussed in a later chapter. Park et al. (1997) do not attempt to explain the origin of the remaining 57% of the $\frac{3}{4}$ keV emission which must originate from a more local origin than a Galactic bulge centred on the Galactic Centre. It is this emission which is likely to be associated with the Loop 1 superbubble providing further evidence that the sources responsible for the $\frac{3}{4}$ keV emission in the Galactic Plane, the southern bulge region and the North Polar Spur are all related. If this is indeed the case then in order to reconcile the emission in front of the molecular clouds measured by Park et al. (1997) with the substantial absorption column in front of the source (as independently measured by *XMM-NEWTON* and by Snowden et al. (1997)), without having to invoke an unlikely plane-aligned interaction with the LHB, an intermediate distance must be chosen for the centre of the superbubble. Figure 3.17 shows schematic cross-sections, perpendicular to the Galactic Plane, at longitudes 0°and 20°, with the centre of the superbubble located at distance of $\sim$ 1 kpc from the Sun. The space available for HI gas then becomes $\sim$ 500 pc, requiring a mean HI density of $\sim 3\ \mathrm{cm}^{-3}$.

Also shown in Figure 3.17 (in blue) is a local absorption feature, within a larger than predicted LHB, to account for both the enhanced absorption seen by Hutchinson et al. (1998) and the absorbed 0.1 keV plasma (assumed to be part of the LHB) responsible for O VII line emission in the Galactic Plane and, to a lesser extent (due to the contribution of the Galactic Halo), in the higher latitude fields.

This intermediate model represents a further possibility rather than a unique solution as significant problems continue to exist. The source of the Loop 1 bubble (and subsequently the NPS) has previously been attributed to stellar winds and supernovae originating in the Sco-Cen OB association, located at (l,b)$\sim$ 355°,17°and at a distance of $\sim$ 160 pc (de Geus et al. 1989, de Geus 1992). This cluster of O-type and B-type stars can be broken down into three sub groups;Upper Sco, Upper Cen & Lower Cen, each of which

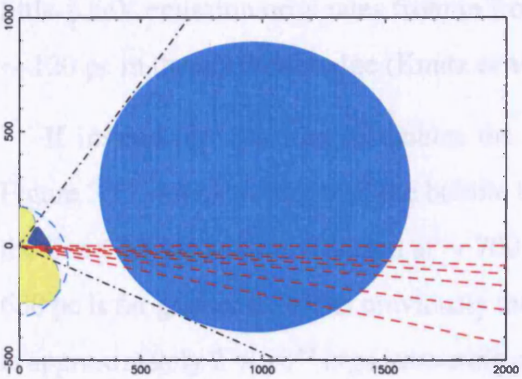

(a) l=0°

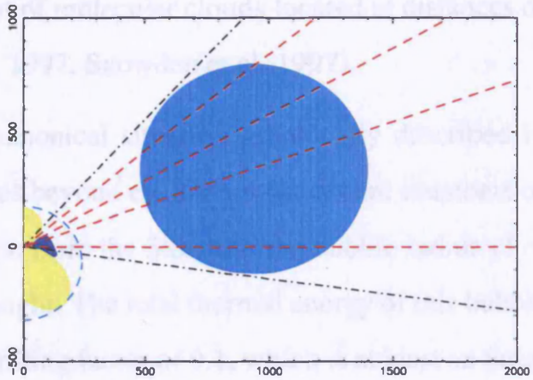

(b) l=20°

FIGURE 3.17. Speculative schematic representations of LHB and Loop 1 superbubble geometry using perpendicular slices to the Galactic Plane at two different longitudes. The black dotted lines represent the angular extent of the bubble on the sky, as seen in the $\frac{3}{4}$ keV RASS map. The red dotted lines delineate the directions of *XMM-NEWTON* observations at the relevant longitude. The coloured regions represent as follows:yellow - LHB plasma, light blue - hotter superbubble plasma, dark blue - absorption cloud in front of proposed additional LHB plasma, bounded by a light blue dotted line.

is associated with an HI shell or loop. Berkhuijsen et al. (1971) suggested that the NPS might be due to a single supernova originating in the Upper Sco region. This idea was based on the existence of a high velocity O9.5V star, ζ Ophiucus, located $\sim$ 200 pc from the Sun in Upper Sco. The trajectory and velocity of ζ Ophiucus indicate that it would have passed close to the centre of Loop 1 some 3×10^6 years ago and the hypothesis is that it was part of a binary system with a high mass star that became a type II supernova, kicking ζ Ophiucus out from the centre of the OB association. de Geus (1992) map a much smaller HI shell (*i.e.* not coincident with the NPS), again centred on Upper Sco, and similarly postulate that a partner to ζ Ophiucus is responsible for the both the high velocity of the star and the HI shell itself. However, due to the kinematical properties of the neutral gas associated with the NPS, de Geus (1992) conclude that the NPS is not part of one of their loops around the Sco-Cen association and instead must be a more local supernova remnant such as that proposed by Davelaar et al. (1980). If the NPS is indeed comprised of the same plasma that forms the northern and southern bulge then this cannot be the correct solution as X-ray shadowing experiments have shown that very little $\frac{3}{4}$ keV emission originates from in front of molecular clouds located at distances of $\sim$ 120 pc in the northern bulge (Kuntz et al. 1997, Snowden et al. 1997).

If instead the situation resembles the canonical situation graphically described in Figure 3.17, then the centre of the bubble lies beyond even the most distant members of the Sco-Cen association (located at $\sim$ 700 pc from the Sun) and the bubble radius of $\sim$ 600 pc is far greater than was previously thought. The total thermal energy of this bubble is approximately 2×10^{52} ergs, assuming a filling factor of 0.1, which is at least an order of magnitude greater than the energy released in a single supernova explosion. Indeed as the size of the bubble is substantially larger than an single known supernova remnant, the mechanism behind the X-ray plasma would almost certainly have to consist of multiple stellar winds / supernovae.

3.5 Conclusion

High resolution *XMM-NEWTON* data has been used to address several distinct problems in our understanding of the soft X-ray background. Using joint fits with *ROSAT* data the results have shown that the local hot bubble is indeed consistent with an unabsorbed plasma at a temperature of 0.1 keV. Furthermore, the detection of a strong O VII emission line, to which *ROSAT* was relatively insensitive, along the Galactic Plane implies that this plasma extends further than previously thought, beyond a local absorption cloud which lies in the general direction of the Galactic Centre.

This increased LHB is also implied at higher latitudes where the situation is complicated by Galactic Halo emission. The large variance in emission measure of the halo is likely to be caused, at least in part, by the presence of a locally absorbed plasma at a temperature of 0.1 keV, identical to that of both the halo and the unabsorbed LHB. The only fields unbiased by this effect yield a two temperature halo model, in good agreement with previous results, with the additional temperature lying around 0.2 keV, although highly dependent on the temperature of the cooler component.

Two of the very bright regions in the $\frac{3}{4}$ keV *ROSAT* All-Sky Survey maps have been shown to have very similar properties, in terms of temperature and emission measure, not just to each other but also to the heavily absorbed $\frac{3}{4}$ keV emission from the Galactic Plane. This implies a common origin for the different hot plasmas, with the gaps in the RASS map being due only to absorption. However, if this is the case then the strong band of absorption lying along the Galactic Plane in front of the emission source, coupled with the significant fraction of the emission measured to originate in front of distant molecular clouds, necessarily results in a more distant (but non-Galactic Centre) location for the hot plasma than previously thought. This in turn means that any plasma bubble responsible for all the observed emission is significantly larger than any single supernova remnant and must be the result of a sequence of processes or SN events. This intermediate model, lying in between a local Loop 1 shell model or the Galactic Bulge, is proposed as a possible alternative rather than a unique solution. Therefore although the nature of the $\frac{3}{4}$ keV emission has been investigated in far more detail by *XMM-NEWTON* , the fundamental question of where the X-ray emitting plasma is located has yet to be adequately resolved.

Chapter 4

X-ray Source Populations

4.1 Overview

To date the *XMM-NEWTON* Galactic Plane Survey (XGPS) has been targeted at several locations in the Galactic segment between the Galactic Centre and the Scutum Spiral Arm. This chapter present the results from the first phase of the XGPS (hereafter XGPS-I), which has entailed a total of 22 *XMM-NEWTON* pointings, covering a region of approximately three square degrees between $\sim 19°- 22°$ in Galactic longitude and $\pm\ 0.6°$ in latitude. Over 400 discrete point-like X-ray sources have been detected in XGPS-I, enabling us to focus on the properties of this source population and the contribution these discrete sources make to the GRXE.

4.2 Observations

The XGPS-I programme comprises 22 *XMM-NEWTON* pointings carried out during the period between October 2000 and April 2003 (see Table 4.1). Five of these observations formed part of SSC Guaranteed Time programme (the Ridge 1-5 fields), whereas the remaining time was awarded to an AO1 programme (PI: Warwick; the XGPS 1-17 fields). The allocated exposure times for these two sets of observation were 9 ks and 5 ks respectively, although in most instances somewhat longer exposure times were actually

Table 4.1. Observation log for the XGPS-I.

Field Name	Field Centre (J2000) R.A.	DEC	MOS exposure[a]	pn exposure[b]	MOS fraction[c]	pn fraction[c]
Ridge 1	18 26 0.4	-12 14 55.9	8393	5914	0.95	0.85
Ridge 2	18 26 48.4	-11 52 48.7	13667	12046	1.0	1.0
Ridge 3	18 27 36.4	-11 30 40.4	12044	9648	0.95	0.85
Ridge 4	18 28 17.0	-11 7 53.0	9256	12998	0.94	0.42
Ridge 5	18 29 6.0	-10 45 3.0	13667	12046	0.98	0.93
XGPS 1	18 25 4.6	-11 50 0.4	7794	4797	1.0	1.0
XGPS 2	18 27 34.0	-12 9 20.0	9144	-	1.0	-
XGPS 3	18 25 49.0	-11 28 42.7	9144	-	1.0	-
XGPS 4	18 28 19.4	-11 48 5.2	9144	-	1.0	-
XGPS 5	18 26 35.7	-11 7 32.1	9994	7348	0.96	0.95
XGPS 6	18 29 5.9	-11 26 57.4	8794	6148	0.44	0.23
XGPS 7	18 27 21.2	-10 46 17.8	7637	4998	0.95	0.98
XGPS 8	18 29 50.8	-11 5 41.2	13167	11546	1.0	1.0
XGPS 9	18 28 6.4	-10 25 10.0	11894	9248	0.92	0.62
XGPS 10	18 30 36.2	-10 44 29.3	9767	8146	0.97	0.83
XGPS 11	18 29 43.9	-10 24 9.6	8409	6788	0.92	0.81
XGPS 12	18 28 59.1	-10 6 50.9	7367	5746	1.0	1.0
XGPS 13	18 31 25.5	-10 24 32.5	6666	5047	0.73	0.66
XGPS 14	18 30 29.3	-10 2 47.1	7269	4998	1.0	1.0
XGPS 15	18 29 36.6	- 9 42 41.1	7274	4998	0.82	0.96
XGPS 16	18 32 6.5	-10 1 51.8	7762	5486	1.0	1.0
XGPS 17	18 31 13.9	- 9 41 39.4	7274	4998	0.99	0.94

[a] Total exposure for the MOS 1 camera (s)
[b] Total exposure for the pn camera (s)
[c] Fraction of the exposure time used in producing images

scheduled (see Table 4.1). In all cases the EPIC cameras were operated in *Full Window Mode* with the medium filter selected. In the event the completion of this survey proved problematic due to the impact of intervals of high instrumental background (proton flaring, see §2.5.1) on the data quality, at least for a subset of the pointings. Several of the pointings were in fact repeated to overcome the worst effects of this contamination (Table 4.1 refers to the observations actually used in the present work). The light curves for these observations can be seen in §2.

Although the search for point sources was conducted on an observation by observa-

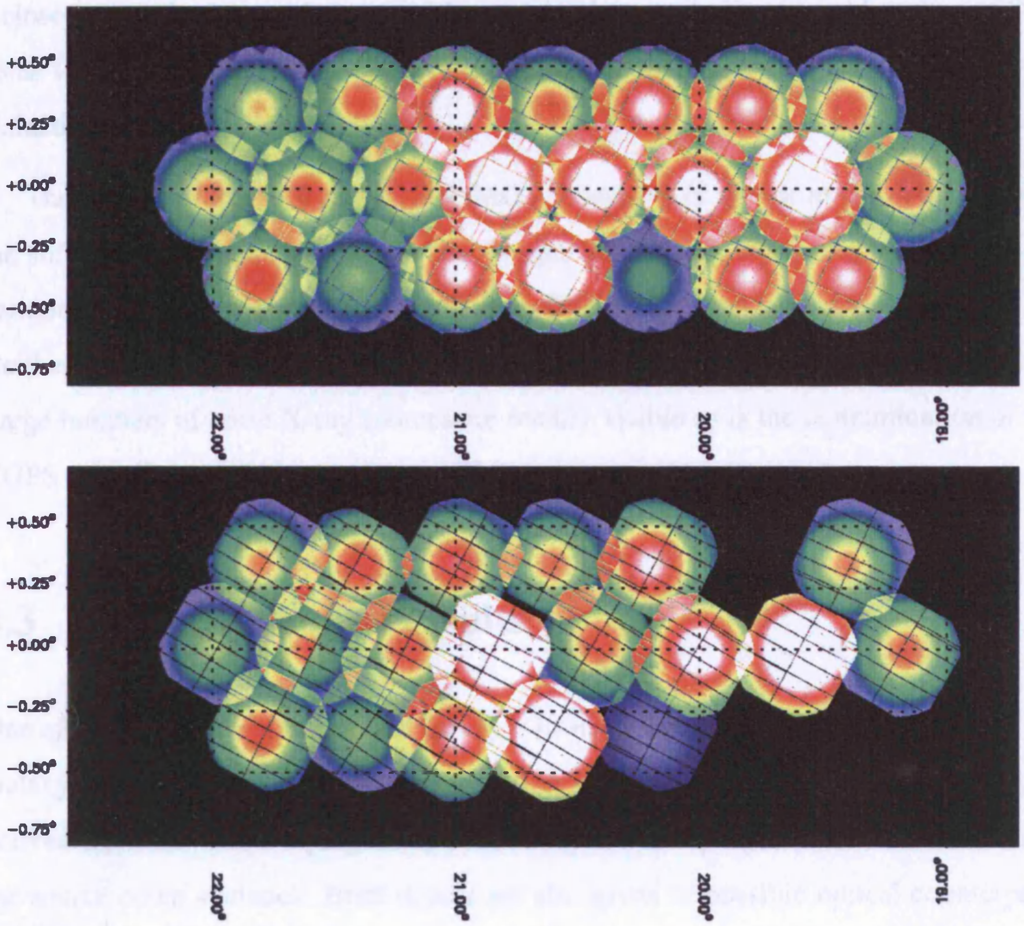

FIGURE 4.1. *Top panel:* A mosaiced (2–4.5 keV) exposure map showing the sky coverage provided by the MOS cameras over the full set of XGPS-I observations. The image is plotted in Galactic coordinates and employs a simple rectangular projection. The colour-scale corresponds to the accumulated (MOS 1 + MOS 2) exposure time at different points in the survey region, with the variation for each individual pointing largely reflecting the vignetting function of the *XMM-NEWTON* mirrors. *Bottom panel:* The same information for the pn camera. The gaps in the pn exposure map correspond to XGPS-I observations for which pipeline-processed pn data are not available. The maximum exposure (shown as white) is 18 ks and 6.5 ks in the MOS and pn images respectively.

tion basis, a mosaic of the full set of observations was also produced. To illustrate the process, Fig. 4.1 shows a mosaic of the exposure maps for both the MOS and pn cameras for the complete set of observations. In effect the survey uses three rows of pointings in a close-packed hexagonal pattern (with a spacing between adjacent field centres of 24′), so as to give efficient (but not particularly uniform) coverage of a narrow strip of the Galactic plane.

The mosaiced image for MOS 1 + MOS 2 datasets is shown in Fig. 4.2 for both the soft and hard bands. These are raw images which have not been corrected for the variation in exposure across each individual field or for field overlaps (see Fig. 4.1). Neither has any allowance been made for the varying level of instrumental background. Large numbers of point X-ray sources are readily visible as is the contamination of the XGPS 14 & XGPS 15 observations by high instrumental background.

4.3 Source detection results

One of the main aims of the present survey is to study the X-ray source population of the Galaxy at relatively faint fluxes. In this section we consider the X-ray source catalogue derived from the XGPS-I programme, the X-ray spectral properties of the sources and the source count statistics. Brief details are also given of possible optical counterparts based on available wide-field optical data and other published catalogue information.

4.3.1 The XGPS-I Source Catalogue

A total of 424 discrete X-ray sources satisfied the detection criteria in the 22 observations which comprise the XGPS-I. The full source catalogue is presented in Appendix A. For each source entry the following information is quoted:

1. The X-ray source designation;

2. The XGPS-I survey field in which the source was detected;

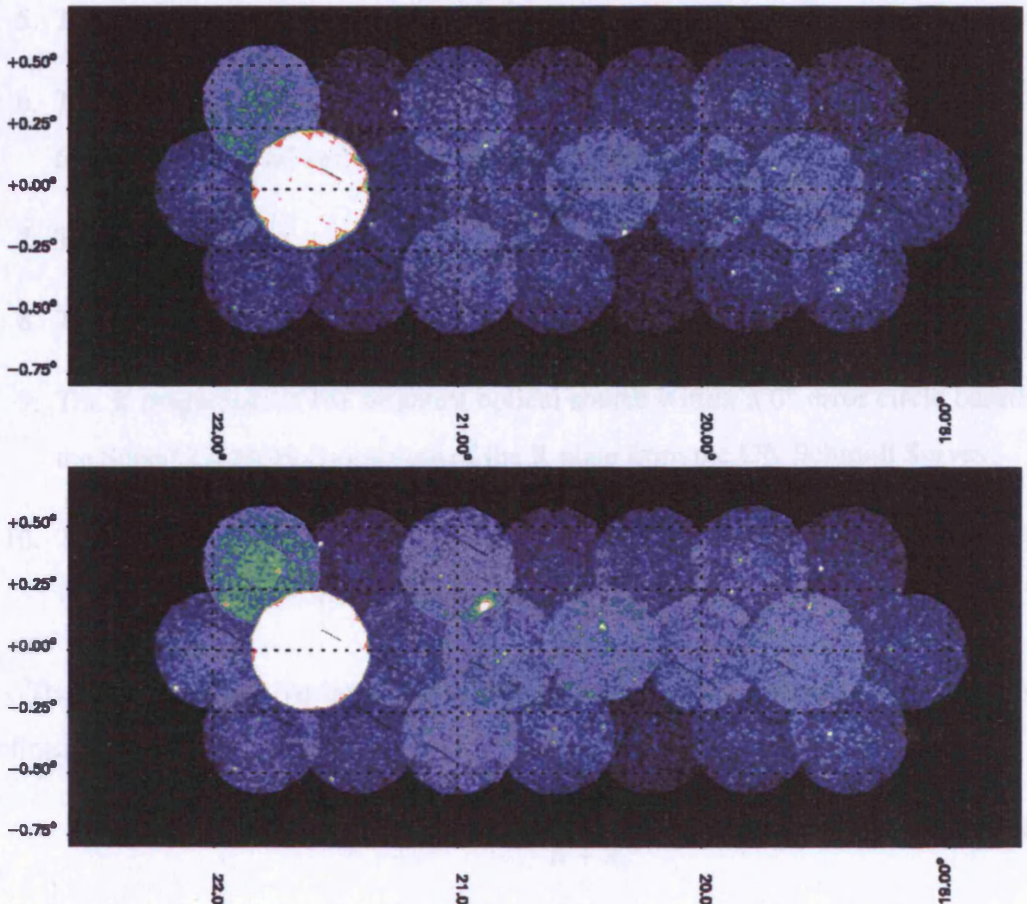

FIGURE 4.2. *Top Panel:* Image of the X-ray emission recorded in the soft (0.4–2 keV) band from the mosaiced XGPS-I fields. No correction has been applied for the varying exposure time, although a the requirement that the minimum MOS 1 + MOS 2 exposure be 1 ks, has been applied. The gross field-to-field brightness variations reflect the changes in the instrumental background, with the XGPS 14 & XGPS 15 observations being particularly badly contaminated. The image has been smoothed with a circular Gaussian of width 16 arcsec to accentuate the individual point sources. *Bottom Panel:* The corresponding hard (2–6 keV) band image.

3. The X-ray position;

4. The derived MOS count rates in the soft (s), hard (h) and broad-bands (b) with detections shown in bold and negative fluxes suppressed;

5. The MOS *quality* flag;

6. The derived pn count rates in the soft (s), hard (h) and broad-bands (b) with detections shown in bold and negative fluxes suppressed;

7. The pn *quality* flag;

8. The X-ray hardness ratio HR (see below);

9. The R magnitude of the brightest optical source within a 6″ error circle based on the SuperCOSMOS digitisation of the R plate from the UK Schmidt Survey;

10. The designation of the optical source, if any, within a 6″ X-ray error circle. Here, U = USNO, with all the other references taken from the SIMBAD database.

The X-ray spectral hardness ratio (HR) quoted for each source in Appendix A is defined as:

$$HR = \frac{h-s}{h+s} \tag{4.1}$$

where h is the measured hard band count rate and s the count rate in the soft band. For sources detected in both camera systems the MOS and pn count rates were summed in the two energy bands before calculating HR.

The numbers of sources detected in each camera system and in each energy band are given in Table 4.2. Of the 424 sources in the catalogue, 132 are detected in both the pn and MOS cameras, which represents 59% of the pn sample but only 38% of the MOS sources. The fact that there are more source detections in the MOS channel than in the pn camera reflects both the lack of pn data for some of the fields and also the longer exposures times typically achieved for the MOS detectors (the set-up time for the pn camera is a significant overhead for these rather short observations). For both the MOS and pn

Table 4.2. Summary of source detections in each camera and energy band.

	Energy Band					
Camera	Soft	Hard	Broad	H&S [a]	B-only[b]	Total
pn	90	128	171	22	26	222
MOS	135	215	266	43	38	345

[a] Number of sources detected in *both* the hard and soft bands.
[b] Number of sources detected *only* in the broad band.

instruments, considerably more sources were detected in the hard energy band than in the soft band. It is surprising that the overlap between the spectral channels, *i.e.* the number of sources independently detected in both the hard and soft spectral bands, is so small (only $\sim 10 - 15\%$ of the sample). This spectral characteristic presumably also explains why the broad-band channel is only marginally more sensitive than its component bands, as demonstrated by the fact that only $\sim 11\%$ of the sources were detected solely in the broad band. Ebisawa et al. (2001) have noted a similar lack of overlap between the soft and hard source populations detected in deep *CHANDRA* observations of the Galactic plane.

4.3.2 The spectral properties of the XGPS-I sources

The range of spectral hardness exhibited by the XGPS-I sources is illustrated in Fig. 4.3 which shows HR versus MOS count rate for sources detected in the MOS cameras. There is clearly a huge spread encompassing the full range of the HR parameter (*i.e.* $HR = -1$ to $+1$). Given this scatter, it is not surprising that there is little evidence for a variation of the average HR with decreasing count rate (as might be predicted, for example, if fainter sources are on average more distant and as a consequence are more strongly absorbed).

The typical spectral form of the XGPS-I source population are investigated by considering the integrated spectra of different subsets of sources. In fact, the population is split into three groups depending on the HR parameter as follows: (i) soft sources with HR < -0.5; (ii) mid-range sources with $-0.5 \leq$ HR ≤ 0.5 and (iii) hard sources with HR > 0.5. The procedure described in §2.7 is used to extract the integrated spectra

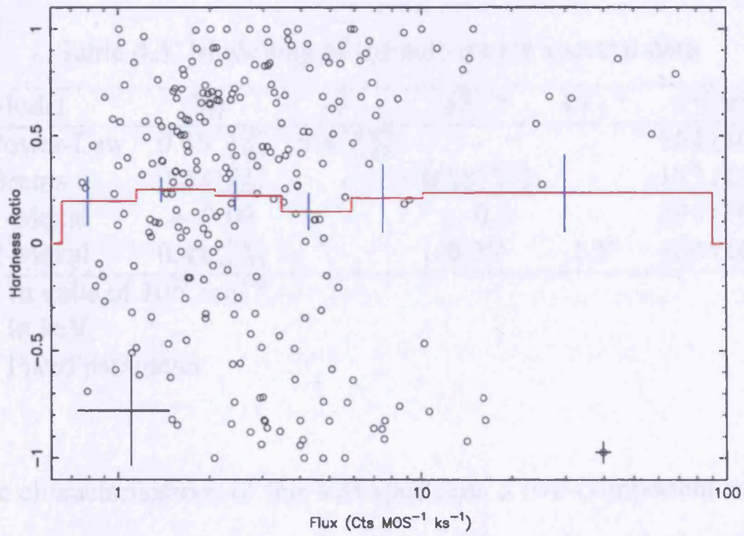

FIGURE 4.3. The relationship between spectral hardness and source count rate for sources detected in the MOS cameras. Error bars are shown for representative high and low count-rate points. The histogram charts the variation in the average HR with count rate.

for the individual fields which are then summed over the set of observations to obtain the average spectrum for each source group. To avoid undue bias, an extremely bright source detected in XGPS 9 (XGPS-I J182834-103700 - see §4.3.5), which contains a comparable number of counts to all the other sources put together was excluded from this process.

The integrated MOS spectra obtained as above were analysed using the XSPEC software package. Following standard practice, the spectra were binned prior to analysis to give a minimum of 20 counts per spectral channel. From Fig. 4.4 it is immediately evident that the spectra of the three groups of sources are very different.

Initially the soft-source spectrum in the 0.4–6.0 keV range was fitted with three different models namely a power-law, bremsstrahlung and Mekal thermal plasma model, including absorption in each case. The pure continuum models provided the best-fits (albeit with modest reduced χ^2) with the power-law model requiring a very steep spectral index and the bremsstrahlung model requiring a relatively low temperature (see Table 4.3). In contrast, a single temperature solar-abundance Mekal model provided a poor fit to the spectrum. However, since the pure continuum models are probably not physi-

Table 4.3. Modelling of the soft-source spectral data

Model	$N_H{}^a$	Γ	$kT_1{}^b$	$kT_2{}^b$	χ^2(dof)
Power-Law	$0.65^{+0.08}_{-0.05}$	$5.8^{+0.06}_{-0.03}$	-	-	164 (107)
Brems	$0.32^{+0.13}_{-0.04}$	-	$0.38^{+0.03}_{-0.02}$	-	173 (106)
1-Mekal	~ 0.60	-	~ 0.5	-	299 (107)
2-Mekal	$0.44^{+0.03}_{-0.03}$	-	0.25^c	1.5^c	160 (107)

[a] In units of 10^{22} cm^{-2}.
[b] In keV
[c] Fixed parameter

cally realistic characterisations of this soft spectrum, a two-component solar-abundance Mekal model (plus absorption) was also tried. The result, with the two temperature parameters fixed at representative values (here kT=0.25 and 1.5 keV respectively are used), was a slight improvement in terms of χ^2 to those obtained for the power-law and bremsstrahlung models. Table 4.3 provides details of the fit and Fig. 4.4 compares the best-fitting 2-temperature model with the data.

An initial investigation of both the mid-range and hard-source spectra (over the spectral range 0.4–8 keV) demonstrated that a simple power-law continuum plus absorption model provided a good description of both datasets with a fairly similar value for the spectral index ($\Gamma \approx 1.6$) but with the absorption column density for the mid-range sample significantly lower than for the hard-spectrum sources. On this basis, the two spectra were fitted *simultaneously* with the absorbed power-law model, but with the spectral index as the only tied parameter. The result was a good fit ($\chi^2 = 440$ for 421 dof) with $\Gamma = 1.60^{+0.10}_{-0.13}$ and N_H values of $0.5^{+0.08}_{-0.08} \times 10^{22}$ cm^{-2} and $3.7^{+0.3}_{-0.4} \times 10^{22}$ cm^{-2} for the mid-range and hard-source spectra respectively. With Γ fixed at 1.7 (representative of the predominant extragalactic population of Seyfert galaxies and quasars) the respective N_H values became $0.6^{+0.06}_{-0.05} \times 10^{22}$ cm^{-2} and $3.9^{+0.2}_{-0.3} \times 10^{22}$ cm^{-2}. A comparison of the best-fitting models with the data are again shown in Fig. 4.4.

Both the medium and hard source spectra contain a line emission feature in the 6–7 keV band, consistent with Fe K_α emission. Although the data are of limited quality, the line centroid values are determined to be 6.59 ± 0.07 keV and 6.88 ± 0.06 keV for the medium and hard sources respectively and the equivalent widths are measured to be 370 ± 250 and 240 ± 110 eV.

The fact that the soft-source spectrum is well fitted by a canonical 2-temperature model with a relatively low absorption column, is consistent with the bulk of the soft population being relatively nearby active stars. The spectra of the mid-range and hard-source samples are less easy to characterise. Certainly many of the faint hard sources may be AGN (see §4.4.1) but the relatively hard continuum spectrum and iron-line properties also match the spectral properties of cataclysmic variables (CVs) and RS CVns. For example, CVs often exhibit a two-temperature thermal spectrum with $kT \sim 0.5 - 1$ keV and $\sim 5 - 10$ keV (*e.g.* Baskill 2002). With significant line of sight absorption the latter component dominates and readily mimics the hard power-law form inferred above.

4.3.3 The XGPS-I Source Counts

In order to study the number density of discrete X-ray sources as a function of count rate it is necessary to correct for the variation in the source detection sensitivity across the set of XMM fields which comprise the survey. Here we concentrate solely on the sources detected in the MOS cameras.

The first step in the correction process was to calculate a sensitivity map for source detection (in "on-axis" count-rate units) for each XGPS-I observation based on the exposure map (which accounts for vignetting and other relevant factors such as chip gaps) and the derived MOS background map. The total survey area over which a source of a given count rate was detectable was then readily calculated by summing over the set of sensitivity maps comprising the XGPS-I survey. The derived effective area curves are shown in Fig. 4.5 for the three energy bands of the survey.

The X-ray source counts are then constructed by summing the contributions of individual sources after correction for the survey sensitivity. For example, consider a source detected at some particular offset angle in one of the XGPS-I observations. Its on-axis count rate is obtained by simply dividing its measured net counts by the value of the exposure map at the source position. The derived sensitivity curves are then used to de-

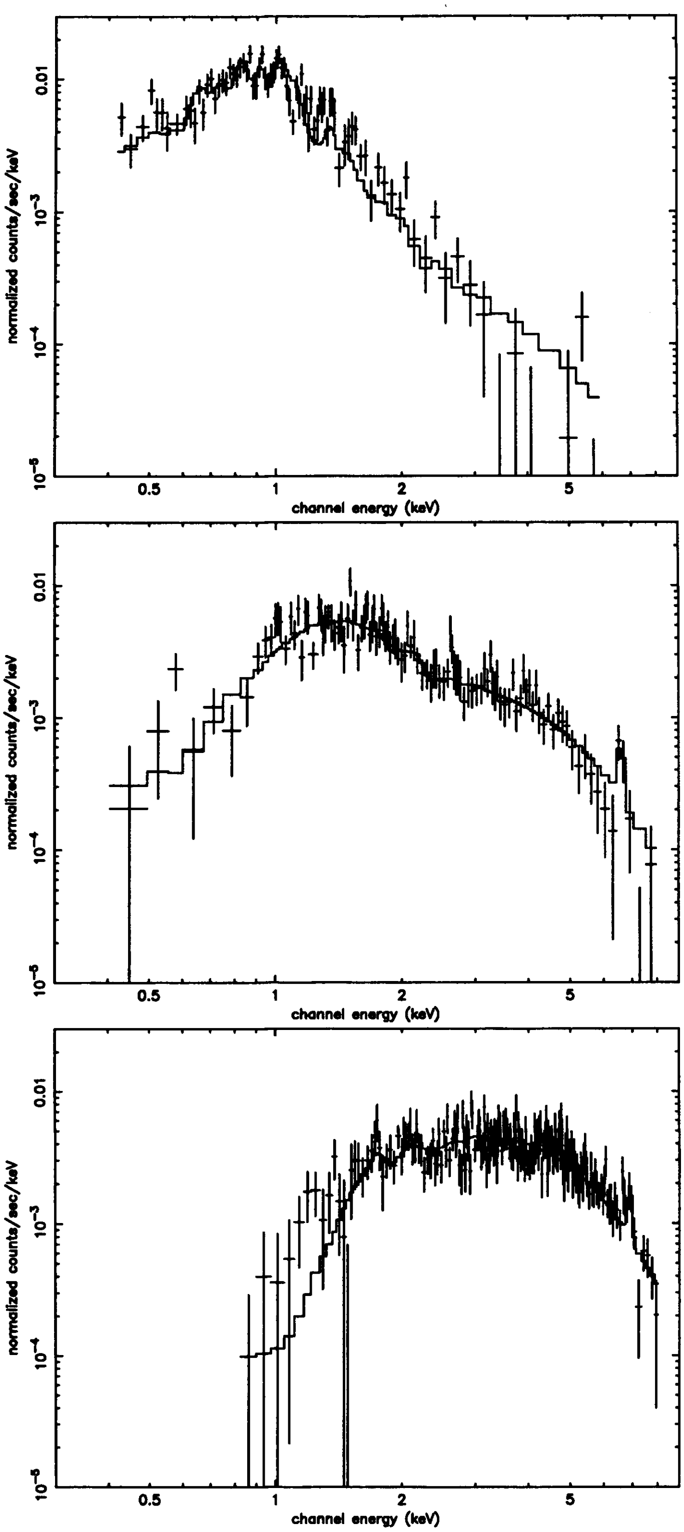

FIGURE 4.4. *Top Panel:* The integrated EPIC MOS spectrum of the soft XGPS-I sources with HR < -0.5. *Middle Panel:* The integrated EPIC MOS spectrum of the XGPS-I sources with mid-range hardness ratios *i.e.,* $-0.5 \leq$ HR ≤ 0.5. *Bottom Panel:* The integrated EPIC MOS spectrum of the hard XGPS-I sources with HR > 0.5. In each case the histogram represents the besting-fitting spectral model described in the text.

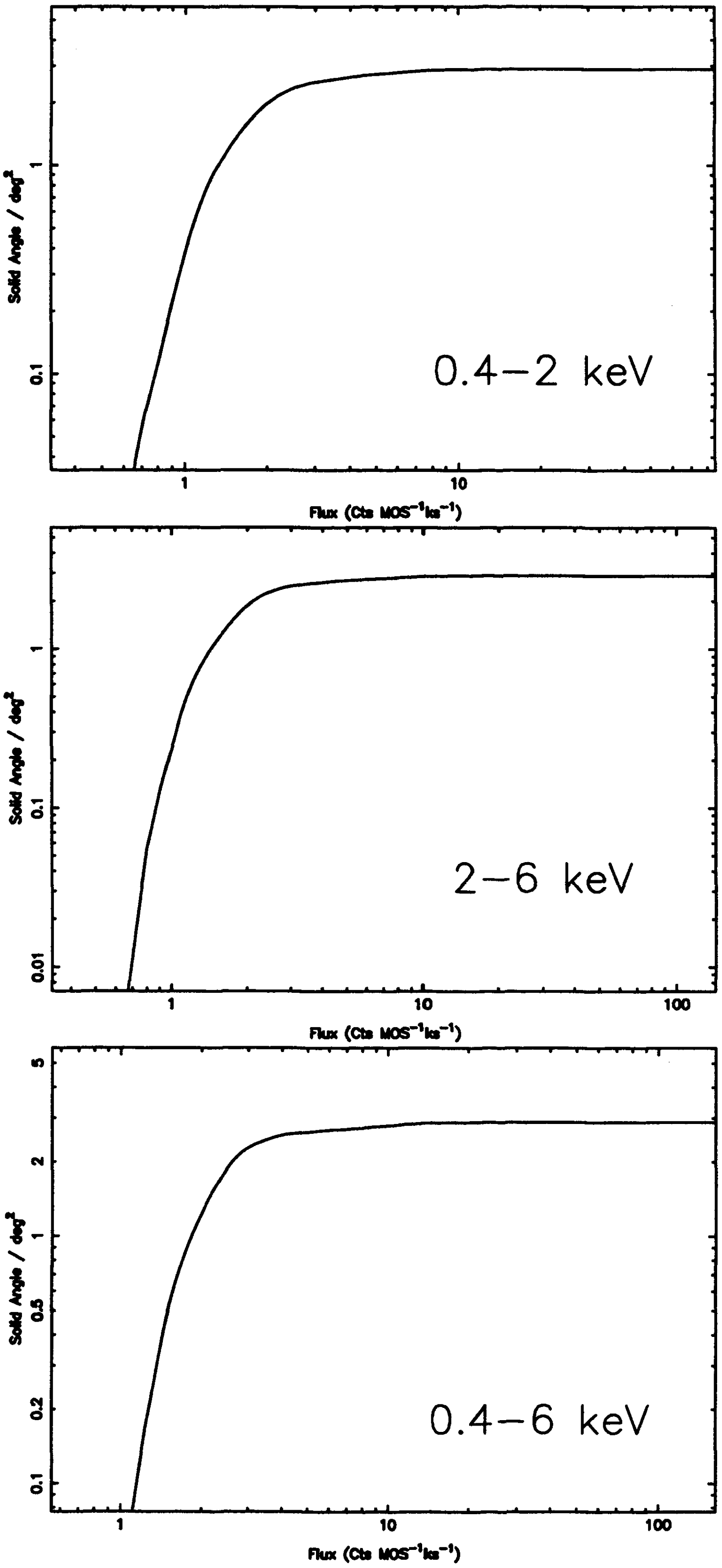

FIGURE 4.5. Sensitivity curves for the source count analysis in three energy bands. The total solid angle coverage of the survey (for very bright sources) is $\sim$ 3 square degrees.

termine the solid angle (Ω) over which a source of that count rate was detectable. This source then contributes $1/\Omega$ to the source counts at its measured count-rate value. The final source count is obtained by summing the contributions of all the detected sources[1].

In order to obtain an estimate of the magnitude of the error that should be assigned to the derived source counts at a given flux a Monte Carlo simulation was carried out of the *post-detection* process used to construct the source counts (*nb.* bearing in mind that with integral counts the measurements are not independent from point to point). This simulation also demonstrated that the changing gradient of the sensitivity curves at low fluxes introduces a significant bias in the source counts; in effect the Poissonian variation in the measured flux of a source has an asymmetric effect on the value of Ω that is derived. This bias is corrected for by simulating the source counts both with and without such flux errors, noting the differences and adjusting the measured data accordingly. In practice this procedure resulted in a reduction in the inferred number density of sources at the survey limit by up to 40 per cent.

Fig. 4.6 shows the corrected integral source counts in the three bands. It is evident that XGPS-I survey detects discrete X-ray sources in the Galactic plane down to surface density of roughly 200 per square degree.

By linearly fitting the data in binned, differential form, the slope of the integral counts was determined to be 1.5 ± 0.2 for both the soft and hard sources and 1.3 ± 0.2 for the broad band sources. (These values represent the slopes of the source counts after excluding, in each case, a handful sources at the bright end of the flux range.)

4.3.4 Optical - X-ray Source Correlations

Although the X-ray positions typically have statistical errors of $\leq 4''$ (see §2.6), optical counterparts were searched for within a nominal $6''$ error circle. Specifically the optical data used was from the SuperCOSMOS digitisation of the sky survey plates from the UK Schmidt telescope (UKST). Appendix A identifies the brightest optical source (if

[1]Sources with $quality < 0.8$, such as those located at a CCD chip edge or strongly affected by bad pixels were excluded.

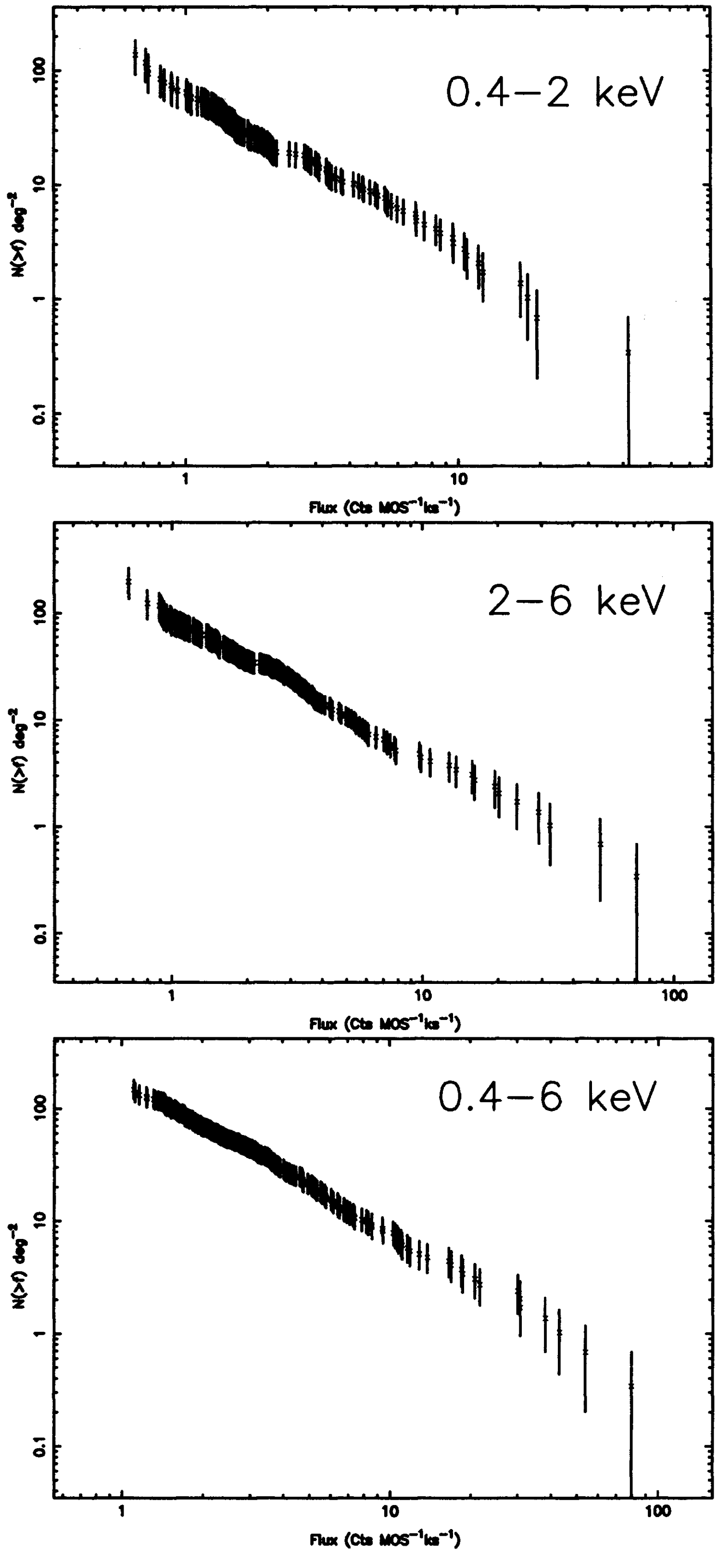

FIGURE 4.6. The derived X-ray source counts plots in three energy bands, corrected at faint fluxes for the bias in the coverage correction induced by flux errors (see text).

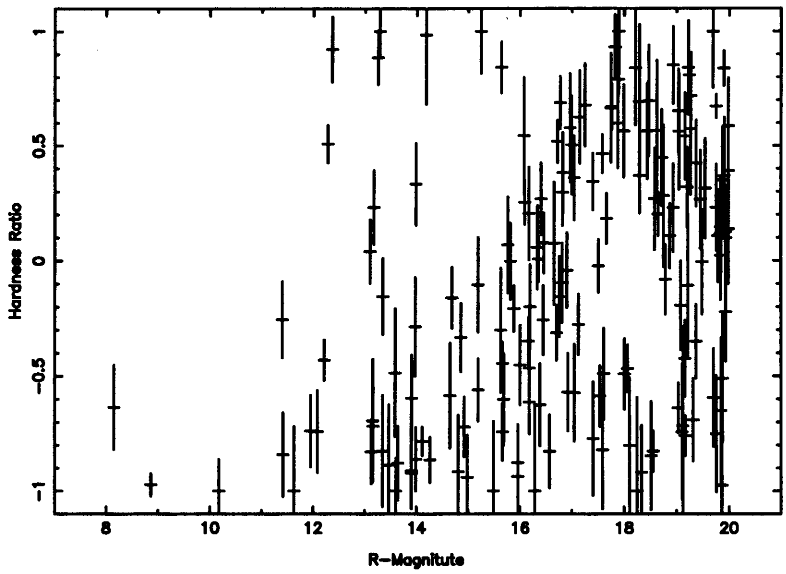

FIGURE 4.7. X-ray spectral hardness ratio versus optical R magnitude. This refers to the brightest optical object in the X-ray error circle of each XGPS-I source.

any) on the red (R) plate within the error circle of each XGPS-I source and quotes the corresponding optical R magnitude. Cross references to the optical source in the USNO-A2.0 catalogue and/or the SIMBAD database are also noted. Of the 424 X-ray point sources, 188 have possible optical counterparts identified by this procedure.

The correlation of optical magnitude versus X-ray count rate (here the focus is on detections with $quality > 0.8$ in the MOS cameras) is a scatter diagram. Similarly a plot of X-ray hardness ratio versus optical R magnitude also shows significant scatter (Fig. 4.7), although there is hint of X-ray spectral hardening as one goes to optically fainter sources.

Let us now investigate how the number of optical/X-ray correlations varies with optical magnitude for three subsets of sources divided according to the X-ray hardness ratio (*i.e.* the soft-, mid-range and hard-spectrum samples defined earlier). Fig. 4.8 shows how the fraction of X-ray sources with an associated optical source rises with increasing R. For the hard X-ray source sample, the rate of optical correlation is essentially the same as the chance rate. However, both the soft and mid-range samples have significantly higher rates of optical/X-ray associations than expected by chance. For these, we can compare the observed and chance rates to estimate the fraction of genuine optical identifications within the full list of optical associations (see Fig. 4.8, *lower panel*). The chance rate is calculated by searching for optical counterparts at four separate locations, each within 30" of the X-ray source position, and averaging the results.

The X-ray sources with soft spectra (HR < -0.5) have a particularly high rate of association with bright optical objects. For example, ~ 45 per cent of such sources have an optical object brighter than R=18 within $6''$ of the X-ray position and of these roughly 75 per cent are likely to be the correct counterpart. At R=20 the two factors become ~ 65 and ~ 55 per cent respectively. On the basis of the inferred X-ray/optical ratio and the X-ray spectral characteristics discussed earlier, it is likely that many of these soft X-ray sources are nearby late-type stars with active coronae.

Having identified a subset of the optical/X-ray associations which have a relatively high probability of being the correct identification, we can use the measured optical to X-ray positional offsets to check the astrometry of the X-ray positions. (Up to this point no corrections have been applied for any astrometric errors relating to the pointing of the *XMM-NEWTON* spacecraft other than those included in the routine SAS processing). Fig. 4.9 shows the radial distribution of the optical/X-ray offsets for the soft sources with associated optical objects brighter than R=20. Allowing for a uniform distribution of chance coincidences the radius encompassing 68 per cent (90 per cent) of the "real" identifications is found to be $3.3''$ ($4.7''$) which is very comparable to an earlier estimate of the statistical errors associated with the X-ray positions. Of the 22 XGPS fields, 17 have at least one soft source with an optical counterpart brighter than R=20 within $4.7''$. Conversely it is simple to calculate that an incidence of 5 fields with zero correlations is not a particularly unlikely event. Unfortunately this does mean that for the latter fields there is no independent check of the *XMM-NEWTON* aspect solution (the fields in question are Ridge 4 and XGPS 2,4, 6 & 14). However, it seems reasonable to conclude that the astrometry is generally at least as good as the typical statistical errors on the measured X-ray positions.

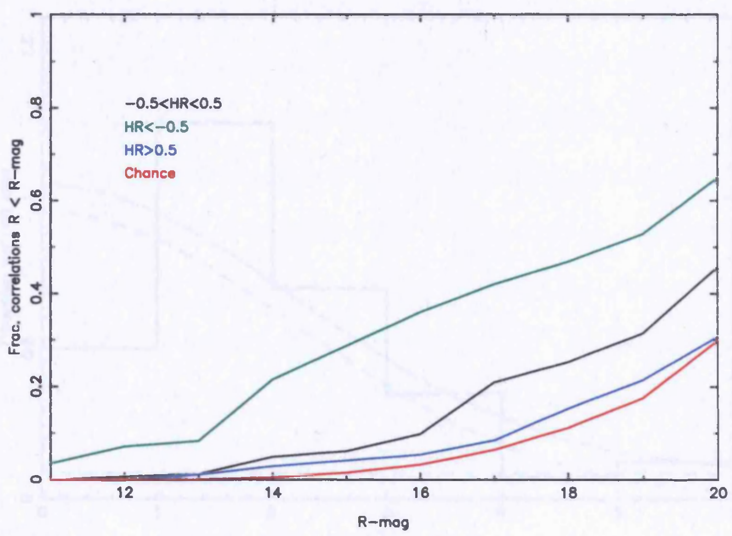

(a) Optical correlation fraction

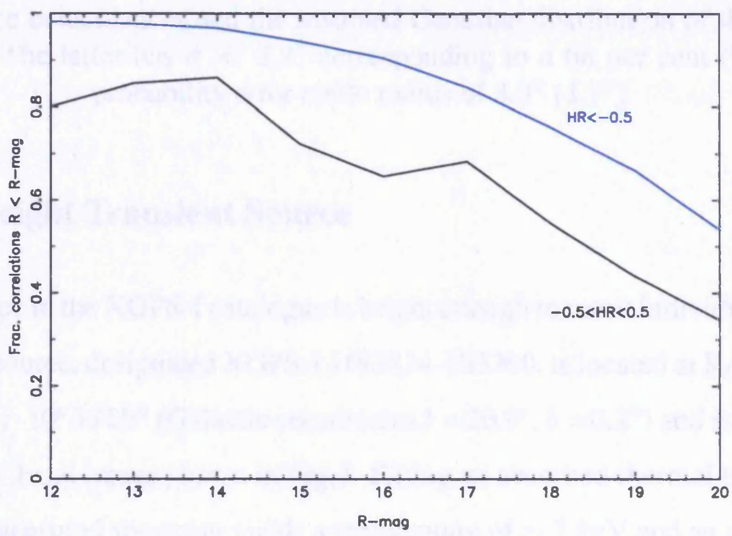

(b) Genuine correlation fraction

FIGURE 4.8. *Top Panel:* The fraction of X-ray sources with an associated optical source plotted versus the limiting R magnitude of the optical sample. The three upper curves correspond to X-ray sources with spectral hardness in three ranges, namely soft sources with HR < -0.5, mid-range sources with $-0.5 \leq$ HR ≤ 0.5 and hard sources with HR > 0.5. The lower curve shows the chance coincidence rate for finding an optical source in a $6''$ error circle in this region of the sky. *Bottom Panel:* The fraction of the optical/X-ray associations that are likely to represent real identifications. The two curves correspond to the soft (upper) and mid-range (lower) spectral samples.

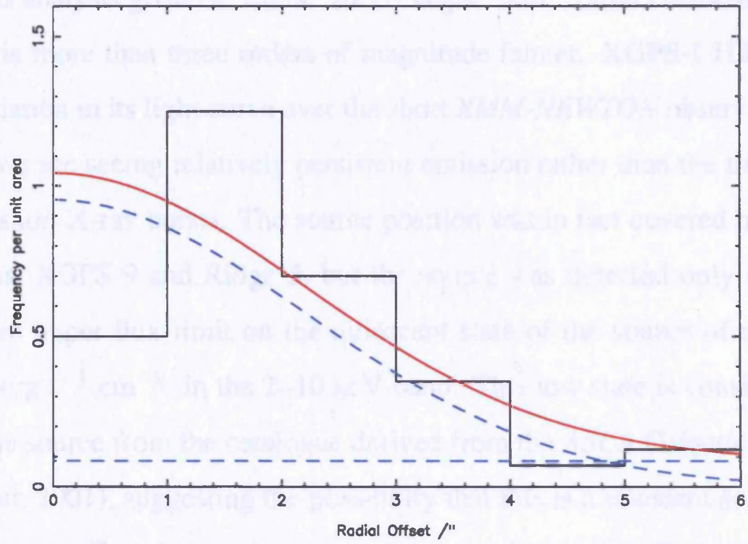

FIGURE 4.9. The radial distribution of the optical/X-ray offsets measured for the soft source sample. The solid-line represents the sum of the uniform distribution of the chance coincidences and the assumed Gaussian distribution of the real identifications. The latter has $\sigma = 2.2''$ corresponding to a 68 per cent (90 per cent) probability error circle radius of 3.3″ (4.7″).

4.3.5 A Bright Transient Source

Only one source in the XGPS-I catalogue is bright enough to merit individual spectral extraction. The source, designated XGPS-I J182834-103700, is located at RA, Dec (J2000) $18^{h}\ 28^{m}\ 34.0^{s}$, -10°36′59″ (Galactic coordinates l =20.9°, b =0.2°) and is clearly visible in the 2–6 keV band image shown in Fig.4. Fitting an absorbed thermal bremsstrahlung model to the measured spectrum yields a temperature of $\sim$ 7 keV and an absorption column of $\sim 5 \times 10^{22}$ cm^{-2} (see Fig. 4.10). This column density is consistent with either an extragalactic or a distant Galactic origin. In the latter case (assuming a distance of $\sim$ 15 kpc) the observed flux is equivalent to an X-ray luminosity of $\sim 10^{35}$ erg s^{-1}.

Cornelisse et al. (2002) discovered 6 type I X-ray bursters in *BeppoSAX* Wide Field Camera (WFC) observations, one of which is positionally coincident with this bright XGPS-I source, although the WFC 99 per cent confidence error circle of 2.8′ is relatively large. The peak flux measured by *BeppoSAX* for this source was $(1.1 \pm 0.4) \times 10^{-8}$ erg s^{-1} cm^{-2}(2–10 keV) with a burst duration of $\sim$ 30 seconds, whereas in the same waveband this analysis gives $\sim$ 7.5×10^{-12} erg s^{-1} cm^{-2}(after correcting for absorption), which is more than three orders of magnitude fainter. XGPS-I J182834-103700 shows no variation in its light curve over the short *XMM-NEWTON* observation, demonstrating that we are seeing relatively persistent emission rather than the time average of one or more short X-ray bursts. The source position was in fact covered by two XGPS-I observations, XGPS 9 and Ridge 5, but the source was detected only in the former. This places an upper flux limit on the quiescent state of the source of approximately 2×10^{-14} erg s^{-1} cm^{-2} in the 2–10 keV band. This low state is consistent with the absence of the source from the catalogue derived from the *ASCA* Galactic Plane Survey (Sugizaki et al. 2001), suggesting the possibility that this is a transient source observed in an outburst state. Type I X-ray bursts are thermonuclear helium flashes on the surface of an accreting neutron star in a binary system. The picture which emerges for XGPS-I J182834-103700 is one in which the persistent X-ray emission of the binary varies by large factors but at levels several orders of magnitude below the Eddington limit, except when the behaviour is punctuated by a burst.

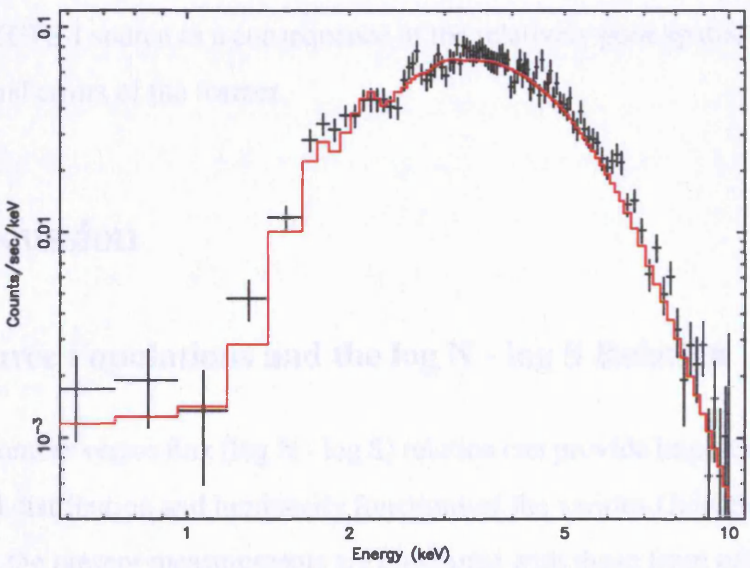

FIGURE 4.10. The measured count-rate spectrum of a bright transient source. The histogram corresponds to the best-fitting model detailed in the text.

Table 4.4. Correlation of XGPS-I sources with the *ASCA* catalogue.

XMM ID	*ASCA* Name
XGPS-I J182534-121454	AX J182538-1214
XGPS-I J182846-111711	AX J182846-1116
XGPS-I J182525-114525	AX J182530-1144
XGPS-I J183038-100249	AX J183039-1002
XGPS-I J183117-100921	AX J183116-1008
XGPS-I J183209-093906	AX J183206-0938 / AX J183206-0940
-	AX J183114-0943
-	AX J182651-1206

4.3.6 Comparison with *ASCA*

The region surveyed by XGPS-I is entirely covered by the *ASCA* Galactic Plane Survey (Sugizaki et al. 2001) which resolved 163 sources in the Galactic Plane within a longitude span of 90°centred on $l = 0°$. Of these 163 sources nine fall within the nominal region covered by the XGPS-I observations. *XMM-NEWTON* has possibly detected seven of these sources as summarised in Table 4.4. Note that, two of the *ASCA* sources are linked to the same XGPS-I source as a consequence of the relatively poor spatial resolution and large positional errors of the former.

4.4 Discussion

4.4.1 Source Populations and the log N - log S Relation

The source number versus flux (log N - log S) relation can provide important information on the spatial distribution and luminosity functions of the various Galactic source populations. Here the present measurements are combined with those from other missions to examine how various categories of source may contribute to the observed source counts.

In order to relate the *XMM-NEWTON* measurements to observations from other satellites it is necessary to convert the measured source counts from count-rate to flux units. Table 4.5 lists the conversion factors from MOS count rate in the 2–6 keV band to the

Table 4.5. Factors[a] to convert from the MOS count rate in the 2–6 keV band to the observed flux in the 2–10 keV band for different power-law spectra with a range of interstellar absorptions.

$\Gamma \backslash N_H{}^b$	0.0	1.0	3.0	5.0	7.0
1.4	2.7	3.0	3.4	3.9	4.4
1.7	2.4	2.6	3.0	3.4	3.9
2.0	2.1	2.3	2.7	3.1	3.4

[a] In units of 10^{-14} erg s^{-1} cm^{-2} / (MOS count ks^{-1})
[b] In units of 10^{22} cm^{-2}.

corresponding flux (in erg s^{-1} cm^{-2}) in the 2–10 keV band for a variety of spectral forms calculated using PIMMS (Mukai 1993).

In the present analysis a factor 2.6×10^{-14} erg s^{-1} cm^{-2} / MOS count ks^{-1} is adopted, corresponding to a power-law source spectrum with spectral index $\Gamma = 1.7$ absorbed by a column density $N_H = 1 \times 10^{22}$ cm^{-2}. This is clearly a compromise given the range of spectral form established earlier (see §4.3.2); the effective uncertainty in the flux scaling may be as large as $\pm 30\%$.

Figure 4.11 shows the measured log N - log S relation in the 2–10 keV band based on the XGPS-I measurements. Here one high flux point with large error bars has been clipped as have two low-flux points requiring very large coverage correction from the equivalent representation in Fig. 4.6. For comparison the source counts derived from the extensive survey of the Galactic Plane between $l = \pm 45°$carried out by *ASCA* (Sugizaki et al. 2001) and from recent deep *CHANDRA* observations in the Galactic Plane at l =28° (Ebisawa et al. 2001) are also shown.

As can be seen from Fig. 4.11, the flux range probed by the XGPS-I measurements is intermediate between that sampled by the *ASCA* and *CHANDRA* programmes. The agreement between the XGPS-I and *ASCA* surveys is rather good given the very different coverage of the Galactic Plane inherent in the two programmes. The agreement between the XGPS-I and *CHANDRA* source counts is also good bearing in mind the different pointing directions and the fact that at $\sim 3 \times 10^{-14}$ erg s^{-1} cm^{-2} there are only ~ 6 sources in the latter survey. Based on this compilation the log N - log S relation appears

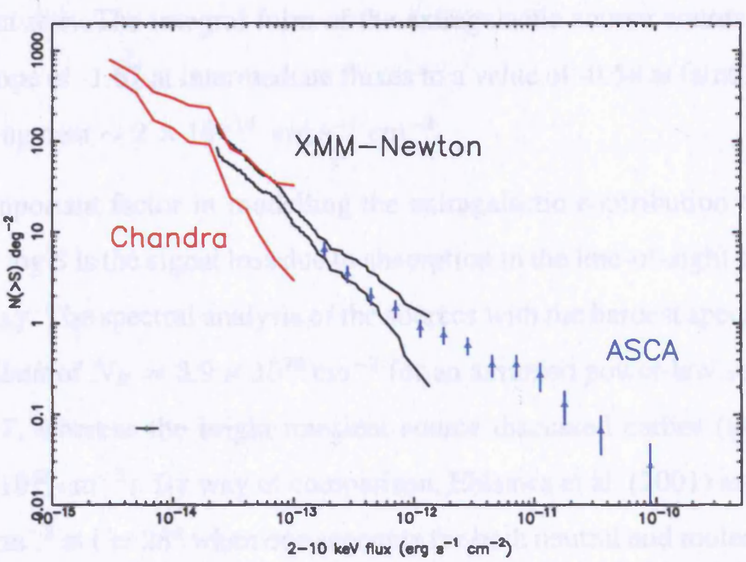

FIGURE 4.11. The 2–10 keV log N - log S relation measured in the Galactic Plane based on *ASCA* , *XMM-NEWTON* and *CHANDRA* observations (see the text for references). In the case of both the *XMM-NEWTON* and *CHANDRA* measurements the upper and lower bounds of the derived source counts are shown rather than individual data points. The magnitude of the relative flux scaling uncertainty applicable to the three data sets is indicated by the horizontal error bar.

to first flatten, then steepen, then flatten again as one moves from bright sources at $\sim 10^{-10}$ erg s^{-1} cm^{-2} to faint sources at a limiting flux of $\sim 3 \times 10^{-15}$ erg s^{-1} cm^{-2} in the 2–10 keV band.

The first step in modelling the measured composite log N - log S relation in terms of various underlying source populations is to quantify the contribution of extragalactic sources. It has in fact been recently demonstrated that even in heavily obscured regions of the Galactic plane the X-ray source counts measured at faint fluxes in the hard band are dominated by this component (Ebisawa et al. 2001). The extragalactic log N - log S relation in the 2–10 keV band has been determined over a wide range of X-ray flux from HEAO-1 A2 observations at the bright end (Piccinotti et al. 1982) through to recent ultra-deep *CHANDRA* observations which probe below $\sim 10^{-15}$ erg s^{-1} cm^{-2}(Rosati et al. 2002; Cowie et al. 2002; Alexander et al. 2003; Moretti et al. 2003). For the extragalactic 2–10 keV log N - log S the empirical form specified by Campana et al. (2001) is used, this was based on a comparison of deep *CHANDRA* observations with *ASCA* , *BeppoSAX* and other data sets. The integral form of the extragalactic source counts flatten from a power-law slope of -1.67 at intermediate fluxes to a value of -0.58 at faint fluxes with the break occurring near $\sim 2 \times 10^{-14}$ erg s^{-1} cm^{-2}.

A very important factor in modelling the extragalactic contribution to the Galactic Plane log N - log S is the signal loss due to absorption in the line-of-sight column density through Galaxy. The spectral analysis of the sources with the hardest spectra (see §4.3.2) sets a *lower limit* of $N_H = 3.9 \times 10^{22}$ cm^{-2} for an assumed power-law source spectrum with $\Gamma = 1.7$, whereas the bright transient source discussed earlier (§4.3.5) required $N_H = 5.0 \times 10^{22}$ cm^{-2}). By way of comparison, Ebisawa et al. (2001) argue that $N_H = 4 - 6 \times 10^{22}$ cm^{-2} at $l = 28°$ when one accounts for both neutral and molecular hydrogen along the line of sight. Based on the HI measurements of Dickey & Lockman (1990) and molecular hydrogen measurements of Dame et al. (2001) one might infer a similar value for the XGPS-I region. On the other hand Nevalainen et al. (2001) measure a foreground Galactic column density of $7.9 \pm 0.5 \times 10^{22}$ cm^{-2} for a cluster of galaxies at (l,b) = (21.3,-0.7). Here a hard band transmission factor of 0.68 is adopted corresponding to a line of sight column density of 5×10^{22} cm^{-2} (for a power-law $\Gamma = 1.7$ source spectrum) which, in broad terms, aligns the extragalactic prediction with the observed *CHANDRA* source counts at faint fluxes (see Fig. 4.12). Clearly variation in the Galactic N_H from field to field in the Galactic Plane will introduce a significant variance in the extragalactic contamination of the log N - log S relation; the situation presented here is only an approximate description of a very complicated situation.

The possible contribution of various Galactic source populations to the measured composite log N - log S relation is investigated through the use of relatively simple prescriptions for the source luminosity function, the source distribution in the Galaxy and the effects of absorption. In brief, the predicted source counts are calculated by a numerical integration along a line of sight at (l,b) = (20,0). The maximum diameter of the Galaxy is assumed to be 20 kpc and the Galactocentric radius of the Sun is 8.5 kpc. The absorption in the plane is modelled in terms of a local hydrogen density of 0.55 cm^{-3}. The source and particle densities are assumed to decline exponentially with respect to Galactocentric radius (R) and height above the plane (z) (the assumed scale factors were

8500 kpc and 200 pc in R and z for the sources and 8500 kpc and 100 pc for the particle density).

Let us first consider relatively luminous Galactic X-ray binary sources containing either a neutron star or (in a few cases) a stellar mass black-hole. Low-mass X-ray binaries (LMXBs) are found preferentially in the Galactic Bulge and Galactic Centre regions whereas high-mass X-ray binaries (HMXB) tend to avoid the inner 3-4 kpc of the Galaxy but are widely distributed in the Galactic disk (Grimm et al. 2002). The composite log N - log S measured at $l = 20°$ might therefore include contributions from both populations. In order to model the combined LMXB/HMXB contribution a power-law form for the luminosity function is assumed with a slope of -1.3 in the differential form (cf. Grimm et al. 2002). In practice, a luminosity function restricted to the range $10^{34} - 10^{36}$ erg s^{-1}proved sufficient to account for the observed form of the log N - log S relation at the bright source end (see Fig. 4.12). The normalisation of the binary luminosity function need to match the log N- log S relation translates via the source distribution model to a Galactic population of 200 such X-ray binaries with an integrated Galactic X-ray luminosity of 1.6×10^{37} erg s^{-1}.

With the bright and faint ends of the measured log N – log S relation represented respectively by Galactic X-ray binaries and the breakthrough of extragalactic sources, an excess number of sources (relatively to the prediction) is most apparent in the flux range 10^{-13} to 10^{-12} erg s^{-1} cm^{-2}. The requirement on any source population invoked to fill this gap is that its source count must be relatively steep at the top end of this range but should gradually turn over below 10^{-13} erg s^{-1} cm^{-2}, so as not to over-predict the total source density in the flux range sampled by the *CHANDRA* observations.

For illustrative purposes let us consider a source population with an X-ray luminosity function described by a log-normal function centred on $L_X = 10^{31}$ erg s^{-1}with $\sigma = 1.0$ and a local spatial density of $\sim 10^{-6}$ pc^{-3}. A source with $L_X = 10^{31}$ erg s^{-1}, at a distance of 1 kpc has an X-ray flux of 10^{-13} erg s^{-1} cm^{-2}. At larger distances (and hence lower fluxes), the effects of increasing absorption will serve to flatten the counts of such sources. In addition by $\sim 10^{-14}$ erg s^{-1} cm^{-2}the most luminous sources in the population are detectable out to the edge of the Galaxy with the result that the overall log

N - log S relation flattens further. Fig. 4.12 shows the predicted source count relation for the low-luminosity source population considered above. In combination the two Galactic source populations plus the extragalactic component provide an excellent match to the observed composite log N - log S curve.

What class of X-ray source might comprise the low-luminosity population considered above? The most likely candidate population is cataclysmic variables (CVs), close binary systems in which a white dwarf accretes material from a Roche-lobe filling late-type companion, which are often relatively bright X-ray sources with $L_X = 10^{30} - 10^{32}$ erg s^{-1}(*e.g.* Verbunt et al. 1997). In an earlier analysis, Watson (1999) suggested that X-ray faint CVs might show up in large numbers in deep Galactic surveys carried out in the hard X-ray band if their typical X-ray luminosity is $L_X = 10^{31}$ erg s^{-1}(2–10 keV) and space density is $\sim 10^{-5}$ pc^{-3}. The latter value is compatible with the CV space density derived empirically by Patterson (1984) and is not out of line with at least some theoretical estimates (eg. Kolb 1993). In this context, the space density assumed in the modelling of the low- luminosity population is a very conservative estimate particularly since other categories of source, such as RS CVn binaries (*e.g.* Makarov 2003 and references therein), might also contribute to the low-luminosity population. The overall requirement is for a Galactic population of 1.2×10^5 objects which produce an integrated Galactic X-ray luminosity of 1.3×10^{37} erg s^{-1} in the 2–10 keV band.

4.4.2 Contribution of Discrete Sources to the GRXE

Using all XGPS-I observations except the two most contaminated by flaring and the one containing the bright transient source, the total count rate (including the resolved sources) in the hard *XMM-NEWTON* band (2–6 keV), corrected for the underlying instrumental background (eg. see Willingale et al. 2003) and for mirror vignetting of the sky background signal, is measured to be 3.7 ± 0.1 MOS count s^{-1} deg^{-1}. This signal is substantially larger than that measured at high Galactic latitude in the MOS cameras consistent with the presence of the GRXE in the field of view for all the XGPS-I pointings. By integrating the *observed* hard band X-ray source counts the resolved sources

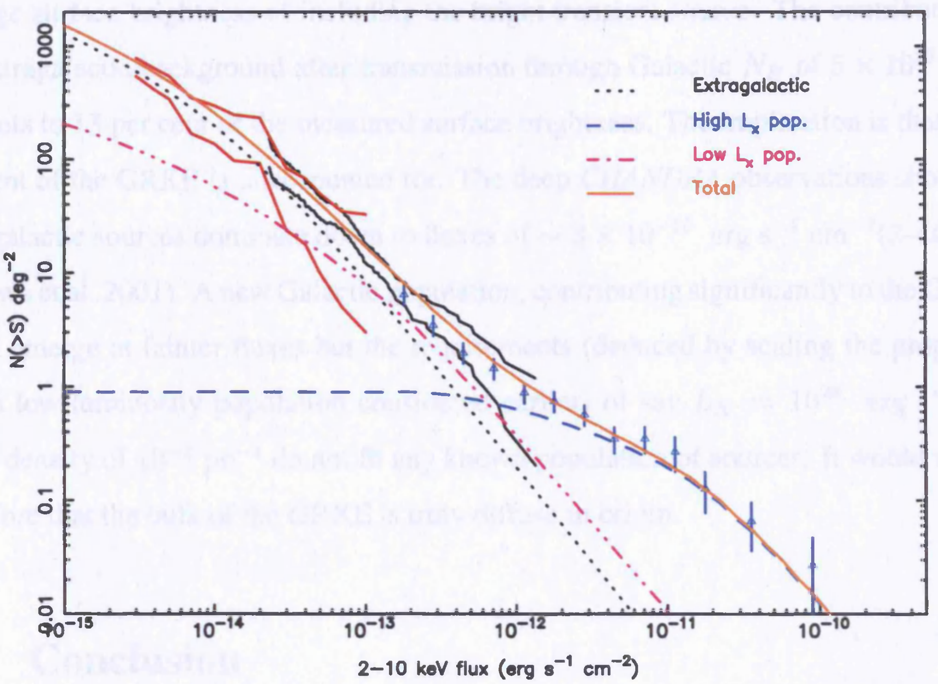

FIGURE 4.12. The measured 2–10 keV log N - log S relation compared with with the predicted contributions of various X-ray source populations (see the text).

with fluxes in the range 0.7 to 70 MOS count ks^{-1} (2–6 keV) (on-axis) are found to contribute 0.34 count s^{-1} deg^{-1}, *i.e.* 9% of the observed surface brightness.

Applying the same count-rate to flux conversion factor as used in §4.4.1, the *total* surface brightness of the GRXE corresponds to 0.96×10^{-10} erg s^{-1} cm^{-2} deg^{-2}in the 2–10 keV band. Earlier estimates put the value at 1.1 $\times10^{-10}$ erg s^{-1} cm^{-2} deg^{-2} (Ebisawa et al. 2001), 0.52 $\times10^{-10}$ erg s^{-1} cm^{-2} deg^{-2} (*ASCA* , Sugizaki et al. 2001), and 0.25 $\times10^{-10}$ erg s^{-1} cm^{-2} deg^{-2} (*RXTE* , Valinia & Marshall 1998), depending on the region of sky surveyed.

In Fig. 4.12 the Galactic contribution to the log N - log S curve is modelled in terms of high-luminosity and low-luminosity source populations. By integrating the two model curves over a flux range of 10^{-16} to 10^{-11} erg s^{-1} cm^{-2}, contributions of 2 per cent and 4 per cent are found for these two populations respectively. In the case of the X-ray binaries integrating the model log N - log S curve to higher fluxes produces a further 6 per cent contribution; coincidentally this roughly matches the effect on the average surface brightness of including the bright transient source. The contribution of the extragalactic background after transmission through Galactic N_H of 5×10^{22} cm^{-2} amounts to 13 per cent of the measured surface brightness. The implication is that ~ 80 per cent of the GRXE is unaccounted for. The deep *CHANDRA* observations show that extragalactic sources dominate down to fluxes of $\sim 3 \times 10^{-15}$ erg s^{-1} cm^{-2}(2–10 keV; Ebisawa et al. 2001). A new Galactic population, contributing significantly to the GRXE, might emerge at fainter fluxes but the requirements (deduced by scaling the properties of the low-luminosity population considered earlier) of say $L_X = 10^{28}$ erg s^{-1} and space density of 10^{-2} pc^{-3} do not fit any known population of sources. It would appear therefore that the bulk of the GRXE is truly diffuse in origin.

4.5 Conclusion

The XGPS-I programme, which covers approximately three square degrees of the Galactic Plane near $l = 20°$, has resulted in a catalogue containing over 400 discrete X-ray sources. The resulting X-ray source counts trace the source population down to a limiting flux of $\sim 2 \times 10^{-14}$ erg s^{-1} cm^{-2} in the 2–10 keV band at which point the source density is between 100–200 sources per square degree. Consistent with an earlier *CHANDRA* study, the source counts at this flux are probably dominated by extragalactic sources, despite the fact that the fluxes of extragalactic sources are significantly suppressed by absorption in the Galactic plane. However, the conclusion of the present work is that at fluxes above 10^{-13} erg s^{-1} cm^{-2} (2–10 keV) Galactic source populations do come to the fore.

The Galactic source population observed between 10^{-13} and 10^{-12} erg s^{-1} cm^{-2} could comprise largely CVs and RS CVn systems with X-ray luminosities in the range $10^{30} - 10^{32}$ erg s^{-1} but the details remain uncertain on the basis of the X-ray information alone. Extensive programmes to identify and characterise optical/infra-red counterparts are required, although this will be taxing given the high obscuration and high object density in the Galactic Plane.

Chapter 5

Diffuse Hard X-ray emission in the Galactic Plane

5.1 Overview

The focus of this chapter is split into the analysis of two distinct types of diffuse emission in the Galactic Plane. The first of these is the background hard X-ray flux which is distributed across a central region of the Galactic Plane generally referred to as the Galactic ridge. Secondly there are several patches of emission which stand out above the diffuse background and are correlated with known extended objects such as supernova remnants (SNRs) and HII regions. Analysis of these bright spots, hereafter referred to as extended rather than diffuse emission, is conducted using data from the cluster of XGPS observations centred on (l,b) $\sim$ (20°,0°), *i.e.* the same as those used for point source analysis in §4.

5.2 Diffuse Background Maps

Using the image creation processes outlined in §2, mosaiced images of the Galactic Plane, after point source exclusion, were produced in both the soft (0.4–2 keV) and hard

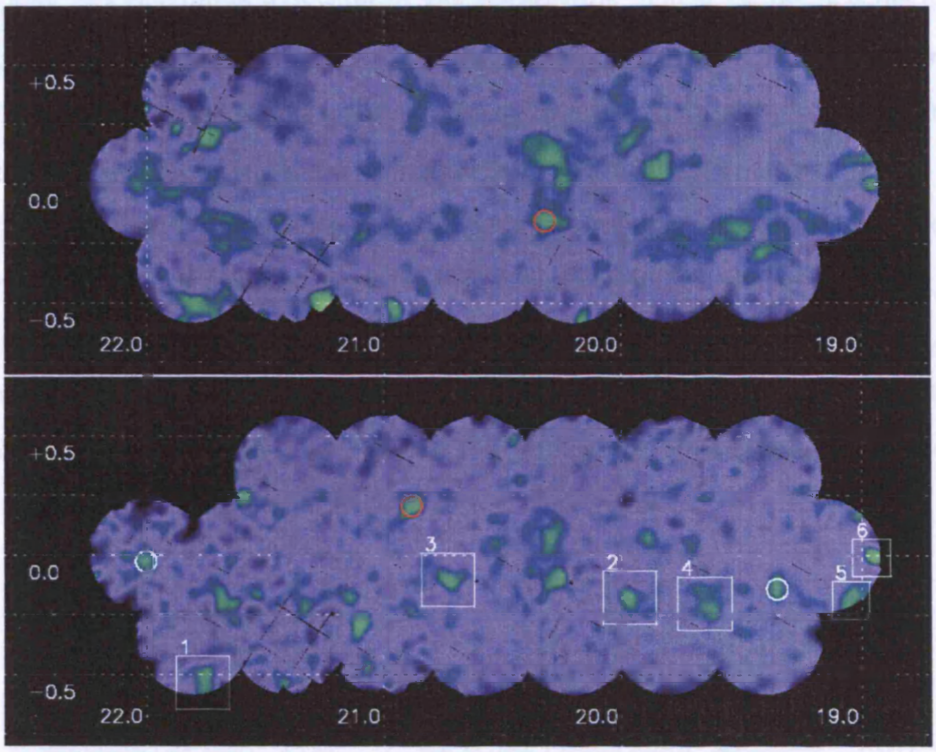

FIGURE 5.1. Diffuse background mosaics for both soft (top) and hard (bottom) energy bands. The non-sky background has been subtracted and the images have been corrected for the effect of vignetting and smoothed with a Gaussian function of width 1.3'. See text for references to highlighted features. Regions with < 1 ks of clean exposure are excluded.

(2–6 keV) energy bands. Although the focus of investigation is on the hard X-ray image, for comparison both are shown in Figure 5.1[1].

5.2.1 Extended Features

Several extended objects can clearly be seen in each image, standing out as green above a relatively flat blue background. Due to the short exposure times of each observation the background count rate is only $\sim 3 \times 10^{-3}$ cts ks^{-1} pixel^{-1}, or roughly 500 counts per ksec for each single MOS field of view in each energy band. Each image is normalised

[1]The observations XGPS 14 & XGPS 15 listed in Table 2.1 were too contaminated to yield useful diffuse data. However, where possible, data from recent re-scheduled observations are included in Figure 5.1 in order to make the images more comprehensive.

to 26.4 ks, the maximum exposure of any observation, which means that the number of background counts in each large white box (see Figure 5.1) is ~ 800. The number of counts above background in each box (*i.e.* the green patches) is typically ~ 500, although how many real source counts this corresponds to depends on the total exposure at that point. This means that there is significant potential for spurious features and therefore any extended emission region must be well correlated with a known extended object from another catalogue in order to be considered as potentially real. Although source masks were increased in size for particularly bright sources, each image still contains at least one bright spot which is probably due to the leakage of an underlying bright point source. These are highlighted with a red circle in each case.

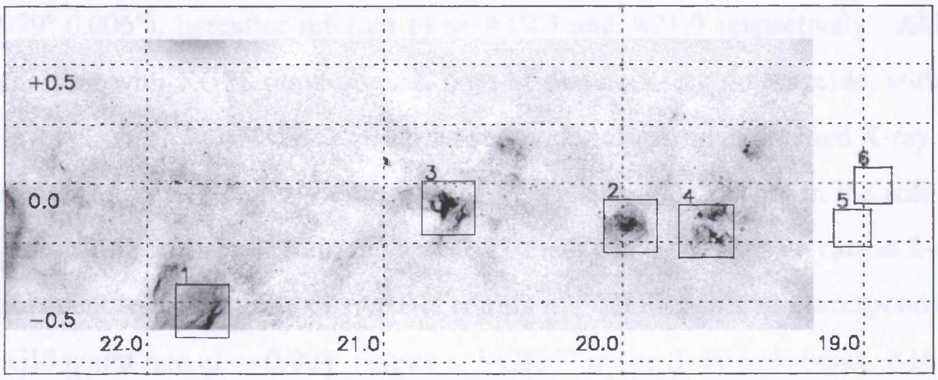

FIGURE 5.2. 20 cm (1.5 GHz) VLA radio data in the XGPS survey region. The border and coordinate grid are the same as those used for the X-ray maps, as are the numbered boxes.

The soft diffuse image, by the nature of Galactic absorption, represents local X-ray emission rather than features in the Galactic Plane. Perhaps for this reason the fluctuations in the diffuse emission are on a slightly larger angular scale across the field of view and foreground features are less prominent than in the hard diffuse image. Therefore the soft image in Figure 5.1 is included more for completeness than for study and the focus of analysis is instead placed on the hard image. In essence this represents the first "high" resolution image of the Galactic ridge. It is in this energy band that known (or as yet unknown) extended objects such as SNRs and HII regions are observable in the Galactic Plane. In the survey region shown at least six such objects are detected, highlighted in white boxes in Figure 5.1. By cross-correlating with high resolution 20 cm radio data, shown in Figure 5.2, we can identify two of these with Galactic SNRs (boxes 1 & 2 in Figure 5.1) and another two with HII regions (no.s 3 & 4). The remaining two are also probably HII regions although they fall outside the regime of the high resolution radio data The white circles are patches of emission that are positionally coincident with *ASCA* point sources but which have no point source counterpart in the XGPS catalogue.

ASCA 'Point' Sources

Of the nine sources from *ASCA* 's Galactic Plane survey (Sugizaki et al. 2001) which lie in the XGPS region, *XMM-NEWTON* counterparts are detected for all but two (see §4). These are AX_J182651-1206 (l,b $\sim$ 19.376°,-0.141°) and AX_J183114-0943 (l,b $\sim$ 21.979°,0.006°), hereafter referred to as A19.3 and A21.9 respectively. Although not coincident with XGPS point objects, both of these sources do coincide, within the *ASCA* error circle of 3', with small patches of extended emission in the hard X-ray image shown in Figure 5.1. Neither source shows any apparent flux excess in the soft X-ray image, indicating a hardness ratio of close to 1. Each patch contains an excess 2–6 keV flux equivalent to a count rate of $\sim$ 0.01 counts s^{-1} MOS^{-1} which corresponds to an *ASCA* GIS count rate of $\sim$ 0.004 counts s^{-1} GIS^{-1} in the 2–10 keV band. A19.3 is a soft source that is not detected in *ASCA* 's hard band and therefore it is highly unlikely that the patch of hard flux in Figure 5.1 has the same origin as this source. This is not a surprising anomaly however, as the region in question is located on the edges of two *XMM-NEWTON* observations and therefore has a low fraction of the total exposure time. Regions such as this, overlapping very small gaps in the survey area, are most sensitive to spurious bright spots caused by relatively small numbers of counts. In contrast A21.9 is very close to the centre of a fairly clean *XMM-NEWTON* exposure, XGPS 17, and therefore although the inferred count rate of the source is very similar to that of A19.3, the number of counts recorded is far higher ($\sim$ 200). The measured *ASCA* count rate for A21.9 is 0.0022 counts s^{-1} GIS^{-1}, *i.e.* within a factor of 2 of the predicted value from the excess flux in the *XMM-NEWTON* image. However A21.9 is also detected in the soft and medium energy bands of the *ASCA* survey, with in fact a very similar count rate in the 0.7–2 keV band. As no sufficiently bright point-like or extended source is present in the soft XGPS image there is no evidence other than positional coincidence to suggest that A21.9 is the *ASCA* source. If the *ASCA* source is indeed point-like then it must have been in a transient outburst state when observed by *ASCA* , otherwise it would certainly be detected in the XGPS.

In summary, of the patches of hard emission which seem to be coincident with *ASCA* 'point sources' not detected by XGPS, one (at l=19.3°) is very likely to be spurious due to spectral differences and the near-edge location, and the other (at l=21.9°) cannot be confidently identified with the *ASCA* source. Indeed the presence of similar patches of emission at other locations, which do not seem to coincide with any known X-ray object, indicates that it would not be surprising if this latter source was also a spurious fluctuation in the diffuse background.

HII regions

Using high resolution 20 cm radio data it is possible to identify at least two of the extended features in Figure 5.1 as HII regions. Figure 5.3 shows close-up images of the regions identified in Figure 5.1 as boxes 3 & 4. Radio contours are overlayed at intensities of 0.008, 0.010 & 0.015 Janskys respectively. Box 4 actually covers three HII regions, as resolved by radio data, however in X-ray terms only two distinct patches of emission can be seen and these are labelled 4a and 4b respectively, 4a being the brighter and larger of the two. Two other features in Figure 5.1 (boxes 5 & 6) may also correspond to HII regions which, although in areas not yet covered by the high resolution 1.5 GHz VLA survey data, can be seen in the 5 GHz (6cm) radio maps of Altenhoff et al. (1979). The estimated X-ray luminosities of the three HII regions which do have corresponding VLA data are given in Table 5.1. Distances used to calculate luminosity were derived from the line velocities (with respect to the local standard of rest) of Lockman (1989) and the Galactic rotation curve of Burton & Gordon (1978). This method necessarily yields two very different line-of-sight distances and for these calculations the lower value is used as it is unlikely that these sources are located on the far side of the Galactic disc.

This is not the first time that compact Galactic HII regions have been detected in the

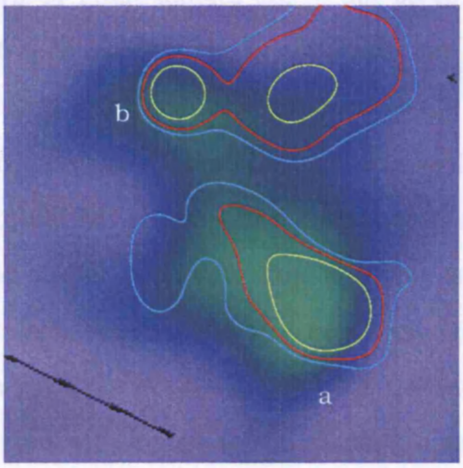

(a) H19.6-0.2

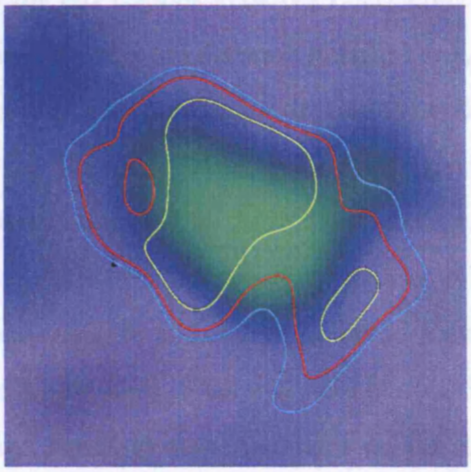

(b) H20.7-0.1

FIGURE 5.3. HII regions with 1.5 GHz radio contours plotted at 0.008 (blue), 0.010 (red) and 0.015 (yellow) Janskys.

X-ray band. Using data from the *CHANDRA* observatory Hofner et al. (2002) not only detected X-rays from the core of the W3 complex of massive star forming regions, but also were able to resolve most of the flux into point sources coincident with peaks in radio data. Several of these point sources were identified as early-type stars which are thus probably the ionising stars of the W3 core. Although the HII regions detected by *XMM-NEWTON* are not resolved into point sources, we are at least able to put a lower limit on the number of point sources that are required to produce the extended signal without attaining sufficient flux per source to be detected as individual sources. Using a hard band point source detection threshold of 10^{-3} cts^{-1} s^{-1} MOS^{-1} the minimum

Table 5.1. 2–6 keV count rates & additional information for HII regions.

Name	Box ref.	Count Rate [a]	Peak radio flux [b]	Distance / kpc	Log(L_x [c])
H20.7-0.1	3	28	2.84	4.6	33.2
H19.6-0.2a	4a	18	4.98	3.6	32.8
H19.6-0.2b	4b	6	1.0	4.5	32.5

[a] cts ksec^{-1} MOS^{-1} (2–6 keV)
[b] Janskys (based on 6cm data)
[c] erg s^{-1} (2–10 keV)

number of point sources are $\sim$ 30, 20 & 5 for HII regions H20.7-0.1, H19.6-0.2a & H19.6-0.2b respectively. Interestingly, two point sources are detected in H20.7-0.1, each consisting $\sim$ 15 counts in the hard band (*i.e.* just above detection threshold) and zero in the soft band. These do not necessarily lie within the HII region itself (given the size of the HII region and the number of sources detected by XGPS we would expect to find one or two point sources in this area). However the spectral hardness of both the sources does suggest that they may indeed coincide with the brightest of a number of stars responsible for ionising the surrounding medium. This will remain speculative until data with higher spatial resolution and/or signal to noise is obtained. As Hofner et al. (2002) used infrared counterparts to identify the W3 ionising stars, it is worthwhile to make a similar IR comparison with the *XMM-NEWTON* data. Figure 5.4 shows 8.3 micron images of the two HII regions taken from the mid-infrared MSX survey. Several point sources can clearly be seen in each image with particular evidence in H19.6-0.2 for coincidence with peaks in X-ray brightness. The combination of the radio and mid-infrared data confirm these as compact HII regions. A more detailed analysis of IR data could potentially highlight a link between the IR brightness and X-ray brightness, however for the purposes of this thesis it is sufficient to show that there is evidence for the presence of several ionising stars in the vicinity of each of the observed HII regions.

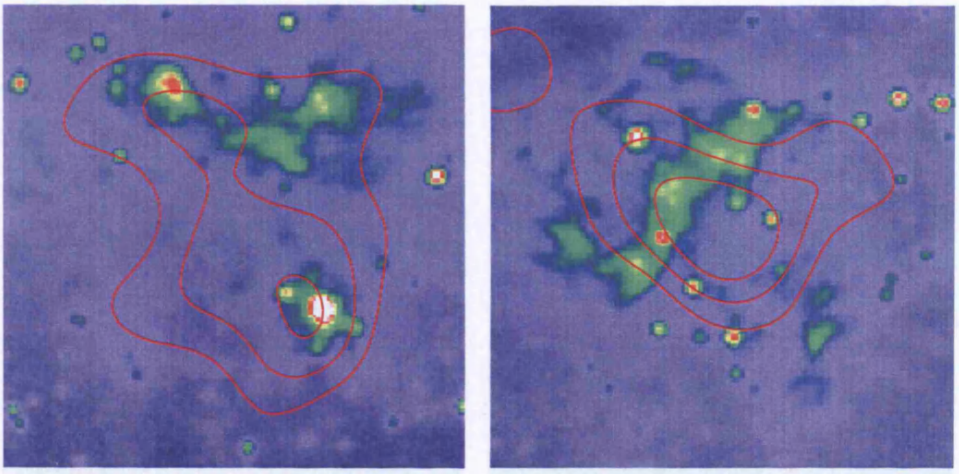

(a) H19.6-0.2 (b) H20.7-0.1

FIGURE 5.4. 8.3 μm images of two HII regions detected in XGPS. Each image is 13.3' square and 2–6 keV X-ray contours have been overlayed.

SNRs

There are two known Galactic SNRs which fall within the current XGPS region (Green 1988, Green 1996). Both of these are visible as extended regions in Figure 5.1 (labeled as boxes 1 and 2) and, unsurprisingly, also in Figure 5.2. These two objects will be referred to hereafter as G20.0-0.2 and G21.8-0.6 (the latter is also known as Kes 69). The detection of G20.0-0.2 is the first time this particular SNR has been seen in the X-ray wave band. In contrast G21.8-0.6 was observed by the *Einstein* X-ray satellite over two decades ago (Seward 1990). Figure 5.5 shows zoomed-in smoothed images of the two remnants with radio contours overlayed at 0.008, 0.010 & 0.015 Janskys (1.5 GHz) respectively. Depiction of the full extent of G21.8-0.6 is hampered by the lack of both XGPS and radio coverage in the desired region.

Table 5.2 gives a summary of the physical parameters for each SNR, including X-ray and radio fluxes and the estimated distance to the remnant. In the case of G20.0-0.2 the distance estimate comes from the kinematical distance to a nearby OH maser, rather than the remnant itself (Becker & Helfand 1985). The lower limit put on the distance to G21.8-0.6 has been obtained from H_2CO absorption studies (Wilson 1972). Luminosities are estimated using the distance stated and, unlike the HII regions where

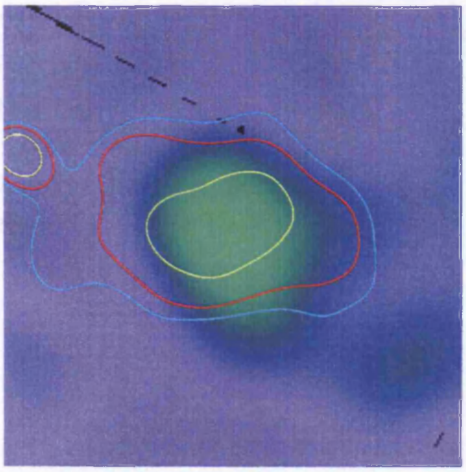

(a) G20.0-0.2

(b) G21.8-0.6

FIGURE 5.5. SNRs with 1.5 GHz radio contours plotted at 0.008 (blue), 0.010 (red) and 0.015 (yellow) Janskys.

an absorption column density of 10^{22} cm^{-2} is assumed, the count rate to flux conversion factor is based on physical models derived from spectral fits. The X-ray spectra of the SNRs are shown in Figures 5.6 & 5.7. Both are fitted with an absorbed power law, although very different parameters are derived from the fits. G20.0-0.2 has a power law slope of $2.1^{+1.1}_{-0.6}$ (90% errors), similar to the spectrum of the Crab SNR (Willingale et al. 2001) and other Crab-like remnants (Asaoka & Koyama 1990), and an absorbing column of $4.3^{+3.2}_{-1.1} \times 10^{22}$ cm^{-2}. By comparison G21.8-0.6 has an extremely steep but poorly constrained slope of $3.8^{+1.2}_{-1.0}$ and an absorbing column of $2.6^{+1.0}_{-1.0} \times 10^{22}$ cm^{-2}. The poor statistics do not allow for much emphasis to be placed on the difference in spectral slope. However the relatively low absorption present in the spectrum of G21.8-0.6 is surprising as it is at roughly the same longitude as G20.0-0.2, but apparently further away. This is not merely a feature resulting from the potentially spuriously steep slope of the remnant as fixing the slope at 2.0 in fact reduces the column density to less than 10^{22} cm^{-2}. This may be an indication that G20.0-0.2 is in fact more distant than the OH maser it is associated with, or, more probably, a reflection of the great uncertainty in the parameters due to the poor signal to noise in each case.

Table 5.2. 2–6 keV count rates and additional information for the two SNRs.

Name	Box ref.	Count Rate [a]	Peak radio flux [b]	Distance / kpc	Log(L_x [c])
G20.0-0.2	2	20	1.2	4.0	32.9
G21.8-0.6	1	21	2.0	>6.3	>33.1

[a] cts ksec^{-1} MOS^{-1} (2–6 keV)
[b] Janskys (based on 6cm data)
[c] erg s^{-1} (2–10 keV)

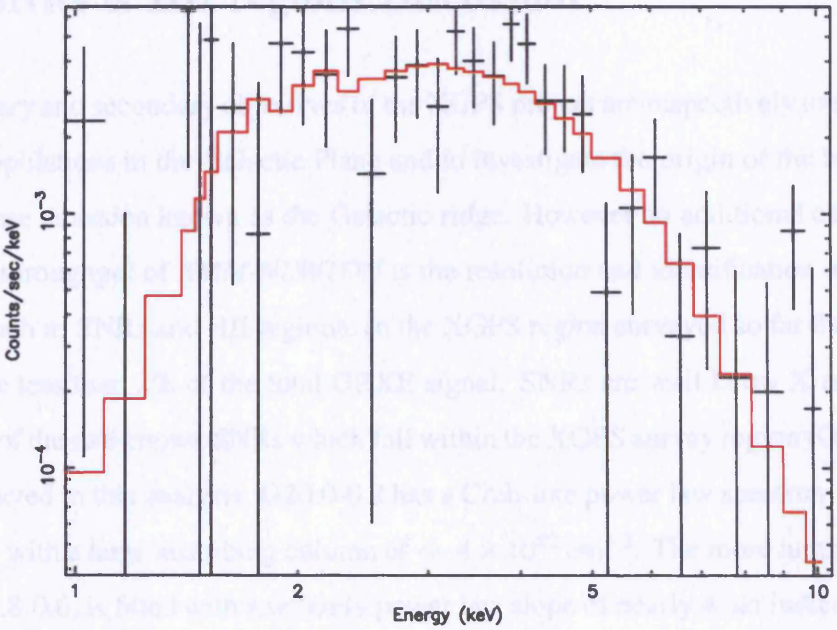

FIGURE 5.6. Spectrum of SNR G20.0-0.2. The model plotted is a power law with a spectral index of 2.1 and an absorbing column of 4.3×10^{22} cm^{-2}.

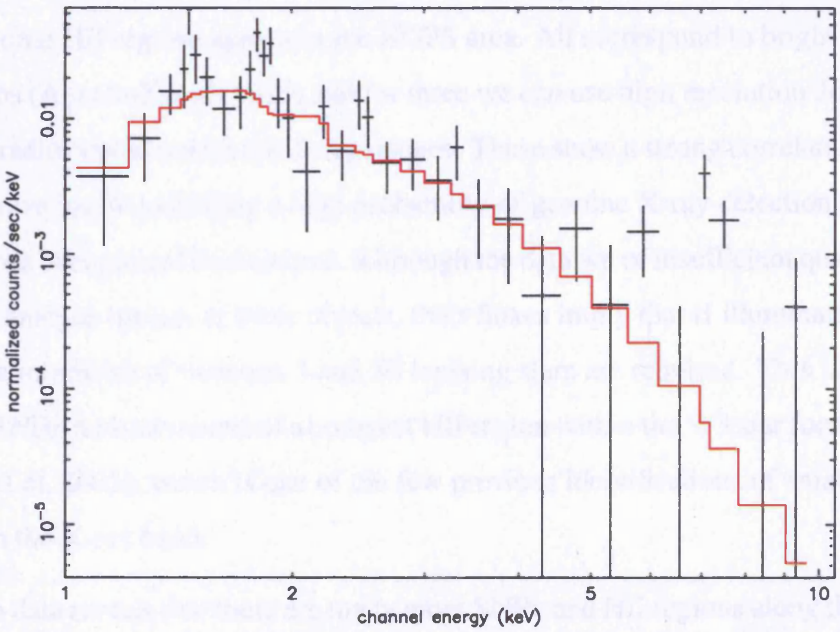

FIGURE 5.7. Spectrum of SNR G21.8-0.6 fitted with an absorbed power law with Γ=3.8 and N_H=2.6 $\times$ 10^{22} cm^{-2}.

5.3 SNRs & HII regions:Discussion

The primary and secondary objectives of the XGPS project are respectively to study point source populations in the Galactic Plane and to investigate the origin of the background hard diffuse emission known as the Galactic ridge. However an additional capability of the large throughput of *XMM-NEWTON* is the resolution and identification of extended objects such as SNRs and HII regions. In the XGPS region surveyed so far these objects contribute less than 2% of the total GRXE signal. SNRs are well know X-ray emitters and both of the two known SNRs which fall within the XGPS survey region (Green 1996) were detected in this analysis. G20.0-0.2 has a Crab-like power law spectrum of spectral index 2.1 with a large absorbing column of $\sim 4 \times 10^{22}$ cm^{-2}. The more luminous of the two, G21.8-0.6, is fitted with a unlikely power law slope of nearly 4, an indication of the limitations imposed by the poor signal to noise in the spectrum.

A less anticipated class of extended objects detected in the XGPS is that of HII regions. These are clouds of ionised gas which are often associated with star formation. Five potential HII regions appear in the XGPS area. All correspond to bright features in radio maps (Altenhoff et al. 1979) and for three we can use high resolution 20cm data to compare radio contours with the X-ray images. These show a strong correlation between the two wave bands indicating a high probability of genuine X-ray detection rather than the spurious background fluctuations. Although the data are of insufficient quality to produce and analyse spectra of these objects, their fluxes imply that if illuminated by point sources, a minimum of between 5 and 30 ionising stars are required. This is consistent with *CHANDRA* observations of a compact HII region within the W3 star forming region (Hofner et al. 2002), which is one of the few previous identifications of small scale HII regions in the X-ray band.

Radio data reveals that there are many more SNRs and HII regions along the Galactic Plane. *XMM-NEWTON* has demonstrated the ability to see in X-rays nearly all the bright extended radio objects visible in Figure 5.2, thus we can expect that the continuation of the XGPS towards the Galactic Centre will prove equally successful at detecting such objects, providing useful X-ray properties for comparison with other wave bands.

5.4 GRXE Spectrum

In order to investigate the variation of the GRXE with both longitude and latitude, the spectra of observations from on and off the Galactic Plane are analysed. Figure 5.8 shows the positions of all the observations used, it is noteworthy that the observations GC 3 & GC 7 are close to GC 1 but are included because they contain the nebulae Sgr B and Sgr C respectively. The additional contribution these nebulae make to the X-ray spectra is discussed in §5.5.

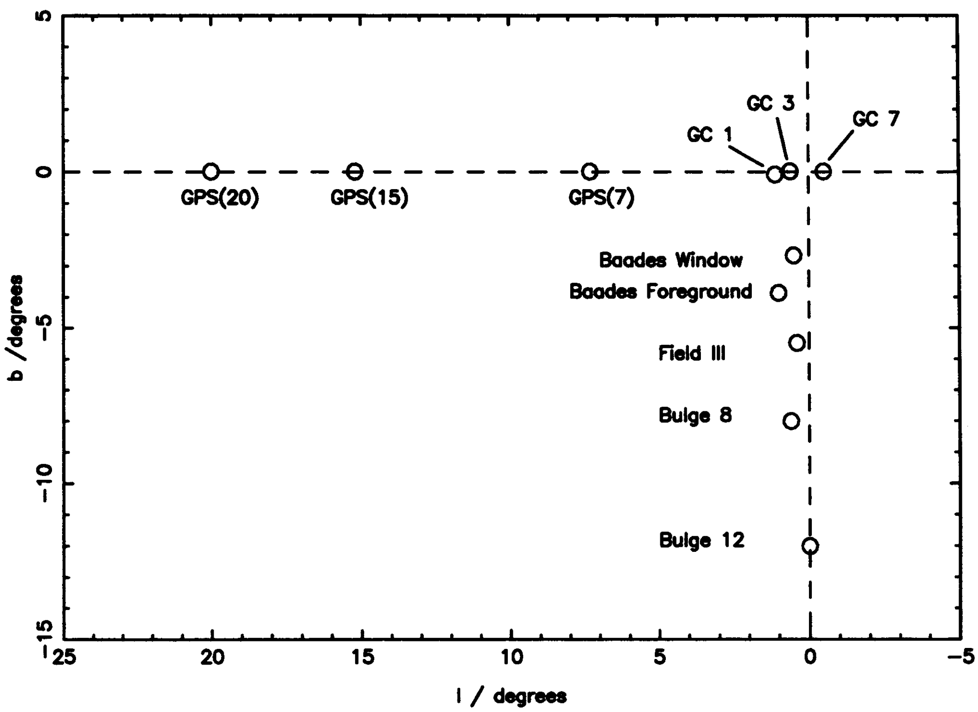

FIGURE 5.8. Diagram showing the relative locations, in Galactic coordinates, of the different regions analysed in this chapter. Each circle corresponds to a single spectrum rather than an observation as some spectra are accumulated using data from several different, but overlapping, pointings.

All spectra have several model components in common, such as extragalactic power law (EPL), instrument fluorescence lines *etc.* . In order to illustrate the relative contributions to the total model, the different components in each spectrum are plotted separately. Table 5.3 gives a key to the colours used to represent each separate model component. For the purpose of outlining the spectral fitting process the data sets are subdivided into three groups as follows:

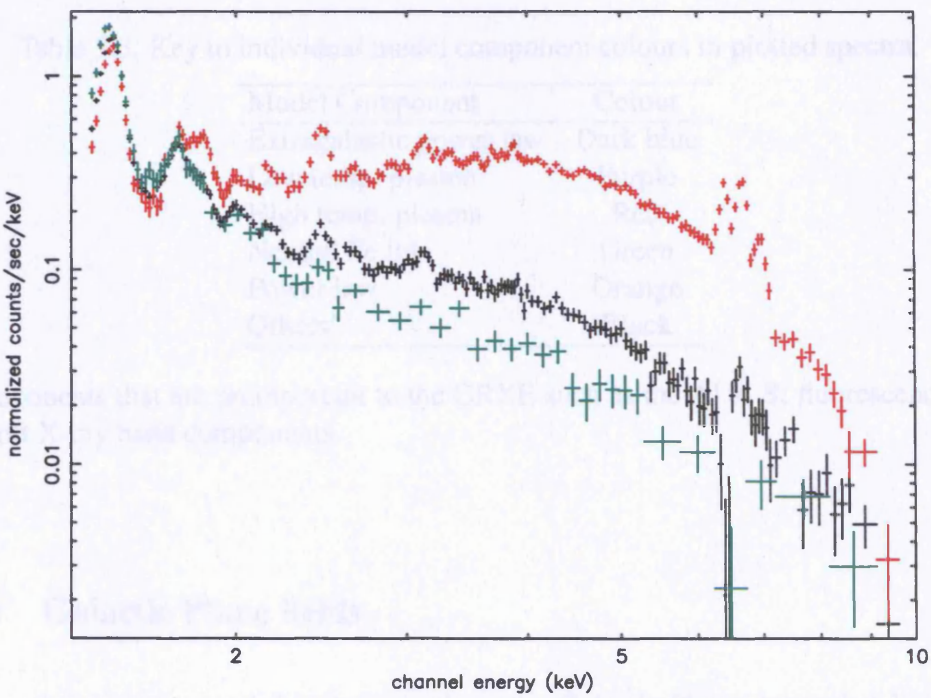

FIGURE 5.9. Comparative plot showing the variation in count rate in three distinct directions. The spectra plotted are as follows:*black:*GPS (20°) in the Galactic Plane, *red:*GC 7 in the Galactic Centre, and *green:*Baades Window ~ 4°below the Galactic Centre.

- Three summed spectra from Galactic Plane observation clusters centred at l=20°, l=15°& l=7°respectively (identical to those analysed in §3.3).
- Three Galactic Centre observations:GC 1, GC 3 & GC 7, all located within ~ 1°of the GC.
- Four southern bulge fields:Baades Window, Baades Foreground, Bulge 8 & Field III, located below the Galactic Centre (Bulge 12 does not have a significant hard flux excess).

Figure 5.9 shows an example spectrum from each of these groups, illustrating the large variation in hard count rate.

Table 5.3. Key to individual model component colours in plotted spectra.

Model Component	Colour
Extragalactic power law	Dark blue
Low temp. plasma	Purple
High temp. plasma	Red
Neutral Fe line	Green
Power law	Orange
Others*	Black

* Components that are unimportant to the GRXE such as the Al & Si fluorescence lines and soft X-ray band components.

5.4.1 Galactic Plane fields

Three separate clusters of observations along the Galactic Plane, located at longitudes 20°, 15°& 7°, were fitted independently to highlight any potential longitudinal dependence of GRXE. The energy band used for these (and all other fits in this chapter) is 1.4–10.0 keV which includes the strong, unsubtracted, fluorescence lines at $\sim$ 1.5 keV (Al) and $\sim$ 1.8 keV (Si) respectively. The resulting models include components which only contribute significantly at lower energies and therefore these parameters are frozen following spectral fitting in a soft energy band (see §3). In addition to these softer components each model includes an absorbed power law to represent extragalactic flux and two thermal components, at very different temperatures, which each produce both continuum and line emission. Silicon and Sulphur elemental abundances were allowed to vary (with respect to solar) in the low temperature plasma component as emission lines from the Hydrogen-like and Helium-like ions of both of these are visible in the spectra. Helium-like Argon emission is also visible but at too weak a level to allow for the relative abundance to be constrained. These spectra are shown in Figure 5.10 and the parameters for each model component are summarised in Table 5.4. One problem which occurs in this energy band is the background subtraction of a neutral Fe-K$_\alpha$ line at 6.4 keV. As the spatial distribution of this instrumental line is not constant (see §2.7.2), the line is over-subtracted when the required background scaling is applied. To prevent this affecting the

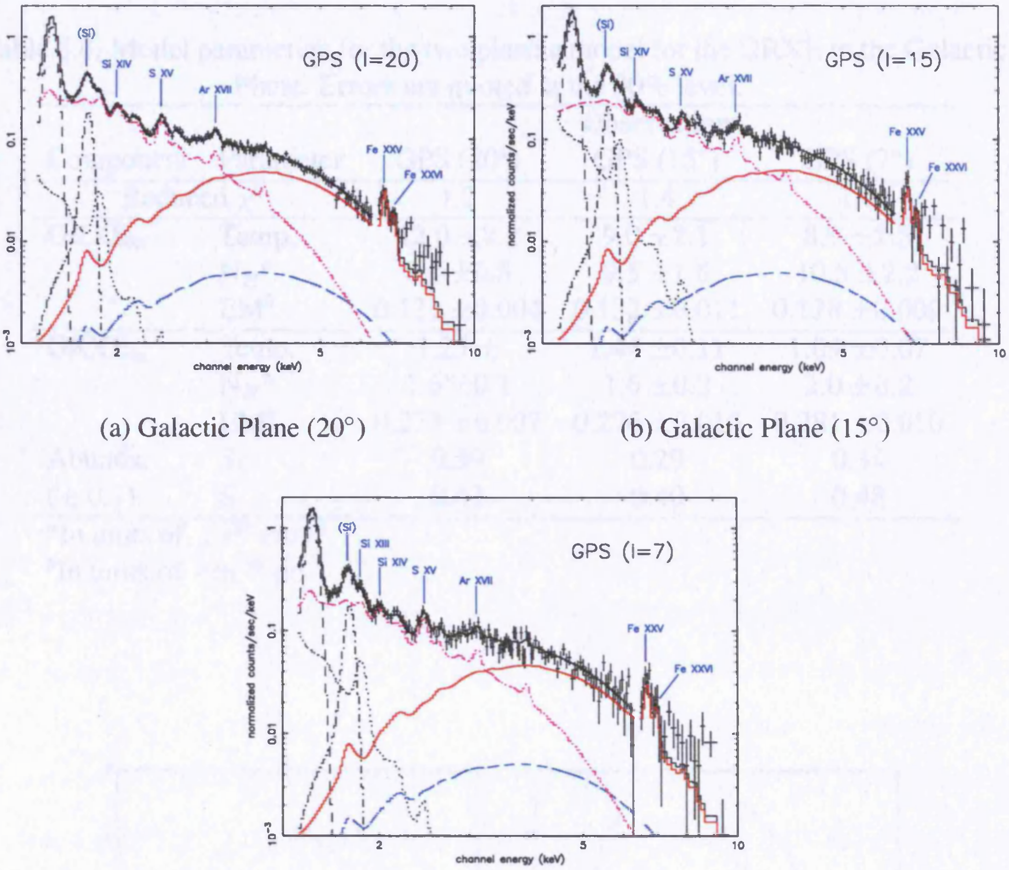

(a) Galactic Plane (20°) (b) Galactic Plane (15°)

(c) Galactic Plane (7°)

FIGURE 5.10. Spectral fits for Galactic Plane at 20°, 15°& 7deg. The separate components are shown individually to illustrate the contribution of each to a particular energy band, see Table 5.3 for key to colours/components.

spectral fits, several data points around this line were excluded from the spectra.

The temperature of the hotter thermal plasma given in Table 5.4 is largely constrained by the relative strengths of the emission lines from highly ionised iron at $\sim$ 6.8 keV. The strongest of these is from Helium-like iron (Fe XXV) at 6.7 keV, while slightly less prominent is a Hydrogen-like iron (Fe XXVI) at 6.9 keV. In broad terms a higher ratio of Hydrogen-like to Helium like emission implies a hotter plasma temperature. As the temperature of the hot plasma (if indeed this is the correct physical model) is very important in determining the nature of the GRXE, especially with regards to its tight confinement to the Galactic Plane, the spectra were re-fitted in a narrower energy band

Table 5.4. Model parameters for the two plasma model for the GRXE in the Galactic Plane. Errors are quoted at the 90% level.

Component	Parameter	Observation GPS (20°)	GPS (15°)	GPS (7°)
	Reduced χ^2	1.2	1.4	1.0
GRXE$_{hi}$	Temp.	12.0 ±2.2	9.0 ±2.1	8.9 ±2.5
	N$_H$^{a}	8.1 ±0.8	9.5 ±1.6	10.5 ±2.2
	EM^b	0.121 ±0.004	0.132 ±0.011	0.128 ±0.009
GRXE$_{lo}$	Temp.	1.25 ±	1.44 ±0.11	1.09 ±0.07
	N$_H$^{a}	1.6 ±0.1	1.6 ±0.2	2.0 ±0.2
	EM^b	0.273 ±0.007	0.276 ±0.016	0.281 ±0.010
Abunds.	Si	0.39	0.29	0.34
(± 0.1)	S	0.43	0.40	0.48

^{a}In units of 10^{22} cm^{-2}
^{b}In units of cm^{-6} pc

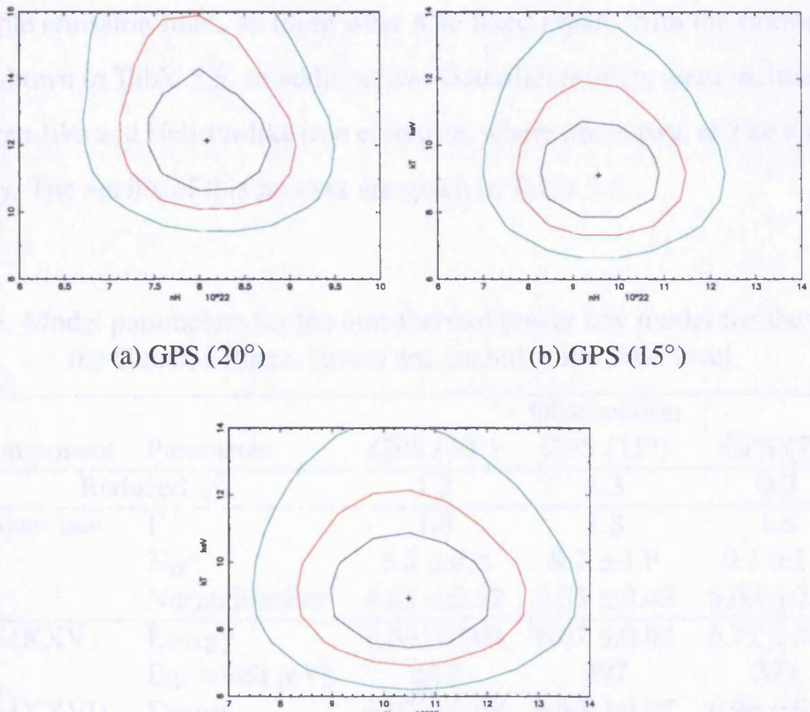

(a) GPS (20°) (b) GPS (15°)

(c) GPS (7°)

FIGURE 5.11. Temperature vs. N_H contour plots for hot GRXE plasma at three different longitudes along the Galactic Plane. Contours are plotted at the 68%, 90% and 99% confidence levels.

(3–10 keV) with only the hot plasma parameters free to float. In all fits the normalisation of the EPL is fixed at 9 photons keV^{-1} s^{-1} cm^{-2} sr^{-1} (normalised at 1 keV), which is the figure quoted by Lumb et al. (2002). The resulting contour plots of these fits, showing the effect on χ^2 of variation in both N_H and temperature are shown in Figure 5.11.

Non-thermal model

A non-thermal model was also used to fit each spectrum to establish whether this can provide an alternative to the thermal model. The spectra were all re-fitted with the high temperature plasma component replaced with a simple absorbed power law. It was found that allowing both the power law slope and the column density to vary resulted in unphysical models and therefore the slope, Γ, was fixed at 1.8 (Valinia & Marshall 1998). It was also found that the parameters of the lower temperature plasma were almost entirely unaffected by the re-fitting process, presumably due to the presence of several distinct and inflexible emission lines, so these were also fixed (apart from the normalisation) at the values shown in Table 5.5. In addition two Gaussian profiles were included to model the Hydrogen-like and Helium-like iron emission, where necessary, at 7 keV and 6.7 keV respectively. The results of this process are given in Table 5.5.

Table 5.5. Model parameters for the non-thermal power law model for the GRXE in the Galactic Plane. Errors are quoted at the 90% level.

Component	Parameter	Observation GPS (20°)	GPS (15°)	GPS (7°)
Reduced χ^2		1.2	1.3	0.9
Power law	Γ	1.8	1.8	1.8
	N_H[a]	8.2 ±0.4	9.7 ±1.0	9.1 ±1.0
	Normalisation[c]	4.81 ±0.22	5.35 ±0.48	5.00 ±0.50
Fe (XXV)	Energy	6.64 ±0.04	6.67 ±0.03	6.71 ±0.04
	Eq. width (eV)	223	397	371
Fe (XXVI)	Energy	6.97 ±0.08	6.95 ±0.07	6.96 ±0.08
	Eq. width (eV)	161	78	119

[a]In units of 10^{22} cm^{-2}
[b]In units of cm^{-6} pc
[c] 10^{-3} photons keV^{-1} s^{-1} cm^{-2} at 1 keV

5.4.2 Galactic Centre fields

Spectroscopic data were analysed from three locations close to the Galactic Centre. Unlike the Galactic Plane spectra, where due to short exposure times data from several observations were summed in each direction, each spectrum corresponds to a single *XMM-NEWTON* observation. Each model contains identical to those used for the Galactic Plane fields, *i.e.* EPL, two thermal plasmas, fixed soft components and fluorescence lines. In addition an extra emission line component was required in each case to account for the presence of neutral iron at 6.4 keV. This feature is present in spite of the moderate over-subtraction of background data at this energy which affects the Galactic Plane

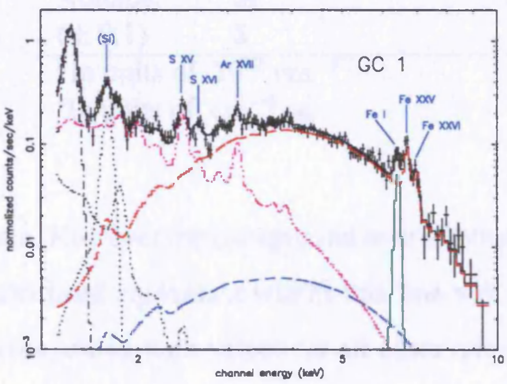

(a) GC 1

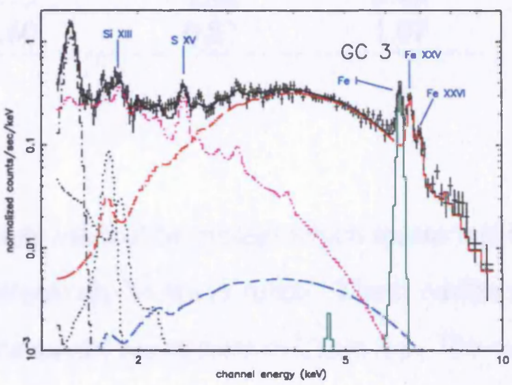

(b) GC 3

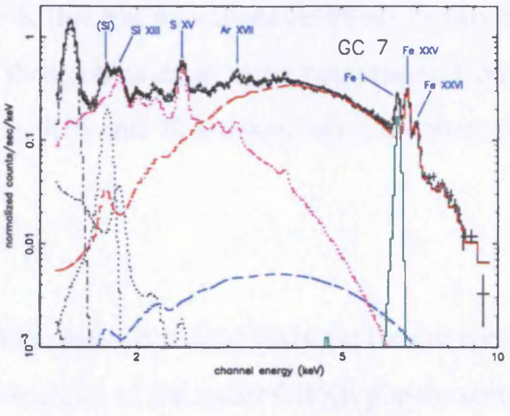

(c) GC 7

FIGURE 5.12. Spectral fits for three Galactic Centre observations. The separate components are shown individually to illustrate the contribution of each to a particular energy band, see Table 5.3 for key to colours/components.

Table 5.6. Model parameters for the two plasma model for the GRXE in the Galactic Centre. Errors are quoted at the 90% level.

Component	Parameter	GC 1	GC 3	GC 7
			Observation	
Reduced χ^2		1.4	1.3	1.7
GRXE$_{hi}$	Temp.	8.5 $\pm$1.0	7.9 $\pm$0.7	8.4 $\pm$0.4
	$N_H{}^a$	9.0 $\pm$1.9	10.4 $\pm$0.7	10.2 $\pm$0.3
	EM^b	0.372 $\pm$0.010	1.00 $\pm$0.02	1.08 $\pm$0.01
Neutral Fe	Energy	6.41 $\pm$0.05	6.38 $\pm$0.02	6.40 $\pm$0.02
	Eq. width (eV)	146	312	169
GRXE$_{lo}$	Temp.	1.32 $\pm$0.12	0.95 $\pm$0.06	0.76 $\pm$0.07
	$N_H{}^a$	1.8 $\pm$0.3	2.9 $\pm$0.2	4.5 $\pm$0.3
	EM^b	0.167 $\pm$0.018	0.730 $\pm$0.040	2.11 $\pm$0.70
Abunds.	Si	0.75	0.42	0.44
($\pm$ 0.1)	S	1.60	0.87	1.07

^{a}In units of 10^{22} cm^{-2}
^{b}In units of cm^{-6} pc

data. However the background over-subtraction will still be present which means that the calculated equivalent widths this line will effectively be lower limits. These widths are given, along with values for all other relevant model parameters in Table 5.6. The temperature of the hotter plasma component was derived using the same method as with the Galactic Plane observations, *i.e.* re-fitting in a narrower energy band. The added complication of the neutral Fe-K line has no noticeable effect on this process so the results are directly comparable to those obtained at larger longitudes. Contour plots at constant χ^2 values representing 68%, 90% and 99% confidence are shown in Figure 5.13.

Non-thermal model

As with the Galactic Plane fields the three Galactic Centre spectra were re-fitted with a non-thermal power law in place of the hotter GRXE plasma component. Again the slope was fixed at 1.8 so that a better constraint could be placed on the column density in front of the emission. The results of these alternative fits are shown in Table 5.7.

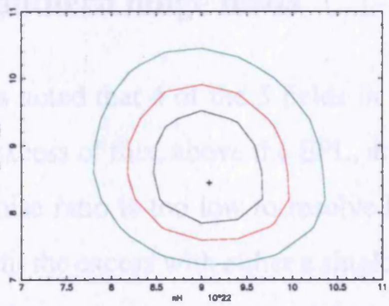

(a) GC 1

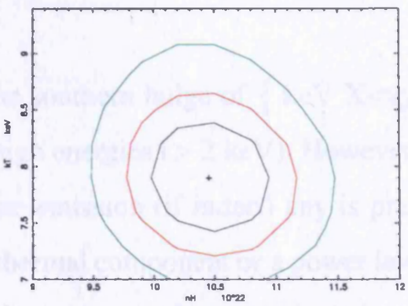

(b) GC 3

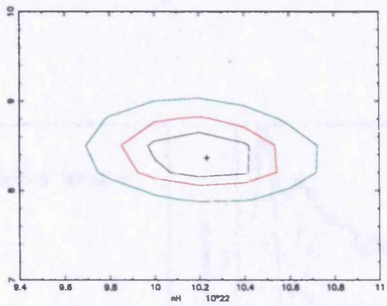

(c) GC 7

FIGURE 5.13. Temperature vs. N_H contour plots for hot GRXE plasma in 3 Galactic Centre fields. Contours are plotted at the 68%, 90% and 99% confidence levels.

Table 5.7. Model parameters for the non-thermal power law model for the GRXE in the Galactic Centre. Errors are quoted at the 90% level.

		Observation		
Component	Parameter	GC 1	GC 3	GC 7
Reduced χ^2		1.2	1.1	1.5
Power law	Γ	1.8	1.8	1.8
	N_H[a]	8.8 ±0.5	10.4 ±0.6	10.1 ±0.2
	Normalisation[c]	14.2 ±0.6	36.3 ±1.1	38.8 ±0.5
Fe (XXV)	Energy	6.66 ±0.02	6.67 ±0.02	6.67 ±0.01
	Eq. width (eV)	274	251	267
Fe (XXVI)	Energy	6.94 ±0.03	6.98 ±0.03	6.98 ±0.02
	Eq. width (eV)	160	143	152

[a] In units of 10^{22} cm^{-2}

[b] In units of cm^{-6} pc

[c] 10^{-3} photons keV^{-1} s^{-1} cm^{-2} at 1 keV

5.4.3 Southern bulge fields

In §3 it was noted that 4 of the 5 fields in the southern bulge of $\frac{3}{4}$ keV X-ray emission exhibit an excess of flux, above the EPL, at high energies (> 2 keV). However, since the signal to noise ratio is too low to resolve line emission (if indeed any is present), it is possible to fit the excess with either a single thermal component or a power law. It is also possible to fit a two temperature model, similar to that used to model in-plane emission, however the data are insufficient to adequately separate the components and therefore

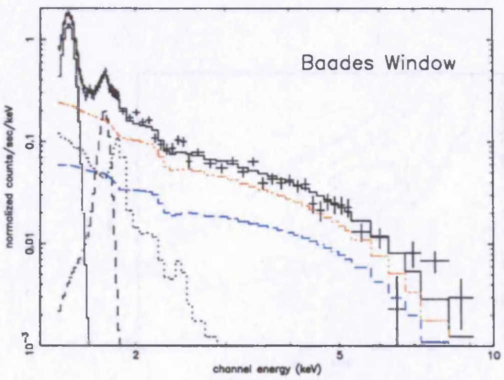

(a) Baades Window

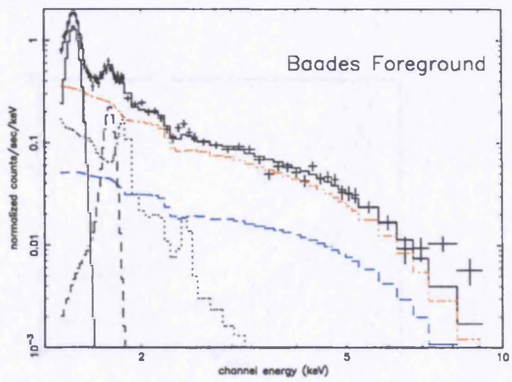

(b) Baades Foreground

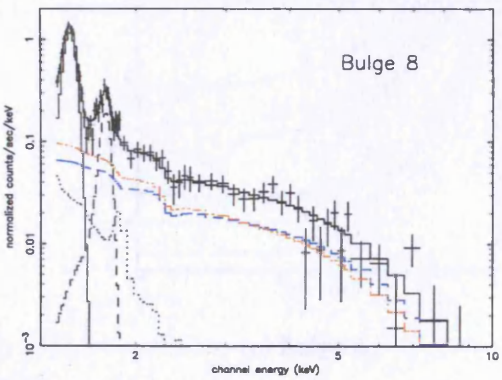

(c) Bulge 8

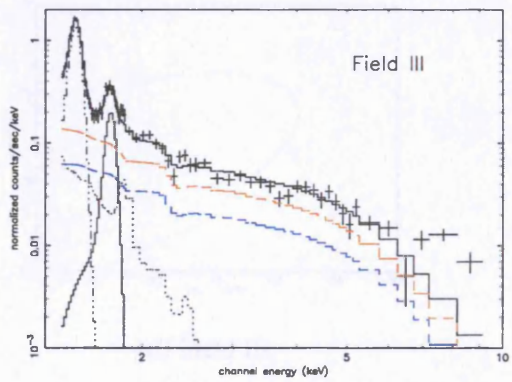

(d) Field III

FIGURE 5.14. Spectral fits for four observations at varying latitudes south of the Galactic Centre. Different model components are plotted separately to illustrate the relative contributions of each in a given energy range, see Table 5.3 for key to colours/components.

this technique can be regarded as over-fitting.

Table 5.8 lists the parameters for both thermal and non-thermal models of the hard flux excess. The featureless nature of the data leads to poor constraints on the values, especially for the thermal models. In the case of Field III the data are insufficient to place even an upper limit on the temperature of a plasma model, hence no adequate spectral fit could be obtained. The correlation of the principle parameter of each model (Γ for the power law & temperature for the plasma) with absorption varied considerably between observations and therefore a range of values were considered to demonstrate the dependence. The contour plots resulting from this analysis are shown in Figures 5.15 and 5.16.

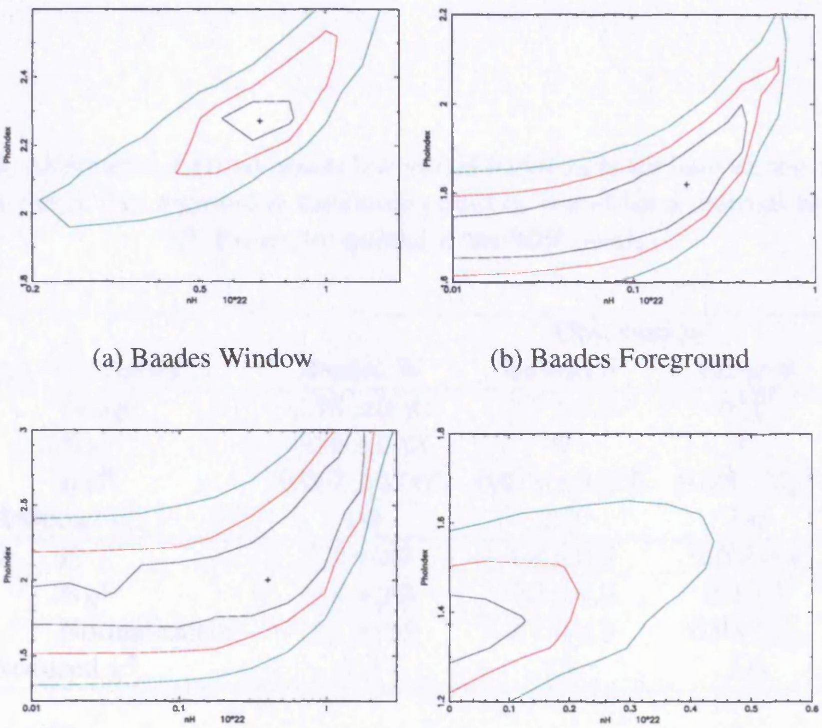

(a) Baades Window (b) Baades Foreground

(c) Bulge 8 (d) Field III

FIGURE 5.15. Contour plots showing the variation of power law index with absorption column. There is a strong correlation between the parameters which hampers the identification of a best-fit scenario. Contours are plotted at 68%, 90% and 99% confidence intervals.

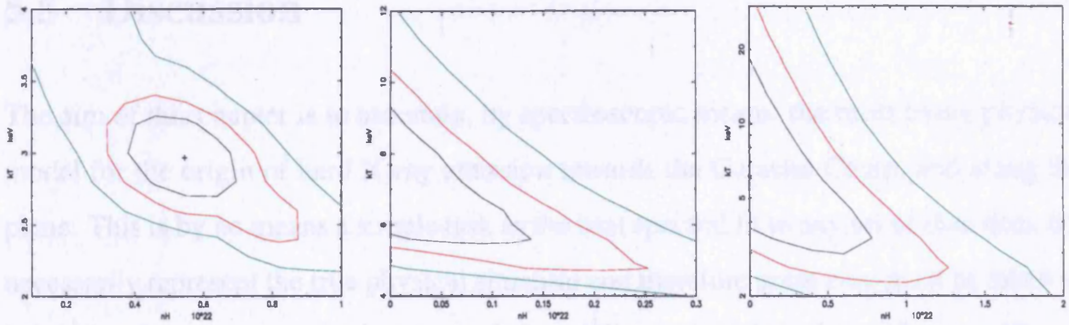

(a) Baades Window (b) Baades Foreground (c) Bulge 8

FIGURE 5.16. Contour plots showing the correlation of plasma temperature with absorption column. Contours are plotted at 68%, 90% and 99% confidence intervals. Field III is absent because the data were insufficient to constrain the plasma temperature.

Table 5.8. Alternative thermal/power law model parameters for hard excess in southern bulge fields. No reasonable minimum could be found for a thermal fit to Field III. Errors are quoted at the 90% level.

		Observation			
Component	Parameter	Baades W	Baades F	Bulge 8	Field III
Thermal	Temp.	2.95 ±0.40	7.7 ±2.5	6^{+20}_{-3}	-
	$N_H{}^a$	0.55 ±0.28	0	0	-
	EM^b	0.067 ±0.005	0.071 ±0.005	$0.020^{+0.013}_{-0.003}$	-
	Reduced χ^2	1.4	1.9	1.0	-
Power law	Γ	2.3 ±0.2	1.8 ±0.2	2.0 ±0.4	1.35 ±0.15
	$N_H{}^a$	0.7 ±0.3	0.2 ±0.2	$0.4^{+2.0}_{-0.4}$	0
	Normalisation^c	3.1 ±0.6	2.7 ±0.9	$0.93^{+5.3}_{-0.36}$	0.76 ±0.25
	Reduced χ^2	1.5	1.8	1.0	1.9

^{a}In units of 10^{22} cm^{-2}
^{b}In units of cm^{-6} pc
^{c} 10^{-3} photons keV^{-1} s^{-1} cm^{-2} at 1 keV

5.5 Discussion

The aim of this chapter is to ascertain, by spectroscopic means, the most likely physical model for the origin of hard X-ray emission towards the Galactic Centre and along the plane. This is by no means a simple task as the best spectral fit to any set of data does not necessarily represent the true physical situation and therefore great care must be taken in balancing the separate considerations of plausibility and statistical significance. This is especially relevant to diffuse emission where the signal to noise quality of the data may be insufficient to distinguish between more than one physical model. The focus of the discussion below is therefore on the very prominent stripe of emission mapped originally by *EXOSAT* , however consideration is also given to the off-plane fields with regards to whether or not the excess flux seen in these observations is related to the GRXE itself.

5.5.1 A note on absorption

A key feature of this analysis is the constraints placed on Galactic absorption by the spectral modelling process. Whether the source of the GRXE is thermal or non-thermal it is a prerequisite that a large amount of absorbing material is present in front of the source of the emission, otherwise the softer end of the spectrum would contain a significantly higher level of flux than is observed. The total Galactic HI column can be deduced by various means including Lyman-alpha studies and observations of the 21cm fine structure line of atomic Hydrogen. These techniques consistently estimate a total Galactic column density towards the Galactic Plane, ranging from l=20°to the Galactic centre, of $1 - -2 \times 10^{22}$ cm^{-2}. This figure is significantly lower than those derived from spectral fitting along the plane and in the Galactic Centre. Therefore, if the spectral fits are to be believed, additional absorbing material must be present.

The most likely cause of this additional absorption is neutral molecular Hydrogen bound within extensive clouds along the Galactic Plane. The presence of these clouds result in the under-estimation of the total column density by an as yet unknown factor (see Morrison & McCammon 1983 for HI absorption cross-section). Dame et al. (2001) have constructed detailed maps of these molecular clouds using carbon monoxide as a tracer. Although these maps reach saturation point at the Galactic centre, it is can be inferred that the column density of molecular Hydrogen (N_{H_2}) ranges from $\sim 2 \times 10^{22}$ cm^{-2}, at l ~20°, to nearer $\sim 5 \times 10^{22}$ cm^{-2} at the Galactic Centre. These values of course need to be corrected for the relative photo-electric cross-sections of HI and H_2 and this process is slightly problematic as the ratio varies as a function of energy. At low energies the cross-section of molecular Hydrogen is approximately double that of a neutral Hydrogen atom, however at higher energies (*i.e.* a few keV and above) the ratio rises to approximately 2.8 (Yan et al. 1998, Crasemann et al. 1974). Fortunately the exact conversion between absorption cross-sections is not crucial for this work, but it is important to note that with these values for molecular Hydrogen density and cross-section it is possible to account for absorbing columns of up to 15×10^{22} cm^{-2} towards the Galactic Centre. Of course this is a limit on the total absorption through the Galaxy so the expected value of absorption column density in front of the GRXE is somewhat lower. As an example Nevalainen et al. (2001) measure the absorption column in front of a cluster of Galaxies at (l,b) ~ 21.5°, -0.9°to be ~ 8×10^{22} cm^{-2} which is fully consistent with the calculations above.

5.5.2 The Galactic ridge

The nature of the hard X-ray emission along the Galactic Plane has long been uncertain. Until very recently theories fell into two categories; those which predicted that the GRXE was the due to a large number of very faint point sources and those which assumed the emission to be diffuse. However a recent *CHANDRA* observation (Ebisawa et al. 2001) has now firmly established that the bulk of the GRXE in the plane must be diffuse emission, which is in agreement with the analysis of *XMM-NEWTON* data presented in §4. Other high resolution observations have highlighted the presence of similar diffuse emission in the Galactic Centre (Muno et al. 2003,Wang et al. 2001). Therefore the following discussion proceeds with the assumption that the diffuse hard flux observed from the Galactic centre and the Galactic Plane are of common origin.

What is the mechanism responsible for this hard X-ray flux? The fits shown in Figures 5.10 and 5.12 show the results of fitting thermal plasma models to the EPIC-MOS data. In both the Galactic Plane and the Galactic Centre two distinct temperatures are required to adequately fit the spectra. The cooler plasma components have temperatures in the range 0.8–1.4 keV and the hotter plasma components have temperatures around 8–9 keV, with the exception of GPS (20°) which is fitted with a plasma temperature of 12 keV.

In all these data sets the key factor in establishing the nature of the source of the emission is the presence of the H-like Fe line at 7 keV. This line is visible in the Galactic Plane observations but it is the additional signal to noise in the Galactic Centre which enhances the significance of the line beyond doubt. The H-like Fe line, combined with the more prominent He-like Fe line at $\sim$ 6.7 keV, provide a crucial diagnostic to calculate the temperature of the plasma behind the emission, as shown by the relatively narrow confidence contours in Figures 5.11 and 5.13. This evidence strongly supports a thermal origin for the bulk of the GRXE above 5 keV as non-thermal models, which generally consist of a power law coupled with a plasma of intermediate temperature (around 3 keV), predict a negligible contribution from the H-like Fe line (Valinia et al. 2000,Tanaka 2002). It should be noted that the non-thermal fits to the GRXE (parameters given in Tables 5.5 and 5.7) are, in general, slightly better than their equivalent thermal fits. However this does not support the case for a non-thermal origin for the GRXE as there still needs to be a mechanism for producing both prominent emission lines of highly ionised iron (Fe XXVI and Fe XXV) and this cannot be achieved by simply increasing the iron abundance in the cooler plasma component. Coupled with this problem is the fact that if a $\sim$ 10 keV thermal plasma is fitted to just the continuum part of the spectrum in the 5–10 keV range, with all lines excluded, then the predicted Fe line strengths and line ratio of the resultant model very closely match the data when it is re-included, without any requirement for altering abundance or temperature. This would be quite a coincidence if the GRXE was produced by a non-thermal mechanism. However the power-law fits do at least provide a useful confirmation of the high level of absorption that is required on the source of the $>$5 keV flux, whatever its nature. Also it is of interest that the Gaussian lines used to model Fe XXV and Fe XXVI emission are narrow. This is in contrast to the results of Tanaka (2002) who measured the same lines in an *ASCA* SIS spectrum to be significantly broadened. The question of broadening is important as lines which are broadened beyond the amount expected for thermal or bulk motions imply a non-thermal origin. Tanaka (2002) assumed the two iron lines to be of equal intrinsic width and established that width to be $\approx$ 70 eV. By contrast the *XMM-NEWTON* spectra do not require similarly broad lines to achieve a good fit, although the signal to noise is insufficient to rule out the possibility. The one exception is GC 7 which yields a width of only $\sim$ half that measured by Tanaka 2002 for Fe XXV. This is therefore much more consistent with the value expected from bulk plasma motions. This can be seen more clearly in Figure 5.17 which traces the effect on χ^2 had by with varying the line widths of the Gaussian profiles used to fit the ionised Fe emission lines in the spectrum of the GRXE at several different positions. Importantly the widths measured for the ionised Fe lines are not significantly greater than those measured for neutral Fe, in contrast with the results from *ASCA* data (Tanaka et al. 2000).

Therefore the *XMM-NEWTON* data is largely in agreement with the thermal model used by Kaneda et al. (1997), which consisted of two plasma temperatures at 0.8 keV and 7 keV. However the plasma code used for this two temperature model was a non-equilibrium ionisation (NEI) code, whereas the APEC code used to model the *XMM-NEWTON* spectra is an equilibrium code. This may simply be a feature of the relatively poor spectral resolution of *ASCA* or alternatively a symptom of flaws in earlier ionisation equilibrium codes, either way there is no evidence for a non-equilibrium plasma based on the *XMM-NEWTON* data. The lack of a need for NEI code is, however, in agreement with the uniformity in spectral shape across the longitudinal and latitudinal range of the GRXE (Kaneda et al. 1997, Tanaka 2002).

Before attempting to explore the physical mechanisms which may be responsible for producing such a high temperature plasma, consideration must be given to the flux *above* 10 keV. Previous observations have demonstrated that there is a hard tail to the GRXE which extends to well beyond the flux range considered in this analysis. The slope of this extremely high energy flux is approximately 1.8 at around 10 keV (Valinia & Marshall 1998), although Yamasaki et al. (1997) have calculated a slope of 2.1 us-

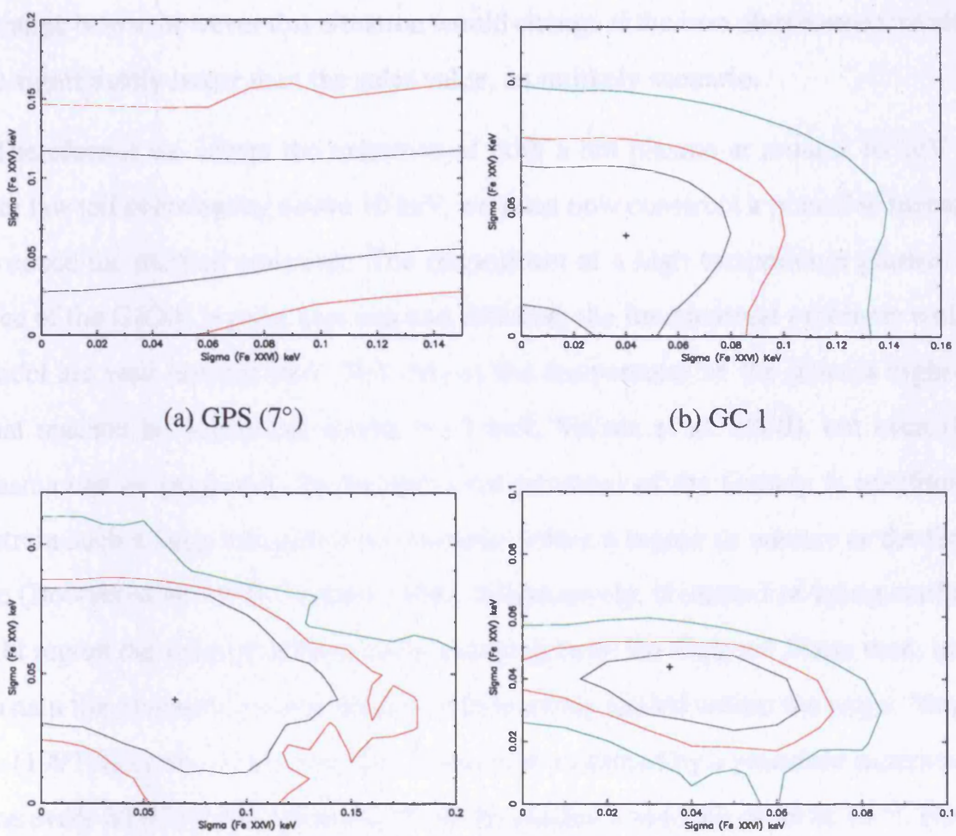

(a) GPS (7°) (b) GC 1

(c) GC 3 (d) GC 7

FIGURE 5.17. Contour plot for the spectral fits to GPS (7°), GC 1, GC 3 and GC 7 as examples of the variation of χ^2 with intrinsic Gaussian widths of He-like and H-like Fe emission lines. Contours are plotted at the 68%, 90% and 99% confidence levels and show that broad lines are not required to fit the data in either case, although the signal to noise ratio in the GPS data is only barely sufficient to draw conclusions.

ing data from a variety of instruments covering a very large flux range extending up to nearly 10^7 keV. The source of this flux is likely to be non-thermal cosmic ray electrons which produce very high energy electrons via an unknown mechanism which may be bremsstrahlung, inverse Compton scattering, synchrotron *etc.* . Although the continuation of this cosmic ray sourced flux into *XMM-NEWTON* 's spectral regime is implied, uncertainty in the effects of absorption mean that it is unclear how much of the observed <10 keV flux can be attributed to a non-thermal origin. The fact that the Fe XXVI and Fe XXV line strengths are correctly predicted by a $\sim$ 10 keV plasma, normalised to account for virtually all of the continuum flux, implies that the non-thermal contribution in this flux range is low, however this situation would change if the iron abundance was allowed to be significantly larger than the solar value, an unlikely scenario.

Therefore if we accept the existence of both a hot plasma at around 10 keV and a power law tail contributing above 10 keV, we must now construct a plausible mechanism to produce the thermal emission. The proposition of a high temperature plasma as the source of the GRXE is not a new one and therefore the fundamental problems with such a model are well documented. Not only is the temperature of the plasma higher than is that reached by supernova shocks ($\sim$ 3 keV, Valinia et al. 2000), but even if such a plasma can be produced, the Gravitational potential of the Galaxy is insufficient to constrain such a large amount of hot material within a region as narrow as the Galactic ridge (Bowyer et al. 1968, Townes 1989). Alternatively, if instead of being confined to a tight region the ridge plasma is freely escaping from the Galactic Plane then, in order to sustain the emission, plasma must be continuously heated within the ridge. Yamasaki et al. (1997) have shown that the GRXE could be sustained by a plausible supernova rate of one every 50 years if the filling factor of the plasma was of the order of 10^{-3}. However this does not solve the problem of plasma temperature as there have been few detections of supernovae with temperatures $>$3 keV.

One model which may provide a solution to the high plasma temperature problem is magnetic reconnection. This is the process, already known about in the context of the solar atmosphere, whereby magnetised turbulent plasmas are heated by magnetic energy that is released when magnetic fields with different field directions interact with each other. The energy for this process originates in Galactic rotational energy which is converted to magnetic energy by the Galactic dynamo (Makishima 1994). Tanuma et al. (1999) have performed 2-dimensional simulations of this effect using supernova shocks as the mechanism to trigger reconnection. They found that to produce the required plasma temperature a local magnetic field strength of $\sim$ 30 μG, ten times higher than the line-averaged value of a few μG, is needed. Tanuma et al. (1999) argue that this is plausible as locally strong magnetic fields have indeed been observed at this high field strength (*e.g.* Simard-Normandin & Kronberg 1980). However whether or not this could be maintained over a large enough region to encompass the ridge is open to question and further observations are required to clarify the situation. A bonus of the reconnection model is that in addition to heating the plasma, it also accounts for its confinement to a relatively small volume. In the simulations of Tanuma et al. (1999) the process of magnetic reconnection forms a helical magnetic field (or magnetic islands in the 2D view) which isolates the hot plasma and prevents leakage into the surrounding medium outside the reconnection region. This process continues as long as the Galaxy rotates. In summary the reconnection model provides a self-contained explanation of both the temperature and confinement of the Galactic ridge, but relies on a magnetic field strength that is as yet unconfirmed by observation.

Another model, which takes an intermediate approach to the temperature problem, has been outlined by Dogiel et al. (2002) and Masai et al. (2002). In this model a plasma temperature of 0.3–0.6 keV is the basis for in-situ electron acceleration, via Coulomb collisions, which produces a population of quasi-thermal electrons that provide much of the highly ionised Fe line emission. The spectrum of the quasi-thermal electrons can be approximated by a Maxwellian distribution of roughly 4 or 5 times the temperature of the plasma itself. This non-equilibrium effects introduced by this population alters the profile of ion emission lines and ultimately results in a stronger Fe XXVI line than would be expected for a cool plasma. This prediction goes some way towards agreement with observational data in the Galactic Plane but is unlikely to be able to reproduce the much more statistically significant Fe XXVI lines visible in the spectra of the Galactic Centre. In addition Masai et al. (2002) also include a population of non-thermal cosmic ray electrons to account for the emission around and above 10 keV, similar to the population modelled by Valinia et al. (2000). However the quasi-thermal model predicts a strong 6.4 keV neutral iron line which is not seen by either *XMM-NEWTON* (see below) or *ASCA* away from the Galactic Centre, although it has been suggested that this could be because the effective iron abundance is low if iron is largely contained within dust grains (Tanaka 2002). Also they use a column density of only 10^{20} cm^{-2} which is dramatically lower than the expected value for a significant penetration into the Galactic Plane. Therefore although this intermediate model does solve some problems by removing the need for a particularly hot plasma, the predicted line profiles of neutral and ionised Fe do not match those observed either at the Galactic Centre or at larger longitudes within the plane.

The neutral iron line

The existence or not of neutral Fe K_α line emission in the GRXE plays a vital role in determining the mechanism behind the emission. The APEC plasma code, used to model all thermal components, does not include a neutral iron line, however this should be of little importance as at temperatures of the order of keV virtually all elements, including iron, will be highly ionised. In the Galactic Plane spectra at 20°, 15°& 7° the data around this line are excluded because the spatial variation of instrumental iron results in an over-subtraction of the background (see §2.7.2) at this energy. This makes it difficult to establish whether or not a neutral Fe line is in the GRXE spectrum. The closed filter wheel observation, MS1054.4-0321, which was used to show that an over-subtraction of neutral Fe is expected, does not provide a good enough signal to noise ratio for background subtraction, however it is possible to get an upper limit to the strength of a any 6.4 keV line which may be in the spectrum by removing the neutral Fe from the background spectrum entirely. This results in a clear line being visible in the net spectrum (for example at 20°) with an equivalent width of $\sim$ 180 eV. This is significantly larger than the 70 eV upper limit set by Tanaka (2002) because the line must contain at least some fluorescence emission and is probably dominated by it.

In the case of the Galactic Centre fields there is substantial 6.4 keV line emission in each of the three fields at various strengths, with GC 3 having the line with the largest equivalent width. Due to same background subtraction problem the equivalent widths given in Table 5.6 are lower limits rather than measurements. GC 3 and GC 7 lie over the Sgr B2 and Sgr C complexes respectively in the Galactic Centre and GC 1 is also very close to Sgr B2. The nature of these complexes is not precisely known. They may be X-ray reflection nebulae (XRN) which were irradiated by the massive black hole Sgr A* (Koyama et al. 1996, Murakami et al. 2001), implying that Sgr A* was more luminous 300 years ago (the travel time between Sgr A* and Srg B2/Sgr C). However Predehl et al. (2003) have measured 6.4 keV emission from several X-ray filaments closer to Sgr

A* and found that the surface brightness does not seem to vary with distance. This is contrary to what would be expected if the emission is indeed reflection from a Sgr A* flare, although it does not rule out the XRN hypothesis entirely.

It should also be noted that another neutral Fe emission line exists near this energy band. Fe K_β emission will occur at 7.05 keV with an intensity roughly an order of magnitude lower than that of Fe K_α. Although at first glance it seems possible that this could be confused with H-like Fe emission at 6.97 keV, it is clear from a comparison of the spectra of GC 1 and GC 3 that a large change in the strength of 6.4 keV emission does not have a noticeable effect on the $\sim$ 7 keV line. Therefore Fe K_β emission can be ignored in this analysis.

5.5.3 Latitude & Longitude variation

The GRXE can be readily identified at low Galactic latitudes because there is sufficient flux to resolve its characteristic emission lines from highly ionised metals. At greater latitudes, such as in the southern bulge fields, a hard excess is clearly present but the signal to noise does not allow the detection of such lines. In order to compare the strength of the excess the southern bulge fields were re-fitted with a constant power law slope of index 1.8. The respective normalisations of the power law are plotted in Figure 5.18 along with a the line of best fit, calculated assuming an exponential dependence on distance from the plane. The scale height derive from this fit was 0.6 kpc, similar to the broad disk GRXE spatial component scale height measured by Valinia & Marshall (1998) of 500 pc. Extrapolating the exponential brightness decay curve a normalisation of $\sim 4 \times 10^{-3}$ photons kev^{-1} cm^{-2} s^{-1} is predicted for the Galactic Centre region. The actual values (given in Table 5.7) are up to an order of magnitude higher. This is consistent with there being an additional narrower disk component, with a much smaller scale height, as found by Valinia & Marshall (1998).

The thermal plasma fits to the excess flux above 2 keV in the southern bulge fields yielded temperatures in between the two temperatures measured for the on-plane GRXE which probably means that the observed flux is a mixture of the two, although there is no noticeable trend towards a higher temperature at lower latitude which would indicate a difference in the scale heights of the two plasmas.

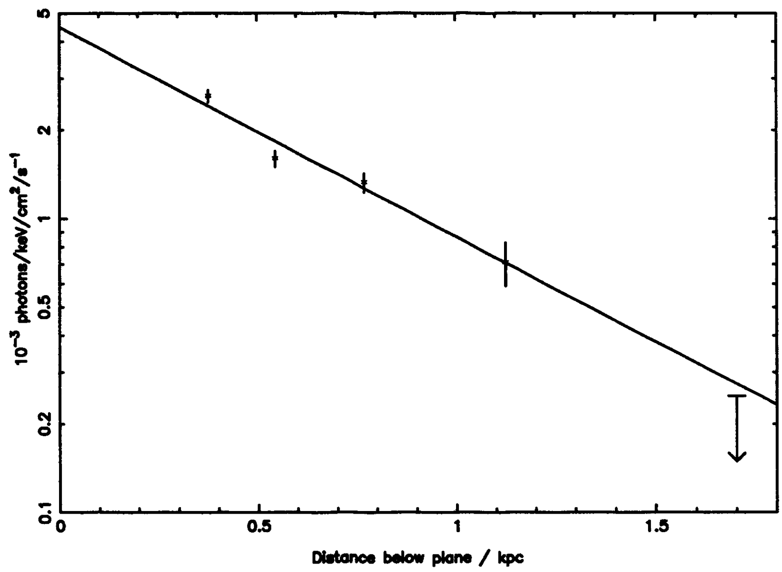

FIGURE 5.18. The exponential dependence of 'GRXE' brightness on Galactic latitude. The normalisation (at 1 keV) refers to a power law with Γ=1.8 (fixed) and the distance below the plane is calculated using a distance to the Galactic Centre of 8 kpc. A 90% confidence upper limit to the normalisation of an equivalent component in Bulge 12 (1.7 kpc below the GC) is also shown. The best fit line yields a scale height of 600 pc.

Establishing the variation with Galactic longitude is simplified by the fact that in each of the on-plane fields two distinct plasmas are observed and are thus directly comparable with each other. Figure 5.19 shows the emission measures of the hot and cool plasma components plotted against Galactic longitude. Clearly there is insufficient data to find an accurate functional dependence on longitude, although in any case it is highly unlikely to be representable by a simple single-parameter decay. The lack of significant variation between 7°and 20°implies that the strongly enhanced Galactic Centre emission requires an additional component which rapidly diminishes away from the GC. Whether or not the mechanism behind this flux is the same as the rest of the GRXE is uncertain but the similarities between the spectral fits at all observed longitudes imply this is the case. One feature which stands out in Figure 5.19 is the unexpectedly low value of cool plasma emission measure at 1°. It is possible this is because GC 1, which produces this data point, is positioned slightly off the Galactic Plane (at -0.14°latitude), although this is unlikely as it would require an extremely small scale height for the cool component. As mentioned earlier this would also imply a temperature variance with latitude (cooler closer to the plane) but this cannot be confirmed due to insufficient data. In order to establish both this and the longitudinal dependence of the GRXE several observations are required within a couple of degrees of the Galactic Centre.

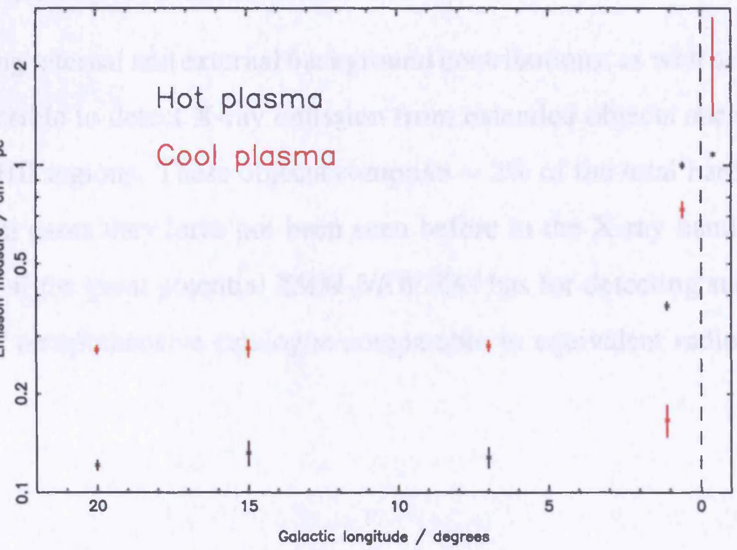

FIGURE 5.19. Hot and cool plasma emission measures as a function of Galactic longitude. Zero longitude is shown by a dotted line. The apparent dip in cool plasma emission measure at 1°is possibly due to the fact that GC 1 is not centred on the plane.

5.6 Conclusion

Detailed analysis of point source populations in §4 has confirmed that the majority of hard flux observed towards the Galactic Plane is indeed diffuse in nature. Analysis of this Galactic ridge emission, with the superior spectral resolution of the EPIC-MOS cameras on board *XMM-NEWTON* , has shown that the best fit model to the hard flux consists of two distinct plasma temperatures;one at a relatively cool temperature of just over 1 keV ($10^{7.1}$ K) and another, approximately an order of magnitude hotter, at $\sim$ 9 keV ($10^{8.0}$ K). Essential to the thermal model argument is the identification of an emission line from

Hydrogen-like Fe at $\sim$ 7 keV, not resolvable by previous missions but seen clearly by *XMM-NEWTON* . The issue of non-thermal line broadening is not yet resolved as the spectra from most observations are equally well fit with narrow and broad lines. The problem of heating and confinement of such a hot plasma is probably best explained by magnetic reconnection, powered by the rotation of the Galaxy itself. In addition to the thermal emission there is also a non-thermal power law tail which extends to very high energies but is unlikely to dominate below 10 keV.

By removing internal and external background contributions, as well as point sources, it has been possible to detect X-ray emission from extended objects such as supernova remnants and HII regions. These objects comprise $\sim 2\%$ of the total hard flux from the GRXE. In most cases they have not been seen before in the X-ray band and therefore are illustrative of the great potential *XMM-NEWTON* has for detecting such objects and creating a new comprehensive catalogue comparable to equivalent radio surveys from decades past.

Chapter 6

Conclusion

6.1 Overview

The work described in this thesis utilises the superb capabilities of the European Space Agency's *XMM-NEWTON* satellite. The multitude of targets have all been observed before by previous generations of X-ray satellites, but the high throughput of *XMM-NEWTON* , combined with enhanced spectral and spatial resolving power, enables a much more detailed analysis of the nature of the emission. The requirement for segregating point sources and diffuse emission throughout this work makes the EPIC instruments, with their CCD imaging capabilities, the detectors of choice. For both the imaging and spectral analysis data are used from across the entire field of view of each EPIC camera. For the present work the best results have been obtained from the MOS cameras; a summary of the background effects which lead to this is given in §6.2. Therefore the results summarised in §6.3 are based on both EPIC-MOS and EPIC-pn data, whereas the results in §6.4 and §6.5 are derived from EPIC-MOS data only.

This chapter is in part a summary of the work presented in previous chapters, and the conclusions which result. However a further purpose is to comment on issues which remain unresolved and to touch upon the prospects for resolving them in the future.

6.2 The detector backgrounds

As with any photon-detecting instrument, the CCD detectors which form part of the EPIC cameras experience a certain amount of contamination from background sources. The two types of contamination which are described in detail in §2 are protons from solar flares, which are focused by *XMM-NEWTON* 's mirrors, and cosmic ray events which pass through the satellite directly on to the CCDs. Although disentangling the non-sky background from the sky background is not necessary for detecting point sources (*e.g.* see Read & Ponman 2003), ascertaining the level and shape (*i.e.* vignetting) of the instrument background is extremely helpful when searching for extended objects against the diffuse sky signal. Accurate estimation of the non-sky background is crucial when analysing full-field spectra of diffuse emission from any region of the sky. Proton events can, for the most part, be adequately removed by filtering the light curve of a particular observation. Cosmic ray events on the other hand are a continuous source of contamination and therefore are more problematic.

The technique of extracting data from the unexposed edges of the MOS CCDs has proven to be an effective method for modelling the internal background. However this method suffers from two problems: a poor signal to noise ratio due to the small number of pixels which can be used (the even smaller number with the pn camera severely hampers the equivalent process for this instrument), and secondly the variation in fluorescence line emission across the CCDs. Due to the relatively short exposures, and subsequent low signal to noise ratio, these problems have only had relatively mild effects on the analysis in this thesis. However longer observations would benefit substantially from an improved understanding of the instrument background.

A worthwhile project for the future is to therefore to create a high quality background spectrum based on the inner CCD regions. This could be achieved with a closed filter wheel observation, similar to MS1054.4-0321 (see §2.7.2), but with a significantly increased exposure time.

6.3 Discrete emission

Every observation considered in this thesis has been subject to the source detection algorithm described in §2, in order to separate point source flux from diffuse flux. However, a more detailed investigation into the source population has been performed only for the 22 XGPS pointings clustered around (l,b) $\sim (20°, 0°)$. This is because a large number of point sources is required to model the different source populations in a given direction. Detailed modelling of the Galactic Plane source population can be found in §4 but the principle results and conclusions are listed below:

- In total the 22 XGPS observations yielded 424 individual point sources, of which 345 were detected in the combined MOS data and 222 were detected in the pn camera. Approximately 75% were detected in the wide energy band (0.4–6 keV) with $\sim$ 40% and $\sim$ 60% detected in the soft (0.4–2 keV) and hard (2–6 keV) energy bands respectively. Only $\sim$ 10% were detected in both the hard and soft bands implying the presence of separate populations. Details of all sources, including positions, count rates and various other information, are included in Appendix A.

- By far the brightest source in the XGPS catalogue exhibits a very hard spectrum with a 2–10 keV flux of $\sim 6 \times 10^{-12}$ erg s^{-1} cm^{-2}, corresponding to an upper limit luminosity (at d=15 kpc) of $\sim 10^{35}$ erg s^{-1}. This source does not have a counterpart in the *ASCA* Galactic Plane catalogue which implies that it is a transient in a relatively high state. The source is coincident, however, with a type I X-ray burster which was detected by *BeppoSAX* in a much more luminous (albeit extremely brief) state. Therefore the luminosity of this object seems to vary over several orders of magnitude, consistent with it being a binary system with a variable accretion rate, possibly also exhibiting very short nova outbursts.

- For each X-ray catalogue source a search was performed for an optical counterpart using data from the SuperCOSMOS digitisation of the sky survey plates from the UK Schmidt telescope (UKST). Counterparts were found for approximately 45% of sources within a 6" radius error circle. This figure was found to be highly dependent on the X-ray hardness ratio of the source with soft sources being far more likely to yield a counterpart than hard sources. This makes it likely that many of the soft sources represent coronal emission from nearby stars. The optical correlations were used to show that the astrometry of source positions is reliable to within 4".

- Combined spectra were extracted for three sets sources grouped by hardness ratio. The soft (HR<-0.5) sources are well fitted by a 2-temperature thermal plasma model with temperatures of 0.25 and 1.5 keV, consistent with the interpretation that the majority of them are nearby active stars. Both the mid-range (-0.5<HR<0.5) and hard (HR>0.5) source spectra are consistent with a simple absorbed power law model, differing only by the level of absorption required on the continuum. The power law slope, Γ, obtained from a joint fit of the two data sets was 1.6 although fixing the slope at 1.7, characteristic of AGN, had a negligible effect on the quality of the fit. Many of the sources may be of extragalactic origin but the mid-range hardness ratio population may include significant numbers of Galactic objects such as cataclysmic variables (CVs) and RS CVn binaries.

- Cumulative source counts, as a function of count rate, were created in the three source detection energy bands after correcting for the total solid angle (across all XGPS fields) over which a source with a specific count rate could be detected. Only sources detected in the MOS data were included. The slopes of the integral counts were found to be 1.5 ± 0.2 for the soft and hard sources and 1.3 ± 0.2 for the broad band sources. For the hard sources, the count rates were converted to flux units to allow comparison with *CHANDRA* data at fainter fluxes (Ebisawa et al. 2001) and *ASCA* data at brighter fluxes (Sugizaki et al. 2001). Using the extragalactic model of Campana et al. (2001), along with models for Galactic populations with different luminosity functions, it is demonstrated that the source counts can be reproduced with a blend of different X-ray emitting objects which include AGN (dominating at fainter fluxes), X-ray binaries (dominating at brighter fluxes) and an intermediate population of low-luminosity sources which are consistent with CVs. Although the respective component models are not directly fitted to the data, the combined model plotted in Figure 4.12 represents a plausible balance between Galactic and extragalactic sources.

- The total 2–6 keV count rate from all 22 XGPS observations, including diffuse emission and corrected for mirror vignetting, is measured to be 3.7 ± 0.1 MOS count s^{-1} deg^{-1}, corresponding to $\sim 10^{-10}$ erg s^{-1} cm^{-2}in the 2–10 keV band. Summing the observed hard band source counts yields a total contribution of 0.34 count s^{-1} deg^{-1}, or 9% of the total signal. Integrating the individual source populations in the flux range 10^{-16} to 10^{-11} erg s^{-1} cm^{-2}gives contributions of 2%, 4% and 13% for binaries, CVs (and other low-luminosity objects) and AGN respectively. The figure for binaries rises substantially to 8% if higher fluxes are considered. Therefore around 80% of the Galactic ridge emission is likely to be truly diffuse in nature.

6.4 Diffuse emission

The observations listed in Table 2.1 encompass a variety of locations within our Galaxy with very different characteristic diffuse X-ray fluxes. The Galactic Plane and Galactic Centre are sources of high levels of hard X-ray flux but, due to the nature of X-ray absorption, are relatively faint in the soft X-ray band. Conversely the higher latitude fields in the North Polar Spur and south of the Galactic Centre are bright in the soft X-ray band but exhibit very little Galactic hard X-ray flux. These observations, along with the SDS fields which are relatively faint in both hard and soft bands, form the basis for investigating the origins of diffuse flux from across the Milky Way. The details of the spectral models for each location are given in §3 and §5 for predominantly soft and hard diffuse emission respectively. The main results and conclusions which result from this work are as follows:

- Unabsorbed soft X-ray emission from the local hot bubble LHB is well fitted by a thermal plasma model at a temperature of ~ 0.1 keV ($10^{6.06}$K). The emission measure varies in the range 0.004–0.007 cm^{-6} pc, consistent with previous measurements (*e.g.* Snowden et al. 1998). The detection of strong O VII line emission in the spectra from observations on the Galactic Plane implies a greater extent to the LHB than previously considered, albeit behind an absorption column of a few times 10^{20} cm^{-2}.

- Emission from the Galactic halo is apparent in all *XMM-NEWTON* fields away from the Galactic Plane, yielding an LHB-like plasma temperature of ~ 0.1 keV. The SDS fields, which are uncontaminated by $\frac{3}{4}$ keV emission from the Loop 1 superbubble, enable the detection of an additional source of halo emission. This weaker component is consistent with thermal emission from a plasma with a temperature of ~ 0.2 keV ($10^{6.4}$K) and is responsible for both O VII and O VIII line emission in the halo spectrum.

- The bright patches of $\frac{3}{4}$ keV emission in the north polar spur (NPS) and southern Galactic bulge have similar properties both in terms of temperature (0.25–0.3 keV or $\sim 10^{6.5}$K), intensity and elemental abundance. These properties are also shared by $\frac{3}{4}$ keV emission towards the Galactic Plane, although the brightness in this direction is much reduced by the strong absorption along the line of sight. If the $\frac{3}{4}$ keV flux from these three regions shares a common origin, namely the Loop 1 superbubble, then the substantial foreground absorption in the plane ($\sim 5 \times 10^{21}$ cm^{-2}) combined with the lack of emission in front of local higher latitude molecular clouds, implies the distance of the centre of the superbubble is up to 1 kpc away. At this distance the bubble radius is ~ 600 pc, *i.e.* too large to be the result of a single supernova explosion.

- The narrow band of hard X-ray emission observed by *EXOSAT* , known as the Galactic ridge, is consistent with a 2-temperature thermal model with plasma temperatures of ~ 1.2 keV ($10^{7.1}$K) and ~ 9 keV ($10^{8.0}$K) respectively. Emission lines are detected in the spectra from various locations along the Galactic Plane, including the Galactic Centre, from highly ionised species of Si, S, Ar & Fe. The detection of line emission from both Helium-like and Hydrogen-like Fe is crucial to accurately establish the temperature of the hot plasma component. The evidence for non-thermal broadening of these lines, which has previously caused problems with a thermal interpretation of the emission (Tanaka 2002), is largely inconclusive due to insufficient signal to noise, although in one field (GC 7) there is evidence for substantially narrower intrinsic widths than has previously been measured. The most likely mechanism for heating the emitting plasma and constraining it within the plane is magnetic reconnection; the interaction of turbulent magnetised plasmas resulting in magnetic heating powered by Galactic rotation. The local magnetic field strength required for this process is $\sim$ 30 μG, roughly an order of magnitude greater than the line-averaged value through the Galaxy.

- Excess hard X-ray emission, above the extragalactic power law (EPL) is detected in *XMM-NEWTON* observations south of the Galactic Centre up to a latitude of 8°. The calculated scale height using four such observations is 600 pc, similar to the 500 pc scale height of one component of the GRXE measured by Valinia & Marshall (1998). The signal to noise of the data is insufficient to reveal ionic metal emission lines, however the best-fit temperatures from single temperature thermal models lie between the values of the two components measured along the plane, implying a similar composite model may be valid at higher latitudes.

6.5 Extended objects

The ability to detect extended objects, such as supernova remnants (SNRs) and HII regions, in short exposure observations and above a substantial diffuse background, is indicative of the extremely high throughput of *XMM-NEWTON* . The flux from these objects represents $\sim$ 2% of the total hard (2–6 keV) flux measured from the Galactic ridge. The correlation of a high fraction of bright patches of extended radio emission with X-ray emission, including both known SNRs in the XGPS region, implies that the extension to the XGPS programme will continue to be successful at detecting such objects. Eventually this has the potential to include a large number of objects such as those listed below:

- In the longitude & latitude range 20°>l>0°, $|b|$ <0.6°there are a further 20 SNRs which may be detectable by *XMM-NEWTON* (Green 1996). Of these at least half have previously been observed in the X-ray band but scope remains for the detection of several new (in X-ray terms) SNRs which will provide invaluable multi-frequency comparisons of their spectral properties and morphologies.

- The high resolution 20cm radio data shown in §5 reveals several bright HII regions which are also seen for the first time in the X-ray band. Although the extension of this project is still in progress we can see from lower resolution radio maps (Altenhoff et al. 1979) that dozens of similar bright regions exist between 20°and the Galactic Centre, some of which are likely to be X-ray emitting HII regions and therefore detectable by XGPS. As little is currently known about the X-ray properties of HII regions, continuation of both XGPS and the VLA radio survey can only help to further our understanding of the physical mechanisms behind these objects.

- The two items above concern objects that have already been observed in another (radio) waveband. However, possibly even more interesting is the potential for discovering entirely new extended objects. For example the predicted number of SNRs in the Galactic Plane, based on extragalactic SN rates, is approximately double the number currently actually observed. Identifying new SNRs based only on XGPS data is problematic due to the shallow observation depth, therefore it is likely that new objects will need to be searched for using a combination of new X-ray data and improved radio data. The simultaneous extension of XGPS and improved resolution radio observations should allow this to be achievable.

6.6 Open questions / future missions

The current capacity for X-ray astronomy is dictated primarily by the *XMM-NEWTON* and *CHANDRA* satellite observatories. Future missions such as *Astro-E2*, *Constellation-X* and *XEUS* will further expand the scope for both spectral, spatial and temporal studies of X-ray sources. Some of the outstanding issues from this thesis will probably require a next-generation X-ray telescope to adequately resolve them. For others, such as the continuation of extended object searches mentioned above, a lot of progress can still be made with the current generation, in this case with *XMM-NEWTON* . A few further open questions for which more data are required are listed below:

- The intermediate scenario suggested in §3 for the source of bright $\frac{3}{4}$ keV emission is by no means certain. Although there is strong evidence for a non-local (and indeed non-Galactic Centre) origin for the $\frac{3}{4}$ keV emission towards the Galactic Plane, a similarly distant location for the NPS and southern bulge emission rests mainly on the hypothesis that all the $\frac{3}{4}$ keV flux shares a common 'superbubble' origin. This in turn is inferred from limited absorption and temperature measurements. Corroboration of this theory could be achieved in two ways: increased *XMM-NEWTON* coverage in and around the bright regions, especially in the northern bulge, and, in terms of future missions, the good quality spectral resolution and effective area of *Constellation-X* (at soft X-ray energies) will be ideal for making more accurate measurements of both temperature and elemental abundances within the emitting plasmas. Therefore although future *XMM-NEWTON* observations should prove interesting in terms of tracing the intensity of $\frac{3}{4}$ keV emission across the superbubble, proper investigation of the variations/similarities in the source(s) of the emission will be greatly boosted by future missions.

- The 400+ sources detected in the XGPS have helped to fill gap left between *ASCA* and *CHANDRA* observations of discrete objects in the Galactic Plane. Although this has enabled broad predictions to be made as to the nature of the source population, clearly the follow-up of individual sources in other wavebands is the only way to ascertain the exact contributions of different classes of source. One important branch to this is optical follow up. Approximately 10% of the XGPS sources have been observed by European Southern Observatory (ESO) telescopes and although the results to date are still preliminary, several distinct types of object have been identified. These include active stellar coronae, X-ray binary systems and CVs, supporting the general picture given in §4. An extension of this project to include as much of the whole sample as possible would provide invaluable information to confirm or deny the source populations predicted by X-ray data. In terms of future X-ray work, clearly the XGPS programme will continue to find sources at various Galactic longitudes but a similar programme of *CHANDRA* observations would make an extremely interesting follow-up, although the reduced field-of-view and throughput makes the prospect of a comprehensive survey seem unlikely. Looking much further into the future the capabilities of *XEUS* will enable sources to be detected with fluxes at least two orders of magnitude lower than the current limit, with spatial resolution comparable to *CHANDRA* .

- One of the most intriguing questions which this thesis addresses is the nature of the Galactic ridge X-ray emission (GRXE). The fundamental issue of whether the emission is truly diffuse has been solved by *CHANDRA* (Ebisawa et al. 2001) and supported by *XMM-NEWTON* , but the mechanism behind the emission is still not yet certain. The emission lines seen in the *XMM-NEWTON* data strongly support a thermal origin for the hard flux, however the explanation of where the hot plasma comes from and how it affects the flux at higher energies is far from trivial. Magnetic reconnection is deemed the most likely source of the thermal emission in §5 because it correctly predicts thermal emission lines without requiring a higher than observed SN rate. However this model only accounts for the flux in *XMM-NEWTON* 's energy range. As a power law component is already known to exist at higher energies (up to GeV!) it is important to understand how the power law and thermal components combine to produce the observed emission.1 Possibly the best candidate for uniting the thermal X-ray regime with higher energies is the proposed Energetic X-ray Imaging Survey Telescope (EXIST) which would conduct the first high sensitivity imaging survey in the hard (5–600) keV band. With sufficient spectral resolution to detect both continuum and line emission features, *EXIST* would be able to detect both thermal and non-thermal emission and establish the relative contributions of the two from both along Galactic Plane and elsewhere in the Galaxy.

Appendix A

The complete XGPS-I source catalogue

XGPS-I		Equinox J2000		MOS count ks^{-1}				pn count ks^{-1}						Optical
Designation	Obs	RA	DEC	s	h	b	q	s	h	b	q	HR	R	Identification
J182416-115554	X1	18 24 16.63	-11 55 54.5	0.67	**2.76**	**3.38**	0.51	0.00	3.67	1.73	1.00	0.72	19.4	GPSR 19.236+0.495
J182426-115918	X1	18 24 26.61	-11 59 18.8	**3.91**	0.02	**4.01**	1.00	**18.65**	0.89	**19.89**	1.00	-0.94	14.9	U0750_13092026
J182436-115127	X1	18 24 36.20	-11 51 27.5	0.26	0.51	**0.83**	1.00	0.00	0.54	0.00	0.63	0.45	-	
J182441-115903	X1	18 24 41.19	-11 59 3.5	1.11	1.41	**2.42**	1.00	1.29	1.38	2.57	0.41	0.08	-	
J182446-120429	X1	18 24 46.45	-12 4 29.5	0.00	0.00	0.00	0.02	**11.16**	2.13	**13.49**	0.98	-0.69	9.8	U0750_13103886
														BD-12 5039
J182448-114454	X1	18 24 48.58	-11 44 54.2	0.03	**2.12**	**2.14**	1.00	0.63	2.41	**3.06**	1.00	0.84	18.2	-
J182502-114320	X1	18 25 2.29	-11 43 20.8	0.74	0.85	**1.58**	1.00	0.00	0.20	0.00	0.18	0.08	16.6	U0750_13113393
J182506-114819	X1	18 25 6.78	-11 48 19.1	0.43	0.48	0.83	1.00	0.86	1.98	**2.87**	1.00	0.22	-	
J182506-120433	X1	18 25 6.85	-12 4 33.6	**7.00**	**10.72**	**17.56**	0.78	62.36	**65.57**	**127.87**	0.27	0.15	13.8	U0750_13116348
J182511-115726	X1	18 25 11.68	-11 57 26.3	**4.01**	0.66	**4.78**	1.00	**8.43**	1.20	**9.71**	1.00	-0.74	11.9	U0750_13119237
J182514-121859	R1	18 25 14.46	-12 18 59.4	0.91	0.34	1.11	1.00	**6.40**	0.00	4.24	1.00	-0.78	-	
J182517-114350	X1	18 25 17.24	-11 43 50.1	0.11	1.09	1.16	1.00	0.20	**4.43**	**4.51**	1.00	0.86	-	
J182521-113533	X3	18 25 21.10	-11 35 33.9	0.00	**1.70**	1.51	1.00	-	-	-	-	1.00	-	
J182524-114525	X1	18 25 24.48	-11 45 25.1	**4.39**	**27.38**	**31.53**	1.00	**13.48**	**54.98**	**67.86**	1.00	0.67	19.7	-
J182530-115610	X1	18 25 30.97	-11 56 10.0	**1.44**	0.08	**1.51**	0.92	2.39	0.46	**2.87**	1.00	-0.82	17.5	U0750_13130699
J182531-114340	X1	18 25 31.58	-11 43 40.3	0.75	0.70	1.49	1.00	2.60	3.13	**5.63**	1.00	0.02	19.8	-
J182532-122055	R1	18 25 32.66	-12 20 55.0	0.36	1.36	**1.67**	1.00	0.00	0.00	0.00	0.73	0.58	19.2	-
J182533-121649	R1	18 25 33.33	-12 16 49.3	0.92	0.68	**1.44**	0.86	1.96	**5.17**	**7.06**	1.00	0.23	13.1	U0750_13132239
J182533-121556	R1	18 25 33.52	-12 15 56.5	1.04	**5.91**	6.30	0.39	1.00	**4.45**	**5.52**	0.73	0.67	19.2	-
J182534-121453	R1	18 25 34.00	-12 14 53.5	**5.14**	0.38	**5.36**	0.80	**41.87**	2.05	**44.02**	1.00	-0.89	13.2	U0750_13132439
J182535-121558	R1	18 25 35.40	-12 15 58.2	0.19	0.11	0.15	1.00	2.27	2.05	**4.27**	1.00	-0.10	-	
J182537-120645	R1	18 25 37.97	-12 6 45.2	0.30	0.24	0.51	1.00	**2.52**	0.06	2.40	1.00	-0.62	-	
J182544-113153	X3	18 25 44.08	-11 31 53.4	**2.77**	0.27	**3.04**	1.00	-	-	-	-	-0.82	-	
J182544-121303	R1	18 25 44.20	-12 13 3.0	**1.40**	**2.19**	**3.53**	1.00	1.06	1.14	1.79	0.31	0.19	-	
J182549-121823	R1	18 25 49.81	-12 18 23.4	0.07	0.00	0.00	1.00	2.67	0.62	**3.29**	1.00	-0.65	19.8	-
J182550-114837	R2	18 25 50.51	-11 48 37.6	**0.92**	0.00	0.88	1.00	0.00	0.00	0.00	0.00	-1.00	-	
J182553-112519	X3	18 25 53.33	-11 25 19.4	**4.11**	1.08	**5.09**	1.00	-	-	-	-	-0.59	17.5	U0750_13144978
J182553-112713	X3	18 25 53.86	-11 27 13.0	0.21	**5.33**	**5.46**	1.00	-	-	-	-	0.92	12.3	U0750_13145056
J182558-120414	R1	18 25 58.37	-12 4 14.2	0.79	0.87	**1.64**	1.00	0.52	3.25	3.80	1.00	0.32	-	
J182559-114710	R2	18 25 59.88	-11 47 10.5	0.00	**2.56**	**2.27**	1.00	0.00	**9.45**	**9.13**	1.00	1.00	-	
J182601-110904	X5	18 26 1.19	-11 9 4.2	0.00	0.00	0.00	0.94	0.49	**2.74**	**3.26**	1.00	0.69	-	
J182601-122031	R1	18 26 1.64	-12 20 31.7	0.52	0.39	0.67	1.00	2.00	0.62	**2.29**	1.00	-0.34	-	
J182603-121952	R1	18 26 3.04	-12 19 52.8	0.00	**1.20**	0.65	1.00	0.06	0.00	0.00	1.00	0.97	18.4	U0750_13151482
J182603-120933	R1	18 26 3.23	-12 9 33.7	0.00	**4.13**	**3.92**	1.00	0.00	0.00	0.00	0.14	1.00	15.2	U0750_13151668
J182603-120640	R1	18 26 3.74	-12 6 40.3	**1.30**	0.31	1.47	1.00	1.28	0.00	0.12	0.35	-0.69	13.1	U0750_13152275
J182604-114719	R2	18 26 4.00	-11 47 19.1	0.13	**8.76**	**8.76**	1.00	0.00	**14.18**	**13.71**	1.00	0.98	-	

J182605-111626	X5	18 26 5.18	-11 16 26.8	0.84	1.52	2.36	1.00	0.67	0.49	1.17	1.00	0.19	-	
J182606-111553	X5	18 26 6.36	-11 15 53.3	0.66	1.61	2.26	1.00	0.45	0.52	0.97	1.00	0.35	19.8	-
J182607-111204	X5	18 26 7.10	-11 12 4.8	0.19	1.32	1.41	1.00	1.21	0.99	2.25	1.00	0.42	-	
J182607-120627	R1	18 26 7.17	-12 6 27.0	3.14	1.72	4.70	1.00	6.06	3.10	8.95	1.00	-0.31	16.7	U0750_13154481
J182608-114317	X3	18 26 8.06	-11 43 17.8	0.00	1.48	1.20	0.98	-	-	-	-	1.00	-	
J182608-121514	R1	18 26 8.21	-12 15 14.7	2.50	0.32	2.74	1.00	6.82	0.00	5.64	1.00	-0.88	13.6	U0750_13155125
J182608-112553	X3	18 26 8.31	-11 25 53.0	0.00	0.62	0.28	1.00	-	-	-	-	1.00	-	
J182608-115614	R2	18 26 8.56	-11 56 14.6	0.35	1.31	1.65	1.00	0.58	1.24	1.68	1.00	0.50	-	
J182609-120659	R1	18 26 9.36	-12 6 59.8	0.53	1.50	1.81	1.00	0.35	1.33	1.48	1.00	0.49	-	
J182609-114319	R2	18 26 9.38	-11 43 19.3	0.87	1.41	2.27	1.00	1.29	3.13	4.25	1.00	0.30	-	
J182614-110616	X5	18 26 14.55	-11 6 16.3	0.67	1.78	2.37	1.00	0.00	0.00	0.00	0.59	0.45	-	
J182614-110549	X5	18 26 14.69	-11 5 49.6	1.99	2.56	4.48	1.00	4.74	5.93	10.64	0.73	0.11	-	
J182615-122429	R1	18 26 15.03	-12 24 29.9	0.55	1.81	2.12	1.00	0.00	3.73	2.44	1.00	0.69	-	
J182617-112930	X3	18 26 17.74	-11 29 30.0	0.60	0.75	1.33	1.00	-	-	-	-	0.10	19.9	-
J182621-105608	X5	18 26 21.66	-10 56 8.3	0.93	4.21	5.08	1.00	0.00	0.00	0.00	0.00	0.63	17.1	-
J182622-122409	R1	18 26 22.23	-12 24 9.9	0.63	2.87	3.27	0.98	0.74	6.63	6.72	0.98	0.70	-	
J182622-110344	X5	18 26 22.71	-11 3 44.2	0.00	2.22	2.10	1.00	0.45	4.61	5.06	1.00	0.91	-	
J182625-113422	X3	18 26 25.05	-11 34 22.7	0.76	1.04	1.80	1.00	-	-	-	-	0.15	19.8	-
J182625-105918	X5	18 26 25.68	-10 59 18.5	0.41	1.78	2.14	1.00	0.00	1.52	0.69	1.00	0.70	18.4	-
J182625-112854	X3	18 26 25.73	-11 28 54.0	1.30	12.59	13.77	1.00	-	-	-	-	0.81	19.2	-
J182628-112224	X3	18 26 28.22	-11 22 24.8	1.06	1.09	2.15	1.00	-	-	-	-	0.00	19.4	-
J182628-120922	R1	18 26 28.66	-12 9 22.5	6.57	0.46	6.99	1.00	11.37	0.97	12.32	1.00	-0.86	13.9	U0750_13170745
J182628-105754	X5	18 26 28.85	-10 57 54.8	0.92	0.00	0.44	1.00	5.19	0.00	3.47	0.67	-1.00	11.6	U0750_13170977
J182629-110057	X5	18 26 29.47	-11 0 57.5	0.88	0.90	1.73	1.00	5.52	3.42	8.94	1.00	-0.16	14.6	U0750_13171480
J182629-114541	R2	18 26 29.70	-11 45 41.3	0.63	0.30	0.93	1.00	2.84	0.48	3.39	1.00	-0.57	16.9	U0750_13171638
J182631-114537	R2	18 26 31.49	-11 45 37.4	1.01	1.48	2.45	1.00	0.48	3.43	4.05	0.86	0.41	-	
J182633-111142	X5	18 26 33.10	-11 11 42.6	0.72	0.50	1.20	1.00	0.00	2.48	1.76	0.88	0.32	19.2	-
J182634-111208	X5	18 26 34.71	-11 12 8.3	0.04	1.19	1.22	1.00	0.00	3.67	3.44	1.00	0.96	-	
J182635-115606	R2	18 26 35.71	-11 56 6.4	0.36	0.47	0.81	1.00	3.34	1.29	4.69	1.00	-0.28	17.1	U0750_13175953
J182636-114648	R2	18 26 36.32	-11 46 48.6	2.44	0.94	3.41	1.00	5.56	2.32	7.91	1.00	-0.43	12.2	U0750_13176371
J182636-105714	X5	18 26 36.60	-10 57 14.4	0.23	1.34	1.56	1.00	0.00	2.32	1.61	1.00	0.80	-	
J182637-121234	R1	18 26 37.20	-12 12 34.9	3.57	0.00	3.11	1.00	0.00	0.66	0.26	0.41	-0.86	-	
J182637-115522	R2	18 26 37.31	-11 55 22.9	0.34	0.58	0.89	1.00	1.12	0.06	1.30	1.00	-0.16	16.7	U0750_13177676
J182638-104341	X7	18 26 38.36	-10 43 41.6	3.45	0.51	4.01	1.00	3.99	0.00	3.29	1.00	-0.83	13.3	U0750_13179391
J182638-110030	X5	18 26 38.46	-11 0 30.2	0.01	0.58	0.58	1.00	0.00	3.68	2.77	1.00	0.99	-	
J182639-114216	R2	18 26 39.76	-11 42 16.4	9.02	1.59	10.64	1.00	34.63	3.25	38.28	1.00	-0.78	14.1	U0750_13179120
J182641-115827	R2	18 26 41.29	-11 58 27.0	0.19	0.97	1.13	1.00	0.05	3.60	3.67	1.00	0.84	-	
J182642-112122	X5	18 26 42.42	-11 21 22.7	3.08	0.73	3.85	1.00	3.63	0.79	4.32	1.00	-0.63	8.1	U0750_13181513 HD 169754
J182643-114230	R2	18 26 43.32	-11 42 30.1	0.00	1.72	1.20	1.00	0.22	3.25	3.36	1.00	0.94	18.9	IRAS 18239-1144
J182643-114735	R2	18 26 43.70	-11 47 35.0	0.58	0.32	0.87	1.00	0.49	0.75	1.25	1.00	-0.10	16.8	U0750_13182208
J182645-111507	X5	18 26 45.05	-11 15 7.7	1.18	1.03	2.18	1.00	3.01	1.03	3.97	1.00	-0.25	-	
J182646-114034	R2	18 26 46.16	-11 40 34.1	0.34	0.47	0.84	1.00	2.43	1.16	3.61	1.00	-0.20	16.1	U0750_13184310
J182649-114903	R2	18 26 49.68	-11 49 3.8	0.19	0.31	0.56	1.00	2.12	2.82	5.05	1.00	0.16	-	
J182650-112640	R3	18 26 50.51	-11 26 40.6	0.27	1.47	1.71	1.00	1.69	2.48	4.24	1.00	0.42	19.3	-
J182651-110339	X5	18 26 51.29	-11 3 39.6	0.46	0.08	0.49	0.98	0.00	0.00	0.00	0.73	-0.72	19.1	-
J182653-110352	X5	18 26 53.35	-11 3 52.1	0.57	0.70	1.22	1.00	1.39	1.13	2.34	1.00	0.01	-	
J182653-105529	X5	18 26 53.88	-10 55 29.4	0.37	2.22	2.38	1.00	0.00	0.00	0.00	0.00	0.70	-	
J182655-114524	R2	18 26 55.10	-11 45 24.4	0.76	0.91	1.56	1.00	0.17	0.54	0.84	1.00	0.15	-	
J182655-105038	X7	18 26 55.39	-10 50 38.2	0.32	1.61	1.86	1.00	1.23	3.83	4.79	1.00	0.59	19.9	-
J182655-114244	R2	18 26 55.80	-11 42 44.2	0.00	0.17	0.09	1.00	3.91	0.32	4.01	1.00	-0.71	-	
J182656-114011	R2	18 26 56.54	-11 40 11.8	1.76	0.75	2.53	1.00	6.64	1.44	8.17	1.00	-0.56	15.1	U0750_13192255
J182658-113300	R3	18 26 58.42	-11 33 0.7	0.48	1.13	1.55	1.00	1.28	2.24	3.72	1.00	0.33	13.9	U0750_13193578
J182658-115544	R2	18 26 58.53	-11 55 44.0	0.84	0.89	1.67	1.00	1.35	0.00	0.00	1.00	-0.26	16.4	U0750_13193888
J182659-110936	X5	18 26 59.18	-11 9 36.0	0.22	1.32	1.52	1.00	0.00	0.00	0.00	0.27	0.71	-	
J182659-115312	R2	18 26 59.20	-11 53 12.0	0.33	0.00	0.27	1.00	1.24	2.66	4.04	1.00	0.16	-	
J182701-114628	R2	18 27 1.62	-11 46 28.0	0.75	0.35	1.17	1.00	3.02	3.73	6.70	1.00	-0.02	17.5	-
J182703-113714	R3	18 27 3.66	-11 37 14.1	3.17	2.07	5.36	1.00	7.58	5.35	12.97	0.88	-0.21	15.8	U0750_13196685
J182705-104302	X7	18 27 5.23	-10 43 2.6	0.49	1.52	1.94	1.00	0.54	2.72	3.24	1.00	0.56	18.4	U0750_13198612
J182705-120453	X2	18 27 5.38	-12 4 53.4	0.63	2.74	3.34	0.59	-	-	-	-	0.62	-	
J182706-112437	R3	18 27 6.40	-11 24 37.4	0.24	3.98	4.21	1.00	0.00	7.69	6.38	1.00	0.93	17.8	U0750_13199496 GPSR5 20.021+0.124
J182708-113459	R3	18 27 8.66	-11 34 59.9	0.16	1.99	2.18	1.00	0.00	0.00	0.00	0.41	0.85	-	

J182709-105318	X7	18 27 9.48	-10 53 18.5	0.74	0.98	**1.72**	1.00	0.00	1.01	0.00	1.00	0.28	-	
J182711-105743	X7	18 27 11.10	-10 57 43.2	0.00	**1.79**	1.46	1.00	4.35	5.41	**9.84**	1.00	0.39	-	
J182711-112550	R3	18 27 11.36	-11 25 50.0	0.69	0.82	**1.51**	1.00	0.00	0.79	0.52	1.00	0.23	18.9	-
J182712-102832	X9	18 27 12.07	-10 28 32.9	0.00	0.00	0.00	0.00	**9.31**	2.68	**12.14**	1.00	-0.57	13.9	U0750_13204067
J182712-112803	R3	18 27 12.12	-11 28 3.6	0.22	**1.17**	**1.40**	1.00	0.66	1.14	1.72	1.00	0.54	19.1	U0750_13204022
J182714-111814	R3	18 27 14.47	-11 18 14.9	1.06	1.31	**2.37**	1.00	2.36	**4.34**	**6.66**	1.00	0.19	-	
J182714-113027	R3	18 27 14.96	-11 30 27.2	**0.87**	0.38	1.23	1.00	**1.74**	0.00	**1.65**	1.00	-0.60	15.6	U0750_13206027
J182716-114832	R2	18 27 16.88	-11 48 32.2	0.63	**3.00**	**3.55**	1.00	1.16	**7.37**	**8.01**	1.00	0.69	16.7	U0750_13207576
J182718-112821	R3	18 27 18.33	-11 28 21.9	**0.58**	**0.83**	**1.40**	1.00	0.00	1.29	1.11	0.88	0.38	16.8	U0750_13208642
J182721-104715	X7	18 27 21.45	-10 47 15.1	0.00	**0.59**	0.36	1.00	0.00	0.00	0.00	1.00	1.00	-	
J182721-120730	X2	18 27 21.71	-12 7 30.2	**2.90**	**1.00**	**3.83**	1.00	-	-	-	-	-0.49	18.0	-
J182721-104355	X7	18 27 21.94	-10 43 55.5	**0.88**	0.39	1.24	1.00	0.55	0.00	0.02	1.00	-0.47	16.1	U0750_13211445
J182722-111149	X5	18 27 22.07	-11 11 49.7	0.63	**1.24**	**1.84**	1.00	3.46	1.68	5.19	1.00	0.00	15.8	U0750_13211722
J182722-105656	X7	18 27 22.85	-10 56 56.2	0.48	1.59	**1.92**	1.00	2.61	0.00	1.14	1.00	0.07	15.7	-
J182723-110910	R4	18 27 23.88	-11 9 10.4	0.78	**2.86**	**3.46**	1.00	0.00	0.00	0.00	0.00	0.56	-	
J182726-121304	X2	18 27 26.28	-12 13 4.8	**0.94**	0.01	0.95	1.00	-	-	-	-	-0.97	19.8	-
J182726-120641	X2	18 27 26.35	-12 6 41.1	**0.82**	0.00	0.67	1.00	-	-	-	-	-1.00	-	
J182726-101550	X9	18 27 26.88	-10 15 50.5	0.00	0.00	0.00	0.00	**24.47**	0.00	**24.89**	0.59	-1.00	-	
J182726-112041	R3	18 27 26.89	-11 20 41.4	**1.53**	0.89	**2.42**	1.00	**2.88**	1.17	**4.07**	0.88	-0.33	14.8	U0750_13215286
J182727-122036	X2	18 27 27.10	-12 20 36.5	1.29	**2.62**	**3.89**	1.00	-	-	-	-	0.32	-	
J182727-112851	R3	18 27 27.66	-11 28 51.0	**0.77**	0.09	0.89	1.00	0.00	0.00	0.00	0.65	-0.80	18.1	U0750_13216023
J182728-113742	R3	18 27 28.76	-11 37 42.6	**2.90**	0.16	**3.07**	1.00	**8.16**	1.09	**9.33**	1.00	-0.83	13.1	U0750_13216684
J182730-113514	R3	18 27 30.76	-11 35 14.3	0.31	0.55	0.90	0.82	**2.58**	2.31	**5.07**	1.00	0.05	-	
J182731-105123	X7	18 27 31.86	-10 51 23.1	**1.13**	0.45	**1.49**	1.00	**5.14**	0.61	**5.62**	1.00	-0.62	16.3	U0750_13219420
J182732-113358	R3	18 27 32.46	-11 33 58.5	**1.01**	**3.05**	**4.09**	1.00	2.30	**7.75**	**10.01**	1.00	0.52	16.7	U0750_13220110
J182733-120734	X2	18 27 33.35	-12 7 34.5	**0.85**	**0.79**	**1.61**	1.00	-	-	-	-	-0.04	-	
J182734-120645	X2	18 27 34.25	-12 6 45.7	0.00	**0.70**	0.69	1.00	-	-	-	-	1.00	19.6	-
J182734-112305	R3	18 27 34.47	-11 23 5.7	**1.04**	0.00	**0.79**	1.00	**3.53**	1.23	**4.82**	1.00	-0.69	19.3	-
J182735-121059	X2	18 27 35.62	-12 10 59.9	0.00	**0.88**	0.83	1.00	-	-	-	-	1.00	-	
J182736-105340	X7	18 27 36.57	-10 53 40.3	1.42	**3.78**	**5.13**	1.00	0.79	**4.49**	**5.21**	0.59	0.51	-	
J182737-111338	R4	18 27 37.25	-11 13 38.6	0.62	1.50	2.02	1.00	0.29	**7.05**	**7.22**	1.00	0.64	-	
J182738-105328	X7	18 27 38.52	-10 53 28.8	1.35	**2.26**	**3.57**	1.00	1.11	**5.78**	**6.82**	1.00	0.41	-	
J182738-104359	X7	18 27 38.64	-10 43 59.0	0.51	**1.54**	**2.00**	1.00	0.30	**4.28**	**4.34**	1.00	0.65	19.0	U0750_13225258
J182740-102812	X9	18 27 40.08	-10 28 12.4	**6.75**	0.63	**7.44**	1.00	**21.02**	1.13	**22.31**	1.00	-0.86	14.2	U0750_13226146
														1RXS J182742.4-102813
J182740-113955	R3	18 27 40.40	-11 39 55.3	**7.10**	0.37	**7.58**	1.00	**28.88**	3.82	**33.26**	1.00	-0.83	18.5	U0750_13226450
J182740-120327	X2	18 27 40.66	-12 3 27.3	0.09	**1.26**	1.31	1.00	-	-	-	-	0.87	19.3	-
J182740-120553	X2	18 27 40.97	-12 5 53.4	**0.82**	0.27	**1.11**	1.00	-	-	-	-	-0.51	19.8	-
J182741-121344	X2	18 27 41.04	-12 13 44.7	0.04	**1.01**	0.95	1.00	-	-	-	-	0.92	-	
J182741-112715	R3	18 27 41.26	-11 27 15.9	**1.19**	0.03	**1.18**	1.00	**4.32**	1.80	**6.17**	0.98	-0.61	16.1	U0750_13227020
J182742-115731	X4	18 27 42.57	-11 57 31.1	0.36	**1.75**	1.90	1.00	-	-	-	-	0.65	-	
J182744-113955	R3	18 27 44.80	-11 39 55.4	**1.96**	0.39	**2.37**	1.00	**6.52**	0.00	**6.01**	0.86	-0.84	11.4	U0750_13229697
J182745-120606	X2	18 27 45.55	-12 6 6.8	**5.32**	**18.88**	**24.14**	1.00	-	-	-	-	0.56	-	
J182746-110255	R4	18 27 46.33	-11 2 55.1	**2.20**	**3.55**	**5.63**	1.00	4.04	**5.95**	**9.86**	1.00	0.21	-	
J182746-103150	X9	18 27 46.74	-10 31 50.1	0.00	**1.74**	0.69	0.59	0.03	1.91	1.92	1.00	0.99	16.2	U0750_13231392
J182748-115625	X4	18 27 48.02	-11 56 25.2	1.68	**2.30**	**3.87**	1.00	-	-	-	-	0.14	19.8	U0750_13232314
J182748-112130	R3	18 27 48.98	-11 21 30.2	**1.13**	0.05	1.20	1.00	**3.46**	0.00	3.40	1.00	-0.96	-	
J182749-105322	X7	18 27 49.17	-10 53 22.4	0.37	**2.86**	**3.20**	1.00	0.79	**4.41**	5.15	1.00	0.74	-	
J182749-102532	X9	18 27 49.42	-10 25 32.8	**0.83**	**1.15**	**1.98**	0.88	2.56	1.97	**4.49**	1.00	0.04	13.1	U0750_13233572
J182749-113725	R3	18 27 49.60	-11 37 25.4	1.13	0.98	**2.11**	1.00	3.23	**5.66**	**8.87**	1.00	0.12	19.9	-
J182749-113341	R3	18 27 49.99	-11 33 41.8	0.00	**0.34**	0.08	1.00	0.47	0.10	0.54	1.00	0.38	19.0	-
J182750-110408	R4	18 27 50.74	-11 4 8.2	0.28	**1.46**	**1.62**	1.00	0.25	2.81	2.82	1.00	0.72	19.2	-
J182750-113547	R3	18 27 50.99	-11 35 47.5	0.94	**3.13**	**4.03**	1.00	**3.17**	**5.56**	**8.71**	1.00	0.42	-	
J182752-105149	X7	18 27 52.54	-10 51 49.6	**1.21**	**2.12**	**3.39**	1.00	0.89	**4.32**	**5.18**	0.73	0.39	19.9	-
J182755-114958	X4	18 27 55.70	-11 49 58.9	0.26	**0.98**	**1.23**	1.00	-	-	-	-	0.57	18.6	-
J182755-120346	X2	18 27 55.75	-12 3 46.3	0.31	**2.34**	**2.60**	1.00	-	-	-	-	0.76	-	
J182756-105124	X7	18 27 56.14	-10 51 24.4	0.59	0.50	**1.13**	1.00	0.07	0.03	0.10	1.00	-0.11	19.2	U0750_13238574
J182756-110450	R4	18 27 56.84	-11 4 50.9	0.49	**11.03**	**11.28**	1.00	1.24	**22.91**	**23.27**	1.00	0.91	-	
J182757-110542	R4	18 27 57.24	-11 5 42.7	0.19	**1.58**	**1.65**	1.00	0.00	0.00	0.00	0.27	0.79	-	
J182757-120941	X2	18 27 57.24	-12 9 41.6	**13.88**	**2.27**	**16.11**	1.00	-	-	-	-	-0.72	-	
J182800-121501	X2	18 28 0.47	-12 15 1.1	**0.89**	0.00	0.73	1.00	-	-	-	-	-1.00	18.2	-
J182803-121638	X2	18 28 3.83	-12 16 38.4	**1.15**	0.95	**2.06**	1.00	-	-	-	-	-0.10	15.1	U0750_13244399
J182804-113337	R3	18 28 4.91	-11 33 37.1	0.24	0.11	0.39	1.00	0.00	**3.33**	2.57	1.00	0.66	-	

J182805-113830	R3	18 28 5.26	-11 38 30.4	0.87	0.60	1.54	1.00	4.24	4.23	**8.04**	1.00	-0.08	18.7	U0750_13245254
J182806-113735	R3	18 28 6.01	-11 37 35.5	**0.96**	0.11	**1.15**	1.00	0.36	0.82	0.55	1.00	-0.49	13.5	U0750_13246006
J182806-103419	X9	18 28 6.07	-10 34 19.6	**1.15**	0.00	1.07	1.00	0.00	0.64	0.00	1.00	-0.74	19.1	-
J182808-105946	R4	18 28 8.10	-10 59 46.7	0.70	**4.12**	**4.74**	1.00	0.00	0.00	0.00	0.14	0.68	-	
J182808-112711	R3	18 28 8.49	-11 27 11.2	0.00	0.07	0.00	1.00	**2.50**	0.00	1.35	0.76	-0.84	-	
J182809-104423	R5	18 28 9.16	-10 44 23.6	**1.29**	0.00	0.97	0.98	0.00	0.00	0.00	0.00	-1.00	16.2	U0750_13248381
J182810-114933	X4	18 28 10.50	-11 49 33.8	**1.94**	0.79	**2.75**	1.00	-	-	-	-	-0.42	19.1	-
J182811-114147	X4	18 28 11.38	-11 41 47.6	0.00	**2.41**	2.14	1.00	-	-	-	-	1.00	17.7	U0750_13249762
J182811-121220	X2	18 28 11.58	-12 12 20.5	0.00	**0.87**	0.61	1.00	-	-	-	-	1.00	18.2	U0750_13249956
J182811-110435	R4	18 28 11.63	-11 4 35.1	**0.65**	**0.82**	**1.40**	1.00	0.76	**4.59**	**5.14**	1.00	0.38	-	
J182811-102540	X9	18 28 11.92	-10 25 40.9	0.00	**1.12**	1.03	1.00	1.34	2.03	3.45	1.00	0.65	13.8	U0750_13250193 IRAS 18254-1027
J182812-115031	X4	18 28 12.51	-11 50 31.0	0.62	0.75	**1.37**	1.00	-	-	-	-	0.09	-	
J182813-102859	X9	18 28 13.49	-10 28 59.7	0.12	**0.54**	0.68	1.00	0.00	0.00	0.00	0.73	0.64	-	
J182813-102035	X9	18 28 13.57	-10 20 35.4	0.22	**1.91**	**2.14**	0.73	0.77	**4.35**	5.09	1.00	0.76	-	
J182813-120730	X2	18 28 13.59	-12 7 30.1	0.39	**3.94**	**4.29**	1.00	-	-	-	-	0.82	-	
J182813-110117	R4	18 28 13.76	-11 1 17.4	0.14	**1.37**	**1.36**	1.00	1.52	1.85	3.17	1.00	0.57	-	
J182813-103808	X9	18 28 13.84	-10 38 8.7	**4.30**	0.61	**4.99**	1.00	**7.55**	0.00	6.35	0.71	-0.83	16.5	U0750_13251657
J182814-103728	X9	18 28 14.23	-10 37 28.9	0.84	**13.78**	**14.44**	1.00	1.64	**15.32**	**16.64**	0.88	0.86	-	
J182814-104859	R5	18 28 14.82	-10 48 59.3	**0.99**	0.10	0.94	1.00	0.00	0.00	0.00	0.00	-0.82	-	
J182815-115432	X4	18 28 15.05	-11 54 32.8	**2.31**	**2.46**	**4.79**	1.00	-	-	-	-	0.02	-	
J182816-103823	X9	18 28 16.15	-10 38 23.8	**1.71**	1.24	**2.98**	1.00	**6.86**	0.00	2.46	1.00	-0.49	-	
J182816-111132	R4	18 28 16.28	-11 11 32.9	**0.67**	0.12	0.72	0.98	2.03	0.20	1.86	1.00	-0.75	19.7	-
J182816-115518	X4	18 28 16.36	-11 55 18.4	0.37	0.60	**0.97**	1.00	-	-	-	-	0.23	-	
J182816-105007	R5	18 28 16.93	-10 50 7.4	0.33	**1.83**	**1.98**	1.00	0.00	0.00	0.00	0.00	0.70	-	
J182817-103109	X9	18 28 17.98	-10 31 9.9	0.30	**0.90**	**1.25**	1.00	1.26	3.72	5.08	1.00	0.49	-	
J182819-100205	X12	18 28 19.27	-10 2 5.8	**1.42**	1.25	**2.49**	1.00	**3.94**	1.27	**5.18**	1.00	-0.25	11.4	U0750_13255545
J182820-114752	X4	18 28 20.65	-11 47 52.9	**1.11**	**0.79**	**1.92**	1.00	-	-	-	-	-0.17	-	
J182821-104245	R5	18 28 21.07	-10 42 45.3	0.00	**0.98**	0.62	1.00	1.07	1.98	2.57	1.00	0.63	-	
J182821-101125	X12	18 28 21.84	-10 11 25.9	**5.03**	0.00	**4.77**	1.00	**23.19**	0.00	**22.39**	1.00	-1.00	10.1	U0750_13257479
J182821-104202	R5	18 28 21.86	-10 42 2.5	0.92	**1.53**	**2.36**	1.00	0.00	4.02	3.03	1.00	0.53	-	
J182822-114927	X4	18 28 22.59	-11 49 27.6	0.31	**0.67**	**1.00**	1.00	-	-	-	-	0.36	-	
J182822-114724	X4	18 28 22.78	-11 47 24.0	0.31	**0.72**	**1.07**	1.00	-	-	-	-	0.40	-	
J182823-114157	X4	18 28 23.43	-11 41 57.4	0.42	**0.92**	**1.30**	1.00	-	-	-	-	0.37	-	
J182823-105107	R5	18 28 23.71	-10 51 7.7	0.00	**1.19**	**0.91**	1.00	1.14	2.61	3.83	1.00	0.68	-	
J182824-121006	X2	18 28 24.17	-12 10 6.5	0.46	**5.99**	**6.28**	1.00	-	-	-	-	0.85	18.9	-
J182824-120833	X2	18 28 24.47	-12 8 33.0	0.29	**1.70**	**1.91**	1.00	-	-	-	-	0.70	-	
J182825-112721	R3	18 28 25.05	-11 27 21.3	0.00	**2.47**	**2.52**	1.00	2.29	4.35	6.56	0.98	0.68	17.2	U0750_13259803
J182827-104131	R5	18 28 27.07	-10 41 31.6	**1.06**	**1.77**	**2.77**	1.00	1.21	**4.93**	**5.76**	1.00	0.41	-	
J182827-113818	X4	18 28 27.44	-11 38 18.0	0.84	**2.30**	**3.11**	1.00	-	-	-	-	0.45	18.7	U0750_13261369
J182827-100245	X12	18 28 27.44	-10 2 45.5	0.87	0.46	**1.29**	1.00	0.29	0.08	0.34	0.59	-0.34	-	
J182827-104454	R5	18 28 27.73	-10 44 54.0	0.47	0.61	**1.05**	1.00	0.00	0.00	0.00	1.00	0.14	19.9	-
J182827-111751	R4	18 28 27.77	-11 17 51.8	1.26	**7.27**	**8.38**	1.00	4.31	**19.69**	**23.39**	1.00	0.67	17.7	U0750_13261547
J182828-102357	X9	18 28 28.14	-10 23 57.3	0.57	**4.39**	**4.95**	1.00	0.00	**9.81**	**8.67**	1.00	0.84	15.6	U0750_13261865
J182828-103741	X9	18 28 28.77	-10 37 41.5	0.30	**6.54**	**6.72**	1.00	0.00	**16.62**	15.64	0.59	0.94	-	
J182829-121406	X2	18 28 29.49	-12 14 6.4	**1.85**	0.97	**2.84**	1.00	-	-	-	-	-0.33	-	
J182830-114516	X4	18 28 30.05	-11 45 16.8	**14.93**	**1.46**	**16.38**	1.00	-	-	-	-	-0.82	-	
J182830-115147	X4	18 28 30.69	-11 51 47.7	**1.01**	**0.73**	**1.71**	1.00	-	-	-	-	-0.16	-	
J182831-100332	X12	18 28 31.01	-10 3 32.8	0.33	0.47	**0.76**	1.00	0.08	0.47	0.48	1.00	0.28	18.7	-
J182831-103123	X9	18 28 31.46	-10 31 23.4	0.00	**1.11**	1.09	0.98	0.22	1.30	1.30	1.00	0.93	-	
J182831-104108	R5	18 28 31.71	-10 41 8.1	0.06	0.35	0.37	1.00	0.00	**2.02**	1.76	1.00	0.90	-	
J182831-095805	X12	18 28 31.91	-9 58 5.9	0.00	**2.16**	**1.94**	1.00	1.63	**5.23**	**6.84**	0.90	0.74	-	
J182833-103823	X9	18 28 33.60	-10 38 23.0	0.00	0.00	0.00	0.00	0.92	**16.26**	15.46	1.00	0.89	-	
J182833-102652	X9	18 28 33.60	-10 26 52.0	**1.86**	**4.04**	**5.96**	1.00	**2.85**	**12.58**	**15.54**	0.73	0.47	17.5	-
J182833-103659	X9	18 28 33.96	-10 36 59.5	**18.70**	**414.14**	**426.67**	0.43	**62.47**	**1249.28**	**1285.13**	1.00	0.91	15.6	U0750_13265703 SAX J1828.5-1037 1RXS J1828.5-1037
J182835-105951	R4	18 28 35.80	-10 59 51.3	0.00	**0.83**	0.72	1.00	0.00	0.00	0.00	0.27	0.84	-	
J182836-103653	R5	18 28 36.23	-10 36 53.3	0.89	**1.23**	**2.06**	1.00	1.78	0.33	1.38	0.41	-0.04	16.9	U0750_13267401
J182836-100207	X12	18 28 36.92	-10 2 7.1	0.84	0.19	**0.98**	1.00	1.29	0.41	1.64	1.00	-0.59	-	
J182836-103603	X9	18 28 36.97	-10 36 3.8	0.00	**6.48**	**5.84**	1.00	0.00	**15.13**	13.92	1.00	1.00	-	
J182839-111630	R4	18 28 39.26	-11 16 30.0	**4.34**	1.63	**5.97**	1.00	**21.24**	1.93	**22.78**	0.86	-0.64	19.0	U0750_13269349
J182839-115324	X4	18 28 39.70	-11 53 24.2	0.00	**0.88**	0.71	1.00	-	-	-	-	1.00	-	

J182841-102931	X9	18 28 41.50	-10 29 31.7	0.41	**1.29**	**1.69**	1.00	0.85	1.57	2.41	1.00	0.46	-	
J182842-104219	R5	18 28 42.26	-10 42 19.3	0.00	**1.07**	**1.01**	1.00	0.00	**2.30**	1.52	1.00	1.00	-	
J182843-101849	X12	18 28 43.54	-10 18 49.9	1.49	**2.69**	**3.92**	1.00	0.00	0.00	0.00	0.00	0.27	18.5	U0750_13272302
J182844-105428	R5	18 28 44.38	-10 54 28.1	0.30	**1.37**	**1.63**	1.00	0.00	3.98	3.74	1.00	0.81	-	
J182844-115653	X4	18 28 44.47	-11 56 53.7	**1.09**	0.40	**1.47**	1.00	-	-	-	-	-0.47	-	
J182845-101000	X12	18 28 45.86	-10 10 0.9	1.39	0.71	**1.95**	1.00	0.00	0.00	0.00	0.14	-0.33	-	
J182845-111711	R4	18 28 45.94	-11 17 11.0	**71.35**	**5.61**	**78.46**	0.00	**217.81**	**17.82**	**238.37**	1.00	-0.86	11.8	U0750_13273777
J182846-115552	X4	18 28 46.86	-11 55 52.3	**1.98**	**2.51**	**4.46**	1.00	-	-	-	-	0.11	18.8	U0750_13274575
J182847-100616	X12	18 28 47.10	-10 6 16.3	0.04	0.34	0.25	1.00	1.10	1.24	**2.41**	0.98	0.28	-	
J182847-101334	X12	18 28 47.76	-10 13 34.6	**38.70**	0.84	**39.74**	1.00	**135.63**	1.14	**137.79**	0.88	-0.97	8.8	U0750_13275198
														HD 170248
														1RXS J182846.4-101336
J182848-104942	R5	18 28 48.30	-10 49 42.5	**0.65**	0.03	0.59	1.00	0.00	0.00	0.00	1.00	-0.92	-	
J182849-104344	R5	18 28 49.12	-10 43 44.4	0.06	0.63	0.65	1.00	0.00	**2.27**	1.15	1.00	0.93	-	
J182850-114608	X4	18 28 50.00	-11 46 8.0	0.34	**1.17**	**1.51**	1.00	-	-	-	-	0.54	16.0	U0750_13277273
J182850-104649	R5	18 28 50.77	-10 46 49.5	0.22	**0.87**	**0.96**	1.00	0.49	**1.69**	1.95	1.00	0.58	-	
J182851-101313	X12	18 28 51.04	-10 13 13.4	0.93	0.00	0.43	1.00	**4.36**	1.75	**5.63**	1.00	-0.59	19.7	-
J182851-103535	R5	18 28 51.05	-10 35 35.1	**1.01**	0.96	**1.95**	1.00	0.75	1.72	1.80	1.00	0.12	19.8	-
J182851-105539	R5	18 28 51.15	-10 55 39.6	0.31	0.12	0.45	1.00	0.73	**5.05**	**5.54**	1.00	0.56	-	
J182851-101730	X9	18 28 51.22	-10 17 30.4	0.87	**2.03**	**2.88**	1.00	0.00	0.00	0.00	0.00	0.23	19.7	-
J182851-103047	X9	18 28 51.63	-10 30 47.1	0.96	0.71	**1.68**	1.00	1.06	2.95	4.15	1.00	0.06	16.3	U0750_13278214
J182854-105017	R5	18 28 54.72	-10 50 17.8	0.04	**1.11**	**1.03**	1.00	0.00	0.00	0.00	0.27	0.94	-	
J182854-112656	X6	18 28 54.86	-11 26 56.1	**3.81**	**5.13**	**8.79**	1.00	**9.57**	**16.11**	**25.12**	1.00	0.18	17.6	U0750_13280318
														F3R 673
														RFS 302
J182855-104003	R5	18 28 55.49	-10 40 3.6	**0.54**	0.01	0.47	1.00	0.00	0.00	0.00	0.27	-0.95	-	
J182855-111148	R4	18 28 55.74	-11 11 48.7	**1.55**	0.78	**2.30**	0.98	1.94	**3.79**	**5.77**	1.00	-0.13	-	
J182856-095413	X12	18 28 56.04	-9 54 13.5	**2.54**	**42.92**	**44.62**	1.00	**7.87**	**88.25**	**94.61**	1.00	0.86	-	
J182856-101702	X12	18 28 56.31	-10 17 2.2	0.09	**2.40**	**2.26**	0.98	0.69	**8.28**	**9.33**	1.00	0.88	-	
J182856-100401	X12	18 28 56.61	-10 4 1.2	0.65	0.02	0.45	1.00	1.03	1.29	**2.29**	1.00	-0.33	-	
J182857-103502	R5	18 28 57.85	-10 35 2.1	0.50	**1.16**	**1.61**	1.00	0.00	0.86	0.24	1.00	0.50	16.9	U0750_13282507
J182858-100002	X12	18 28 58.17	-10 0 2.7	0.00	0.83	0.61	0.71	0.51	**2.65**	**3.13**	1.00	0.81	-	
J182858-113600	X6	18 28 58.36	-11 36 0.2	0.28	2.09	**2.15**	1.00	0.66	0.00	0.36	1.00	0.66	-	
J182858-103908	R5	18 28 58.55	-10 39 8.1	0.31	**1.34**	**1.61**	1.00	0.72	**2.50**	**2.81**	1.00	0.59	-	
J182858-104511	R5	18 28 58.59	-10 45 11.7	0.03	**0.74**	0.63	1.00	0.14	1.12	0.88	1.00	0.86	-	
J182858-095921	X12	18 28 58.70	-9 59 21.6	0.00	**1.29**	**1.05**	1.00	0.67	1.28	2.08	1.00	0.74	-	
J182859-100043	X12	18 28 59.49	-10 0 43.8	0.37	0.20	0.48	1.00	0.81	2.88	**3.53**	1.00	0.31	19.5	-
J182900-111001	X8	18 29 0.38	-11 10 1.9	0.59	**2.89**	**3.32**	1.00	0.00	0.00	0.00	0.00	0.65	-	
J182900-100658	X12	18 29 0.58	-10 6 58.2	0.14	0.04	0.02	1.00	1.05	**2.47**	**3.51**	1.00	0.29	-	
J182901-103925	R5	18 29 1.42	-10 39 25.4	0.34	0.05	0.34	1.00	0.35	**2.36**	2.33	1.00	0.36	-	
J182901-101448	X12	18 29 1.90	-10 14 48.8	0.62	**1.49**	**1.88**	1.00	0.11	4.30	**4.14**	1.00	0.65	-	
J182902-103720	R5	18 29 2.00	-10 37 20.8	0.04	**1.54**	**1.54**	1.00	1.09	**3.72**	**4.60**	1.00	0.72	-	
J182902-115341	X4	18 29 2.65	-11 53 41.8	0.17	**1.27**	**1.35**	1.00	-	-	-	-	0.76	-	
J182903-110230	X8	18 29 3.02	-11 2 30.4	0.36	**1.21**	**1.52**	0.59	0.00	0.00	0.00	0.00	0.52	19.3	-
J182905-104634	R5	18 29 5.70	-10 46 34.7	0.34	**5.21**	**5.41**	1.00	1.36	**12.37**	**13.38**	1.00	0.84	19.8	U0750_13288301
J182907-104432	R5	18 29 7.32	-10 44 32.4	**1.15**	**2.58**	**3.65**	1.00	**2.27**	**6.63**	**8.77**	0.59	0.44	-	
J182907-104604	R5	18 29 7.37	-10 46 4.7	0.24	**0.67**	**0.78**	1.00	1.34	1.66	2.73	1.00	0.26	-	
J182908-102053	X11	18 29 8.29	-10 20 53.4	0.50	**1.14**	**1.71**	1.00	0.09	2.82	2.62	1.00	0.57	-	
J182908-104930	R5	18 29 8.71	-10 49 30.6	**0.52**	**1.36**	**1.82**	1.00	1.37	**2.11**	**3.54**	1.00	0.34	17.4	U0750_13290417
J182909-105644	R5	18 29 9.95	-10 56 44.3	0.00	0.81	0.23	1.00	**2.53**	0.63	1.98	1.00	-0.01	-	
J182911-104245	R5	18 29 11.06	-10 42 45.6	0.55	0.47	0.91	1.00	1.37	**2.01**	**3.35**	1.00	0.08	16.4	U0750_13292023
J182911-105544	R5	18 29 11.61	-10 55 44.9	**7.91**	0.80	**8.50**	1.00	**14.71**	2.68	**16.55**	0.98	-0.76	19.1	-
J182913-095729	X12	18 29 13.59	-9 57 29.1	**2.54**	0.68	**3.01**	1.00	**6.22**	0.45	**6.73**	1.00	-0.72	13.1	U0750_13293780
J182914-104629	R5	18 29 14.34	-10 46 29.7	0.56	0.83	**1.28**	1.00	0.23	0.00	0.00	0.41	0.11	-	
J182914-102448	X11	18 29 14.36	-10 24 48.4	**1.37**	0.23	**1.57**	1.00	**14.08**	0.00	12.61	0.27	-0.85	18.5	U0750_13294401
J182914-104419	R5	18 29 14.86	-10 44 19.3	**0.66**	0.70	**1.29**	1.00	0.00	0.00	0.00	0.20	0.03	-	
J182914-105744	X8	18 29 14.94	-10 57 44.5	0.00	0.00	0.00	1.00	0.47	2.69	2.71	1.00	0.69	18.2	-
J182916-104601	R5	18 29 16.15	-10 46 1.4	0.18	2.68	2.82	1.00	0.72	**6.45**	6.79	1.00	0.83	-	
J182916-105444	R5	18 29 16.20	-10 54 44.2	0.00	**1.25**	**1.03**	1.00	0.00	**4.80**	**4.41**	1.00	1.00	-	
J182916-105348	R5	18 29 16.47	-10 53 48.3	0.00	**0.91**	0.64	1.00	0.91	2.28	2.75	0.73	0.65	-	
J182917-094723	X15	18 29 17.37	-9 47 23.2	0.75	0.00	0.43	1.00	**15.49**	0.92	13.35	1.00	-0.90	-	
J182918-103240	R5	18 29 18.37	-10 32 40.4	**2.82**	0.24	**2.98**	1.00	**10.35**	0.00	**9.85**	1.00	-0.94	15.9	U0750_13297244
J182918-112951	X6	18 29 18.67	-11 29 51.4	0.56	1.12	**1.56**	1.00	0.00	0.00	0.00	0.88	0.33	-	

J182918-104451	R5	18 29 18.80	-10 44 51.7	0.23	**0.98**	1.15	1.00	0.31	0.17	0.11	1.00	0.48	-	
J182919-110708	X8	18 29 19.12	-11 7 8.1	0.20	**0.99**	1.23	1.00	0.38	1.34	1.64	0.88	0.62	-	
J182919-104433	R5	18 29 19.35	-10 44 33.4	0.16	**0.78**	0.85	1.00	0.00	0.00	0.00	0.59	0.66	-	
J182920-104237	R5	18 29 20.39	-10 42 37.3	0.33	0.15	0.37	1.00	**1.88**	0.00	1.12	1.00	-0.77	-	
J182920-105042	R5	18 29 20.83	-10 50 42.2	0.79	0.79	1.15	0.39	1.34	**3.10**	**4.43**	1.00	0.34	-	
J182921-100304	X12	18 29 21.80	-10 3 4.6	0.09	**2.04**	**2.06**	1.00	0.00	0.00	0.00	0.00	0.91	-	
J182922-103239	R5	18 29 22.16	-10 32 39.5	0.25	**2.19**	**2.34**	1.00	1.01	2.96	3.58	1.00	0.67	-	
J182923-101211	X12	18 29 23.68	-10 12 11.3	0.29	**3.03**	**3.04**	1.00	0.30	**3.64**	**3.71**	0.73	0.83	-	
J182924-100456	X12	18 29 24.24	-10 4 56.7	0.01	0.56	0.39	1.00	1.80	2.53	**4.50**	1.00	0.34	-	
J182924-102957	X11	18 29 24.41	-10 29 57.6	**2.97**	1.10	**4.15**	1.00	**10.99**	**6.46**	**16.85**	1.00	-0.35	16.1	U0750_13301346
J182924-111634	X8	18 29 24.51	-11 16 34.3	**0.97**	**4.40**	**5.36**	1.00	2.12	**11.87**	**13.62**	1.00	0.66	-	
J182924-094624	X15	18 29 24.76	-9 46 24.6	1.08	0.22	1.24	1.00	**10.20**	3.68	9.75	1.00	-0.51	-	
J182924-105114	R5	18 29 24.93	-10 51 14.5	**1.08**	**2.56**	**3.56**	1.00	**3.66**	**4.54**	**8.11**	1.00	0.25	16.0	U0750_13301735
J182926-095147	X15	18 29 26.99	-9 51 47.1	**2.81**	0.00	1.59	1.00	8.65	0.68	7.52	1.00	-0.92	18.3	U0750_13303273
J182927-095218	X15	18 29 27.26	-9 52 18.9	1.05	0.00	0.00	1.00	**18.51**	6.08	23.09	1.00	-0.56	-	
J182927-102919	X11	18 29 27.34	-10 29 19.1	**0.88**	0.16	1.12	1.00	0.14	0.29	0.13	1.00	-0.58	-	
J182928-105257	R5	18 29 28.43	-10 52 57.9	0.00	0.00	0.00	0.43	2.73	2.22	**4.46**	1.00	-0.10	-	
J182929-094224	X15	18 29 29.82	-9 42 24.4	1.05	0.00	0.27	1.00	3.78	**10.80**	11.58	1.00	0.26	-	
J182930-105926	X8	18 29 30.87	-10 59 26.3	1.31	**6.17**	**7.29**	1.00	1.38	**6.99**	**8.46**	0.96	0.65	-	
J182930-113013	X6	18 29 30.94	-11 30 13.9	0.43	1.44	**1.82**	0.86	4.50	7.42	11.63	1.00	0.38	-	
J182931-110418	X8	18 29 31.22	-11 4 18.6	0.05	0.17	0.37	1.00	**1.45**	0.16	1.54	1.00	-0.54	-	
J182933-103150	X11	18 29 33.11	-10 31 50.3	0.08	**1.69**	**1.76**	1.00	0.65	**6.06**	**6.07**	1.00	0.85	-	
J182934-105142	R5	18 29 34.13	-10 51 42.7	0.56	**1.60**	**2.01**	1.00	0.17	2.91	2.69	1.00	0.65	-	
J182935-111552	X8	18 29 35.23	-11 15 52.5	0.48	0.68	1.28	1.00	2.23	**4.41**	**6.63**	1.00	0.27	-	
J182936-100726	X12	18 29 36.14	-10 7 26.9	0.38	2.14	**2.38**	1.00	1.54	**8.97**	**10.56**	1.00	0.70	-	
J182937-104503	R5	18 29 37.07	-10 45 3.2	0.01	0.96	0.88	1.00	0.00	**3.25**	2.83	1.00	0.99	-	
J182937-093750	X15	18 29 37.59	-9 37 50.9	2.04	2.58	**4.63**	1.00	0.00	0.00	0.00	1.00	0.11	-	
J182938-094900	X15	18 29 38.87	-9 49 0.8	2.41	2.59	**4.90**	1.00	16.04	9.83	**22.53**	1.00	-0.15	-	
J182938-094818	X15	18 29 38.90	-9 48 18.8	0.89	**6.28**	**7.06**	1.00	4.72	11.43	13.27	1.00	0.60	-	
J182939-105834	X8	18 29 39.73	-10 58 34.1	**2.76**	0.24	**2.95**	1.00	**5.68**	1.46	**7.07**	1.00	-0.72	14.9	U0750_13311799
J182940-113225	X6	18 29 40.30	-11 32 25.1	0.91	1.43	**2.33**	1.00	0.82	4.03	3.86	0.98	0.32	-	
J182942-110050	X8	18 29 42.30	-11 0 50.6	0.10	0.79	0.94	1.00	0.65	**1.42**	1.84	0.59	0.56	17.9	-
J182943-105801	X8	18 29 43.98	-10 58 1.4	0.44	**4.50**	**4.84**	1.00	0.18	**7.40**	**7.24**	0.73	0.87	-	
J182944-095122	X15	18 29 44.17	-9 51 22.7	0.00	**2.23**	1.07	1.00	0.00	0.00	0.00	1.00	1.00	18.9	GAL 021.7+00.3
J182946-104357	X10	18 29 46.62	-10 43 57.0	**1.48**	0.01	1.31	1.00	0.00	0.00	0.00	0.00	-0.99	-	
J182947-110945	X8	18 29 47.69	-11 9 45.1	0.04	0.05	0.10	1.00	1.15	1.42	**2.55**	1.00	0.10	-	
J182948-110604	X8	18 29 48.80	-11 6 4.3	**0.81**	**3.38**	**4.26**	1.00	**3.90**	**10.38**	**14.20**	0.88	0.52	-	
J182949-110319	X8	18 29 49.21	-11 3 19.4	0.00	0.01	0.00	1.00	1.17	1.04	**2.10**	1.00	-0.05	-	
J182949-103611	X11	18 29 49.78	-10 36 11.1	0.54	**2.08**	2.39	0.73	2.04	2.94	4.72	1.00	0.41	-	
J182950-110159	X8	18 29 50.27	-11 1 59.8	0.02	0.25	0.24	1.00	0.63	**1.51**	2.03	1.00	0.51	-	
J182950-110942	X8	18 29 50.77	-11 9 42.1	0.00	0.46	0.43	1.00	0.79	**2.24**	2.91	1.00	0.61	-	
J182950-111634	X8	18 29 50.87	-11 16 34.2	0.00	**1.82**	**1.80**	1.00	0.03	**5.78**	**5.63**	1.00	0.99	-	
J182951-100441	X14	18 29 51.57	-10 4 41.0	**12.61**	0.00	10.88	1.00	0.00	0.00	0.00	0.14	-1.00	-	
J182952-110700	X8	18 29 52.94	-11 7 0.0	0.01	0.34	0.44	1.00	1.37	**1.64**	**2.93**	1.00	0.27	16.4	U0750_13321102
J182954-102852	X11	18 29 54.79	-10 28 52.3	0.07	**0.98**	**1.02**	1.00	0.73	0.66	1.21	0.59	0.56	19.0	-
J182955-110533	X8	18 29 55.97	-11 5 33.8	0.05	0.43	0.57	1.00	0.52	1.57	**1.88**	1.00	0.60	17.8	U0750_13323591
J182956-111313	X8	18 29 56.52	-11 13 13.5	**0.84**	**2.21**	**3.00**	1.00	2.04	**5.51**	**7.45**	1.00	0.45	-	
J182956-110458	X8	18 29 56.85	-11 4 58.8	**0.69**	**0.55**	**1.27**	1.00	0.58	1.14	1.63	1.00	0.05	-	
J182957-110235	X8	18 29 57.14	-11 2 35.8	**0.64**	0.48	**1.11**	1.00	0.66	0.00	0.59	1.00	-0.32	-	
J182958-103054	X11	18 29 58.20	-10 30 54.0	**1.68**	**2.53**	**4.17**	0.88	**8.21**	**6.26**	**14.31**	1.00	0.01	16.3	U0750_13325431
J183000-110720	X8	18 30 0.38	-11 7 20.3	0.15	**1.71**	**2.04**	1.00	1.17	**4.99**	**5.96**	1.00	0.71	-	
J183000-094118	X15	18 30 0.85	-9 41 18.9	1.35	0.98	2.39	1.00	5.90	**14.09**	17.67	1.00	0.27	-	
J183002-094953	X15	18 30 2.04	-9 49 53.8	**2.56**	1.56	3.75	1.00	0.00	0.00	0.00	1.00	-0.25	-	
J183002-110735	X8	18 30 2.31	-11 7 35.6	0.08	**1.36**	**1.56**	1.00	0.00	0.00	0.00	0.27	0.67	-	
J183005-104205	X10	18 30 5.60	-10 42 5.5	**1.29**	0.40	1.63	1.00	0.00	1.04	0.00	1.00	-0.29	13.9	U0750_13332059
J183006-102221	X11	18 30 6.89	-10 22 21.1	0.49	0.00	0.44	1.00	0.00	**2.89**	2.43	0.86	0.37	19.9	-
J183012-110759	X8	18 30 12.70	-11 7 59.4	**0.54**	0.33	**0.90**	1.00	**2.04**	**1.15**	**3.39**	1.00	-0.27	-	
J183013-102759	X11	18 30 13.43	-10 27 59.7	0.10	**3.21**	**3.16**	1.00	8.15	24.26	29.97	0.27	0.84	19.2	-
J183013-110450	X8	18 30 13.72	-11 4 50.2	0.05	0.00	0.00	1.00	0.14	**1.90**	1.72	1.00	0.77	-	
J183015-104538	X10	18 30 15.94	-10 45 38.5	0.46	**6.24**	**6.55**	1.00	0.00	**4.83**	**4.34**	0.49	0.89	13.2	U0750_13340834
J183015-102458	X11	18 30 15.98	-10 24 58.0	**1.27**	**1.54**	**2.86**	1.00	2.54	0.45	2.53	0.41	-0.16	13.3	-
J183017-103143	X11	18 30 17.03	-10 31 43.5	0.00	**1.70**	1.54	1.00	0.00	0.95	0.28	1.00	1.00	-	
J183017-095326	X14	18 30 17.12	-9 53 26.3	**9.70**	0.24	9.41	1.00	19.35	18.00	37.19	1.00	-0.44	15.6	U0750_13341855

J183017-110215	X8	18 30 17.34	-11 2 15.6	0.00	0.84	0.78	0.73	1.14	1.81	2.90	1.00	0.50	19.7	-
J183017-102730	X11	18 30 17.99	-10 27 30.5	1.78	0.73	2.43	1.00	7.53	0.00	7.13	1.00	-0.74	12.0	U0750_13342616
J183018-100340	X14	18 30 18.43	-10 3 40.7	0.00	0.97	0.00	1.00	2.79	20.47	24.11	1.00	0.79	-	
J183021-105040	X10	18 30 21.31	-10 50 40.1	0.70	0.00	0.35	1.00	4.36	1.68	5.90	1.00	-0.60	13.9	U0750_13345799
J183029-111110	X8	18 30 29.38	-11 11 10.9	0.33	0.00	0.12	1.00	1.10	2.20	3.17	1.00	0.11	19.7	-
J183031-105152	X10	18 30 31.90	-10 51 52.1	1.59	0.00	1.66	0.63	2.64	0.00	1.74	0.37	-1.00	8.3	U0750_13355585 HD 170566
J183031-094030	X17	18 30 31.99	-9 40 30.5	0.00	11.01	10.03	1.00	0.00	17.88	17.88	0.73	1.00	19.6	-
J183032-094726	X17	18 30 32.64	-9 47 26.4	0.26	2.58	2.81	1.00	1.26	4.64	5.33	1.00	0.70	14.1	U0750_13355870
J183035-102105	X11	18 30 35.91	-10 21 5.9	13.15	0.79	14.19	1.00	36.36	1.02	38.21	1.00	-0.92	13.9	U0750_13358796
J183037-110831	X8	18 30 37.74	-11 8 31.2	1.03	0.00	0.92	1.00	2.07	1.11	3.09	0.98	-0.57	17.0	U0750_13360556
J183038-100248	X14	18 30 38.11	-10 2 48.6	3.41	24.53	26.68	1.00	11.65	42.47	55.61	1.00	0.68	-	
J183040-100155	X14	18 30 40.92	-10 1 55.9	0.40	3.01	2.38	1.00	6.40	26.66	34.20	1.00	0.65	-	
J183041-103320	X10	18 30 41.11	-10 33 20.5	0.16	0.00	0.04	1.00	2.73	5.69	8.23	1.00	0.27	19.4	-
J183041-104121	X10	18 30 41.19	-10 41 21.4	0.42	1.15	1.55	1.00	0.37	3.46	3.74	1.00	0.62	19.6	-
J183041-103939	X10	18 30 41.46	-10 39 39.2	0.27	3.52	3.73	1.00	0.00	9.26	9.48	1.00	0.92	-	
J183045-104414	X10	18 30 45.50	-10 44 14.2	0.14	0.77	1.00	1.00	2.80	1.62	4.17	1.00	0.08	-	
J183046-104623	X10	18 30 46.63	-10 46 23.8	0.10	1.52	1.57	1.00	1.40	1.16	2.47	0.88	0.52	-	
J183047-103853	X10	18 30 47.15	-10 38 53.9	0.00	2.12	2.04	1.00	0.00	0.00	0.00	0.53	1.00	-	
J183047-093925	X17	18 30 47.85	-9 39 25.0	0.25	0.23	0.48	1.00	4.97	0.00	4.19	1.00	-0.79	-	
J183048-095941	X14	18 30 48.02	-9 59 41.6	0.40	2.29	1.29	1.00	12.83	31.53	44.79	1.00	0.46	-	
J183048-100036	X14	18 30 48.26	-10 0 36.3	1.10	2.37	2.12	1.00	5.34	20.11	26.47	1.00	0.51	-	
J183049-102428	X13	18 30 49.98	-10 24 28.0	1.07	0.00	0.76	1.00	3.12	7.17	9.17	1.00	0.11	-	
J183050-103817	X10	18 30 50.02	-10 38 17.3	0.15	2.94	3.12	1.00	0.00	5.54	4.64	1.00	0.94	-	
J183050-104735	X10	18 30 50.08	-10 47 35.4	0.05	0.85	0.91	1.00	0.00	3.11	2.67	0.88	0.95	-	
J183050-102955	X13	18 30 50.31	-10 29 55.5	3.99	0.31	4.09	1.00	6.79	0.00	4.76	1.00	-0.92	14.8	U0750_13371710
J183051-104809	X10	18 30 51.54	-10 48 9.3	0.29	0.75	1.06	1.00	2.31	3.71	5.26	1.00	0.30	16.8	U0750_13373184
J183052-095053	X17	18 30 52.78	-9 50 53.1	0.98	5.35	6.33	1.00	0.00	0.00	0.00	0.12	0.68	-	
J183053-101936	X13	18 30 53.32	-10 19 36.3	3.39	1.49	4.54	0.37	6.26	8.51	13.96	1.00	-0.08	15.3	U0750_13374636
J183053-111255	X8	18 30 53.53	-11 12 55.2	0.00	0.00	0.00	0.00	4.09	2.60	6.74	1.00	-0.18	-	
J183057-103452	X13	18 30 57.96	-10 34 52.3	1.90	5.21	6.73	1.00	4.82	8.62	11.92	1.00	0.37	18.2	U0750_13379212
J183058-104157	X10	18 30 58.20	-10 41 57.4	1.18	0.63	1.95	1.00	2.70	1.18	3.42	1.00	-0.35	19.3	-
J183059-105719	X10	18 30 59.12	-10 57 19.4	0.00	4.04	3.63	1.00	0.49	9.83	9.48	1.00	0.95	-	
J183101-093619	X17	18 31 1.65	-9 36 19.8	1.56	0.00	0.96	1.00	4.81	0.60	5.52	1.00	-0.89	13.4	U0750_13382260
J183102-094607	X17	18 31 2.57	-9 46 7.7	0.61	0.46	1.07	1.00	0.00	2.78	0.60	0.86	0.36	-	
J183103-095813	X14	18 31 3.69	-9 58 13.5	7.17	3.66	10.24	1.00	8.63	0.00	0.00	0.88	-0.47	18.0	G 155-20
J183104-094433	X17	18 31 5.55	-9 44 33.7	0.15	0.00	0.00	1.00	4.77	3.72	8.29	1.00	-0.17	-	
J183109-105113	X10	18 31 9.98	-10 51 13.9	1.79	0.00	1.34	0.71	10.47	1.58	12.10	1.00	-0.81	12.5	U0750_13390292
J183113-094924	X17	18 31 13.12	-9 49 24.5	3.64	5.52	9.16	1.00	5.38	8.36	13.15	0.73	0.20	18.6	U0750_13393881
J183113-102941	X13	18 31 13.74	-10 29 41.8	0.83	2.14	2.88	1.00	1.95	3.23	4.83	1.00	0.36	17.0	U0750_13394553
J183113-094745	X17	18 31 13.83	-9 47 45.5	0.02	0.41	0.49	1.00	0.00	5.83	5.23	1.00	0.99	14.1	U0750_13394829
J183115-102757	X13	18 31 15.01	-10 27 57.8	1.20	1.35	2.29	1.00	3.63	3.46	6.30	0.63	0.01	-	
J183116-100517	X16	18 31 16.22	-10 5 17.3	1.37	0.94	2.31	1.00	6.64	0.00	4.01	1.00	-0.65	-	
J183116-105242	X10	18 31 16.43	-10 52 42.4	2.23	0.06	2.19	1.00	0.82	1.55	2.08	1.00	-0.58	14.6	U0750_13397375
J183116-100921	X16	18 31 16.51	-10 9 21.2	0.00	0.00	0.00	0.00	5.80	42.26	46.60	1.00	0.69	13.2	U0750_13397443
J183119-103230	X13	18 31 19.79	-10 32 30.9	0.27	3.00	3.11	1.00	0.00	0.00	0.00	0.63	0.83	-	
J183119-102546	X13	18 31 19.98	-10 25 46.5	0.00	0.69	0.30	1.00	4.31	0.83	4.97	0.88	-0.22	19.9	-
J183122-101912	X13	18 31 22.84	-10 19 12.4	0.13	1.89	1.82	0.82	0.05	3.41	2.65	1.00	0.91	-	
J183123-094005	X17	18 31 23.78	-9 40 5.8	0.84	0.00	0.24	1.00	1.46	0.82	1.69	1.00	-0.69	-	
J183124-104751	X10	18 31 24.77	-10 47 51.5	5.55	0.00	5.62	1.00	17.21	0.00	9.34	0.27	-1.00	-	
J183129-103435	X13	18 31 29.34	-10 34 35.0	0.74	1.48	2.14	0.86	1.15	6.51	6.59	1.00	0.52	-	
J183131-102957	X13	18 31 31.52	-10 29 57.0	0.00	0.00	0.00	0.73	1.89	4.63	7.16	1.00	0.42	-	
J183133-102208	X13	18 31 33.08	-10 22 8.7	0.37	0.16	0.51	1.00	4.34	3.20	7.52	0.98	-0.19	19.0	-
J183134-095155	X17	18 31 34.29	-9 51 55.2	0.25	1.52	1.72	1.00	1.65	4.29	5.68	1.00	0.58	16.9	U0750_13416775
J183134-100945	X16	18 31 34.47	-10 9 45.1	0.00	2.48	2.13	1.00	0.28	0.00	0.00	1.00	0.91	17.4	U0750_13416951
J183135-102452	X13	18 31 35.20	-10 24 52.5	0.86	0.91	1.61	1.00	0.00	0.00	0.00	0.16	0.03	-	
J183135-100142	X16	18 31 35.64	-10 1 42.6	1.43	2.58	3.91	1.00	3.83	6.59	9.94	1.00	0.27	-	
J183135-102855	X13	18 31 35.72	-10 28 55.4	0.00	0.68	0.59	1.00	1.81	5.20	6.43	1.00	0.60	-	
J183140-093550	X17	18 31 40.77	-9 35 50.4	1.20	0.51	1.55	1.00	0.00	0.57	0.00	1.00	-0.30	15.6	U0750_13423792
J183142-100525	X16	18 31 42.00	-10 5 25.5	0.34	0.98	1.25	1.00	0.00	0.00	0.00	0.98	0.48	-	
J183144-103328	X13	18 31 44.90	-10 33 28.7	1.61	0.25	2.04	1.00	8.67	1.04	9.64	1.00	-0.77	17.4	U0750_13428311
J183153-102449	X13	18 31 53.26	-10 24 49.3	1.54	0.78	2.39	1.00	3.87	0.00	2.46	0.41	0.42	-	
J183155-094706	X17	18 31 55.46	-9 47 6.3	0.22	1.92	2.06	1.00	2.74	10.75	13.35	1.00	0.66	-	

J183156-102447	X13	18 31 56.36	-10 24 47.8	1.54	3.17	4.75	1.00	3.04	7.53	8.87	0.88	0.37	-	
J183157-100033	X16	18 31 57.46	-10 0 33.3	0.00	3.68	3.61	1.00	0.07	1.01	0.70	1.00	0.99	-	
J183157-101123	X16	18 31 57.91	-10 11 23.8	0.00	3.22	2.71	1.00	0.00	5.05	4.02	1.00	1.00	-	
J183201-095342	X16	18 32 1.94	-9 53 42.6	1.28	1.99	3.27	1.00	0.00	0.00	0.00	0.41	0.21	16.1	-
J183204-100035	X16	18 32 4.18	-10 0 35.9	0.82	1.26	2.10	1.00	0.00	1.81	0.47	0.98	0.40	-	
J183204-100601	X16	18 32 4.76	-10 6 1.3	0.32	0.02	0.36	1.00	3.93	1.61	5.55	1.00	-0.49	17.6	U0750_13450456
J183208-093906	X17	18 32 8.93	-9 39 6.2	7.08	62.85	68.77	1.00	0.00	0.00	0.00	0.00	0.79	17.8	GPSR 22.154-0.154
J183209-100648	X16	18 32 9.14	-10 6 48.4	0.00	0.49	0.24	1.00	0.70	0.14	0.73	1.00	0.37	-	
J183210-100031	X16	18 32 10.80	-10 0 31.1	0.88	2.27	3.18	1.00	1.93	4.52	6.43	1.00	0.42	-	
J183213-100633	X16	18 32 13.12	-10 6 33.3	4.11	0.00	4.13	1.00	8.29	0.00	7.78	1.00	-1.00	13.6	U0750_13460167
J183213-095648	X16	18 32 13.88	-9 56 48.6	0.24	1.42	1.64	1.00	0.00	1.74	1.17	1.00	0.78	-	
J183216-102303	X13	18 32 16.38	-10 23 3.1	14.03	44.56	57.50	1.00	0.00	0.00	0.00	0.00	0.51	12.2	U0750_13463736
J183222-095546	X16	18 32 22.54	-9 55 46.8	0.00	2.10	2.01	1.00	0.00	3.06	0.00	0.88	1.00	17.8	U0750_13471175
J183225-100158	X16	18 32 25.19	-10 1 58.7	0.69	0.89	1.52	1.00	0.21	1.42	1.33	1.00	0.28	-	
J183228-100946	X16	18 32 28.44	-10 9 46.8	1.54	3.17	4.75	1.00	3.04	7.53	8.87	0.88	0.15	-	
J183228-100133	X16	18 32 28.59	-10 1 33.8	0.03	1.07	1.03	1.00	0.49	3.18	3.53	1.00	0.83	-	
J183234-100437	X16	18 32 34.32	-10 4 37.7	0.00	3.00	3.07	1.00	0.00	8.79	8.13	1.00	1.00	-	
J183236-101144	X16	18 32 36.64	-10 11 44.8	1.58	5.25	6.87	1.00	0.03	19.33	19.11	1.00	0.75	-	
J183246-100530	X16	18 32 46.78	-10 5 30.6	1.81	0.00	1.93	1.00	1.37	0.00	0.00	1.00	-1.00	15.4	U0750_13500933
J183251-100106	X16	18 32 51.65	-10 1 6.7	8.82	16.42	25.23	1.00	14.56	24.33	38.75	0.51	0.27	-	
J183256-100729	X16	18 32 56.28	-10 7 29.4	0.55	1.42	2.12	1.00	0.00	4.80	4.25	0.59	0.67	17.7	U0750_13512064

See §4.3.1 for details of column contents

Bibliography

Alexander, D. M., Bauer, F. E., Brandt, W. N., Schneider, D. P., Hornschemeier, A. E., Vignali, C., Barger, A. J., Broos, P. S., Cowie, L. L., Garmire, G. P., Townsley, L. K., Bautz, M. W., Chartas, G. & Sargent, W. L. W. 2003, 'The chandra deep field north survey. xiii. 2 ms point-source catalogs', *AJ* **126**, 539–574.

Altenhoff, W. J., Downes, D., Pauls, T. & Schraml, J. 1979, 'Survey of the galactic plane at 4.875 ghz', *AAS* **35**, 23–54.

Asaoka, I. & Koyama, K. 1990, 'Do all the crab-like supernova remnants have an x-ray photon index near a value of 2?', *PASJ* **42**, 625–632.

Baskill, D. B. 2002, 'The x-ray properties of non-magnetic cataclysmic variable stars', *PhD thesis* .

Becker, R. & Helfand, D. 1985, 'Identification of g20.0-0.2 as a crab-like snr', *ApJ.* pp. L25–L28.

Berkhuijsen, E. M., Haslam, C. G. T. & Salter, C. J. 1971, 'Are the galactic loops supernova remnants ?', *A&A* **14**, 252–+.

Bowyer, C. S., Field, G. B. & Mack, J. E. 1968, 'Detection of an anisotropic soft x-ray background flux.', *Nature* **217**, 32–34.

Brown, G. V., Beiersdorfer, P., Liedahl, D. A., Widmann, K. & Kahn, S. M. 1998, 'Laboratory measurement and modeling of the fe xvii x-ray spectrum', *ApJ* **502**, 1015–+.

Bumner, A. N., Coleman, P. C., Kraushaar, W. L., McCammon, D., Palmieri, T. M., Shilepsky, A. & Ulmer, M. 1969, 'Soft x-ray background flux', *Nature* **223**, 1222–1226.

Burton, W. & Gordon, M. 1978, 'Carbon monoxide in the galaxy', *A&A* **63**, 7–27.

Campana, S., Moretti, A., Lazzati, D. & Tagliaferri, G. 2001, 'The deepest x-ray look at the universe', *ApJ* **560**, L19–L22.

Cornelisse, R., Verbunt, F., in't Zand, J. J. M., Kuulkers, E., Heise, J., Remillard, R. A., Cocchi, M., Natalucci, L., Bazzano, A. & Ubertini, P. 2002, 'Bepposax wide field camera observations of six type i x-ray bursters', *A&A* **392**, 885–893.

Cowie, L. L., Garmire, G. P., Bautz, M. W., Barger, A. J., Brandt, W. N. & Hornschemeier, A. E. 2002, 'The 2-8 kev x-ray number counts determined from chandra blank field observations', *ApJ* **566**, L5–L8.

Crasemann, B., Kobias, P., Wang, T., Birdseye, H. & Chen, M. 1974, 'Measurement of the photoelectric cross section of h 2 at 5.4 and 8.4 kev', *Phys.Rev.A* **9**.

Dame, T. M., Hartmann, D. & Thaddeus, P. 2001, 'The milky way in molecular clouds: A new complete co survey', *ApJ* **547**, 792–813.

Davelaar, J., Bleeker, J. A. M. & Deerenberg, A. J. M. 1980, 'X-ray characteristics of loop i and the local interstellar medium', *A&A* **92**, 231–237.

de Geus, E. J. 1992, 'Interactions of stars and interstellar matter in scorpio centaurus', *A&A* **262**, 258–270.

de Geus, E. J., de Zeeuw, P. T. & Lub, J. 1989, 'Physical parameters of stars in the scorpio-centaurus ob association', *A&A* **216**, 44–61.

de Korte, P. A. J., Bleeker, J. A. M., Deerenberg, A. J. M., Hayakawa, S., Yamashita, K. & Tanaka, Y. 1976, 'Features in the brightness distribution and spectra of the soft x-ray background', *A&A* **48**, 235–244.

Dickey, J. M. & Lockman, F. J. 1990, 'H i in the galaxy', *ARA&A* **28**, 215–261.

Diplas, A. & Savage, B. D. 1994, 'An iue survey of interstellar h i ly alpha absorption. 1: Column densities', *ApJS* **93**, 211–228.

Dogiel, V. A., Inoue, H., Masai, K., Schönfelder, V. & Strong, A. W. 2002, 'The origin of diffuse x-ray emission from the galactic ridge. i. energy output of particle sources', *ApJ* **581**, 1061–1070.

Ebisawa, K., Maeda, Y., Kaneda, H. & Yamauchi, S. 2001, 'Origin of the hard x-ray emission from the galactic plane', *Science* **293**, 1633–1635.

Egger, R. J. & Aschenbach, B. 1995, 'Interaction of the loop i supershell with the local hot bubble', *A&A* **294**, L25–L28.

Garmire, G. P., Nousek, J. A., Apparao, K. M. V., Burrows, D. N., Fink, R. L. & Kraft, R. P. 1992, 'The soft x-ray diffuse background observed with the heao 1 low-energy detectors', *ApJ* **399**, 694–703.

Giacconi, R., Kellogg, E., Gorenstein, P., Gursky, H. & Tananbaum, H. 1971, 'An x-ray scan of the galactic plane from uhuru', *ApJ* **165**, L27+.

Green, D. A. 1988, 'A revised reference catalogue of galactic supernova remmnants', *Ap&SS* **148**, 3–74.

Green, D. A. 1996, 'A catalogue of galactic supernova remnants (green 1995)', *VizieR Online Data Catalog* **7187**, 0–+.

Grimm, H.-J., Gilfanov, M. & Sunyaev, R. 2002, 'The milky way in x-rays for an outside observer. log(n)-log(s) and luminosity function of x-ray binaries from rxte/asm data', *A&A* **391**, 923–944.

Gursky, H., Giacconi, R., Paolini, F. & Rossi, B. B. 1963, 'Further evidence for the existence of galactic x-rays', *Phys.Rev.Lett.* **11**, 530–535.

Haberl, F. 2002, 'First xmm-newton results from intermediate polars', *ASP Conf. Ser. 261: The Physics of Cataclysmic Variables and Related Objects* pp. 151–+.

Hayakawa, S., Kato, T., Nagase, F., Yamashita, K. & Tanaka, Y. 1978, 'Distribution and energy spectrum of diffuse soft x-rays', *A&A* **62**, 21–28.

Henry, R. C., Fritz, G., Meekins, J. F., Friedman, H. & Byram, E. T. 1968, 'Possible detection of a dense intergalactic plasma', *ApJ* **153**, L11+.

Hofner, P., Delgado, H., Whitney, B., Churchwell, E. & Linz, H. 2002, 'X-ray detection of the ionizing stars in ultracompact hii regions', *ApJ* **579**, L95–L98.

Hutchinson, I. B., Warwick, R. S. & Willingale, R. 1998, 'Mapping cool gas in the ism with rosat', *LNP* **506**, 283–286.

Hutchinson, I. B., Warwick, R. S. & Willingale, R. 2003, 'The distribution of cool gas in the local interstellar medium', *MNRAS* **inpress**.

Ikhsanov, N. R. 2003, 'On the accretion luminosity of isolated neutron stars', *A&A* **399**, 1147–1150.

Kaneda, H., Makishima, K., Yamauchi, S., Koyama, K., Matsuzaki, K. & Yamasaki, N. Y. 1997, 'Complex spectra of the galactic ridge x-rays observed with asca', *ApJ* **491**, 638–+.

Kolb, U. 1993, *A&A* **271**, 149.

Koyama, K., Maeda, Y., Sonobe, T., Takeshima, T., Tanaka, Y. & Yamauchi, S. 1996, 'Asca view of our galactic center: Remains of past activities in x-rays?', *PASJ* **48**, 249–255.

Kunte, P. K., Rao, A. R. & Vahia, M. N. 1988, 'Variation of stellar coronal activity with age', *Ap&SS* **143**, 207–210.

Kuntz, K. D., Snowden, S. L. & Verter, F. 1997, 'X-ray shadows by high-latitude molecular clouds. i. cartography', *ApJ* **484**, 245–+.

Kuntz, K. & Snowden, S. 2000, 'Deconstructing the spectrum of the soft x-ray background', *ApJ* **543**, 195–215.

Lockman, F. 1989, 'A survey of radio hii regions in the northern sky', *ApJS* **71**, 469–479.

Long, K. S., Garmire, G. P. & Agrawal, P. C. 1976, 'Soft x-rays from the large magellanic cloud - implications on the origin of the diffuse x-ray background', *ApJ* **206**, 411–417.

Lumb, D. H., Warwick, R. S., Page, M. & De Luca, A. 2002, 'X-ray background measurements with xmm-newton epic', *A&A* **389**, 93–105.

Makarov, V. V. 2003, 'The 100 brightest x-ray stars within 50 parsecs of the sun', *AJ* **126**, 1996–2008.

Makishima, K. 1994, 'Elementary processes in dense plasmas', *(Addison and Wesley,Reading)* **p47**.

Marshall, F. J. & Clark, G. W. 1984, 'Sas 3 survey of the soft x-ray background', *ApJ* **287**, 633–652.

Masai, K., Dogiel, V. A., Inoue, H., Schönfelder, V. & Strong, A. W. 2002, 'The origin of diffuse x-ray emission from the galactic ridge. ii. nonequilibrium emission due to in situ accelerated electrons', *ApJ* **581**, 1071–1079.

McCammon, D., Bunner, A. N., Coleman, P. L. & Kraushaar, W. L. 1971, 'A search for absorption of the soft x-ray diffuse flux by the small magellanic cloud', *ApJ* **168**, L33–L37.

Moretti, A., Campana, S., Lazzati, D. & Tagliaferri, G. 2003, 'The resolved fraction of the cosmic x-ray background', *ApJ* **588**, 696–703.

Morrison, R. & McCammon, D. 1983, 'Interstellar photoelectric absorption cross sections, 0.03-10 kev', *ApJ* **270**, 119–122.

Mukai, K. 1993, 'Pimms and viewing: proposal preparation tools', *Legacy* **3**, 21–31.

Muno, M. P., Baganoff, F. K., Bautz, M. W., Brandt, W. N., Broos, P. S., Feigelson, E. D., Garmire, G. P., Morris, M. R., Ricker, G. R. & Townsley, L. K. 2003, 'A deep chandra catalog of x-ray point sources toward the galactic center', *ApJ* **589**, 225–241.

Murakami, H., Koyama, K., Tsujimoto, M., Maeda, Y. & Sakano, M. 2001, 'Asca discovery of diffuse 6.4 kev emission near the sagittarius c complex: A new x-ray reflection nebula', *ApJ* **550**, 297–300.

Nevalainen, J., Lumb, D., dos Santos, S., Siddiqui, H., Stewart, G. & Parmar, A. N. 2001, 'Discovery of an absorbed cluster of galaxies (xmmu j183225.4-103645) close to the galactic plane with xmm-newton', *A&A* **374**, 66–72.

Park, S., Finley, J. P., Snowden, S. L. & Dame, T. M. 1997, 'Evidence for an x-ray–emitting galactic bulge: Shadows cast by distant molecular gas', *ApJ* **476**, 28–+.

Patterson, J. 1984, 'On the origin of the iron k line in the spectrum of the galactic x-ray background', *ApJS* **54**, 443.

Piccinotti, G., Mushotzky, R. F., Boldt, E. A., Holt, S. S., Marshall, F. E., Serlemitsos, P. J. & Shafer, R. A. 1982, 'A complete x-ray sample of the high-latitude /absolute value of b greater than 20 deg/ sky from heao 1 a-2 - log n-log s and luminosity functions', *ApJ* **253**, 485–503.

Predehl, P., Costantini, E., Hasinger, G. & Tanaka, Y. 2003, 'Xmm-newton observation of the galactic centre - evidence against the x-ray reflection nebulae model?', *Astronomische Nachrichten* **324**, 73–76.

Read, A. M. & Ponman, T. J. 2003, 'The xmm-newton epic background: Production of background maps and event files', *A&A* **409**, 395–410.

Rosati, P., Tozzi, P., Giacconi, R., Gilli, R., Hasinger, G., Kewley, L., Mainieri, V., Nonino, M., Norman, C., Szokoly, G., Wang, J. X., Zirm, A., Bergeron, J., Borgani, S., Gilmozzi, R., Grogin, N., Koekemoer, A., Schreier, E. & Zheng, W. 2002, 'The chandra deep field-south: The 1 million second exposure', *ApJ* **566**, 667–674.

Schlegel, D. J., Finkbeiner, D. P. & Davis, M. 1998, 'Maps of dust infrared emission for use in estimation of reddening and cosmic microwave background radiation foregrounds', *ApJ* **500**, 525–+.

Schwope, A. D., Brunner, H., Buckley, D., Greiner, J., Heyden, K. v. d., Neizvestny, S., Potter, S. & Schwarz, R. 2002, 'The census of cataclysmic variables in the rosat bright survey', *A&A* **396**, 895–910.

Seward, F. 1990, 'Einstein observations of galactic supernova remnants', *ApJS* **73**, 781–819.

Simard-Normandin, M. & Kronberg, P. P. 1980, 'Rotation measures and the galactic magnetic field', *ApJ* **242**, 74–94.

Snowden, S. L. 2000, 'The interstellar medium (disk plus halo). the hot part (x-ray and euv)', *'The Century of Space Science', Kluwer Academic Publishers* .

Snowden, S. L., Egger, R., Finkbeiner, D. P., Freyberg, M. J. & Plucinsky, P. P. 1998, 'Progress on establishing the spatial distribution of material responsible for the 1/4 kev soft x-ray diffuse background local and halo components', *ApJ* **493**, 715–+.

Snowden, S. L., Egger, R., Freyberg, M. J., McCammon, D., Plucinsky, P. P., Sanders, W. T., Schmitt, J. H. M. M., Truemper, J. & Voges, W. 1997, 'Rosat survey diffuse x-ray background maps. ii.', *ApJ* **485**, 125–+.

Snowden, S. L., Freyberg, M. J., Plucinsky, P. P., Schmitt, J. H. M. M., Truemper, J., Voges, W., Edgar, R. J., McCammon, D. & Sanders, W. T. 1995, 'First maps of the soft x-ray diffuse background from the rosat xrt/pspc all-sky survey', *ApJ* **454**, 643–653.

Sofue, Y. 1994, 'Giant explosion at the galactic center and huge shocked shells in the halo', *ApJ* **431**, L91–L93.

Sofue, Y. 2000, 'Bipolar hypershell galactic center starburst model: Further evidence from rosat data and new radio and x-ray simulations', *ApJ* **540**, 224–235.

Strüder, L., Briel, U., Dennerl, K., Hartmann, R., Kendziorra, E., Meidinger, N., Pfeffermann, E., Reppin, C., Aschenbach, B., Bornemann, W. & 48 coauthors 2001, 'The european photon imaging camera on xmm-newton:the pn-ccd camera', *A&A* **365**, L18–L26.

Sugizaki, M., Mitsuda, K., Kaneda, H., Matsuzaki, K., Yamauchi, S. & Koyama, K. 2001, 'Faint x-ray sources resolved in the asca galactic plane survey and their contribution to the galactic ridge x-ray emission', *ApJ* **134**, 77–102.

Tanaka, Y. 2002, 'Asca observation of x-ray emission from the galactic ridge', *A&A* **382**, 1052–1060.

Tanaka, Y., Koyama, K., Maeda, Y. & Sonobe, T. 2000, 'Unusual properties of x-ray emission near the galactic center', *PASJ* **52**, L25–L30.

Tanuma, S., Yokoyama, T., Kudoh, T., Matsumoto, R., Shibata, K. & Makishima, K. 1999, 'Magnetic reconnection as the origin of galactic-ridge x-ray emission', *PASJ* **51**, 161–172.

Townes, C. H. 1989, 'The galactic center: Outstanding puzzles and challenges (introductory review)', *IAU Symp. 136* pp. 1–+.

Turner, M. J. L., Abbey, A., Arnaud, M., Balasini, M., Barbera, M., Belsole, E., Bennie, P. J., Bernard, J. P., Bignami, G. F., Boer, M. & 53 coauthors 2001, 'The european photon imaging camera on xmm-newton:the mos cameras', *A&A* **365**, L18–L26.

Valinia, A. & Marshall, F. 1998, 'Rxte measurement of the diffuse x-ray emission from the galactic ridge:implications for the energetics of the interstellar medium', *ApJ* **505**, 134–147.

Valinia, A., Tatischeff, V., Arnaud, K., Ebisawa, K. & Ramaty, R. 2000, 'On the origin of the iron k line in the spectrum of the galactic x-ray background', *ApJ* **543**, 733–739.

Verbunt, F., Bunk, W. H., Ritter, H. & Pfeffermann, E. 1997, 'Cataclysmic variables in the rosat pspc all sky survey.', *A&A* **327**, 602–613.

Wang, Q. D., Gotthelf, E. V. & Lang, C. C. 2001, 'Umass/columbia galactic center chandra survey: The nature of the x-ray emission from the galactic central region', *American Astronomical Society Meeting* **199**, 1429–+.

Warwick, R. S., Barber, C. R., Hodgkin, S. T. & Pye, J. P. 1993, 'The euv source population and the local bubble', *MNRAS* **262**, 289–300.

Warwick, R. S., Turner, M. J. L., Watson, M. G. & Willingale, R. 1985, 'The galactic ridge observed by exosat', *Nature* **317**, 218–221.

Watson, M. G. 1999, 'Faint cvs, the galactic ridge and cv surveys with xmm and axaf', *ASP Conf. Ser. 157: Annapolis Workshop on Magnetic Cataclysmic Variables* **291**, 291–+.

White, N. E. 1989, 'X-ray binaries', *A&A Rev.* **1**, 85–110.

Willingale, R., Aschenbach, B., Griffiths, R. G., Sembay, S., Warwick, R. S., Becker, W., Abbey, A. F. & Bonnet-Bidaud, J.-M. 2001, 'New light on the x-ray spectrum of the crab nebula', *A&A* **365**, L212–L217.

Willingale, R., Bleeker, J. A. M., van der Heyden, K. J. & Kaastra, J. S. 2003, 'The mass and energy budget of cassiopeia a', *A&A* **398**, 1021–1028.

Willingale, R., Hands, A. D. P., Warwick, R. W., Snowden, S. L. & Burrows, D. N. 2003, 'The x-ray spectrum of the north polar spur', *MNRAS* **343**, 995–1001.

Wilson, T. L. 1972, '4830 milz observations of the formaldehyde molecule in the direction of discrete radio sources', *A&A* **19**, 354–+.

Worrall, D., Marshall, F., Boldt, E. & Swank, J. 1982, 'Heao 1 measurements of the galactic ridge', *ApJ* **255**, 111–121.

Yamasaki, N. Y., Ohashi, T., Takahara, F., Yamauchi, S., Koyama, K., Kamae, T., Kaneda, H., Makishima, K., Sekimoto, Y., Hirayama, M., Takahashi, T., Yamagami, T., Gunji, S., Tamura, T., Miyazaki, S. & Nomachi, M. 1997, 'Hard x-ray emission from the galactic ridge', *ApJ* **481**, 821–+.

Yan, M., Sadeghpour, H. R. & Dalgarno, A. 1998, 'Photoionization cross sections of he and h 2', *ApJ* **496**, 1044–+.